Complexity

New Methods for Analyzing Complex Biomedical Systems and Signals

Lead Guest Editor: Irini Reljin
Guest Editors: Zoran Obradović, Mirjana Popović, and Valeri Mladenov

New Methods for Analyzing Complex Biomedical Systems and Signals

Complexity

New Methods for Analyzing Complex Biomedical Systems and Signals

Lead Guest Editor: Irini Reljin
Guest Editors: Zoran Obradovic, Mirjana Popovic, and Valeri Mladenov

Copyright © 2018 Hindawi. All rights reserved.

This is a special issue published in "Complexity." All articles are open access articles distributed under the Creative Commons Attribution License, which permits unrestricted use, distribution, and reproduction in any medium, provided the original work is properly cited.

Editorial Board

José A. Acosta, Spain
Tarek Ahmed-Ali, France
Rodrigo Aldecoa, USA
Basil M. Al-Hadithi, Spain
Juan A. Almendral, Spain
Diego R. Amancio, Brazil
David Arroyo, Spain
Mohamed Boutayeb, France
Arturo Buscarino, Italy
Guido Caldarelli, Italy
Eric Campos-Canton, Mexico
Mohammed Chadli, France
Diyi Chen, China
Giulio Cimini, Italy
Danilo Comminiello, Italy
Manlio De Domenico, Italy
Pietro De Lellis, Italy
Albert Diaz-Guilera, Spain
Thach Ngoc Dinh, France
Jordi Duch, Spain
Marcio Eisencraft, Brazil
Joshua Epstein, USA
Mondher Farza, France
Thierry Floquet, France
Mattia Frasca, Italy
Lucia Valentina Gambuzza, Italy
Bernhard C. Geiger, Austria
Carlos Gershenson, Mexico
Peter Giesl, UK
Sergio Gómez, Spain
Wesley N. Gonçalves, Brazil
Lingzhong Guo, UK
Xianggui Guo, China
Sigurdur F. Hafstein, Iceland
Chittaranjan Hens, Israel
Giacomo Innocenti, Italy
Sarangapani Jagannathan, USA
Mahdi Jalili, Australia
Jeffrey H. Johnson, UK
M. Hassan Khooban, Denmark
Vincent Labatut, France
Lucas Lacasa, UK
Xiaoping Liu, Canada
Rosa M. Lopez Gutierrez, Mexico
Vittorio Loreto, Italy
Didier Maquin, France
Eulalia Martínez, Spain
Marcelo Messias, Brazil
Ana Meštrović, Croatia
Ch. P. Monterola, Philippines
Marcin Mrugalski, Poland
Roberto Natella, Italy
Irene Otero-Muras, Spain
Yongping Pan, Singapore
Daniela Paolotti, Italy
Mahardhika Pratama, Singapore
Luis M. Rocha, USA
Miguel Romance, Spain
Avimanyu Sahoo, USA
Matilde Santos, Spain
Hiroki Sayama, USA
Michele Scarpiniti, Italy
Enzo Pasquale Scilingo, Italy
Dan Selişteanu, Romania
Dimitrios Stamovlasis, Greece
Samuel Stanton, USA
Roberto Tonelli, Italy
Shahadat Uddin, Australia
Gaetano Valenza, Italy
Dimitri Volchenkov, USA
Christos Volos, Greece
Zidong Wang, UK
Yan-Ling Wei, Singapore
Honglei Xu, Australia
Xinggang Yan, UK
Massimiliano Zanin, Spain
Hassan Zargarzadeh, USA
Rongqing Zhang, USA

Contents

New Methods for Analyzing Complex Biomedical Systems and Signals
Irini Reljin, Zoran Obradović, Mirjana B. Popović, and Valeri Mladenov
Editorial (3 pages), Article ID 6405121, Volume 2018 (2018)

Factor Analysis for Finding Invariant Neural Descriptors of Human Emotions
Vitor Pereira, Filipe Tavares, Petya Mihaylova, Valeri Mladenov, and Petia Georgieva
Research Article (8 pages), Article ID 6740846, Volume 2018 (2018)

High-Density Lipoproteins-Associated Proteins and Subspecies Related to Arterial Stiffness in Young Adults with Type 2 Diabetes Mellitus
Xiaoting Zhu, Amy S. Shah, Debi K. Swertfeger, Hailong Li, Sheng Ren, John T. Melchior, Scott M. Gordon, W. Sean Davidson, and L. Jason Lu
Research Article (14 pages), Article ID 7514709, Volume 2018 (2018)

Vector Autoregressive Hierarchical Hidden Markov Models for Extracting Finger Movements Using Multichannel Surface EMG Signals
Nebojša Malešević, Dimitrije Marković, Gunter Kanitz, Marco Controzzi, Christian Cipriani, and Christian Antfolk
Research Article (12 pages), Article ID 9728264, Volume 2018 (2018)

Sparse Learning of the Disease Severity Score for High-Dimensional Data
Ivan Stojkovic and Zoran Obradovic
Research Article (11 pages), Article ID 7120691, Volume 2017 (2018)

HSimulator: Hybrid Stochastic/Deterministic Simulation of Biochemical Reaction Networks
Luca Marchetti, Rosario Lombardo, and Corrado Priami
Research Article (12 pages), Article ID 1232868, Volume 2017 (2018)

Identification of S1 and S2 Heart Sound Patterns Based on Fractal Theory and Shape Context
Ana Gavrovska, Goran Zajić, Vesna Bogdanović, Irini Reljin, and Branimir Reljin
Research Article (9 pages), Article ID 1580414, Volume 2017 (2018)

Interpolative Boolean Networks
Vladimir Dobrić, Pavle Milošević, Aleksandar Rakićević, Bratislav Petrović, and Ana Poledica
Research Article (15 pages), Article ID 2647164, Volume 2017 (2018)

New Perspectives for Computer-Aided Discrimination of Parkinson's Disease and Essential Tremor
P. Povalej Bržan, J. A. Gallego, J. P. Romero, V. Glaser, E. Rocon, J. Benito-León, F. Bermejo-Pareja, I. J. Posada, and A. Holobar
Research Article (17 pages), Article ID 4327175, Volume 2017 (2018)

Monitoring Effective Connectivity in the Preterm Brain: A Graph Approach to Study Maturation
M. Lavanga, O. De Wel, A. Caicedo, K. Jansen, A. Dereymaeker, G. Naulaers, and S. Van Huffel
Research Article (13 pages), Article ID 9078541, Volume 2017 (2018)

Follow-Up and Risk Assessment in Patients with Myocardial Infarction Using Artificial Neural Networks
Tatjana Gligorijević, Zoran Ševarac, Branislav Milovanović, Vlado Đajić, Marija Zdravković, Saša Hinić, Marina Arsić, and Milica Aleksić
Research Article (8 pages), Article ID 8953083, Volume 2017 (2018)

On Consistency of Cross-Approximate Entropy in Cardiovascular and Artificial Environments
Tamara Skoric, Olivera Sarenac, Branislav Milovanovic, Nina Japundzic-Zigon, and Dragana Bajic
Research Article (15 pages), Article ID 8365685, Volume 2017 (2018)

Hindawi
Complexity
Volume 2018, Article ID 6405121, 3 pages
https://doi.org/10.1155/2018/6405121

Editorial

New Methods for Analyzing Complex Biomedical Systems and Signals

Irini Reljin,[1] **Zoran Obradović**,[2] **Mirjana B. Popović**,[1,3] **and Valeri Mladenov**[4]

[1]*School of Electrical Engineering, University of Belgrade, 11000 Belgrade, Serbia*
[2]*Center for Data Analytics and Biomedical Informatics, Temple University, Philadelphia, PA 19122, USA*
[3]*Institute for Medical Research, University of Belgrade, 11000 Belgrade, Serbia*
[4]*Department of Theoretical Electrical Engineering, Technical University of Sofia, 1000 Sofia, Bulgaria*

Correspondence should be addressed to Irini Reljin; irinitms@gmail.com

Received 13 March 2018; Accepted 13 March 2018; Published 24 May 2018

Copyright © 2018 Irini Reljin et al. This is an open access article distributed under the Creative Commons Attribution License, which permits unrestricted use, distribution, and reproduction in any medium, provided the original work is properly cited.

In recent years, there has been significant progress in the applications of sensing devices in acquiring biomedical signals. Availability of big and/or high dimensional data obtained by new instruments inspired the development of novel information processing methods aimed at significantly improving the understanding of subtle and complex mechanisms of biomedical processes. Such data have proved useful in diagnosis, prediction of health state, survival prognosis, and therapy optimization. New sensing devices generate precise signals, large-scale biomedical data which has opened challenging problems for managing, processing, storing, retrieving, transferring, and interpreting such data. Therefore, we have invited the researches to contribute their research on new algorithms and tools for modeling, processing, and analyzing complex biomedical signals. After rigorous review, this special issue accepted eleven articles on this topic which are summarized here.

In the paper "High-Density Lipoproteins-Associated Proteins and Subspecies Related to Arterial Stiffness in Young Adults with Type 2 Diabetes Mellitus," X. Zhu et al. analyzed the correlation of phospholipid-associated protein with a pulse wave velocity (PWV) in order to find which protein is related to arterial stiffness in persons with type 2 diabetes mellitus (T2D). Five adolescents with T2D and six lean controls with no evidence of chronic disease were under consideration. By integrating patient clinical data, biological experiments, and bioinformatics analysis to reveal arterial stiffness-related high-density lipoproteins and subspecies, the authors found, among 68 detected phospholipid-associated proteins, seven as negatively correlated with PWV, indicating they may be atheroprotective, and nine proteins as positively correlated with PWV, suggesting they may be related to arterial stiffness.

Pathological tremor is a complex movement disorder of different causes, affecting about 5% of the population over the age of 65. The quantification and discrimination of Parkinsonian disease (PD) and essential tremor (ET) have significant impact on both patient treatment and the development of new interventions in clinical practice. In the paper "New Perspectives for Computer-Aided Discrimination of Parkinson's Disease and Essential Tremor," P. P. Bržan et al. proposed novel metrics to quantify and discriminate PD and ET tremor. These metrics, as well as other known tremor-related movement metrics, were tested over 27 PD and 27 ET patients. The discriminatory power of all of these metrics was evaluated based on the receiver operating characteristics, decision tree modeling, and binary logistic regression. After testing the discriminative power of individual metrics, it was found that the new metrics outperformed alternative methods.

Auscultation is widely used for evaluation of cardiac function. Such analysis mostly depends on the individual skills of the physician, and therefore there is a growing demand for automatic heart sound interpretation methods. The initial step in heart sound analysis is to identify primary heart sounds, S1 and S2. Proper identification of these sounds is of key importance for identifying other components of

heart signal, such as extra sounds and murmurs. In the paper "Identification of S1 and S2 Heart Sound Patterns Based on Fractal Theory and Shape Context," A. Gavrovska et al. proposed a new method for identifying and differentiating primary heart sounds S1 and S2, without the electrocardiogram reference. The new method is based on adaptive filtering and a modified blanket approach, which describe the shape of the heart signal. After determining proposed characteristic descriptors, the SVM-based classification and the fivefold cross-validation have been performed. Nine hundred sound sequences collected from the University Children's Hospital in Belgrade, Serbia, were analyzed. The evaluation results are obtained by using the receiver operating characteristic (ROC) curve. Calculated AUC (area under the curve) and the classification accuracy and F-measure were used as performance measures. Results are compared with other known shape related methods. The proposed method, using only three descriptors, is of high accuracy (higher than 95%) and outperforms other methods by at least 6%.

In the paper "Follow-Up and Risk Assessment in Patients with Myocardial Infarction Using Artificial Neural Networks," T. Gligorijević et al. described a novel method for identifying individuals with high risk of death after acute myocardial infarction by using artificial neural networks (ANNs). Training data for ANN was 1,705 patients admitted between 2003 and 2013 to Coronary Care Unit of Clinical Hospital Center Bežanijska Kosa, Belgrade, Serbia, who underwent 24-hour ECG monitoring, short ECG analysis, noninvasive beat-to-beat heart rate variability, and baroreflex sensitivity. The proposed neural network classifier showed good performance for survival prediction: 88% accuracy, 81% sensitivity, 93% specificity, 0.85 F-measure, and area under the curve value of 0.77. These findings support the theory that patients with high sympathetic activity (reduced baroreflex sensitivity) have an increased risk of mortality independent of other risk factors and that artificial neural networks can indicate higher risk individuals.

The approximate entropy (ApEn) is one of the most used nonlinear techniques for quantifying the complexity and unpredictability of time series. The ApEn is approved as a supporting tool in preclinical and clinical studies, with the most prominent applications in cardiovascular studies. One of the very first ApEn modifications is the Cross-ApEn (XApEn) that estimates mutual predictability of two simultaneously recorded time series. In view of ApEn as a complexity measure of solitary signal, XApEn should have become an equivalent tool for paired physiological processes. In the paper "On Consistency of Cross-Approximate Entropy in Cardiovascular and Artificial Environments," T. Skoric et al. studied the problems that preclude wider XApEn implementation and proposed methods for their adjustment. Their study used three types of data: artificial (for testing the stability of estimated values), animal (for method development and for repeated testing), and human (to validate the derived methods in typical real applications where the records are short). The new approach is verified by using cardiovascular signals recorded from rats (long signals) and healthy volunteers (short clinical signals), proposing a change of traditional parameter guidelines.

In the paper "Sparse Learning of the Disease Severity Score for High-Dimensional Data," I. Stojkovic and Z. Obradovic proposed a novel approach to the problem of learning disease severity scores in presence of irrelevant or high-dimensional measurements. The proposed formulation of sparse severity score learning forces weights of most of the features to be exactly zero, therefore effectively performing feature selection by learning the sparse linear scoring function. This novel severity score objective function is convex and nonsmooth and it precludes the direct use of convenient optimization tools like gradient-based methods. They defined the severity score as a linear combination of intensities of the most relevant features. The proposed approach might be used as an effective and reliable tool for both scoring function learning and biomarker discovery, as demonstrated by identifying a stable set of genes related to influenza symptoms' severity, which are enriched in immune-related processes.

Modeling and representing biological processes are a challenging problem for biochemical researchers. Computational systems biology is becoming a fundamental tool of life-science research, which aims at developing models representing biological phenomena and reliable computational techniques for their simulation. In the paper "HSimulator: Hybrid Stochastic/Deterministic Simulation of Biochemical Reaction Networks," L. Marchetti et al. considered this problem and described the simulator for mass-action reaction. They combined several strategies including exact stochastic simulation, deterministic simulation, and hybrid simulation. For deterministic and hybrid simulations, the simulator automatically translates the mass-action reaction network into a set of ordinary differential equations suitable for further resolving. Their simulator provides a suite of state-of-the-art simulation algorithms including the exact algorithm, RSSA (rejection-based stochastic simulation algorithm), and the first publicly available implementation of its hybrid version, HRSSA. The benchmarks in the paper show that their simulator implementation is often faster than the state-of-the-art COPASI (complex pathway simulator) simulator.

In the paper "Interpolative Boolean Networks," V. Dobrić et al. proposed a generalized Boolean network adaptive with respect to the nature of input variables which offers greater descriptive power as compared with traditional models. Instead of classical Boolean networks, which are binary, by introducing the gradation in this model more descriptive power can be provided. This approach, called by authors the interpolative Boolean networks, is based on interpolative Boolean algebra: the $[0, 1]$-valued realization of Boolean algebra. Interpolative Boolean networks can be used to predict behavior of complex systems. For the purpose of their practical application, a simple software tool is developed. When applied on two examples from the literature and compared against other real-valued logical approaches, the proposed interpolative Boolean networks provided a superior descriptive power.

In the paper "Monitoring Effective Connectivity in the Preterm Brain: A Graph Approach to Study Maturation," M. Lavanga et al. investigated effective electroencephalography (EEG) based brain connectivity in premature infants, whose postmenstrual age ranged from 27 to 42 weeks. Results

showed that the EEG-graphs changed with age in terms of topology. In particular, the clustering coefficient and the spectral radius decreased with maturation, while the path length increased. Results showed that the EEG-connectivity, assessed using graph theory indices, moved from a small-world network to a random one, since the clustering coefficient increases and the path length decreases. Their results showed that it is possible to predict the age of the infant with a root mean-squared error equal to 2.11 weeks. These results are consistent with the ones reported in the literature for age prediction in preterm babies.

Over the last decade, various methods were proposed for characterizing human emotions from electroencephalogram (EEG). In the paper "Factor Analysis for Finding Invariant Neural Descriptors of Human Emotions," V. Pereira et al. proposed a new spatial-temporal feature set with clear physical ground over selected EEG electrodes and the factor analysis (FA) as an alternative method to extract the most important components of the feature set. In contrast to the widely used principal component analysis, FA preserves the relation between the factors and the feature set and therefore the conclusions are more easily interpreted by psychologists and neurophysiologists. The combination of the proposed features and FA resulted in finding the most representative neural descriptors of the emotion valence, invariant with respect to trials and subjects. The authors provided evidence that the factor analysis of event-related potentials is a promising approach to extract statistical underlying correlations of the brain activity among subjects and therefore decode human emotional states. By extracting temporal and spatial EEG features, they showed that it is possible to build Brain Computer Interface for decoding human emotions across various subjects.

In the paper "Vector Autoregressive Hierarchical Hidden Markov Models for Extracting Finger Movements Using Multichannel Surface EMG Signals," N. Malešević et al. presented a novel computational technique intended for the robust and adaptable control of a multifunctional prosthetic hand using multichannel surface electromyography (EMG). Their study indicates that using mean absolute value feature coupled with hierarchical hidden semi-Markov models algorithm leads to movement decoding accuracy higher than other combinations of features and classifiers. This combination also guaranties the shortest motion selection and motion completion times, influencing a response of a prosthetic hand to a user intent. Their algorithm is characterized by low computational complexity for the execution, easy expansion, and noise resiliency.

We believe this special issue is useful for investigators who work with complex biomedical signals. We hope that the papers from this issue will initiate further interest in analyzing complex biomedical systems.

Acknowledgments

The guest editorial team thanks the authors who submitted their papers to this special issue. Also, our sincere thanks go to reviewers for their dedicated efforts in evaluating the submitted papers and providing helpful comments. Finally, we thank the journal's Editorial Board for their help and assistance.

Irini Reljin
Zoran Obradović
Mirjana B. Popović
Valeri Mladenov

Hindawi
Complexity
Volume 2018, Article ID 6740846, 8 pages
https://doi.org/10.1155/2018/6740846

Research Article

Factor Analysis for Finding Invariant Neural Descriptors of Human Emotions

Vitor Pereira,[1] Filipe Tavares,[1] Petya Mihaylova,[2] Valeri Mladenov,[2] and Petia Georgieva[1]

[1]*Department of Electronics Telecommunications and Informatics/IEETA, University of Aveiro, Aveiro, Portugal*
[2]*Technical University of Sofia, Sofia, Bulgaria*

Correspondence should be addressed to Petia Georgieva; petia@ua.pt

Received 2 August 2017; Accepted 16 January 2018; Published 19 March 2018

Academic Editor: Vittorio Loreto

Copyright © 2018 Vitor Pereira et al. This is an open access article distributed under the Creative Commons Attribution License, which permits unrestricted use, distribution, and reproduction in any medium, provided the original work is properly cited.

A major challenge in decoding human emotions from electroencephalogram (EEG) data is finding representations that are invariant to inter- and intrasubject differences. Most of the previous studies are focused in building an individual discrimination model for every subject (subject dependent model). Building subject-independent models is a harder problem due to the high data variability between different subjects and different experiments with the same subject. This paper explores, for the first time, the Factor Analysis as an efficient technique to extract temporal and spatial EEG features suitable to build brain-computer interface for decoding human emotions across various subjects. Our findings show that early waves (temporal window of 200–400 ms after the stimulus onset) carry more information about the valence of the emotion. Also, spatial location of features, with a stronger impact on the emotional valence, occurs in the parietal and occipital regions of the brain. All discrimination models (NN, SVM, kNN, and RF) demonstrate better discrimination rate of the positive valence. These results match closely experimental psychology hypothesis that, during early periods after the stimulus presentation, the brain response—to images with highly positive valence—is stronger.

1. Introduction

Electroencephalography (EEG) is an efficient noninvasive technique to analyze brain activity by measuring the electrical activity on the surface of the subject's scalp. EEG is particularly useful for development of brain-computer interfaces (BCIs). BCI refers to the direct communication pathway between the brain and an external device, such as a computer. In this paper, we focus on a subarea of BCI known as affective computing, which studies the neural mechanisms of emotions. The goal of the present work is to reliably discriminate between human emotions with positive or negative valence based on extracted EEG neural signatures. The valence, when used in psychology, refers to the "positiveness" or "negativeness" perceived by a person when exposed to some stimulus or events.

Working with EEG data brings several challenges. Brain waves recorded in the EEG have a very low signal-to-noise ratio and the noise comes from a variety of sources. For instance, the sensitive recording equipment can easily pick up electrical line noise from the surroundings. Other unwanted electrical noise can come from muscle activity, eye movements, or blinks. The EEG lacks spatial resolution; however it has a good (millisecond) time resolution to record both slowly and rapidly changing dynamics of the brain activity. Therefore, in order to identify the brain activity of interest, the relevant content of the EEG signal needs to be separated from the noise and the background processes.

EEG offers many advantages for construction of a BCI system but also several disadvantages. Most importantly, EEG is a noninvasive method for measuring brain activity. This removes the need for costly and risky surgical procedures, such as electrophysiology, in which intracortical devices such as needles or tubes may be inserted directly into the brain material, or electrocorticography, in which an array of electrodes is implanted under the skull. Both systems risk permanent and life threatening damage to a patient's brain and require costly surgical expertise to carry them out safely. Also useful for designing a BCI, EEG does not require the

patient to be stationary like other noninvasive imaging systems such as functional magnetic resonance imaging (fMRI) and magnetoencephalography (MEG), both of which can only be carried out by large scale and expensive equipment. EEG has the ability to produce high time resolution data, which is a necessity for near-real-time systems.

Research on methods of extracting emotions from EEG patterns has intensified over the last decade. A comprehensive list of EEG-based emotion recognition systems is provided in [1]. Effective features that correlate EEG patterns and emotions are discovered both in time and in frequency domains. In the frequency domain, the EEG energy and power, the Power Spectral Density (PSD), and the Spectral Power Asymmetry (ASM) of certain bands, such as beta (16–32 Hz) and gamma (32–64 Hz), are most frequently selected. In the time domain, the Fractal Dimension (FD), Higher Order Crossings (HOC), and sample entropy have been successfully utilized [2]. More recent strategies propose Deep Learning networks to extract high-level representations of the raw EEG signals [3, 4]. To alleviate overfitting problem, principal component analysis (PCA) is applied to extract the most important components of the initial feature set. Hybrid approaches using multidimensional information, such as EEG and facial expression [5] and EEG combined with Biometric and Eye Tracking Technologies [6], proved to outperform the single modality (only EEG signals) emotion classification.

The refereed studies usually build an individual discrimination model for every subject (subject dependent model). Building subject-independent models is a harder problem due to the high data variability between different subjects and different experiments with the same subject. The extracted features improve the emotion discrimination performance indeed; however their computational nature (e.g., entropy, FD, and wavelet transform) turn to be more difficult to be interpreted by nonexperts in machine learning and data mining.

The contribution of this paper is twofold. First, we propose a new spatial-temporal feature set with clear physical ground, that is, local amplitudes and their latencies (time of occurrence) over selected EEG electrodes. Second, we propose, for the first time in affective computing, the Factor Analysis (FA) as an alternative method to extract the most important components of the feature set. In contrast to the widely used PCA, FA preserves the relation between the factors and the feature set and therefore the conclusions are more easily interpreted by psychologists and neurophysiologists. The combination of the proposed features and FA resulted into finding the most representative neural descriptors of the emotion valence, invariant with respect to trials and subjects.

Many of the previous studies are based on the publicly available dataset for emotion analysis DEAP, where EEG and peripheral physiological signals of 32 subjects are simultaneously recorded as they watched music videos [7]. In the present work, data generated during experiments in the University of Aveiro are used. Time-locked EEG signals, a.k.a. Event-Related Potentials (ERPs), were registered during periods when the subjects have been exposed to high arousal images [8]. Though the present results were obtained with different data, our findings support previous neurophysiological studies regarding the correlation between early and late EEG waves (P1, N1, P2, and N2 components) and their respective latencies with human emotional states [9–11]. This is also a valuable contribution to the efforts of understanding the neural correlations of the emotions.

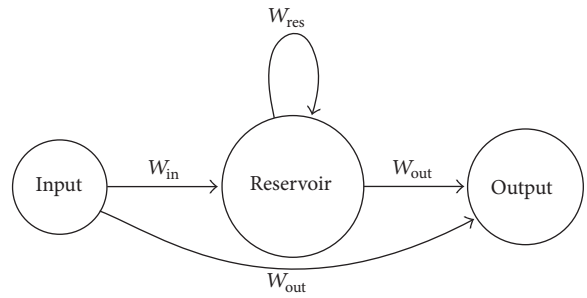

Figure 1: Echo State Network (ESN) architecture. Image by C. Areshenkoff. Obtained from http://areshenk-research-notes.com/echo-state-networks-in-r/.

This paper is organized in the following way. In Section 2 an overview of state-of-the-art feature extraction techniques is provided. In Section 3 the experimental dataset is described. In Section 4 the selected discrimination models are detailed. The results of decoding human emotions based on the extracted neural descriptors are disused in Section 5. The conclusions are summarized in Section 6.

2. Invariant Feature Extraction

In this section some of the most successfully applied feature extraction and dimensionality reduction techniques in multisubject data framework are reviewed.

2.1. Echo State Networks for Feature Extraction. Bozhkov et al. [12] introduced a feature extraction method using Echo State Networks (ESN). ESN is a particular type of Recurrent Neural Networks, also known as a *reservoir computing*, Figure 1. The connections in the reservoir are initialized randomly and remain unaltered during the ESN's training. The input layer is connected to the reservoir and to the output layer and its weights are also randomly initialized and untrained. Only the weights connecting the output of the reservoir to the output layer are trained [13]. The computational advantage of the ESN due to lower number of training weights limits its capacity to extract the underlying data characteristics.

A modification of the ESN is proposed in [14] to fix this problem, where the reservoir weights are iteratively updated applying intrinsic plasticity (IP) adaptation rule. IP computes the equilibrium states of the reservoir neurons and this adaptation step greatly improves the low dimensional projections of the equilibrium states at the output layer.

2.2. Interval Feature Extraction. Kuncheva and Rodríguez [15] introduced interval feature extraction (IFE) which consists of extracting features derived from the signal over time segments of various lengths.

If x_i is the value of the signal at time i where $i = 1, \ldots, T$ spans the ERP episode then nested time intervals are formed

for each i using the remaining samples $x_i, \ldots, x_T$. The interval length is varied, and, for example, a sequence of such intervals can be $\{x_i, x_{i+1}\}, \{x_i, x_{i+1}, x_{i+2}, x_{i+3}\}, \ldots, \{x_{i+1}, x_{i+2}\}$, ending with $\{x_{T-1}, x_T\}$. The following quantities are extracted from each interval:

(i) Average amplitude: μ

(ii) Standard deviation: σ

(iii) Covariance:

$$\gamma = \frac{1}{l}\sum_{k=i_b}^{i_e} k x_k - \mu\frac{i_b + i_e}{2}, \tag{1}$$

where i_b and i_e are the starting and ending time indexes and the length of the interval is $l = i_e - i_b + 1$.

2.3. Independent Component Analysis. Independent component analysis (ICA) is typically used to "clean up" EEG data by removing noisy electrodes, blinks, and other artefacts. ICA produces a matrix s of maximally independent components when multiplying an unmixing linear static transformation matrix W to the original data x.

$$s = Wx. \tag{2}$$

Stewart et al. [16] combine ICA with support vector machine (SVM) to classify whether the EEG readings indicate the presence of visual object stimuli. Mueller et al. [17] also use ICA and SVM to discriminate ADHD versus healthy adults through EEG data captured during a Go/NoGo task. In both studies [16, 17] the matrix W is found applying Infomax algorithm [18]. Infomax maximizes the joint entropy of nonlinearly transformed ensembles of zero-mean input vectors.

Solving the previous equation for x,

$$x = W^{-1}s. \tag{3}$$

Further,

$$x = \sum x_i = \sum W_i^{-1} s_i, \tag{4}$$

where s_i is the ith independent component and W_i^{-1} is its respective cofactor. s_i can be obtained as

$$s_i = W_{zi}x. \tag{5}$$

W_{zi} is a sparse matrix with all entries equal to zero except the ith raw. Finally,

$$x_i = W^{-1}W_{zi}x. \tag{6}$$

$W^{-1}W_{zi}$ is the filter that projects the original data into the space of the independent components. This filter was used to decompose individual ERP waves into individual components.

2.4. Graded Probabilistic Clustering. Masulli et al. [19] proposed a fuzzy Graded Probabilistic Clustering (GPC-II), where each data point x_i can belong to more than one cluster. The centroids y_j of the clusters are given as the mean of all points weighed by their degree (membership) of belonging to the cluster u_{ij}:

$$y_j = \frac{\sum_i u_{ij} x_i}{\sum_i u_{ij}}. \tag{7}$$

GPC-II was applied in experiments involving Go/NoGo task where the participants were shown pictures of faces and asked to press a button when the face shows "expressed neutral emotion." The goal was to find clusters in the recorded multisubject EEG data. GPC-II runs with a high number of clusters and at each iteration a cluster that covers only a single trial (a "singleton") is removed. Neighbor clusters are merged based on the Jaccard index as a measure of closeness of pair of clusters. Two clusters are merged if their index surpasses a threshold Jaccard index value. The new centroid is computed as the average of the centroids of the previous clusters weighed by the membership values of their elements. This procedure is applied iteratively until no more neighboring clusters can be merged.

2.5. Optimal Feature Selection. Optimal feature selection (OFS) is a deterministic greedy algorithm that takes the locally optimal choice at each stage [20]. OFS can be implemented in two ways: forward selection or backward elimination.

Forward Selection. Build data models based on individual features. Choose the best *k1* features. Make all two by two combinations of the *k1* selected features and build new data models. Choose the next group of best *k2* features and make all three by three combinations of them. Repeat the process until there is no more improvement in the model performance. The choice of subsequent feature subset combinations may vary in order to reflect the experience gained during the extraction process and the application in hand.

Backward Elimination. The model is trained on the complete set of features and weights are assigned to each of them. The features with the smallest weights are then pruned from the set. This process is repeated until the model performance deteriorates below a certain threshold.

2.6. Principal Component Analysis. Generally, Principal Component Analysis (PCA) refers to the statistical process used to emphasize variation for which principal data components are computed and bring out strong patterns in the dataset. It is often used to make data easy to explore and to visualize everything in a single 2D graph (usually called a biplot).

Consider that $X = [X_1, \ldots, X_p]$ are the p random variables under study. PCA will consist of obtaining p linear combinations of these p variables as follows:

$$\begin{aligned} Y_1 &= a_{11}X_1 + a_{21}X_2 + \cdots + a_{p1}X_p \\ Y_2 &= a_{12}X_1 + a_{22}X_2 + \cdots + a_{p2}X_p \\ &\cdots \\ Y_p &= a_{1p}X_1 + a_{2p}X_2 + \cdots + a_{pp}X_p \end{aligned} \tag{8}$$

in such a way that $\mathrm{Var}(Y_1) \geq \mathrm{Var}(Y_2) \geq \cdots \geq \mathrm{Var}(Y_p)$ and all pairs (Y_i, Y_j), with $i \neq j$, are uncorrelated variables.

In order to perform a PCA over the dataset, it is necessary to obtain the eigenvalues (and the eigenvectors) of the covariance matrix.

2.7. Factor Analysis. Factor Analysis (FA) is an explorative method similar to PCA. Much like the cluster analysis of grouping similar cases, the FA groups similar variables into the same factor [21]. This process is usually referred to as identifying latent variables. Due to its explorative nature, it does not distinguish between independent and dependent variables; it only uses the data correlation matrix.

In other words, FA reduces the information in a model by decreasing the dimension of the dataset. This procedure can have multiple purposes. It can be used to simplify the dataset, for example, reducing the number of variables in predictive regression models. If Factor Analysis is used for these purposes, normally the factors are rotated after its extraction. FA considers several different rotation methods that ensure that the factors are orthogonal. Therefore, the correlation coefficient between two factors is exactly zero. For example, it totally eliminates problems of multicollinearity in regression analysis.

The most commonly used rotation method is *Varimax*, which is the one that will be used in the following section. *Varimax* consists in an orthogonal rotation method (which produces independent factors) that minimizes the number of variables that have high loadings on each factor. The objective of this method is to simplify the interpretation of each one of the factors.

Steps in Exploratory Factor Analysis

(i) Collect and explore data: choose relevant variables.

(ii) Extract initial factors (via principal components).

(iii) Choose number of factors to retain.

(iv) Choose estimation method and estimate model.

(v) Rotate and interpret the results.

Factor Analysis Mathematical Model

$$\mathbf{X}_{(p\times 1)} = \mathbf{L}_{(p\times m)} \times \mathbf{F}_{(m\times 1)} + \varepsilon_{(p\times 1)}, \tag{9}$$

where each matrix represents the following:

$\mathbf{X}_{(p\times 1)}$: multivariate random vector with p variables

$\mathbf{F}' = [F_1 \; F_2 \; \cdots \; F_m]$: *factors* vector with $m < p$ factors common to all p random variables.

$\mathbf{L}_{(p\times m)}$: matrix of *loadings* of the factors; the coefficient l_{ij} represents the weight of the ith variable to jth factor

$\varepsilon' = [\varepsilon_1 \; \cdots \; \varepsilon_p]$: vector of errors.

To sum up, the Factorial Analysis Model considers that the variables could be grouped by their correlations. It is expected that when a high correlation exists between two variables they will be related to the same factor (in the sense that both will have high loadings on that factor).

3. Data Description and Preprocessing

In this section we describe the data used to demonstrate the search for common neural signatures feasible to decode human emotions of various subjects.

ERPs were collected while 26 female volunteers were exposed to 24 high arousal images with positive or negative content from the International Affective Picture System [22]. Each image was shown 3 times in pseudorandom order and each trial lasted 3500 ms. 12 features (amp1, amp2, amp3, amp4, amp5, amp6, latency1, latency2, latency3, latency4, latency5, and latency6) were extracted from 21 channels of recorded ERPs, positioned according to the 10–12 system, and 2 EOG channels were sampled at 1000 Hz. The maximum and minimum values of the ensemble average signals, computed and filtered using a zero-phase filtering scheme, were detected and the features correspond to the time and amplitude characteristics of the first three minimums and maximums occurring after $T = 0$ [12]. The starting data matrix is composed of 252 ($12 * 21$) columns of features and 52 ($2 * 26$) rows of examples. The examples correspond to the averaged class associated data of each participant. The class of the examples is defined by the positive (1) or negative (0) content of the presented image. Note that the number of features is much higher than the number of examples and therefore feature reduction is strongly recommended.

The recording equipment NeuroScan provides initial filtering, eye-movement correction, baseline compensation, and division of the signals in epochs. Prior to feature extraction the recorded EEG signals were further filtered with 4th-order Butterworth filter with passband [0.5–15] Hz [12]. Data were also normalized as follows:

$$z = \frac{x - \mu}{\sigma}, \tag{10}$$

where x is the original data point and μ and σ are the mean and the standard deviation of the data distribution.

4. Discrimination Models

Typical discrimination models were selected—Neural Network (NN), Random Forest (RF), Support Vector Machine (SVM), and k-Nearest Neighbors (kNN). This choice reflects the focus of the present study in finding suitable neural descriptors, less dependent on the classifier characteristics. Data were split into training and validation subset (76%) and

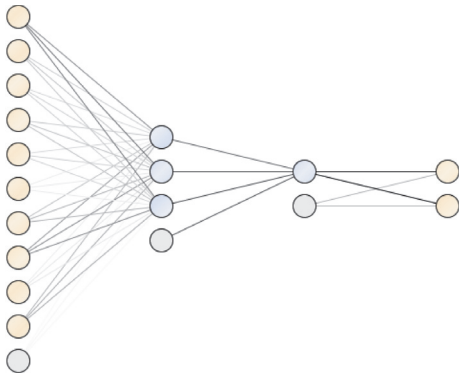

Figure 2: Neural network model.

testing subset (24%). k-fold cross validation (CV) was used with $k = 26$. At each CV iteration, 25 subjects were used for training and a single subject (her positive and negative valence readings) was used for validation. First, emotion detection based on all 252 features was performed and then the feature selection techniques presented in Section 2 were applied prior to the emotion detection. The optimal structure and hyperparameters of the classifiers were chosen after a grid search over a sequence of k-fold CV as described below.

Neural Network (NN)

(i) Fully connected NN with two hidden layers: the first one with 3 neurons and the second layer with one neuron (Figure 2).

(ii) The learning rate was optimized in the range of [0.01 to 1.0], with the optimal value equal to 0.3.

(iii) The momentum was optimized in the range of [0.0 to 1.0], with the optimal value equal to 0.2.

SVM

(i) SVM with dot-type of kernel ($k(x, y) = x * y$) was used.

(ii) C was optimized in the range of [0.1 to 10], with the optimal value equal to 1.

The performance of the SVM was improved applying the adaptive boosting meta-algorithm *(AdaBoost)*. *AdaBoost* fits additional copies of the classifier on the dataset with adjusted weights on the incorrectly classified instances so as to focus the classifier on the most difficult to classify instances [23].

K-Nearest Neighbors (kNN)

(i) k was optimized in the range of [1 to 10], with the optimal value equal to 5.

(ii) Distance measures for computing the k-Nearest Neighbors. Two distance measures were comparatively studied:

(1) Chebyshev distance between two points p and q, with coordinates p_i and q_i, is

$$D_{\text{Chebyshev}}(p, q) := \max_i (\text{abs}(p_i - q_i)). \quad (11)$$

(2) Cosine similarity is a measure of similarity between two nonzero vectors expressed by the cosine of the angle between them [24]. The results in the next section are obtained applying kNN with cosine similarity as this distance measure proves to provide better discrimination.

Random Forest. The Random Forest (RF) consists of multiple decision trees. We run RF with $\{5, 10, 15, 20\}$ trees and maximum tree depth of $\{10, 20, 50, 80\}$. The optimal RF structure was found with 10 trees and maximum depth of 20.

5. Results

In this section the results obtained with the statistical software RapidMiner (RM) are presented, extended with RM Feature Selection [25]. The experiments run on a computer running Windows 10 with an Intel Core i7-5500u CPU and 8 GB of RAM memory.

The performance of all discrimination models on test data is summarized in Table 1. The emotion valence recognition across subjects is far too low when all features are provided as inputs to the classifiers (the second column in Table 1). This is somehow an expected result taking into account the high dimension of the feature space compared to the number of examples. Running the classification task after a preprocessing step with any of the feature selection techniques presented in Section 2 improves the performance compared to a direct brain state discrimination. However, the Factor Analysis (FA) is revealed to be the winning approach in extracting invariant features. Among the four classifiers, SVM and NN present the highest recognition rate.

Table 2 presents the Factor Analysis performed using packages in *software R* library, considering four factors and the standard *Varimax* rotation [26]. FA establishes the general relationship between variables. The first four factors explain about 70% of the total variability of the 252 initial variables. The table shows the strongest relation between factors and original data variables and can be interpreted as follows:

(i) *Temporal features (amplitude, latency)*: early waves (Lmin1, Lmax2, i.e., temporal window of 200–400 ms after the stimulus onset) have higher influence on data variability. This matches experimental psychology hypothesis related to temporal dynamics of emotions. According to [27], early waves carry more information about the valence than the arousal of the emotion. Late waves are less discriminative with respect to the emotion valence.

(ii) *Spatial features (channels)*: spatial location of features, with stronger impact on the emotional valence, occur in the parietal (channels P3, Pz, P4, and P7) and occipital (channels O1, Oz, and O2) regions of the brain.

Table 1: Test Accuracy of 4 classifiers (NN, SVM, RF, and kNN) with feature selection methods: ESN: Echo State Network; IFE: Interval Feature Extraction; ICA: Independent Component Analysis; GPC: Graded Probabilistic Clustering; OFS: Optimal Feature Selection; Factor Analysis (FA).

	-	ESN	IFE	ICA	GPC	OFS	FA
NN	75,0	85,9	78,1	81,8	83,5	80,3	90.4
SVM	58,3	86,7	77,1	72,9	64,2	73,6	90.4
RF	50,0	79,7	71,3	69,4	62,8	65,2	84.6
kNN	56,7	83,3	72,2	72,6	76,8	79,5	88.5

Table 2: Factor Analysis loadings for *Varimax* rotated matrix of four-factor model explaining about 70% of the total dataset variance (presented in bold if absolute values are greater than 0.7).

	F1	F2	F3	F4
P3 (Amin2)	**0.91**	−0.13	0.07	0.02
Pz (Lmin1)	**0.78**	0.10	−0.44	0.01
P4 (Lmax2)	**0.75**	0.04	0.44	0.23
P7 (Amin1)	**−0.73**	0.01	−0.01	−0.25
O1 (Amin2)	−0.14	**0.88**	0.03	0.07
Oz (Lmax2)	−0.02	**0.88**	−0.11	0.09
P8 (Amax2)	0.35	0.46	−0.03	−0.25
C3 (Amin2)	−0.23	−0.11	**0.78**	−0.13
O2 (Lmin1)	−0.34	−0.02	**−0.72**	−0.13
P3 (Amin2)	0.13	0.00	−0.27	**0.80**
P7 (Amin1)	0.15	0.06	0.27	**0.76**
Variance (%)	26	16	15	13

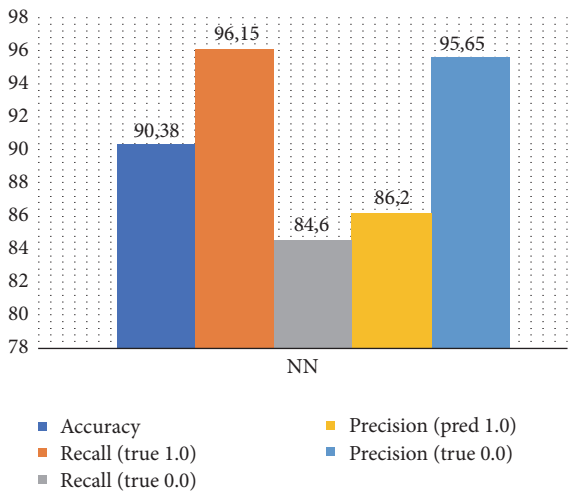

Figure 3: Neural Network (NN) performance measures with Factor Analysis (FA).

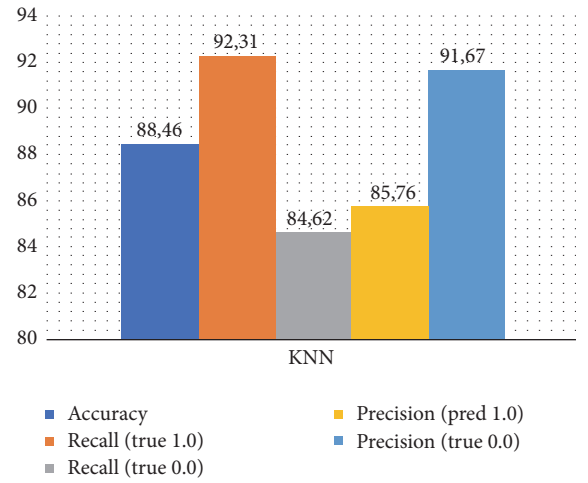

Figure 4: *k*-Nearest Neighbor (kNN) performance measures with Factor Analysis (FA).

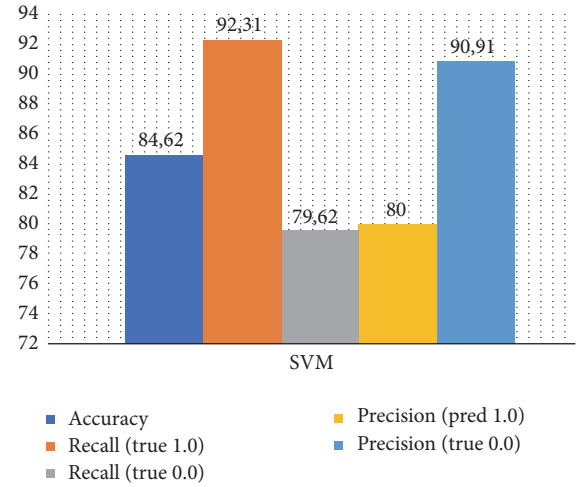

Figure 5: Random Forest (RF) performance measures with Factor Analysis (FA).

The discrimination rates in the last column of Table 1 were obtained with models trained with the four factors. More detailed analysis of the classifiers is depicted in Figures 3–6. The figures resemble the confusion matrix performance metrics. Note that the recall metric (the fraction of correctly classified positive examples) of all classifiers has the highest rate. This result corresponds to better discrimination rate of the positive valence, which is also in accordance with hypothesis of biological psychology [28] that during early periods after the stimulus presentation the brain response, to images with highly positive valence, is stronger.

6. Conclusion

The goal of this study was to identify common neural signatures based on which the positive and negative valence

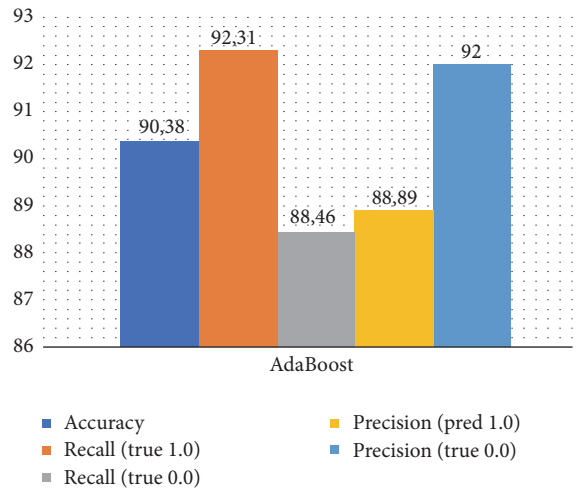

Figure 6: SVM performance measures with Factor Analysis (FA).

of human emotions across multiple subjects can be reliably discriminated. The brain activity is registered by Event-Related Potentials (ERPs). We explored the feasibility of training cross-subject discrimination models to make predictions based extracted invariant neural descriptors, hidden in the ERPs. The core of the present study is the way the features are selected. The combination of a small number of time domain (ERP amplitudes and latencies) and spatial (selected channels) features has the potential to reduce the intersubject variability and improve the learning of representative models valid across multiple subjects.

Based on the results of this study we believe that the Factor Analysis (FA) of ERPs is a promising approach to extract statistical underlying correlations of the brain activity among subjects and therefore decode human emotional states. Nevertheless, before making stronger conclusions on the capacity of the FA to decode emotions, further research is required to answer other questions such as discrimination of more than two emotions. In fact this is a relevant question for all reported works on affective neuroscience [1]. The discrimination is usually limited to two, three, or maximum four valence-arousal emotional classes. An interesting problem is also the human personality clustering based on EEG, for example, distinguishing between high versus low neurotic type of personality. Also, the number of participants in the experiments is important for revealing stable cross-subject features. In the reviewed literature the average number of participants is about 10–15, and the maximum is 32 (DEAP). We need higher dimensional datasets to compare different techniques in order to further progress the affective computing.

Conflicts of Interest

The authors declare that they have no conflicts of interest.

Acknowledgments

This research work is funded by the Sofia Tex Park through R&D&I Consortium and Artificial Intelligence and CAD Systems Lab, in the context of the project "Development and Implementation of Wireless Robot Control Concepts through EEG Signals from Brain Activity," and the National Funds through the FCT (Foundation for Science and Technology), in the context of Project UID/CEC/00127/2013.

References

[1] N. Jatupaiboon, S. Pan-ngum, and P. Israsena, "Real-time EEG-based happiness detection system," *The Scientific World Journal*, vol. 2013, Article ID 618649, pp. 1–12, 2013.

[2] N. Zhuang, Y. Zeng, L. Tong, C. Zhang, H. Zhang, and B. Yan, "Emotion recognition from EEG signals using multidimensional information in EMD domain," *BioMed Research International*, vol. 2017, Article ID 8317357, pp. 1–9, 2017.

[3] S. Jirayucharoensak, S. Pan-Ngum, and P. Israsena, "EEG-based emotion recognition using deep learning network with principal component based covariate shift adaptation," *The Scientific World Journal*, vol. 2014, Article ID 627892, pp. 1–10, 2014.

[4] S. Ding, N. Zhang, X. Xu, L. Guo, and J. Zhang, "Deep extreme learning machine and its application in EEG classification," *Mathematical Problems in Engineering*, vol. 2015, Article ID 129021, pp. 1–11, 2015.

[5] Y. Huang, J. Yang, P. Liao, and J. Pan, "Fusion of facial expressions and EEG for multimodal emotion recognition," *Computational Intelligence and Neuroscience*, vol. 2017, Article ID 2107451, pp. 1–8, 2017.

[6] J. López-Gil, J. Virgili-Gomá, R. Gil et al., "Method for improving EEG based emotion recognition by combining it with synchronized biometric and eye tracking technologies in a non-invasive and low cost way," *Frontiers in Computational Neuroscience*, vol. 10, article 85, 2016.

[7] S. Koelstra, C. Mühl, M. Soleymani et al., "DEAP: a database for emotion analysis; using physiological signals," *IEEE Transactions on Affective Computing*, vol. 3, no. 1, pp. 18–31, 2012.

[8] O. Georgieva, S. Milanov, P. Georgieva, I. M. Santos, A. T. Pereira, and C. F. Silva, "Learning to decode human emotions from event-related potentials," *Neural Computing and Applications*, vol. 26, no. 3, pp. 573–580, 2015.

[9] M.-K. Kim, M. Kim, E. Oh, and S.-P. Kim, "A review on the computational methods for emotional state estimation from the human EEG," *Computational and Mathematical Methods in Medicine*, Article ID 573734, pp. 1–13, 2013.

[10] J. K. Olofsson, S. Nordin, H. Sequeira, and J. Polich, "Affective picture processing: an integrative review of ERP findings," *Biological Psychology*, vol. 77, no. 3, pp. 247–265, 2008.

[11] J. K. Olofsson and J. Polich, "Affective visual event-related potentials: arousal, repetition, and time-on-task," *Biological Psychology*, vol. 75, no. 1, pp. 101–108, 2007.

[12] L. Bozhkov, P. Koprinkova-Hristova, and P. Georgieva, "Learning to decode human emotions with Echo State Networks," *Neural Networks*, vol. 78, pp. 112–119, 2016.

[13] H. Jaeger, "Echo state network," *Scholarpedia*, vol. 2, no. 9, article 2330, 2007.

[14] L. Bozhkov, P. Georgieva, I. Santos, A. Pereira, and C. Silva, "EEG-based subject independent affective computing models," *Procedia Computer Science*, vol. 53, pp. 375–382, 2015.

[15] L. I. Kuncheva and J. J. Rodríguez, "Interval feature extraction for classification of event-related potentials (ERP) in EEG data

analysis," *Progress in Artificial Intelligence*, vol. 2, no. 1, pp. 65–72, 2013.

[16] A. X. Stewart, A. Nuthmann, and G. Sanguinetti, "Single-trial classification of EEG in a visual object task using ICA and machine learning," *Journal of Neuroscience Methods*, vol. 228, pp. 1–14, 2014.

[17] A. Mueller, G. Candrian, J. D. Kropotov, V. A. Ponomarev, and G. M. Baschera, "Classification of ADHD patients on the basis of independent ERP components using a machine learning system," *Nonlinear Biomedical Physics*, vol. 4, no. 1, article S1, 2010.

[18] S. Makeig, A. J. Bell, T. P. Jung, and T. J. Sejnowski, "Independent component analysis of electroencephalographic data," *Advances in Neural Information Processing Systems*, vol. 8, no. 8, pp. 145–151, 1996.

[19] P. Masulli, F. Masulli, S. Rovetta, A. Lintas, and A. E. P. Villa, "Unsupervised analysis of event-related potentials (ERPs) during an emotional Go/NoGo task," in *Fuzzy Logic and Soft Computing Applications*, vol. 10147 of *Lecture Notes in Computer Science*, pp. 151–161, 2017.

[20] L. Bozhkov and P. Georgieva, "Brain neural data analysis with feature space defined by descriptive statistics," in *Pattern Recognition and Image Analysis*, vol. 9117 of *Lecture Notes in Computer Science*, pp. 415–422, Springer International Publishing, New Yorl, NY, USA, 2015.

[21] L. Tucker and R. MacCallum, *Exploratory Factor Analysis*, University of Illinois and Ohio State University, 1997.

[22] "International Affective Picture System data," http://csea.phhp.ufl.edu/media/iapsmessage.html.

[23] R. E. Schapire, "Explaining AdaBoost," in *Empirical inference*, pp. 37–52, Springer, Berlin, Germany, 2013.

[24] Cosine similarity. (n. d.), In Wikipedia, https://en.wikipedia.org/wiki/Cosine_similarity.

[25] https://sourceforge.net/projects/rm-featselext/.

[26] O. O. Omo-Irabor, S. B. Olobaniyi, K. Oduyemi, and J. Akunna, "Surface and groundwater water quality assessment using multivariate analytical methods: a case study of the Western Niger Delta, Nigeria," *Physics and Chemistry of the Earth*, vol. 33, no. 8–13, pp. 666–673, 2008.

[27] M. Stolarova, A. Keil, and S. Moratti, "Modulation of the C1 visual event-related component by conditioned stimuli: evidence for sensory plasticity in early affective perception," *Cerebral Cortex*, vol. 16, no. 6, pp. 876–887, 2006.

[28] B. N. Cuthbert, H. T. Schupp, M. M. Bradley, N. Birbaumer, and P. J. Lang, "Brain potentials in affective picture processing: covariation with autonomic arousal and affective report," *Biological Psychology*, vol. 52, no. 2, pp. 95–111, 2000.

Hindawi
Complexity
Volume 2018, Article ID 7514709, 14 pages
https://doi.org/10.1155/2018/7514709

Research Article

High-Density Lipoproteins-Associated Proteins and Subspecies Related to Arterial Stiffness in Young Adults with Type 2 Diabetes Mellitus

Xiaoting Zhu,[1,2] Amy S. Shah,[3] Debi K. Swertfeger,[2] Hailong Li,[4] Sheng Ren,[2] John T. Melchior,[5] Scott M. Gordon,[6] W. Sean Davidson,[5] and L. Jason Lu[2]

[1]*School of Information Management, Wuhan University, Wuhan 430072, China*
[2]*Division of Biomedical Informatics, Cincinnati Children's Hospital Research Foundation, 3333 Burnet Avenue, MLC 7024, Cincinnati, OH 45229-3039, USA*
[3]*Division of Endocrinology, Cincinnati Children's Hospital Research Foundation, 3333 Burnet Avenue, MLC 7012, Cincinnati, OH 45229-3039, USA*
[4]*Division of Neonatology and Pulmonary Biology, Cincinnati Children's Hospital Research Foundation, 3333 Burnet Avenue, Cincinnati, OH 45229-3039, USA*
[5]*Department of Pathology and Laboratory Medicine, Division of Experimental Pathology, University of Cincinnati, 2120 East Galbraith Road, Cincinnati, OH 45237-0507, USA*
[6]*Lipoprotein Metabolism Section, National Heart, Lung and Blood Institute, National Institutes of Health, Bethesda, MD, USA*

Correspondence should be addressed to L. Jason Lu; long.lu@cchmc.org

Received 25 August 2017; Accepted 11 January 2018; Published 8 March 2018

Academic Editor: Mirjana Popović

Copyright © 2018 Xiaoting Zhu et al. This is an open access article distributed under the Creative Commons Attribution License, which permits unrestricted use, distribution, and reproduction in any medium, provided the original work is properly cited.

Lower plasma levels of high-density lipoproteins (HDL) in adolescents with type 2 diabetes (T2D) have been associated with a higher pulse wave velocity (PWV), a marker of arterial stiffness. Evidence suggests that HDL proteins or particle subspecies are altered in T2D and these may drive these relationships. In this work, we set out to reveal any specific proteins and subspecies that are related to arterial stiffness in youth with T2D from proteomics data. Plasma and PWV measurements were previously acquired from lean and T2D adolescents. Each plasma sample was separated into 18 fractions and evaluated by mass spectrometry. Then, we applied a validated network-based computational approach to reveal HDL subspecies associated with PWV. Among 68 detected phospholipid-associated proteins, we found that seven were negatively correlated with PWV, indicating that they may be atheroprotective. Conversely, nine proteins show positive correlation with PWV, suggesting that they may be related to arterial stiffness. Intriguingly, our results demonstrate that apoA-I and histidine-rich glycoprotein may reverse their protective roles and become antagonistic in the setting of T2D. Furthermore, we revealed two arterial stiffness-associated HDL subspecies, each of which contains multiple PWV-related proteins. Correlation and disease association analyses suggest that these HDL subspecies might link T2D to its cardiovascular-related complications.

1. Background

Type 2 diabetes mellitus (T2D) is a major risk factor for development of cardiovascular disease (CVD) [1]. An important contributor to elevating CVD risk in persons with T2D is dyslipidemia [2], characterized by high concentrations of small dense low-density lipoproteins (LDL) particles and serum triglycerides and low concentrations of high-density lipoprotein-cholesterol (HDL-C). Therapies focusing on improving CVD risk in T2D have largely focused on lowering atherogenic LDL particles. Unfortunately, even with the most effective LDL-lowering drugs, significant residual incidence of CVD remains in this population [3]. This has prompted numerous clinical trials aimed at raising HDL-C [4–6]. However, despite successfully raising HDL-C by >70%, these drugs failed to reduce CVD risk [4, 6, 7]. One recent exception was able to reduce CVD over statin treatment, but the effect was relatively modest [8].

HDL-targeted therapies have significant underlying challenges because HDL is more complex than previously recognized. Proteomic studies of HDL have identified at least 95 distinct proteins associated with HDL [9–14]. It is impossible for all of these proteins to reside on a single particle. Instead, it is likely that several proteins interact on different particles, likely to carry out specific functions. A perfect example is trypanosome lytic factor (TLF), containing apolipoprotein A-I (apoA-I), haptoglobin-related protein, and apoL-I. This particle has been shown to have specific lytic activity against the protozoan *Trypanosoma brucei* via lysosomal disruption [15].

Recent studies have shown that HDL is a heterogeneous group of subspecies with unique protein/lipid compositions that are not reflected in the HDL-C measurement [13, 16–18]. Diverse proteins on HDL subspecies may have physical interactions or be colocalized on the same particle without a physical interaction. Those different HDL subspecies provide a plausible explanation for the many diverse functions of HDL [19]. While HDL is most recognized for its ability to mediate reverse cholesterol transport (RCT) [20], in which it removes excessive cholesterol and other lipids from peripheral tissues and transports them back to the liver for catabolism, HDL has also been shown to have anti-inflammatory, antioxidative, and antiapoptotic properties [21–25].

Using gel filtration chromatography that separates lipoproteins by size, we previously found that adolescents with type 2 diabetes were depleted of large HDL particles compared with obese and lean adolescents [17]. This decrease was inversely and significantly correlated with an increase in pulse wave velocity (PWV), an early measurement of arterial stiffness. Additionally, we detected 45 HDL-associated proteins, seven of which were lower in the T2D group. These results demonstrated an alteration in the HDL composition in young adults with T2D. However, in our previous paper, we had not examined if specific proteins or protein subspecies on these particles may be related to arterial stiffness.

Here we sought to determine if any proteins or groups of proteins may be related to arterial stiffness as measured by PWV. Recently, we have developed a network-based computational method to infer HDL subspecies from complex proteomics data [16]. Supported by multiple lines of evidence, the protein clusters revealed by our method likely correspond to HDL subspecies. In this work, we integrated patient clinical data, biological experiments, and bioinformatics analysis to reveal arterial stiffness-related HDL proteins and subspecies, which may serve as better markers than HDL-C for linking T2D with CVD.

2. Methods

2.1. Study Cohort. Five adolescents with T2D and six lean controls aged 17–27 years were included in this analysis [17]. Table 1 lists the clinical characteristics of the study cohort. Subjects with T2D were diagnosed based on American Diabetes Association criteria [26]. The lean control group had a BMI less than the 85th percentile (age $\leq$ 20) or less than 25 (age > 20). Lean control participants had no evidence of chronic disease. Manual blood pressure was measured three times and averaged using a mercury sphygmomanometer. Arterial stiffness was measured by carotid to femoral PWV, a risk factor for coronary artery disease and stroke [27]. For each subject, PWV was collected using a SphygmoCor SCOR-PVx System. Three PWV values for each participant were measured and averaged.

2.2. Plasma Fractionation and Proteomics. For each subject, blood was fractionated by gel filtration chromatography into 18 lipid-containing fractions by size [13]. By this method, which has been extensively described [13, 18], fractions 13–30 contain detectable phospholipid that corresponds to the plasma lipoproteins VLDL, LDL, and HDL. To relate gel filtration results to traditional density-centric definitions, the VLDL/LDL range was defined as fractions 14–18 due to the presence of apoB. The remaining fractions 19–30 were defined as a HDL range because their diameters are consistent with measurements for density-isolated HDL and because of the abundance of the major HDL protein, apoA-I. Lipid-associated proteins were isolated using a synthetic calcium silicate hydrate, Lipid Removal Agent (Supelco), and their relative abundance in each fraction was determined by mass spectrometry (MS) as previously described [17, 28]. Briefly, samples were delipidated using chloroform and methanol. Next, samples were treated with dithiothreitol and iodoacetamide (Sigma-Aldrich, St. Louis, MO) to reduce and carbamidomethylate the proteins. Finally, proteins were trypsinized and subjected to MS. An Agilent 1100 Series Autosampler/HPLC was used to draw 0.5 μL of sample and inject it onto a C18 reverse phase column (GRACE; 150 $\times$ 0.500 mm), where an acetonitrile concentration gradient (5–30% in water with 0.1% formic acid) was used to elute peptides for inline electrospray ionization tandem MS, by a time of flight QSTAR XL mass spectrometer (Applied Biosystems). Column cleaning was performed automatically with two cycles of a 5–85% acetonitrile gradient lasting 15 min each between runs. PeakView version 2.1 was used to convert the raw data files into the peak list (.mgf) files. The resulting mass spectra were analyzed with Mascot (version 2.2.2, http://www.matrixscience.com) and X! Tandem (version 2001.01.01.1) search engines against the UniProtKB/Swiss-Prot Protein Knowledgebase (2011, containing 540,958 entries). Search criteria included human taxonomy and carbamidomethylation as a variable modification; peptide tolerance was set at ±20 ppm, MS/MS tolerance was set to ±0.6 Da, and up to 3 missed trypsin cleavages were allowed. Peptide and protein identification from the MS/MS was validated using Scaffold software (version 3.3.1) and only peptides with >95% identification probability and proteins with >99% identification probability were included in the analysis. Additionally, at least 2 peptides from each protein were required to be considered in the analysis. False discovery rates were less than 0.6% for peptide identification (calculated as the percentage of the sum of exclusive spectrum counts of decoy proteins divided by the sum of exclusive spectrum counts of target proteins) and less than 0.1% for protein identification (calculated as number of decoy proteins divided by the number of target proteins). MS peptide counts were obtained to semiquantitatively identify differences in

Table 1: Study cohort characteristics.

Variable	Lean	T2D
n	6	5
Age (years)	21.67 ± 2.16	21.6 ± 4.04
Body mass index (mg/kg)	23.97 ± 2.04	37.89 ± 3.75
Total cholesterol (mg/dL)	153.67 ± 26.38	215.6 ± 55.84
Triglycerides (mg/dL)	73.17 ± 27.8	278.6 ± 344.52
High-density lipoprotein-cholesterol (mg/dL)	52.67 ± 10.73	33.8 ± 4.44
Low-density lipoprotein-cholesterol (mg/dL)	86.6 ± 32.24	127.8 ± 53.1
Systolic blood pressure (mmHg)	119.72 ± 11.33	116.0 ± 8.21
Diastolic blood pressure (mmHg)	71.56 ± 7.96	71.2 ± 5.78
Pulse wave velocity (m/s)	5.74 ± 1.11	6.8 ± 1.12
Hemoglobin A1C (%)	N/A	11.3 ± 4.65
Hemoglobin A1C (mmol/mol)	N/A	100.2 ± 50.63

Data are mean and standard deviation (SD). N/A: not available.

proteins across fractions between groups. Although peptide spectral counting has been criticized for its accuracy to reflect the abundance of proteins, it would not compromise our analysis in this work, since we only considered the trends or distribution patterns of HDL proteins. Spectral counts were used in no instance to reflect the absolute quantity of a protein. For data preprocessing, we filtered the MS detected proteins with the HDL Proteome Watch [29] in all lean and T2D participants. The HDL Proteome Watch is a curated database documenting all proteins that have been found to be associated with HDL in multiple MS studies. We further removed extremely low-abundant proteins (less than 3 peptides across all subjects).

2.3. Correlation Analysis. To investigate if any individual HDL proteins were related to arterial stiffness, we calculated Pearson correlation coefficient (PCC) between the relative abundance of HDL proteins in fractions 19–31 and PWV measurements. PCC was calculated for the lean and T2D combined dataset, the lean dataset only, and T2D dataset only. We realized that PCC of the lean and T2D combined dataset may be mainly driven by the lean group (Supplemental Figure 1). If the composition of HDL is indeed altered in T2D, it is possible that, in the same size fractions, lean and T2D datasets exhibit distinct patterns. Thus, in this work, we separated lean and T2D groups and analyzed them individually. Specifically, for each plasma HDL fraction $\in [19 \cdots 30]$, we calculated a univariate PCC between PWV and the peptide counts of HDL-associated proteins in fractions across all subjects within the two groups. We applied a two-tailed t-test followed by the Benjamini-Hochberg procedure to correct for multiple comparisons to test the null hypothesis of no correlation between PWV and proteins.

2.4. Network-Based Identification of HDL Subspecies. To infer HDL subspecies, we applied the network-based approach we previously developed for clustering comigrating proteins [16]. This approach is based on the assumption that proteins with similar elution patterns during plasma fractionation are very likely to reside on the same HDL subspecies. We constructed a comigration protein-protein interaction (PPI) network for the lean and T2D groups, separately, using fractions 13–30. Comigration similarity was measured by univariate PCC, and strongly correlated links are chosen to form the networks. Proteins in the network were clustered using a network clustering approach, ClusterONE [30]. The identified protein clusters found in fractions 19–30 were inferred to be HDL subspecies.

2.5. Disease Association Analysis. To determine whether the HDL subspecies are related to particular diseases, we performed disease association analyses using an independent analyzer, ToppCluster [31]. In disease association analysis, ToppCluster calculated an enrichment score with a hypergeometric distribution test for our identified HDL subspecies associated with human disease annotations that were collected from multiple public human disease databases. A default Bonferroni correction was applied on the tests of associations and the corrected $P < 0.05$ was used to select significant associated diseases.

3. Results

3.1. HDL-Associated Proteins and Arterial Stiffness. We first sought to determine if individual HDL-associated proteins in the plasma HDL fractions were associated with arterial stiffness. A total of 68 HDL-associated proteins were identified across all fractions. Figures 1 and 2 show univariate PCC of 58 proteins within the HDL size fractions versus PWV in the lean and T2D groups, separately. Across the two groups, we identified 14 distinct HDL proteins that exhibited significant correlation with PWV ($|\text{PCC}| \geq 0.9, P < 0.05$ after Benjamini-Hochberg procedure). In the lean group specifically, seven proteins showed strong negative correlation with PWV (Figure 1). Those include classical apolipoproteins apoA-I, apoC-III, and apoJ, as well as complement C1s subcomponent, histidine-rich glycoprotein, inter-alpha-trypsin inhibitor 2, and pigment epithelium-derived factor. The significant proteins were detected across the HDL size range and showed no preferential distribution in larger or smaller

Protein	UniProtKB	Lean HDL fraction number 19	20	21	22	23	24	25	26	27	28	29	30
Alpha-1B-glycoprotein	A1BG_HUMAN								−0.665				
Alpha-2-antiplasmin	A2AP_HUMAN							−0.489	0.310				
Alpha-2-HS-glycoprotein	FETUA_HUMAN								0.160	−0.046	−0.132	−0.140	
Alpha-2-macroglobulin	A2MG_HUMAN	−0.405											
Angiotensinogen	ANGT_HUMAN								0.263				
Antithrombin-III	ANT3_HUMAN									−0.598	−0.209	0.123	
Apolipoprotein A-I	APOA1_HUMAN	−0.546	−0.324	✓ −0.908	✓ −0.955	−0.682	−0.250	−0.125	0.597	−0.209	−0.092	−0.239	0.089
Apolipoprotein A-II	APOA2_HUMAN			−0.531	−0.449	−0.630	−0.416	−0.409	0.322	−0.041			
Apolipoprotein A-IV	APOA4_HUMAN				−0.182	−0.126	0.052			−0.246	0.054	0.042	0.384
Apolipoprotein C-I	APOC1_HUMAN					−0.355	0.449	0.596					
Apolipoprotein C-III	APOC3_HUMAN			−0.764		0.140	✓ −0.957						
Apolipoprotein E	APOE_HUMAN			−0.743	−0.673	−0.336	−0.349						
Apolipoprotein M	APOM_HUMAN						0.233						
Apolipoprotien L1	APOL1_HUMAN												
Apolipoprotein H	APOH_HUMAN								0.077	−0.327	−0.171		
Ceruloplasmin	CERU_HUMAN						−0.447	−0.327	−0.042				
Apolipoprotein J	CLUS_HUMAN	−0.586	−0.311	−0.471		−0.641	✓ −0.982	−0.594	−0.452	−0.262			
Complement C1s subcomponent	C1S_HUMAN					✓ −0.924	−0.620	−0.541					
Complement C2	CO2_HUMAN							−0.516	−0.042				
Complement C3	CO3_HUMAN				−0.404	0.025	−0.284	−0.265	0.015				
Complement C4-B	CO4B_HUMAN		−0.685	−0.615	−0.346	−0.402	−0.504						
Complement C9	CO9_HUMAN								−0.017	−0.528	−0.856		
Complement factor B	CFAB_HUMAN							−0.319	−0.349	−0.210	0.351		
Complement factor H	CFAH_HUMAN	−0.691	−0.413	−0.713	−0.670								
Fibrinogen alpha chain	FIBA_HUMAN	−0.497	−0.262										
Fibrinogen beta chain	FIBB_HUMAN	−0.555	−0.540										
Fibrinogen gamma chain	FIBG_HUMAN	−0.514											
Fibronectin	FINC_HUMAN	−0.593	−0.236										
Gelsolin	GELS_HUMAN								0.457	0.089	−0.069	−0.638	
Haptoglobin	HPT_HUMAN	−0.307	−0.087	−0.325	−0.474	−0.386	−0.318	−0.252					
Haptoglobin related protein	HPTR_HUMAN	−0.632	−0.502	−0.292									
Hemopexin	HEMO_HUMAN							−0.452	0.480	−0.678	−0.339	−0.107	
Heparin cofactor 2	HEP2_HUMAN							−0.389	0.235	−0.237	−0.228		
Histidine-rich glycoprotein	HRG_HUMAN					−0.489	0.034	✓ −0.919	0.351	−0.591	−0.176	−0.294	
Ig alpha-1 chain C region	IGHA1_HUMAN	−0.513	−0.592	−0.356	−0.579	0.342	−0.382						
Ig gamma-1 chain C region	IGHG1_HUMAN			−0.246	−0.331	−0.496	−0.210	−0.424	−0.416	−0.575		−0.298	
Ig kappa chain C region	IGKC_HUMAN			−0.150	0.450	0.084	−0.356	−0.591	0.177				
Ig lambda chain C regions	LAC1_HUMAN			−0.267									
Inter-alpha-trypsin inhibitor 1	ITIH1_HUMAN		−0.416	−0.699	−0.358	−0.308							
Inter-alpha-trypsin inhibitor 2	ITIH2_HUMAN		✓ −0.929	−0.620	−0.410	✓ −0.944							
Inter-alpha-trypsin inhibitor 4	ITIH4_HUMAN					−0.627	−0.645	−0.095	−0.240				
Kallistatin	KAIN_HUMAN									0.061	0.052	−0.447	
Kininogen-1	KNG1_HUMAN				−0.172			−0.568	0.030	−0.262	0.039		
Lumican	LUM_HUMAN							−0.288	0.304				
N-Acetylmuramoyl-L-alanine amidase	PGRP2_HUMAN								−0.113	−0.121			
Phosphatidylinositol-glycan-specific PLD	PHLD_HUMAN					−0.466	−0.098						
Pigment epithelium-derived factor	PEDF_HUMAN										✓ −0.921	0.438	0.500
Plasma kallikrein	KLKB1_HUMAN				−0.226	−0.157	−0.363						
Plasma protease C1 inhibitor	IC1_HUMAN			−0.370	−0.551								
Plasminogen	PLMN_HUMAN								0.115	−0.346	0.276	0.133	
Prothrombin	THRB_HUMAN							−0.254	0.130	−0.513	0.300		
Retinol binding protein 4	RET4_HUMAN											−0.210	
Serotransferrin	TRFE_HUMAN								0.022				
Albumin	ALBU_HUMAN		−0.382	−0.587	−0.306	−0.195	−0.209	−0.527	0.244	−0.369	−0.198	−0.069	0.276
Paraoxonase 1	PON1_HUMAN				−0.286	−0.010	−0.670	0.233	0.099	−0.366	−0.134	−0.545	
Transthyretin	TTHY_HUMAN												0.285
Vitamin D binding protein	VTDB_HUMAN										−0.075	0.017	−0.041
Vitronectin	VTNC_HUMAN							0.353	0.557	0.735	−0.378		

Figure 1: PCCs of peptide counts of individual proteins with PWV for the *lean group* across HDL fractions. Red, white, and blue are used to mark maximal, medium, and minimum value, respectively. Green checkmark indicates significant correlation. The proteins that also correlate with PWV in the T2D group are highlighted in yellow.

particles. The negative correlation with PWV suggests that these proteins may be components of the atheroprotective particles.

In contrast, in the T2D group, nine proteins were found to be positively correlated with PWV (Figure 2). These proteins were mainly distributed across fractions 26~29, the range containing smaller HDL particles. These proteins were alpha-2-HS-glycoprotein, antithrombin-III, apoA-I, gelsolin, hemopexin, histidine-rich glycoprotein, kininogen-1, plasminogen, and albumin. The positive correlation with PWV suggests that these may be atherogenic. It is worth noting that apoA-I and histidine-rich glycoprotein were found in both groups but with negative correlation with PWV in the lean group and positive correlation in the T2D group,

T2D

Protein	UniProtKB ID	HDL fraction number											
		19	20	21	22	23	24	25	26	27	28	29	30
Alpha-1B-glycoprotein	A1BG_HUMAN								0.767				
Alpha-2-antiplasmin	A2AP_HUMAN												
Alpha-2-HS-glycoprotein	FETUA_HUMAN								✓ 0.934	0.838	0.577		
Alpha-2-macroglobulin	A2MG_HUMAN												
Angiotensinogen	ANGT_HUMAN												
Antithrombin-III	ANT3_HUMAN									0.669	0.864	✓ 0.905	
Apolipoprotein A-I	APOA1_HUMAN	0.512	0.530	0.553	0.685	0.331	0.761	✓ 0.970	✓ 0.920	0.864	✓ 0.928	0.719	0.411
Apolipoprotein A-II	APOA2_HUMAN						0.000	0.320	0.848	0.442			
Apolipoprotein A-IV	APOA4_HUMAN					0.842	0.230			0.842	0.703	0.550	0.381
Apolipoprotein C-I	APOC1_HUMAN												
Apolipoprotein C-III	APOC3_HUMAN												
Apolipoprotein E	APOE_HUMAN					0.856							
Apolipoprotein M	APOM_HUMAN												
Apolipoprotien L1	APOL1_HUMAN		−0.189										
Apolipoprotein H	APOH_HUMAN								0.347	0.764	0.861		
Ceruloplasmin	CERU_HUMAN							−0.293					
Apolipoprotein J	CLUS_HUMAN	0.316			0.237		0.258	0.400	0.530	0.861			
Complement C1s subcomponent	C1S_HUMAN						0.269						
Complement C2	CO2_HUMAN							−0.100					
Complement C3	CO3_HUMAN				0.708	0.320	0.282	0.719					
Complement C4-B	CO4B_HUMAN				0.417	0.328	−0.024						
Complement C9	CO9_HUMAN								−0.491	0.848	−0.191		
Complement factor B	CFAB_HUMAN							0.257	0.795	0.562	0.698		
Complement factor H	CFAH_HUMAN	0.587	0.898	0.382									
Fibrinogen alpha chain	FIBA_HUMAN	0.364											
Fibrinogen beta chain	FIBB_HUMAN	0.366											
Fibrinogen gamma chain	FIBG_HUMAN	0.097											
Fibronectin	FINC_HUMAN	0.736	0.342										
Gelsolin	GELS_HUMAN								0.848	✓ 0.921	0.804		
Haptoglobin	HPT_HUMAN	−0.158	0.323	0.122	0.471	0.442	−0.006	−0.031					
Haptoglobin related protein	HPTR_HUMAN	0.424	−0.052	−0.200									
Hemopexin	HEMO_HUMAN							0.827	0.883	0.751	✓ 0.904		
Heparin cofactor 2	HEP2_HUMAN							−0.021	0.632	0.684	0.366		
Histidine-rich glycoprotein	HRG_HUMAN							0.736	0.890	0.786	✓ 0.959		
Ig alpha-1 chain C region	IGHA1_HUMAN	0.875	0.286	0.029	−0.400	0.442							
Ig gamma-1 chain C region	IGHG1_HUMAN			0.848	0.669	0.340	−0.200	−0.328	0.528				
Ig kappa chain C region	IGKC_HUMAN					0.316							
Ig lambda chain C regions	LAC1_HUMAN												
Inter-alpha-trypsin inhibitor 1	ITIH1_HUMAN		0.736	0.496	0.590								
Inter-alpha-trypsin inhibitor 2	ITIH2_HUMAN		0.424	0.000	0.258								
Inter-alpha-trypsin inhibitor 4	ITIH4_HUMAN						0.426	0.414					
Kallistatin	KAIN_HUMAN										0.817	0.574	
Kininogen-1	KNG1_HUMAN							0.267	0.632	✓ 0.947	0.574		
Lumican	LUM_HUMAN												
N-Acetylmuramoyl-L-alanine amidase	PGRP2_HUMAN								0.126	−0.133			
Phosphatidylinositol-glycan-specific PLD	PHLD_HUMAN												
Pigment epithelium-derived factor	PEDF_HUMAN										0.842	0.480	0.842
Plasma kallikrein	KLKB1_HUMAN				0.530	0.450	0.274						
Plasma protease C1 inhibitor	IC1_HUMAN												
Plasminogen	PLMN_HUMAN								✓ 0.978	0.892	0.578		
Prothrombin	THRB_HUMAN							0.856	0.437	0.050			
Retinol binding protein 4	RET4_HUMAN												
Serotransferrin	TRFE_HUMAN												
Albumin	ALBU_HUMAN			−0.126	0.319		0.424		0.670	✓ 0.900	0.870	0.782	0.869
Paraoxonase 1	PON1_HUMAN							−0.126					
Transthyretin	TTHY_HUMAN												
Vitamin D binding protein	VTDB_HUMAN											0.201	
Vitronectin	VTNC_HUMAN							0.692	0.510	0.710	0.872		

Figure 2: PCCs of peptide counts of individual proteins with PWV for the *T2D group* across HDL fractions. Red, white, and blue are used to mark maximal, medium, and minimum value, respectively. Green checkmark indicates significant correlation. The proteins that also correlate with PWV in the lean group are highlighted in yellow.

suggesting that perhaps the protein distribution (what size particles it associates with) is altered in disease, rendering it proatherogenic. Except the significantly PWV-correlated proteins mentioned above, the majority of phospholipid-associated proteins demonstrated no clear correlation with PWV measurements.

3.2. Pattern Distribution of Proteins Associated with PWV. Based on the correlation analysis, we wanted to know if these PWV-related proteins are associated with altered HDL particle sizes. This prompted us to investigate the distributions of these PWV-related proteins. We compared distribution patterns of all the significantly correlated proteins between

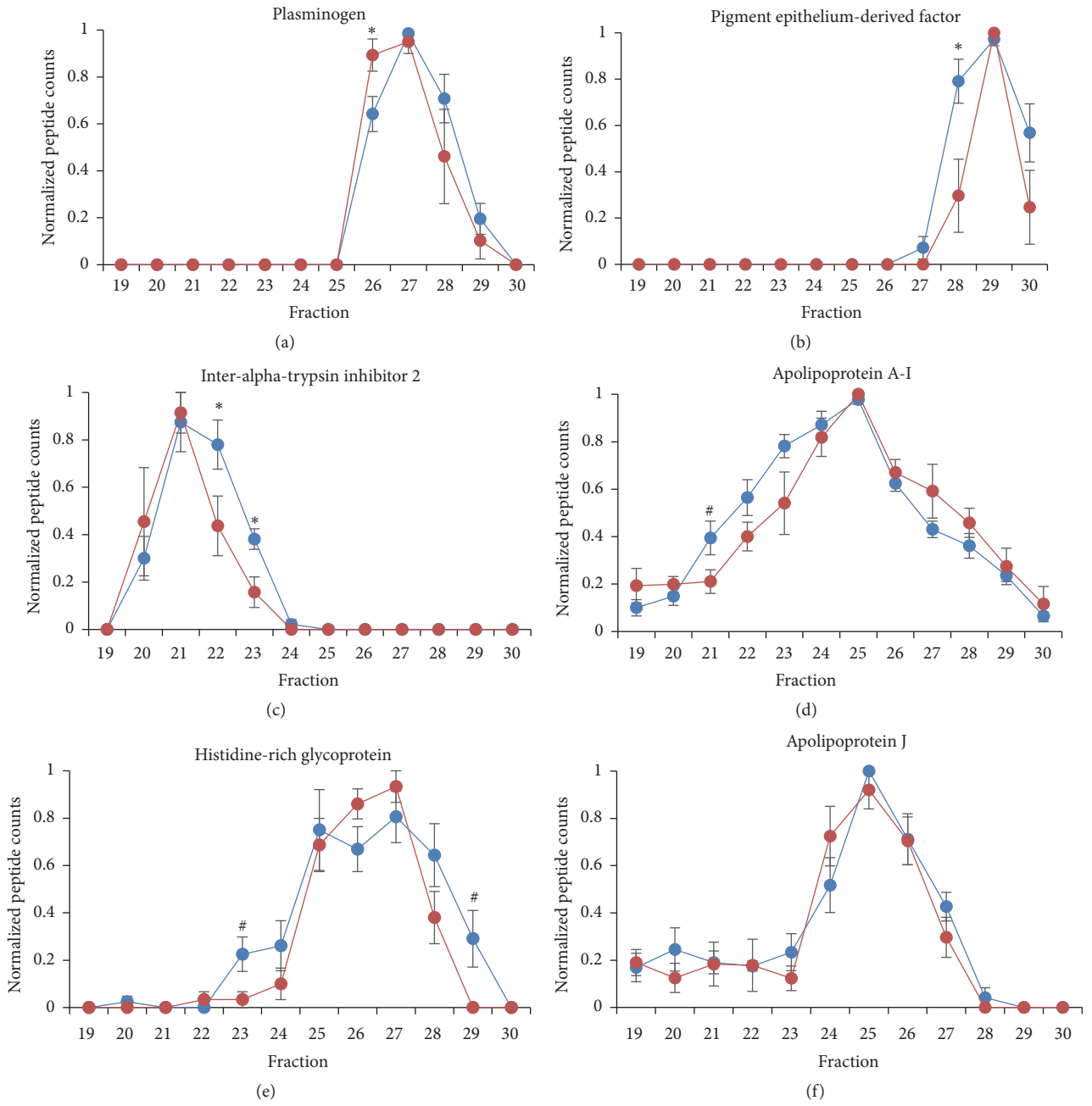

FIGURE 3: *Distribution patterns of example proteins exhibiting high correlations with PWV*. Spectral counts were normalized by dividing by the maximum value across all fractions. Data are mean and standard deviation of normalized spectral counts. Normalized peptide counts across the HDL fractions are shown for lean (blue) and T2D (red): (a) plasminogen, (b) pigment epithelium-derived factor, (c) inter-alpha-trypsin inhibitor 2, (d) apoA-I, (e) histidine-rich glycoprotein, and (f) apoJ. A t-test was performed for comparing normalized peptide counts between lean and T2D groups at individual fractions. $^{*}P < 0.05$. $^{\#}P < 0.08$.

the lean and T2D groups ($n = 14$). Using a t-test, we determined that 5/14 PWV-correlated proteins have significant distribution changes at specific fractions ($P < 0.05$). These include gelsolin, kininogen-1, plasminogen, inter-alpha-trypsin inhibitor 2 (ITIH2), and pigment epithelium-derived factor (PEDF). We noted that an additional five proteins (i.e., apoA-I, alpha-2-HS-glycoprotein, hemopexin, histidine-rich glycoprotein, and albumin) exhibited observable pattern changes but their P value was slightly greater than 0.05. Figures 3(a)–3(c) demonstrate PWV-correlated proteins with significant pattern changes. Plasminogen and PEDF were altered in smaller size HDL range, while ITIH2 was changed in the larger HDL size fractions. Figures 3(d) and 3(e) show two examples whose pattern changes are observable but not significant at certain fractions. For example, compared with the lean subjects, apoA-I is decreased in the T2D subjects at fraction 21 (Figure 3(d)) as well as histidine-rich glycoprotein at fraction 23 (Figure 3(e)). Their changes both appeared in

the larger HDL size fractions. Only four of 14 PWV-correlated proteins exhibited no observable changes in distribution: antithrombin-III, apoC-III, complement C1s subcomponent, and apoJ (Figure 3(f)). The pattern analysis suggests that only a portion of HDL subspecies where these proteins reside were altered in youth with T2D.

3.3. HDL Subspecies and Arterial Stiffness. Next, we sought to identify potential HDL subspecies that may be related to arterial stiffness. We have previously designed a computational method to reveal putative HDL subspecies [16]. In this work, we employed the same approach to construct comigration PPI networks for the lean and T2D subjects, respectively, as described in Section 2. The spectral counts of the 68 proteins across fractions 13–30 were applied in network construction. PPI networks for the lean and T2D groups are shown in Figure 4. The networks only include strongly correlated comigration links (PCC $\geq$ 0.8, $P < 0.05$) and, as a result, 42 associated HDL proteins. The lean network shown in Figure 4(a) contains 62 comigration links, while the T2D network in Figure 4(b) has only 35 links. Fibrinogen alpha chain, fibrinogen beta chain, and fibrinogen gamma chain (yellow) form fibrinogen, a glycoprotein in plasma. These three subunits should be interconnected in the comigration network, since they colocalize and travel together in fractionated plasma as a single protein. Interconnection of the three subunits in both Figures 4(a) and 4(b) was observed, validating our network construction.

In Figure 4(a), we identified several groups of proteins that can be found clustered together using the ClusterONE method [30]. These clusters may comprise distinct HDL subspecies and are marked with various colors in the lean controls. Nodes that are not in any cluster are marked with aqua color. In T2D network (Figure 4(b)), we applied the same layout and color scheme as in Figure 4(a) for comparison. There are global topological differences between the lean and T2D networks. A clustering coefficient (CC) was calculated to measure the degree to which nodes in a network tend to cluster together. The CC of the lean network is 0.508, while the CC of T2D network is reduced to 0.225. This reduction indicates that lean subjects may have more intact protein subspecies than T2D subjects.

Another important topological feature of a network is the number of connected components (NCC). In a graph, its connected components are the set of the largest subgraphs that are each connected. A lower NCC indicates fewer subgraphs and suggests stronger network connectivity. The NCC of lean and T2D networks are 8 and 23, respectively. In terms of number of links, the lean network has more links than the T2D network with the same PCC cutoff. This suggests that HDL proteins in the lean controls have a stronger comigration relationship than the ones in T2D subjects. Loss of the links in the T2D network is mainly within the clusters (e.g., green and yellow clusters). On the other hand, the T2D network involves additional links; for example, kininogen-1 comigrates with the pink cluster. The differences between the networks indicate that the compositional alterations of certain HDL subspecies may occur in youth with T2D.

Upon further examination, we first noted that the edge between apoA-I and apoA-II is absent in the T2D group. Although not all apoA-I containing particles include apoA-II, it is well known that apoA-I and apoA-II often reside on the same HDL complexes [14, 18, 29, 32]. An independent study [32] has reported the apoA-I and apoA-II comigrated after gel filtration-based plasma fractionation (PCC = 0.96). In the current study, the PCC of the apoA-I and apoA-II migration pattern in the lean group is 0.871 ($P < 0.05$), while the PCC in T2D group is reduced to 0.747 ($P < 0.05$). Their comigration patterns were compared between lean and T2D groups (Figures 5(a) and 5(b)). Obvious distribution changes appeared on apoA-II, especially around fractions 21–23. This was previously reported in our original paper [17]. The lower PCC may be due to either a loss of the small HDL particle in T2D patients or the compositional alteration of HDL subspecies containing apoA-II in youth with T2D. Additionally, the link between haptoglobin-related protein and complement factor H is lost in the T2D network. Their comigration patterns (Figures 5(c) and 5(d)) demonstrate that haptoglobin-related protein has a clear pattern alteration in the T2D group. On the other hand, we found some edges that only appear in the T2D network.

Figures 5(e) and 5(f) show that kininogen-1 has a peak at fraction 26 in the lean controls but a peak at fraction 27 in the T2D subjects. This right-shift makes kininogen-1 have a similar migration pattern to apoH in youth with T2D.

In the HDL-associated PPI network, we observed three clusters that contain at least two proteins that were highly correlated with PWV. These are the blue cluster containing four proteins (apoA-IV, antithrombin-III, kallistatin, and albumin), the green cluster containing five proteins (apoA-I, apoA-II, complement C3, complement C1s subcomponent, and Ig gamma-1 chain C region), and the pink cluster containing six proteins (hemopexin, gelsolin, plasminogen, complement C9, apoH, and alpha-2-HS-glycoprotein). The proteins in the blue cluster do not likely form a subspecies. They simply migrate together due to their similar sizes. If they formed a subspecies, their combined MW would be at least 205 kDa, without any associated lipid, and would thus elute in an earlier fraction. Therefore, this grouping will not be referred to as a subspecies. However, the remaining 2 clusters are each likely migrating together as at a subspecies, since they elute in a fraction containing proteins that are larger than any single protein in their respective clusters. The migration patterns for the 2 subspecies in both lean and T2D groups are shown in Figure 6. Again, we first provided fibrinogen as a control shown in Figures 6(a) and 6(b) to illustrate how different proteins comigrate if they reside on the same "particle" and show no difference in the pattern between lean and T2D as previously observed. The rest of panels in Figure 6 demonstrate the patterns of the two newly revealed clusters in lean and T2D. The green cluster (Figures 6(c) and 6(d)) contains two negatively PWV-correlated proteins that were identified in the lean group. Pattern changes are clear in the T2D group, so that links between proteins in the lean group are absent in the T2D group.

It appears that the intact subspecies containing two atheroprotective proteins are remodeled into disconnected

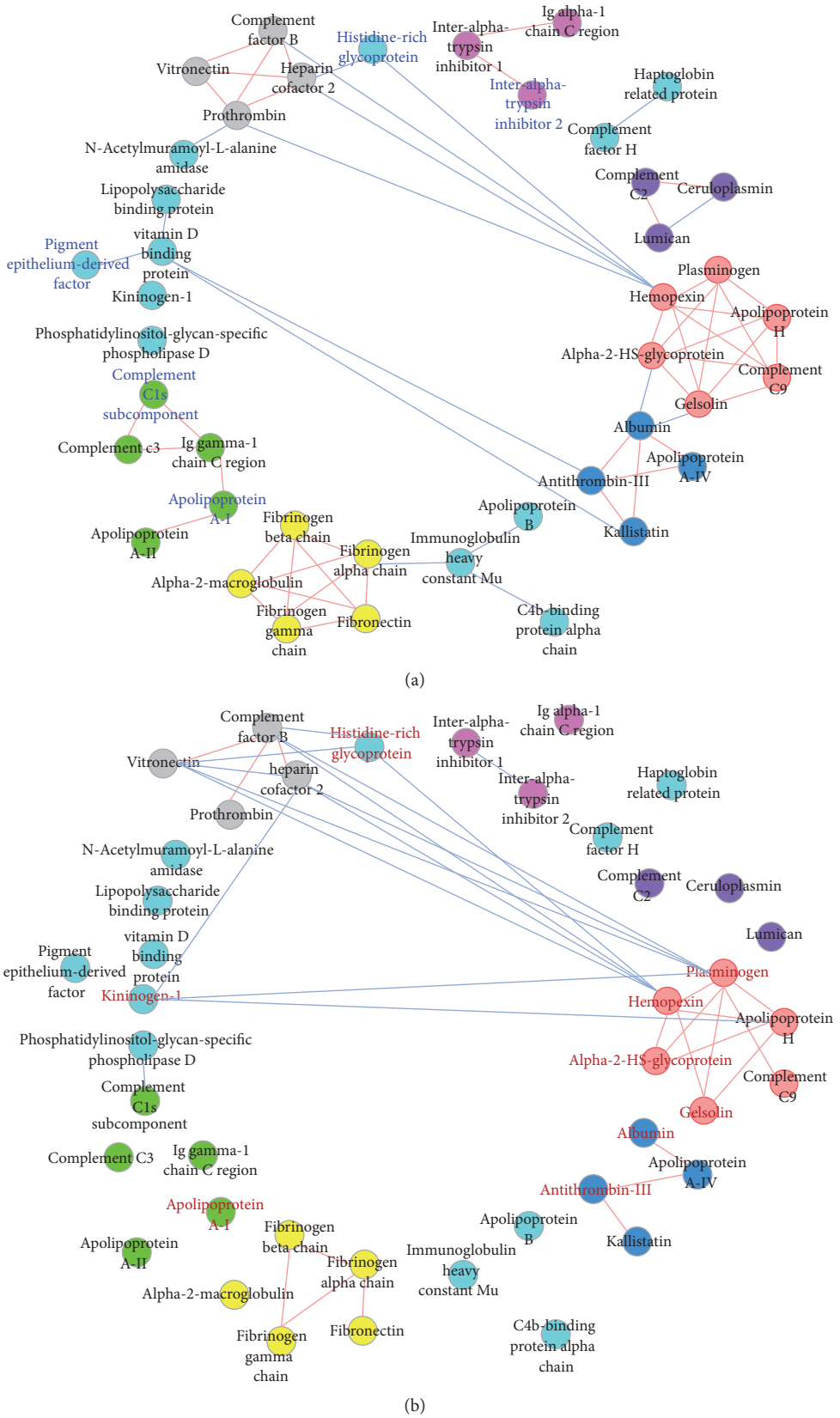

Figure 4: *HDL-associated PPI networks for the (a) lean group and (b) T2D group*. Nodes represent the proteins and edges represent comigration relationship. Intracluster edges are marked as dark pink, and intercluster edges are blue. Significantly PWV-correlated proteins are denoted with red text (positive) and blue text (negative). Clustered protein groups are marked with different colors.

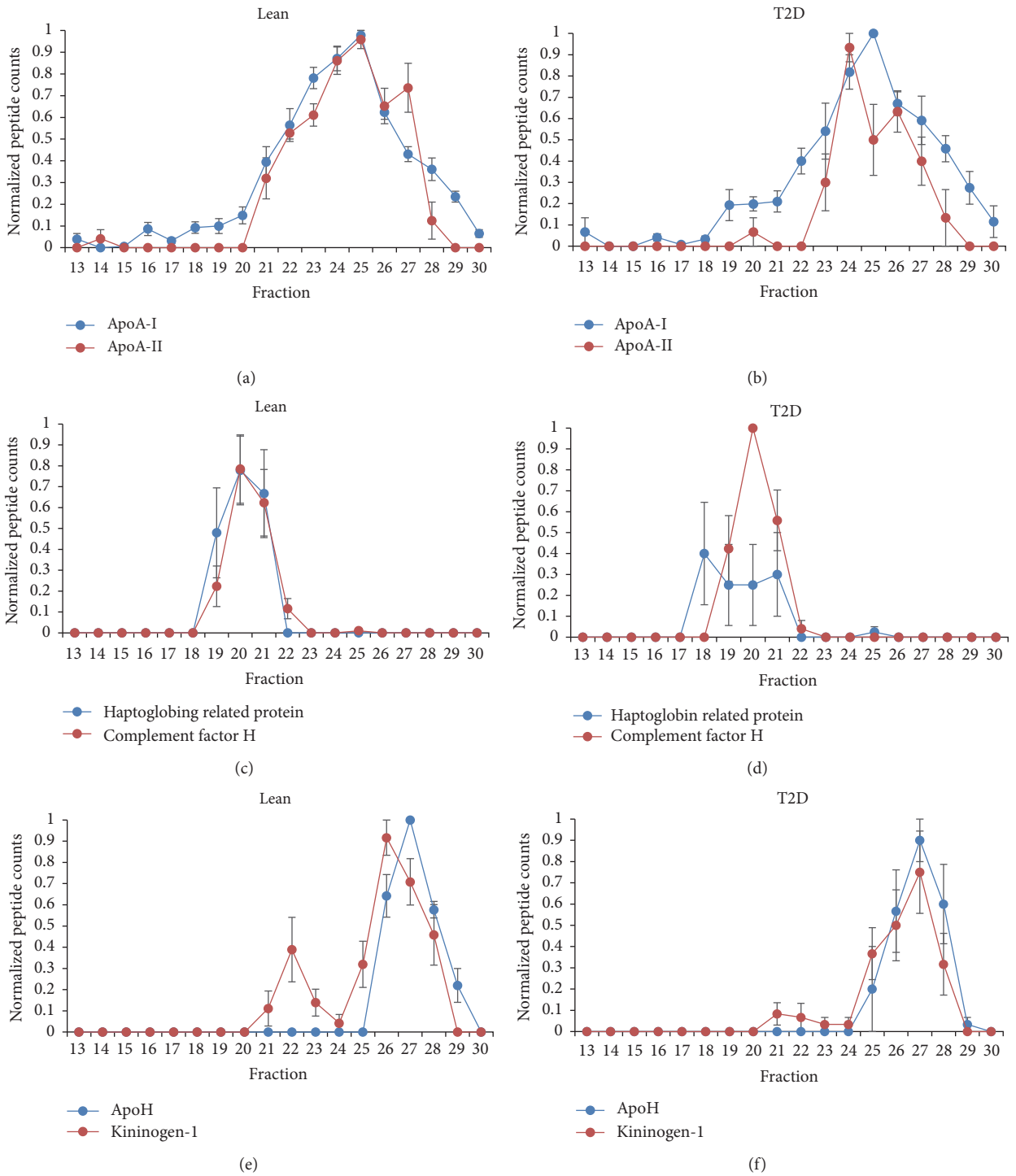

Figure 5: *Comigration patterns of protein pairs.* (a-b) apoA-I and apoA-II, (c-d) haptoglobin-related protein and complement factor H, and (e-f) apoH and kininogen-1, from lean and T2D groups. Spectral counts were normalized by dividing maximum value across all fractions. Data are mean and standard deviation of normalized spectral counts.

proatherogenic elements. Lastly, in the pink cluster (Figures 6(e) and 6(f)), four out of six members are positively PWV-correlated proteins in T2D group. Only alpha-2-HS-glycoprotein demonstrates observable pattern change. Since these two clusters likely correspond to HDL subspecies in plasma, we expect these subspecies to be related to arterial stiffness.

3.4. HDL Subspecies and Disease. Taking our analysis a step further, we sought to explore the human diseases these subspecies are associated with. We used ToppCluster [31] to construct a disease-cluster association network ($P < 0.05$ after Bonferroni correction). As shown in Figure 7, square nodes of the network represent all the diseases significantly

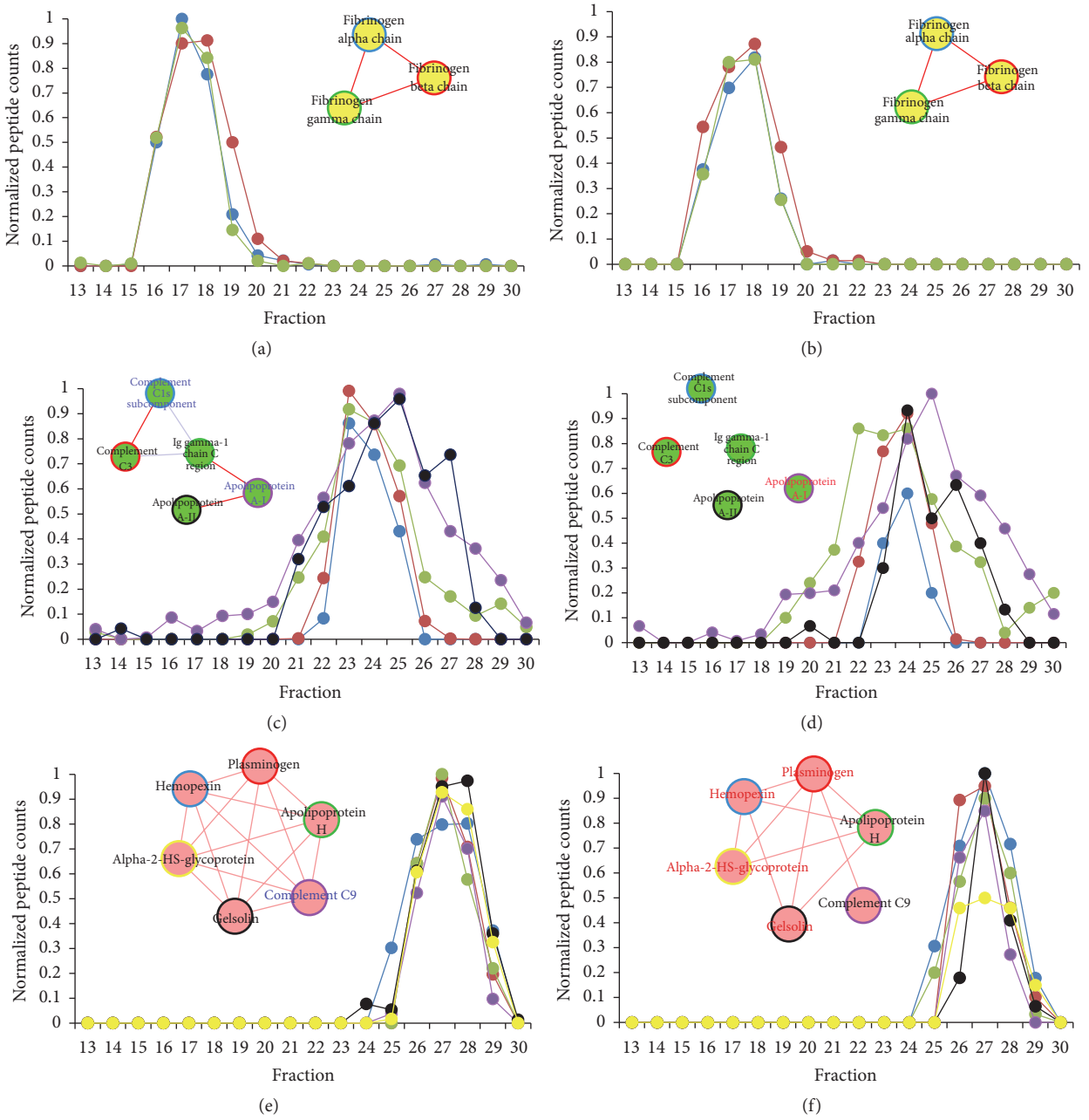

FIGURE 6: *Comigration patterns of the proteins residing on the same subspecies with at least two PWV-correlated proteins in the lean (a, c, e) and the T2D (b, d, f) groups*. Data are mean normalized peptide counts. Colors of distribution patterns are matched to the colors of node outlines. (a-b) Control: comigration pattern of fibrinogen $\alpha/\beta/\Upsilon$ chains (on the same particle) shows no difference between lean and T2D. (c-d) Cluster 1: apolipoprotein A-I, apolipoprotein A-II, Ig gamma-1 chain C region, complement C3, and complement C1s subcomponent. (e-f) Cluster 2: hemopexin, plasminogen, apolipoprotein H, complement C9, gelsolin, and alpha-2-HS glycoprotein.

associated with those clusters. Edges in the network represent significant associations, which are calculated based on hypergeometric tests. We marked diabetes-related, CVD-related, and dyslipidemia-related terms with different colors. Both clusters appeared to be associated with certain CVD-related or dyslipidemia-related diseases. The strong associations indicate that the proteins within the subspecies may work together and contribute to the pathogenesis of those diseases. Therefore, this disease association further supports that these HDL subspecies may be related to arterial stiffness.

4. Discussion

Many pieces of evidence have suggested that alterations of certain HDL proteins or subspecies in T2D patients may be associated with arterial stiffness [17, 33–37]. For example,

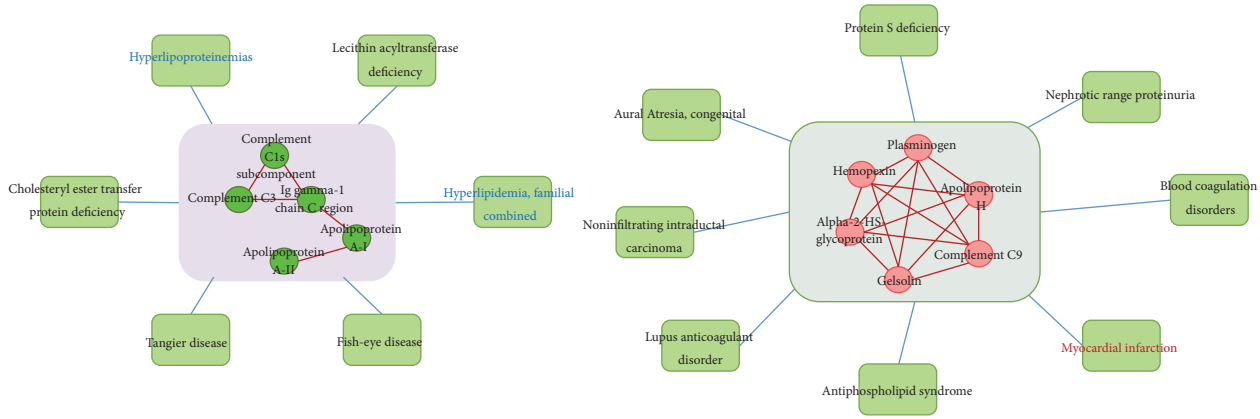

FIGURE 7: *Disease-associated networks for two HDL subspecies*. Each HDL subspecies is linked to its associated diseases (square nodes). Disease labels are marked with pink text (CVD-related), blue text (dyslipidemia-related), and black text (others).

endothelial protective activities of HDL isolated from T2D subjects are reduced compared to those of healthy control subjects [37]. Further, HDL incubated with glucose was shown to have impaired anti-inflammatory and antioxidant activities [36]. Thus, identification of T2D-specific HDL proteins or subspecies could not only serve as early biomarkers of distinct stages of CVD but also help in designing specific HDL-related therapies to protect persons with T2D from CVD complications.

Even though previous studies have shown that HDL-associated proteins are altered in youth with T2D [17], which proteins or subspecies are specifically related to arterial stiffness remains elusive. Here, we set out to identify HDL proteins and subspecies that correlate with arterial stiffness by comparing clinical and proteomics data from lean and T2D participants. This work is novel in two aspects: (1) it reveals a number of significantly PWV-correlated proteins by combining biological assays, clinical measurement, and HDL proteomics and (2) it goes beyond individual proteins and investigates the impact of T2D from a HDL subspecies perspective.

With regard to the individual HDL proteins that were correlated with arterial stiffness, several findings are noteworthy, including changes in the PCC of apoA-I, histidine-rich glycoprotein, and hemopexin with PWV. In the current analysis, apoA-I has both negative and positive correlations with arterial stiffness, which indicates that apoA-I may serve as a platform for HDL particles that can be both atheroprotective and atherogenic. Since the gel filtration technique separates HDL particles by hydrodynamic diameter, an alteration of the distribution pattern indicates a change in particle size and thus a compositional change of HDL subspecies. ApoA-I in the T2D group exhibits lower normalized abundance in the larger HDL range and an increase in the smaller particle fractions. From the HDL subspecies perspective, apoA-I is the major component and structural scaffold of HDL and is likely involved in multiple HDL subspecies. Based on the PCC in different fractions (Figures 1 and 2), it is likely that the balance between larger size apoA-I containing subspecies in fractions 21-22 and the smaller apoA-I containing subspecies in fractions 25–28 may underlie apoA-I's apparent atheroprotection in the lean group and possibly also the increase in arterial stiffness in the T2D group. Unfortunately, based on current analysis, it is impossible to distinguish two possibilities: (1) T2D results in the breakdown of protective HDL particles into harmful smaller ones or (2) there exist two distinct HDL subspecies in the plasma with certain metabolic balance, and T2D tends to alter this balance. It will be important to understand the metabolic origins of these species to address these questions.

Additionally, histidine-rich glycoprotein and hemopexin are positively correlated with PWV in the T2D group. These two proteins play roles in the regulatory functions for the blood coagulation, complement, and fibrinolysis pathways. As of now, we do not have enough information to speculate how these proteins may contribute to vascular stiffness or even if they are causal in this regard.

Our network analysis revealed clear global differences in the protein networks between lean and T2D groups. Global topological parameters of these two networks suggest that the lean network has a stronger connectivity and tends to have more clusters, while the T2D network has a more scattered topology. It is possible that, in T2D, certain proteins are missing from critical HDL subspecies, thus altering their function. Fisher et al. [38] have described the formation of dysfunctional HDL. It is expected that when dysfunctional HDL are generated instead of mature spherical HDL, protein networks of HDL may show obvious topological differences. Our network analysis is consistent with the previous observations that the HDL subspecies in the T2D group are indeed altered by T2D [17, 33, 34], as demonstrated by the decreased intracluster links compared with the lean group (such as loss of the apoA-I and apoA-II link, as well as other links within the clusters).

Two candidate subspecies that contain at least two PWV-correlated proteins that may be related to arterial stiffness were identified. Notably, there are some distribution pattern changes in individual proteins of the identified subspecies between the lean and T2D groups (Figure 6). This indicates that the composition of these particles may be altered in the T2D subjects. It is possible that such compositional

alterations may impact certain functions of HDL and, consequently, the progression of CVD. These HDL subspecies may provide a link between T2D and CVD complications. Currently, our study only focused on arterial stiffness and CVD. Since T2D has various typical complications (e.g., CVD, neuropathy, nephropathy, retinopathy, hearing impairment, and Alzheimer's disease), we speculate that diverse HDL subspecies or lipid-associated particles may be related to different complications.

One limitation of this work was the limited sample size. Due to the limitation of the subject recruiting as well as the relatively limited throughput of the plasma fractionation procedure, this study was carried out on a representative subject group instead of a large population. Thus, we cannot totally exclude the possibility of bias induced by individual differences. However, no other study has endeavored to subfractionate lipoproteins and track their proteome in this much detail. Another limitation of the study is that we cannot know with 100% certainty whether every protein in the analysis resided on an HDL particle. However, the study was specifically designed to increase the likelihood that we are only looking at HDL-associated proteins. The method used in this study involves a multipronged approach to fractionate HDL. First, whole plasma is size-fractionated. Second, LRA is used to isolate lipid-containing particles from each fraction. Although LRA effectively binds lipid-rich species, we cannot confidently exclude the possibility that some plasma proteins bound the LRA. Thus it is possible that, even with the LRA selection process, some plasma proteins were detected by MS analysis. However, finally, the resulting list of MS identified proteins (approximately 110 proteins) was filtered against the HDL Proteome Watch, a curated database that reports proteins that have been detected on HDL by multiple mass spectrometry studies. Thus, it is reasonable that the proteins reported in the final subspecies analysis are likely to be HDL-associated proteins. Future work will focus on validating these results in larger groups.

5. Conclusions

In summary, we identified seven HDL proteins that are negatively correlated with arterial stiffness, as well as nine proteins that positively correlated with arterial stiffness from complex proteomics data. Additionally, we constructed protein comigration networks for the lean and T2D groups, separately. Using the network-based complex identification, we discovered two PWV-related HDL subspecies that are associated with multiple complications of T2D. We caution that current findings are only based on correlation analysis. Nevertheless, the correlations are significant enough to support further experimental investigation. We found that the distribution of those proteins may provide a better understanding on how HDL proteins are altered in youth with T2D and how they are related to arterial stiffness. Our results also indicate that certain HDL proteins (e.g., apoA-I and histidine-rich glycoprotein) may reverse their protective roles and become atherogenic in T2D condition. This may explain why the HDL-C raising therapies [7] have not achieved desirable outcomes. These PWV-related proteins and subspecies could be excellent targets in future deterministic experiments for investigating specific HDL subspecies.

Abbreviations

HDL: High-density lipoproteins
T2D: Type 2 diabetes
PWV: Pulse wave velocity
CVD: Cardiovascular disease
LDL: Low-density lipoproteins
HDL-C: High-density lipoprotein-cholesterol
TLF: Trypanosome lytic factor
apo: Apolipoprotein
RCT: Reverse cholesterol transport.

Data Availability

For data availability, please refer to the original study [17].

Ethical Approval

The study has been approved by IRB committee of Cincinnati Children's Hospital Medical Center.

Consent

Written informed consent was obtained from participants who are 18 years old or older or from the parent or guardian with for participants below 18 years of age.

Conflicts of Interest

The authors declare that there are no conflicts of interest.

Authors' Contributions

L. Jason Lu designed the research plan in this paper; Amy S. Shah and Scott M. Gordon performed experiments and collected clinical data; Xiaoting Zhu, Hailong Li, and Sheng Ren analyzed the data; Amy S. Shah, Debi K. Swertfeger, and John T. Melchior helped in study design; Xiaoting Zhu, Debi K. Swertfeger, Hailong Li, and L. Jason Lu wrote the manuscript; W. Sean Davidson and L. Jason Lu supervised the research.

Acknowledgments

This work was supported by National Institutes of Health (R01-HL111829 to L. Jason Lu, K23-HL118132 to Amy S. Shah, and R01-HL104136 to W. Sean Davidson), a predoctoral fellowship to Scott M. Gordon and postdoctoral fellowship to John T. Melchior from the Great Rivers Affiliate of the American Heart Association, and the National Natural Science Foundation of China (no. 31601083).

Supplementary Materials

Supplemental Figure 1: correlation of apoA-I relative abundance in fraction 21 versus PWV measurement. Lean, T2D, and combined data are marked with blue, red, and green, respectively. The PCC of combined data and PWV appear to be mainly driven by lean group, so that this PCC

fails to reflect the relationship between PWV and proteins. *(Supplementary Materials)*

References

[1] S. M. Grundy and et al., "Prevention Conference VI: Diabetes and Cardiovascular Disease: Writing Group IV: Lifestyle and Medical Management of Risk Factors," *Circulation*, vol. 105, no. 18, pp. e153–e158, 2002.

[2] M.-R. Taskinen, "Diabetic dyslipidemia," *Atherosclerosis Supplements*, vol. 3, no. 1, pp. 47–51, 2002.

[3] J.-C. Fruchart, F. Sacks, M. P. Hermans et al., "The Residual Risk Reduction Initiative: A Call to Action to Reduce Residual Vascular Risk in Patients with Dyslipidemia," *American Journal of Cardiology*, vol. 102, no. 10, 2008.

[4] D. Keene, C. Price, M. J. Shun-Shin, and D. P. Francis, "Effect on cardiovascular risk of high density lipoprotein targeted drug treatments niacin, fibrates, and CETP inhibitors: meta-analysis of randomised controlled trials including 117,411 patients," *British Medical Journal*, vol. 349, Article ID g4379, 2014.

[5] R. S. Birjmohun, B. A. Hutten, J. J. P. Kastelein, and E. S. G. Stroes, "Efficacy and safety of high-density lipoprotein cholesterol-increasing compounds: A meta-analysis of randomized controlled trials," *Journal of the American College of Cardiology*, vol. 45, no. 2, pp. 185–197, 2005.

[6] S. J. Nicholls, H. B. Brewer, J. J. P. Kastelein et al., "Effects of the CETP inhibitor evacetrapib administered as monotherapy or in combination with statins on HDL and LDL cholesterol: a randomized controlled trial," *Journal of the American Medical Association*, vol. 306, no. 19, pp. 2099–2109, 2011.

[7] R. S. Wright, "Recent clinical trials evaluating benefit of drug therapy for modification of HDL cholesterol," *Current Opinion in Cardiology*, vol. 28, no. 4, pp. 389–398, 2013.

[8] L. Bowman, J. C. Hopewell, F. Chen et al., "Effects of anacetrapib in patients with atherosclerotic vascular disease," *The New England Journal of Medicine*, vol. 377, no. 13, pp. 1217–1227, 2017.

[9] F. Rezaee, B. Casetta, J. H. M. Levels, D. Speijer, and J. C. M. Meijers, "Proteomic analysis of high-density lipoprotein," *Proteomics*, vol. 6, no. 2, pp. 721–730, 2006.

[10] T. Vaisar, S. Pennathur, P. S. Green et al., "Shotgun proteomics implicates protease inhibition and complement activation in the antiinflammatory properties of HDL," *The Journal of Clinical Investigation*, vol. 117, no. 3, pp. 746–756, 2007.

[11] H. Karlsson, P. Leanderson, C. Tagesson, and M. Lindahl, "Lipoproteomics II: mapping of proteins in high-density lipoprotein using two-dimensional gel electrophoresis and mass spectrometry," *Proteomics*, vol. 5, no. 5, pp. 1431–1445, 2005.

[12] M. Heller, D. Stalder, E. Schlappritzi, G. Hayn, U. Matter, and A. Haeberli, "Mass spectrometry-based analytical tools for the molecular protein characterization of human plasma lipoproteins," *Proteomics*, vol. 5, no. 10, pp. 2619–2630, 2005.

[13] S. M. Gordon, J. Deng, L. J. Lu, and W. S. Davidson, "Proteomic characterization of human plasma high density lipoprotein fractionated by gel filtration chromatography," *Journal of Proteome Research*, vol. 9, no. 10, pp. 5239–5249, 2010.

[14] W. S. Davidson, R. A. G. D. Silva, S. Chantepie, W. R. Lagor, M. J. Chapman, and A. Kontush, "Proteomic analysis of defined hdl subpopulations reveals particle-specific protein clusters: relevance to antioxidative function," *Arteriosclerosis, Thrombosis, and Vascular Biology*, vol. 29, no. 6, pp. 870–876, 2009.

[15] J. Raper, R. Fung, J. Ghiso, V. Nussenzweig, and S. Tomlinson, "Characterization of a novel trypanosome lytic factor from human serum," *Infection and Immunity*, vol. 67, no. 4, pp. 1910–1916, 1999.

[16] H. Li, S. M. Gordon, X. Zhu et al., "Network-Based Analysis on Orthogonal Separation of Human Plasma Uncovers Distinct High Density Lipoprotein Complexes," *Journal of Proteome Research*, vol. 14, no. 8, pp. 3082–3094, 2015.

[17] S. M. Gordon, W. S. Davidson, E. M. Urbina et al., "The effects of type 2 diabetes on lipoprotein composition and arterial stiffness in male youth," *Diabetes*, vol. 62, no. 8, pp. 2958–2967, 2013.

[18] A. Heink, W. S. Davidson, D. K. Swertfeger, L. J. Lu, and A. S. Shah, "A Comparison of Methods to Enhance Protein Detection of Lipoproteins by Mass Spectrometry," *Journal of Proteome Research*, vol. 14, no. 7, pp. 2943–2950, 2015.

[19] S. M. Gordon, S. Hofmann, D. S. Askew, and W. S. Davidson, "High density lipoprotein: It's not just about lipid transport anymore," *Trends in Endocrinology & Metabolism*, vol. 22, no. 1, pp. 9–15, 2011.

[20] J. A. Glomset, "The plasma lecithins: cholesterol acyltransferase reaction," *Journal of Lipid Research*, vol. 9, no. 2, pp. 155–167, 1968.

[21] M. I. Mackness, S. Arrol, and P. N. Durrington, "Paraoxonase prevents accumulation of lipoperoxides in low-density lipoprotein," *FEBS Letters*, vol. 286, no. 1-2, pp. 152–154, 1991.

[22] J.-R. Nofer and G. Assmann, "Atheroprotective effects of high-density lipoprotein-associated lysosphingolipids," *Trends in Cardiovascular Medicine*, vol. 15, no. 7, pp. 265–271, 2005.

[23] C. Wadham, N. Albanese, J. Roberts et al., "High-density lipoproteins neutralize C-reactive protein proinflammatory activity," *Circulation*, vol. 109, no. 17, pp. 2116–2122, 2004.

[24] J. T. Kuvin, N. A. Harati, N. G. Pandian, R. M. Bojar, and K. R. Khabbaz, "Postoperative cardiac tamponade in the modern surgical era," *The Annals of Thoracic Surgery*, vol. 74, no. 4, pp. 1148–1153, 2002.

[25] S. Kulkarni, K. J. Woollard, S. Thomas, D. Oxley, and S. P. Jackson, "Conversion of platelets from a proaggregatory to a proinflammatory adhesive phenotype: Role of PAF in spatially regulating neutrophil adhesion and spreading," *Blood*, vol. 110, no. 6, pp. 1879–1886, 2007.

[26] American Diabetes Association, "Standards of medical care in diabetes—2012," *Diabetes Care*, vol. 35, pp. S11–S63, 2012.

[27] S. Laurent, J. Cockcroft, L. van Bortel et al., "Expert consensus document on arterial stiffness: methodological issues and clinical applications," *European Heart Journal*, vol. 27, no. 21, pp. 2588–2605, 2006.

[28] D. K. Swertfeger, H. Li, S. Rebholz et al., "Mapping atheroprotective functions and related proteins/lipoproteins in size fractionated human plasma," *Molecular & Cellular Proteomics*, vol. 16, no. 4, pp. 680–693, 2017.

[29] W. S. Davidson, "HDL Proteome Watch, 2016," http://homepages.uc.edu/~davidswm/HDLproteome.html.

[30] T. Nepusz, H. Yu, and A. Paccanaro, "Detecting overlapping protein complexes in protein-protein interaction networks," *Nature Methods*, vol. 9, no. 5, pp. 471-472, 2012.

[31] V. Kaimal, E. E. Bardes, S. C. Tabar, A. G. Jegga, and B. J. Aronow, "ToppCluster: A multiple gene list feature analyzer for comparative enrichment clustering and networkbased dissection of biological systems," *Nucleic Acids Research*, vol. 38, no. 2, Article ID gkq418, pp. W96–W102, 2010.

[32] S. M. Gordon and et al., "Multi-dimensional Co-separation Analysis Reveals ProteinProtein Interactions Defining Plasma Lipoprotein Subspecies," *Molecular and Cellular Proteomics*, vol. 12, no. 11, pp. 3123–3134, 2013.

[33] A. von Eckardstein and J.-R. Nofer, "Frail HDLs and stiff arteries in type 2 diabetes in juveniles," *Diabetes*, vol. 62, no. 8, pp. 2662–2664, 2013.

[34] J. W. Brinck, A. Thomas, E. Lauer et al., "Diabetes mellitus is associated with reduced high-density lipoprotein sphingosine-1-phosphate content and impaired high-density lipoprotein cardiac cell protection," *Arteriosclerosis, Thrombosis, and Vascular Biology*, vol. 36, no. 5, pp. 817–824, 2016.

[35] C. Calvo, C. Talussot, G. Ponsin, and F. Berthézène, "Non enzymatic glycation of apolipoprotein A-I. Effects on its self-association and lipid binding properties," *Biochemical and Biophysical Research Communications*, vol. 153, no. 3, pp. 1060–1067, 1988.

[36] C. C. Hedrick, S. R. Thorpe, M.-X. Fu et al., "Glycation impairs high-density lipoprotein function," *Diabetologia*, vol. 43, no. 3, pp. 312–320, 2000.

[37] S. A. Sorrentino, C. Besler, L. Rohrer et al., "Endothelial-vasoprotective effects of high-density lipoprotein are impaired in patients with type 2 diabetes mellitus but are improved after extended-release niacin therapy," *Circulation*, vol. 121, no. 1, pp. 110–122, 2010.

[38] E. A. Fisher, J. E. Feig, B. Hewing, S. L. Hazen, and J. D. Smith, "High-density lipoprotein function, dysfunction, and reverse cholesterol transport," *Arteriosclerosis, Thrombosis, and Vascular Biology*, vol. 32, no. 12, pp. 2813–2820, 2012.

Hindawi
Complexity
Volume 2018, Article ID 9728264, 12 pages
https://doi.org/10.1155/2018/9728264

Research Article

Vector Autoregressive Hierarchical Hidden Markov Models for Extracting Finger Movements Using Multichannel Surface EMG Signals

Nebojša Malešević,[1] **Dimitrije Marković**,[2] **Gunter Kanitz**,[3] **Marco Controzzi**,[3] **Christian Cipriani**,[3] **and Christian Antfolk**[1]

[1]*Department of Biomedical Engineering, Lund University, 221 00 Lund, Sweden*
[2]*Chair for Neuroimaging, Department of Psychology, Technische Universitat Dresden, 01069 Dresden, Germany*
[3]*The BioRobotics Institute, Scuola Superiore Sant'Anna, Pisa, Italy*

Correspondence should be addressed to Nebojša Malešević; nebojsa.malesevic@bme.lth.se

Received 9 June 2017; Revised 27 December 2017; Accepted 14 January 2018; Published 18 February 2018

Academic Editor: Zoran Obradović

Copyright © 2018 Nebojša Malešević et al. This is an open access article distributed under the Creative Commons Attribution License, which permits unrestricted use, distribution, and reproduction in any medium, provided the original work is properly cited.

We present a novel computational technique intended for the robust and adaptable control of a multifunctional prosthetic hand using multichannel surface electromyography. The initial processing of the input data was oriented towards extracting relevant time domain features of the EMG signal. Following the feature calculation, a piecewise modeling of the multidimensional EMG feature dynamics using vector autoregressive models was performed. The next step included the implementation of hierarchical hidden semi-Markov models to capture transitions between piecewise segments of movements and between different movements. Lastly, inversion of the model using an approximate Bayesian inference scheme served as the classifier. The effectiveness of the novel algorithms was assessed versus methods commonly used for real-time classification of EMGs in a prosthesis control application. The obtained results show that using hidden semi-Markov models as the top layer, instead of the hidden Markov models, ranks top in all the relevant metrics among the tested combinations. The choice of the presented methodology for the control of prosthetic hand is also supported by the equal or lower computational complexity required, compared to other algorithms, which enables the implementation on low-power microcontrollers, and the ability to adapt to user preferences of executing individual movements during activities of daily living.

1. Introduction

The methods for estimating the intention of an amputee to control the movement of a prosthetic hand often relies on the interpretation/decoding of the electrical activity of muscles (electromyograms, EMG) recorded on the skin-surface of the residual limb [1, 2]. Even though information regarding the muscle activity could be obtained in various ways, commercially available prosthetic hands commonly use only a few surface EMG channels. Furthermore, the classification algorithms implemented in such prostheses generally comprise only calculation of an amplitude based EMG feature (e.g., root mean square) that is thresholded to obtain binary control of a single hand function [3]. Even in the case of multifunction prostheses with a plurality of independent joints, the same control paradigm is still employed where switching between different grasps can depend on non-EMG inputs [4], such as smartphone interfaces, specific movements measured using inertial sensors, object recognition algorithms based on camera systems [5], or EMG inputs such as cocontractions (contractions of multiple muscles). Relatively low percentage of users is capable of fully exploiting the capabilities of multifunction prosthetic hands. This suggests that the control strategies need to be improved in order to achieve an intuitive link between intention and the resulting artificial hand function.

With the ongoing development of dexterous prosthetic hands [6–10], the gap between the potential dexterity offered by the new hands and the actual capabilities of human-machine interfaces is even more evident. In contrast to the

commercial devices, a variety of EMG recording techniques [11, 12], signal preprocessing [13], and classifiers have been proposed in the academia [14]. One of the approaches for increasing selectivity and sensitivity of the EMG signals includes surgical intervention in order to place recording electrodes on top of or inside targeted muscles [15]. This technique was shown to provide superior inputs for any type of EMG based controller; however, it is limited by need of surgical intervention and may not be widely accessible. As an alternative, EMG picked up at the surface of the skin provides a safe, noninvasive interface, at the cost of selectivity. Considering that the underlying mechanism of a classification algorithm is to localize the source of the electrical activity (active muscle), the methodology employed for similar problems is often based on multiple recording sites. Therefore, using a multichannel EMG approach provides an interesting perspective for improving the performance of surface EMG controllers. Increasing the number of the input signals also enables advanced data processing and classification techniques. Indeed, computational methods such as support vector regression [16], tree-structured neural network [17], Bayesian inference [18], ICA clustering [19], hidden Markov models [20], nonnegative matrix factorization [21], and various pattern recognition approaches [22–25], demonstrated promising classification results while using multiple discrete EMG channels or high-density surface EMG electrodes.

As one of the approaches for decoding finger movements using only multiple EMG signals, in this study we propose a novel classification algorithms based on the combination of EMG feature extraction and piecewise modeling of the feature temporal dynamics, incorporated in hierarchical hidden semi-Markov models (HHSMM) [26–28] and an online Bayesian classifier implemented through model inversion. We developed and assessed two variations of the aforementioned method and included special cases of these algorithms with reduced computational requirements. In order to assess our algorithm but also to provide an extensive evaluation of the impact of different EMG features on the classification accuracy, we compared its performance with some of the states of the art classifiers. This work is an extension of the study presented in [29].

2. Materials and Methods

2.1. Subjects. Five able bodied subjects participated in the experiment. All the subjects provided informed consent, and the study was approved by the Regional Ethical Review Board in Lund, Sweden.

2.2. Protocol. The methodology presented in this research relies on multielectrode EMG signals for movement classification. During the measurement procedure, a subject was comfortably seated with the right hand resting in a neutral position. The subject was asked to perform a movement to match a hand image shown on the screen in front of him/her. The requested movements were flexion/extension of all five fingers and adduction/abduction of the thumb (12 different movements). Movement and resting periods between movements were of equal length (5 seconds) and were timed by a LabVIEW (National Instruments, Austin, TX) custom application. The participant was visually prompted by the program, which synchronously acquired the EMG signal and the current cue annotation. Two different datasets (one for training and one for testing) each consisting of five repetitions of each movement, totaling 60 movements, and the rest states, were stored with the intended class information, for offline analysis.

2.3. EMG Recording. The dataset used in this paper was previously recorded and used in the publication by Huang et al. [30]. The EMG signals were acquired using a modified version of the amplification and acquisition system [31] and a LabVIEW program. The system acquired 16 channels of EMG, sampled at 1.6 kHz per channel and with a band-pass filter between 0.5 Hz and 800 Hz with 16-bit resolution and a gain of 56 dB per channel. The Red Dot Ag/AgCl (3M Health Care, Germany) electrodes that were used in the study were placed on the forearm of the participants as shown in Figure 1. For the 16 channel recordings, twelve electrodes were placed on the superficial flexor muscles on the volar side of the forearm and four electrodes were placed on the superficial extensor muscles on the dorsal side of the forearm. Electrodes were placed in order to cover as many independent muscles as possible. A sample of recorded EMG signals is provided in Figure 2.

2.4. Feature Extraction. A set of commonly used EMG features in the time domain was selected as an additional comparison criterion in this study. The choice of time domain features, versus spectral or time-frequency domain features, is in line with the tendency of deriving a control chain that could be implemented in an embedded system with limited processing power/speed. Among the relatively high number of reported features, we chose three-amplitude-related and three-frequency-related time-based EMG features. We implemented functions for the following EMG features as reported in [13, 32, 33].

2.4.1. Mean Absolute Value. Mean Absolute Value (MAV) is the favored EMG feature in many myoelectric control applications. It is calculated within a moving average window of the rectified EMG signal:

$$\mathrm{MAV} = \frac{1}{N}\sum_{n=1}^{N} \left|x_n\right|, \tag{1}$$

where N denotes window length and x_n the nth EMG sample within current window.

2.4.2. Root Mean Square. Root Mean Square (RMS) calculation is, similar to MAV, also windowed function:

$$\mathrm{RMS} = \sqrt{\frac{1}{N}\sum_{n=1}^{N} x_n^2}. \tag{2}$$

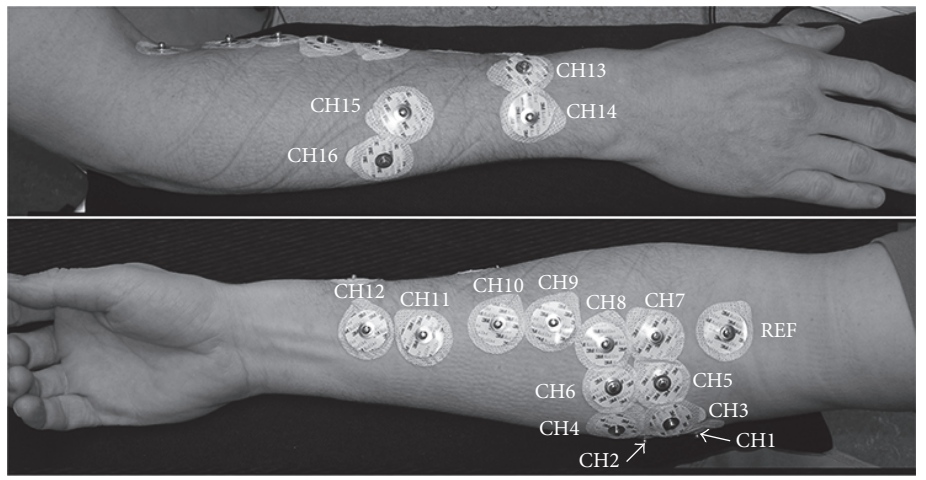

Figure 1: Measurement setup as in [25]. 16 monopolar channels were positioned in accordance with underlying hand muscles. The set of targeted muscles was chosen based on hand movements performed during the measurement protocol.

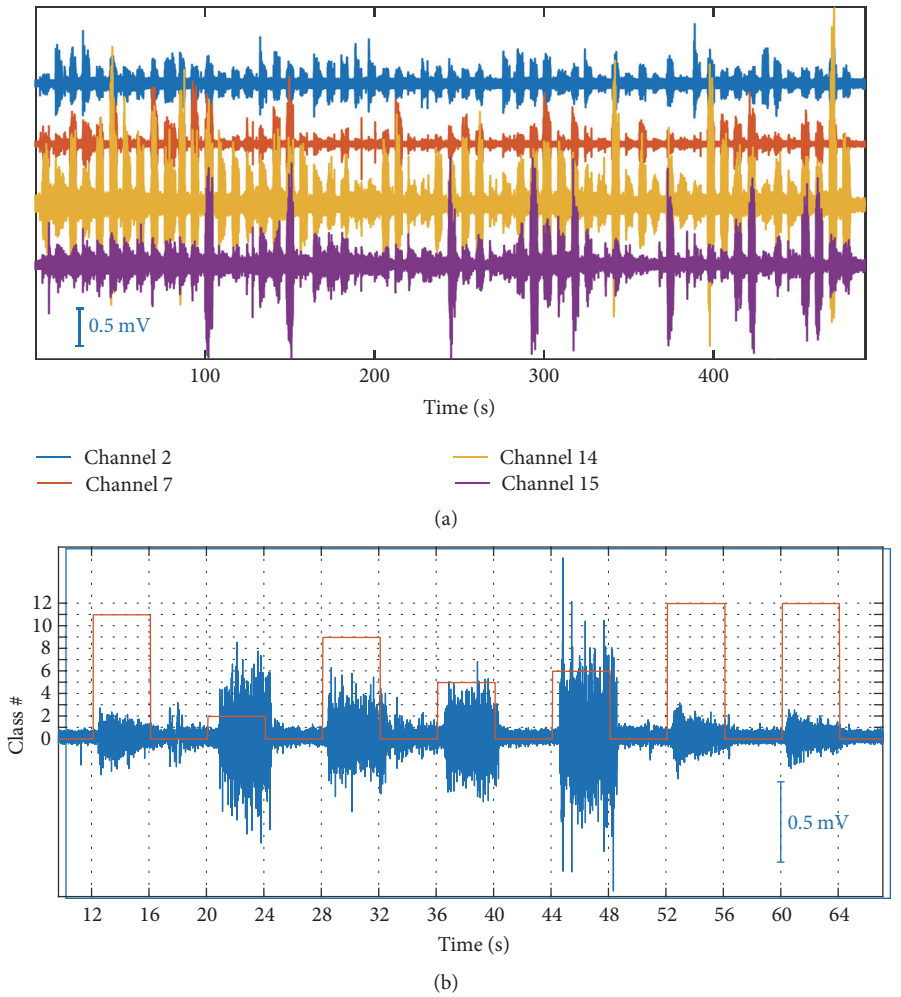

Figure 2: (a) shows sample EMG channels (2, 7, 15, and 15). (b) shows only channel 7 raw EMG signal (blue) with the visual cues/classes (red). This figure is an example of the latencies between visual cue and the EMG onset. This is also noticeable for the movement endings which are delayed with respect to the visual cue. Another important piece of information presented in this figure is similarity between EMG waveforms for the same movements (i.e., class 12).

In the case of the signal with mean value close to zero, such as surface EMG (sEMG) recorded with relatively large transcutaneous electrodes, the RMS becomes standard deviation of the input time series.

2.4.3. Variance. Variance (VAR) in the case of sEMG signal could be simplified enabling fast implementation in an embedded system. The resulting formula is the following:

$$\text{Var} = \frac{1}{N-1}\sum_{n=1}^{N} x_n^2. \tag{3}$$

2.4.4. Slope Sign Change. Slope Sign Change (SSC) is a time domain method used to estimate frequency feature if the EMG signal. The calculation of the SSC relies on counting changes between positive and negative slope among three consecutive samples. To limit SSC calculation only to periods with EMG activity, the threshold function is imposed in the feature extraction method:

$$\text{SSC} = \sum_{n=2}^{N-1} f\left[(x_n - x_{n-1}) \times (x_n - x_{n+1})\right]$$
$$f(x) = \begin{cases} 1, & \text{if } x \geq \text{threshold} \\ 0, & \text{otherwise.} \end{cases} \tag{4}$$

2.4.5. Zero Crossing. Zero Crossing (ZC) is the function that counts the number of consecutive EMG samples that change sign within the sliding window. Similar to SSC calculation, the threshold function is imposed to remove calculation of the ZC during periods without pronounced EMG activity:

$$\text{ZC} = \sum_{n=2}^{N-1} \left[\text{sgn}\left(x_n \times x_{n+1}\right) \times f\left[x_n - x_{n+1}\right]\right]$$
$$f(x) = \begin{cases} 1, & \text{if } x \geq \text{threshold} \\ 0, & \text{otherwise.} \end{cases} \tag{5}$$

2.4.6. Willison Amplitude. Willison amplitude (WA) is a measure related to superimposed action potentials that make the EMG signal. The WA is the number of consecutive differences between consecutive samples that exceed set threshold:

$$\text{WA} = \sum_{n=1}^{N-1} f\left[\left|x_n - x_{n+1}\right|\right]$$
$$f(x) = \begin{cases} 1, & \text{if } x \geq \text{threshold} \\ 0, & \text{otherwise.} \end{cases} \tag{6}$$

To produce comparable input conditions, the sliding window for all feature calculations was the same (250 ms width and 25 ms overlapping).

In the case of SSC, ZC, and WA calculations, thresholds were set based on the estimated white noise level during recording. As each recording session started with a rest period, it was convenient to use first 0.5 s to calculate thresholds that are used throughout the same recording. A sample of calculated features is shown in Figure 3.

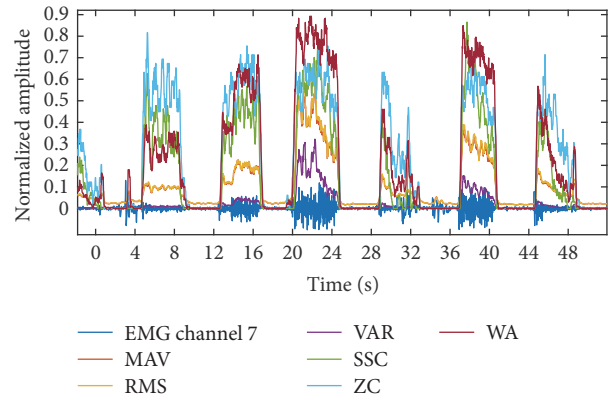

Figure 3: Example of the extracted features calculated from the EMG signal recorded on a single channel. The figure reveals that MAV and RMS features, in this case, almost overlap, but other features contain complementary information regarding EMG signal.

All feature extraction calculations were conducted using MATLAB, with moving window size of 250 ms and a displacement of 25 ms.

2.5. Classification Algorithm. Here, we will extend our previous work [29] in which we derived Bayesian online classifier using vector autoregressive hierarchical hidden Markov models (VARHHMM), with a classifier based on vector autoregressive hierarchical hidden semi-Markov models (VARHHSMM) [26–28]. The flowchart for the classifier's components is shown in Figure 4. The basic presumption of this approach is that the feature dynamics in time domain during a movement could be estimated by a number of VAR(1) segments defined via a unique set of parameters. A movement denotes a finger movement represented in the EMG feature space.

From the basic flowchart, it can be noted that the main difference between the two algorithms is in the top layer of the hierarchy. In the case of the VARHHMM, this layer only takes signal likelihood as the input to for the layer that identifies the current movement. In the case of the VARHHSMM, the current movement label will also depend on the expected duration of individual movements when identifying the active moment label. In what follows, we will refer to these two classifiers as hierarchical hidden Markov model (HMM) and hierarchical hidden semi-Markov model (HSMM), where we dropped the VAR and hierarchical labels for readability.

We assumed here that the selected time domain EMG features could be represented by a number of segments. To accommodate signal dynamics in real-time and enable creating a classifier suitable for embedded implementation, we defined individual segments as vector autoregressive (VAR) models of the first-order VAR(1). Using the VAR process for approximating the dynamics of a segment of an EMG

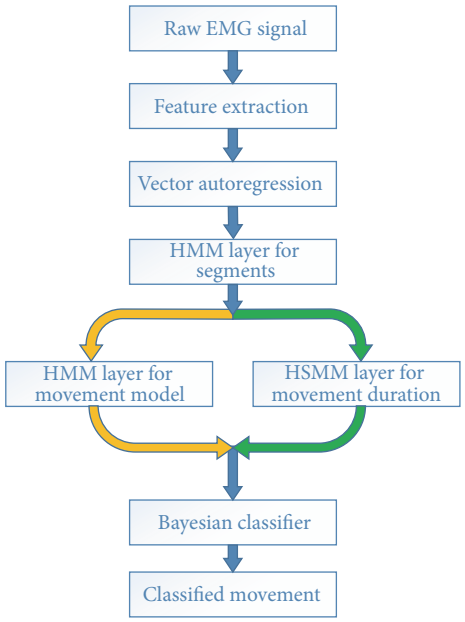

Figure 4: VARHHMM flowchart. At the hierarchically higher HMM layer, the two algorithms are split before the Bayesian inference layer. While one algorithm for HMM (orange path) is the same as the HMM for segments, the other algorithm is based on hidden semi-Markov model (HSMM) paradigm that incorporates movement duration as a free parameter.

time series allows for efficient prediction of feature dynamics and implicitly accounts for the noise presented in the recorded EMG signals. Formally, the VAR(1) process is defined as

$$\vec{y}_t = \vec{\mu}^{(i,m)} + A_1^{(i,m)} \vec{y}_{t-1} + \vec{\psi}_t^{(i,m)}, \tag{7}$$

where $\vec{y}_t$ is the latest acquired signal feature in vector form, $\vec{\mu}^{(i,m)}$ is the mean value of the signal, i denotes the segment within the mth finger movement, $A_1^{(i,m)}$ is the transition matrix of the VAR(1) model, and $\vec{\psi}_t^{(i,m)}$ is the random normal variable with zero mean. Note that the dynamics within each segment i and movement m are completely defined by the following set of parameters $(\vec{\mu}^{(i,m)}, A_1^{(i,m)}, \Sigma^{(i,m)})$, where $\Sigma^{(i,m)}$ denotes covariance of $\vec{\psi}_t^{(i,m)}$.

Based on predicted and measured sample vectors we can calculate which of the possible (fitted) VAR(1) models provides the best description of the recorded time series. The transition between individual segments (between different VAR(1) models) is considered as stochastic; thus, in our realization it is modeled as a HMM (as in [26]). The transitions between segments of a single movement are constrained by additional hidden states which define the currently active movement. For this reason, we introduced another HMM chain that acts as the second level of the hierarchy. The transitions between possible VAR(1) models of a single movement and different movements are defined through the transition

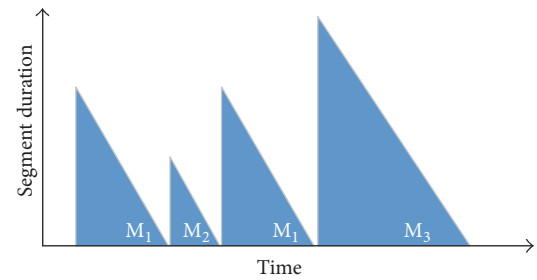

Figure 5: HSMM movement models. M1–M3 denote different dynamic movements. The HSMM algorithm uses distributions of individual movements durations to constrain transitions between them.

matrices for each HMM chain. The transition matrices on both levels of the hierarchy are estimated during the training procedure that relies on Viterbi expectation maximization algorithm [34].

By applying an approximate Bayesian inference procedure to the hierarchically arranged HMM and the emission distributions defined with VAR(1) models, we can classify each of the measured data points in a time series. The Bayesian inference for real-time signal classification relies on estimating the posterior probability for each movement. The posterior probability is calculated by combining expectations over movement probabilities with the evidence provided by the emission distributions (observation likelihoods). The expectations (predictions) are estimated using the posterior distribution at previous time sample and the transition matrices of movements and associated segments. Using the values of the posterior probability $p(M_t = m \mid y_{t:0})$ at the latest acquired signal y_t and the current movement $M_t = m$, we can classify the current sample as

$$l_t = \underset{m}{\operatorname{argmax}} p\left(M_t = m \mid y_{t:0}\right), \tag{8}$$

where l_t is the classification label obtained by our algorithm.

The HSMM algorithm is similar to the HMM algorithm with the only difference being that each movement includes a sequence of durations associated with it. This approach increases the number of free parameters with an additional vector comprising prior duration probabilities of individual movements. In other words, the probability of switching between movements is also influenced by the model of movement duration. An illustration of a specific realization of the movement switching sequence of the HSMM is shown in Figure 5.

The implementation of the HSHMM algorithm relies on a timer, or counter (Cnt) in the case of equidistant sampling. Upon entering a state/movement, the counter is set to predefined value related to that particular state duration and with every new sample is decremented. When the counter reaches 0, the state/movement is free to change. Upon switching to a new state, the counter is reset to zero. This additional condition is defined as

$$p\left(M_t = i \mid M_{t-1} = j,\ \mathrm{Cnt} = d\right) = \begin{cases} \delta(i,j) & \text{if } d > 0 \text{ (remain in the movement)} \\ \Upsilon_{i,j} & \text{if } d = 0 \text{ (free to change movement)}, \end{cases} \quad (9)$$

where M_t denotes movement at time sample t and Υ denotes transition matrix between movements.

In the case of HSMM, the duration of a movement is provided in form of a prior distribution. As the measurement protocol was executed in automated manner, all performed movements are of the same duration (~5 s) with some variability related to subject's reaction times to a visual cue. In order to simulate more realistic end-user scenario, we defined prior distribution to have a duration range with 2-second variability (5 ± 1 s). As the simplest scenario derived a priori, the imposed distribution was defined as uniform within the whole range. To estimate influence of the range of the imposed distribution, the accuracy score was also calculated for ranges from 5 ± 0.05 s to 5 ± 5 s.

As the number of segments per movement is the free parameter of both algorithms, it was of specific interest to evaluate performance of the classification with respect to a movement division by the automated optimization procedure. Specifically, the case of a single segment per movement was analyzed independently. The rationale for this lies in the extracted features dynamics in the time domain. When visualizing the recorded signals, a movement in a feature space reassembles a step response of a dynamic system, with a relatively short transient compared to the constant part. When ignoring the noise part of the vector autoregressive model (see above) we can rewrite the update equation as

$$\vec{y}_t = \vec{y}_{t-1} + B_1\left(\vec{\theta} - \vec{y}_{t-1}\right), \quad (10)$$

where the current sample y_t is a function of previous sample and the distance of the previous value from the terminal value $\vec{\theta}$ in the $t \to \infty$ limit. The constant matrix B_1 defines the rate of change along each dimension of the recorded signal. This form of the basic VAR representation is convenient for illustrating the signal trajectory after the onset of a movement (see Figure 6). The advantages of using single segments per movements area significantly shorter optimization time (explained in the following section) and a simplified real-time processing implementation as the lower HMM layer is removed.

2.6. Optimization. The estimation of the free parameters of all models presents the only computationally demanding procedure of the presented methodology. During the optimization, the free parameters of the VAR models (number of segments per movement, mean signal values of individual segments $\vec{\mu}^{(i,m)}$, covariance matrix $\Sigma^{(i,m)}$, transition matrix $A_1^{(i,m)}$, and between segment's transition matrix $\Upsilon^{(m)}$ which defines the HMM structure) are evaluated using a Viterbi algorithm coupled with an expectation maximization algorithm (EM) [35]. The flowchart of the optimization procedure is shown in Figure 7.

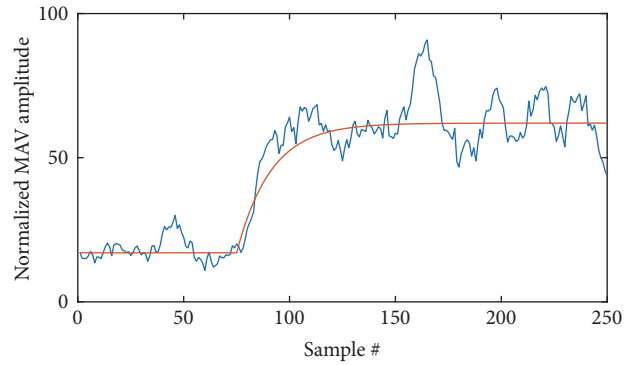

Figure 6: Example of the segment switching with AR(1) model (a one-dimensional VAR(1) model) with the forced one segment per movement. Blue line represents MAV feature dynamics when switching from a rest state to a movement, and the red line represents example of a single AR segment optimized for that movement.

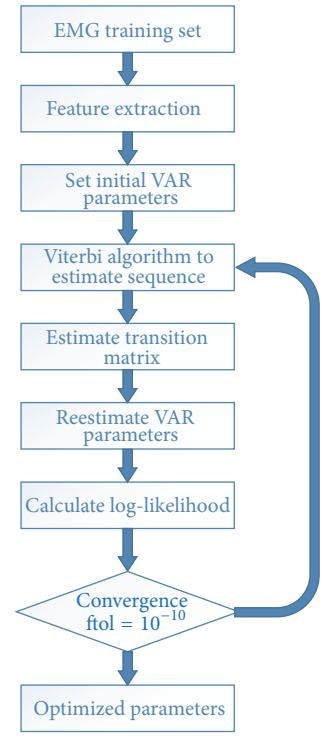

Figure 7: Optimization procedure flowchart. The main load of the optimization procedure is division of movements to segments. With a higher number of segments per movement, the Viterbi algorithm needs a large number of initial conditions for the model to converge to the global minimum instead of converging to a local minimum. This movement dividing method is not deterministic, resulting in slightly different models with every optimization run.

The optimization procedure is an iterative process where from the initial values of VAR parameters the Viterbi algorithm determines the most likely sequence of segments and estimates transition matrices. The following step includes reestimation of VAR parameters based on a maximum likelihood calculation and the most likely separation of training

data suggested by the Viterbi algorithm. The procedure shown in Figure 7 is iterated with the log-likelihood set as the convergence criterion. When the convergence criterion reaches a value of 10^{-10}, the iterations are stopped. The whole optimization method was based on the implementation of the Viterbi EM algorithm provided in the pyhsmm-autoregressive Python library [36].

Bearing in mind that the optimization method could converge towards a local optimum, we repeated the whole optimization procedure for 1000 different initial values of free parameters and only the solution with the lowest value of Bayesian Information Criterion (BIC) [37] was kept as final. This iterative extension of the Viterbi EM algorithm helped us to improve the convergence of the parameter estimation to optimal parameters values. The Python 3.6 codes for the parameters optimization and classification simulation are available upon request sent to the corresponding author.

2.7. Classifiers Used for Benchmarking. To evaluate the effectiveness of our algorithm, we used some of the most commonly used classification methods including

(i) Linear Discriminant Analysis (LDA),

(ii) Quadratic Discriminant Analysis (QDA),

(iii) K-nearest neighbors (knn), with $k = 15$,

(iv) Support Vector Machine with the Error-Correcting Output Codes (SVM ECOC),

(v) Linear Classifier with the Error-Correcting Output Codes (LC ECOC),

(vi) Linear Discriminant Analysis with the Error-Correcting Output Codes (LDA ECOC),

(vii) Naive Bayes (NB),

(viii) Random Forest (RF),

(ix) Decision Tree (DT).

The implementation of selected classifiers was done using *fitc* function in the MATLAB 2016b (The MathWorks Inc., Natick, MA). Similar to the VARHHMM algorithms, the classifiers were trained on only the training data set and tested on the test set and no postprocessing of class-annotations was performed.

3. Results

The ground truth for classification in this paper is set to be the visual cue presented to the subject. Although there is the noticeable latency between the visual cue and the muscle activity in both movement onset and cessation as shown in Figure 2, we decided to use this as a reference to provide the same basis for all of the classification methods. This was done to force classifiers to adapt to the transient processes between consecutive states. As expected, this approach results in lower overall classification accuracy but provides interesting insights into classifiers performances during dynamic, continuous changes of input parameters.

The main metric for comparing features and performance of the classifiers was accuracy. For the accuracy calculation, each feature sample (one observation every 25 ms) was treated individually. Moreover, as the rest state is directly involved in active motor driving by prosthesis control, it was also considered equal to the other movement classes. With this evaluation paradigm, each classification point was categorized as a true positive (TP) if the predicted class matches the visual cue label, or as a false positive (FP) if there is mismatch between predicted class and the visual cue. This approach generates a large number of data points, which was in our case approximately 20000 per dataset that could be used to investigate the performances of various features and classifiers.

The cumulative results for all subjects are presented in Table 1. As the accuracy results for the subjects do not fit into normal distribution, the accuracy values presented in the table are median values among all subjects. The differences between classifier and features are emphasized by ranking top three features and classifiers overall but also top three results for each EMG feature. From Table 1, it could be noted that HSHMM outperforms other classifiers for the majority of tested feature extraction algorithms. It is also interesting that the HSMM with only one segment per movement closely follows performance of the HSMM with multiple segments per movement. Among feature extraction algorithms, the MAV features resulted in the best performance across different classifiers and subjects; RMS and WA lead to slightly lower results compared to MAV, while using VAR, SSC and ZC failed to produce similar results. Among classifiers, only NB underperformed, while other classifiers produced mutually comparable results.

As the average accuracy across all subjects and all classifiers was the greatest in the case of MAV feature, the results obtained using this feature were analyzed in more detail. Table 2 shows accuracy results for each classifier and each subject when the MAV feature was used. The results show that all VARHHMM variations are top-ranked, with the HSMM algorithm having the highest median accuracy score. Although at the top ranks, the difference of median values is not prominent.

With the focus on VARHHMM methodology, to illustrate ability to separate individual finger movements and resting periods, the confusion matrix is shown in Figure 8. For this example, we selected the best performing feature method among all classifiers (MAV) and the subject with the median results (Subject 4). This was done to analyze in more detail the case close to the end-user scenario. The common indicator of the classification effectiveness is the confusion matrix which is used to reveal weak points of a classifier. Figure 8 is showing the confusion matrix for the HSMM algorithm. It could be noted that majority of movements (2, 4, 5, 6, 7, 11, 12, and 13) are classified with just sporadic misclassifications. For these movements, most of the errors are the consequence of the latency between the visual cue (used as the golden standard in this paper) and the actual muscle activity of the targeted movement. This effect is responsible for the movement-to-rest and rest-to-movement misclassifications. The rest class, except the errors related to delayed transitions, is generally well classified. The movements (3, 8, 9, and 10) have more samples that are labeled incorrectly as some other movement.

Table 1: Classifier accuracy in % for LDA, QDA, knn (15), SVM ECOC, LC ECOC, LDA ECOC, KNN ECOC, NB, HHMM, HSMM, and HHMM with only one segment per movement and HSMM with one segment per movement. The top ranked classifiers are marked with $*$ (top ranked), $**$ (second ranked), and $***$ (third ranked).

	LDA	QDA	KNN	SVM ECOC	LC ECOC	LDA ECOC	KNN ECOC	NB	RF	DT	HHMM	HSMM	HHMM S1	HSMM S1
MAV*	80.28	81.94	79.10	82.43	78.06	82.02	79.19	69.36	79.37	64.86	83.00***	84.30*	82.59	83.35**
RMS**	80.16	81.40	78.89	82.11*	76.92	81.37	79.74	69.81	79.44	63.68	81.58**	81.52***	69.95	81.16
VAR	71.77	38.12	78.22	79.76**	70.22	76.23	78.40	51.91	79.44	64.61	78.91***	82.36*	42.08	70.85
SSC	74.80	69.29	73.73	75.78**	75.30***	75.90*	73.99	62.56	73.83	62.70	71.41	75.56	71.41	75.56
ZC	74.75	73.03	72.64	75.90*	75.68**	75.42	73.08	60.17	72.34	59.72	74.26	75.44***	74.26	75.44
WA***	79.20	75.54	76.73	79.50	77.96	80.37***	76.92	63.06	77.74	64.93	78.39	84.09*	78.39	82.05**
Median	77.00	74.29	77.47	79.63**	76.30	78.30	77.66	62.81	78.59	64.15	78.65***	81.94*	72.83	78.36

Table 2: Classifier accuracy in % for the different subjects and MAV feature.

SUB	LDA	QDA	KNN	SVM ECOC	L ECOC	LDA ECOC	KNN ECOC	NB	RF	DT	HMM	HSMM	HMM S1	HSMM S1
1	82.07	86.39	79.10	82.43	80.60	82.65	79.19	65.97	79.65	69.70	87.50	91.18	86.70	90.94
2	80.28	81.94	79.96	84.83	80.85	83.55	80.45	69.36	83.01	65.68	83.51	85.61	83.51	85.42
3	79.69	56.82	77.19	81.26	72.77	80.31	77.98	63.79	79.48	57.75	76.28	75.76	71.51	73.43
4	81.64	82.31	82.95	82.83	77.92	82.02	83.12	75.33	80.56	70.08	83.00	84.30	82.59	83.35
5	80.21	66.88	78.54	80.97	78.06	78.45	78.78	70.25	74.62	63.94	77.20	82.96	62.86	78.39
Median	80.28	81.94	79.10	82.43	78.06	82.02	79.19	69.36	79.65	65.68	83.00	84.30	82.59	83.35
Rank	8	7	11	5	12	6	10	13	9	14	3	1	4	2

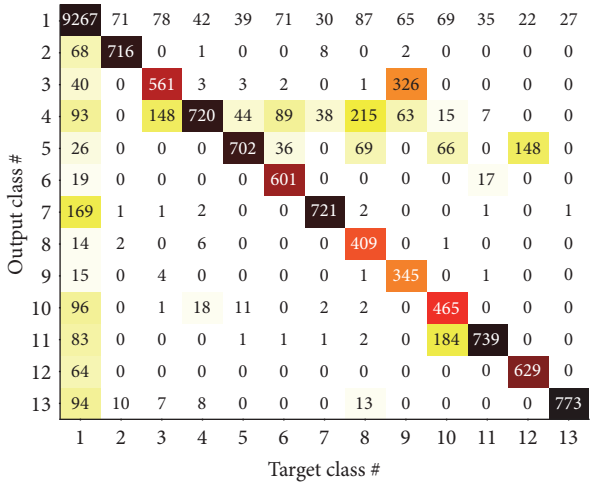

Figure 8: Confusion matrix, HSMM, MAV, Subject 4. There are around 800 observations per movement and 10100 in the rest class. The algorithm underperformed when discriminating classes 3, 8, 9, and 10, with class 9 being most problematic as the majority of observations were misclassified as class 3.

These errors, if consistent, could significantly impede control of a prosthesis. Thus, to examine the behavior of the VARHHMM implementations in a real-time application, the classification outputs were further analyzed.

Figure 9 contains some of the most severe examples of the misclassification errors produced by the HSMM algorithm. Figure 9(c) is an illustration of the proper movement classification where only errors occur during transition between rest and the movement. Compared to this sample, Figure 9(a) depicts an error of the labeling and keeping the incorrect movement active almost from the beginning of the movement onset, Figure 9(b) depicts misclassification at the middle of the movement period, and Figure 9(d) depicts the indecisiveness of the algorithm to label samples at the transient period. Out of these examples, the most severe in terms of real-time application is the first case that could lead to the execution of the false actuation. The other cases are relatively easy to correct using a state machine and/or majority voting algorithm that prevents situations that are less likely to occur by the user's intent.

Other metrics that were implemented to calculate classifier behavior in the real-time are motion selection (MS) and motion completion (MC) times. The calculation of MS and MC is derived from the papers of Li et al. and Ortiz-Catalan et al. [38, 39]. MS was computed as the delay between cue onset and the first correctly classified sample. Due to the difference in features frequency, the condition for the MC was slightly modified compared to other papers. In our algorithm, a new EMG feature was produced every 25 ms, while in [38] every 100 ms, so instead of 10 correct classifications, we waited for 40 correct classifications until the MC condition was fulfilled. This change was done in order to have comparable results with the relevant publications. The same metric for MS and MC was employed for all subjects and all features. Figure 10 is showing MS and MC times mean values across features and classifiers. It could be noted that HSMM has

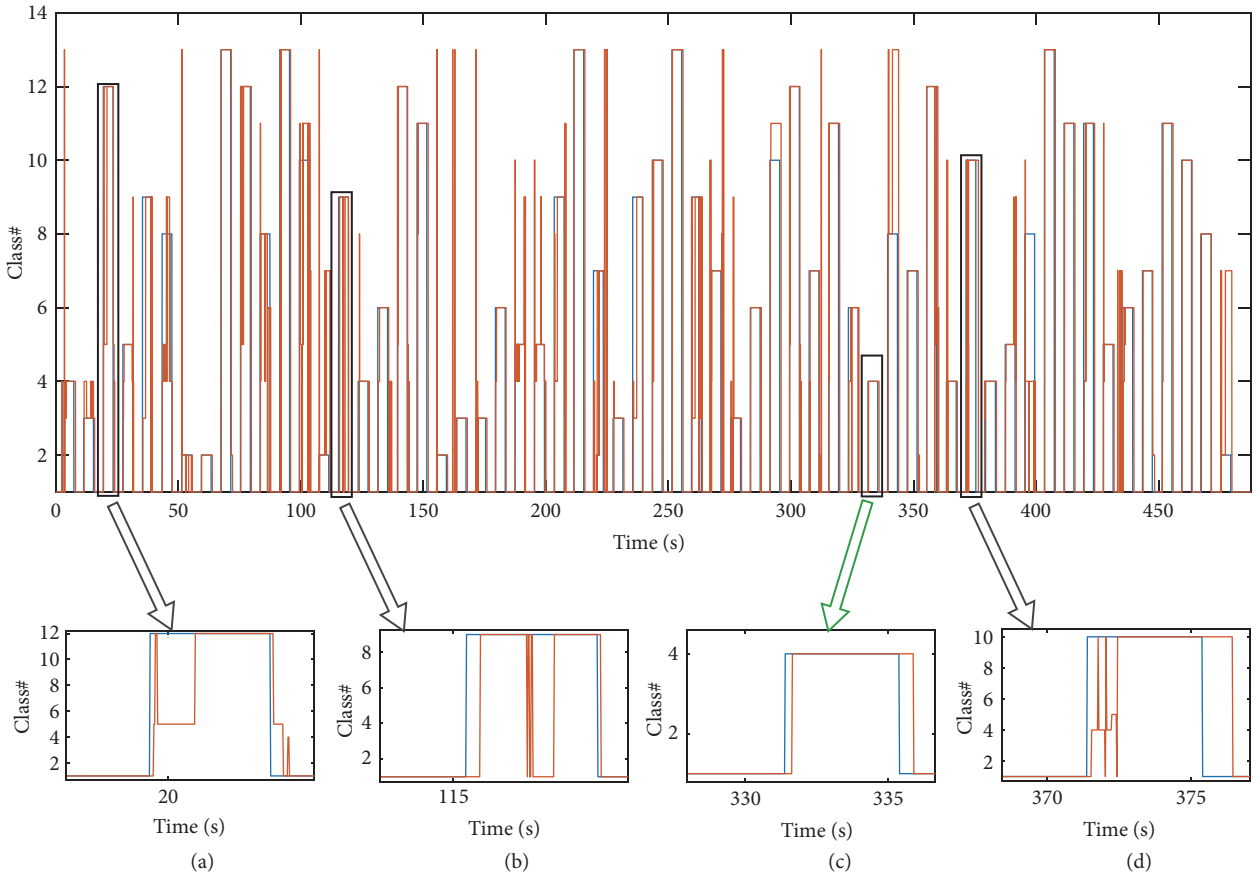

FIGURE 9: Sample classifications of the HSHMM. MAV (feature with the highest accuracies across all classifiers) and Subject 4 (median results).

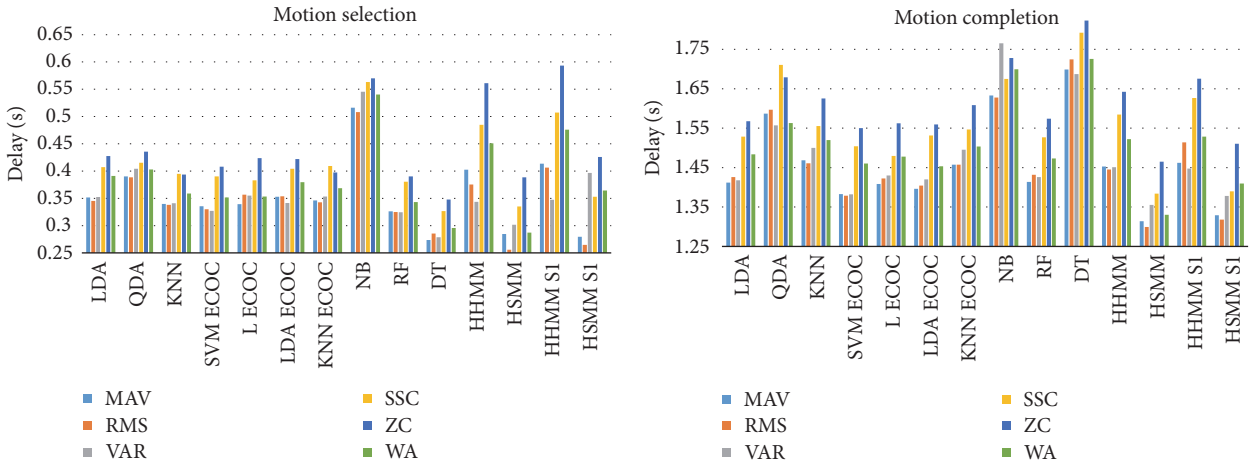

FIGURE 10: Motion selection (MS) and motion completion (MC) time. Mean values for MS time ranged from 0.25 s (HSMM-RMS) to 0.6 s (HHMM S1-ZC) and for MC time ranged from 1.3 s (HSMM-RMS) to 1.8 s (DT-SSC).

the lowest delay between cue and the first correctly classified sample, indicating that the method has a relatively low detection threshold compared to the other classifiers. It is also clear that the HSMM works the best with amplitude based features (MAV, RMS, and WA). Another interesting outcome is that HSMM with only one segment per movement achieves similar results as HSMM with multiple segments per movement when fed with MAV or RMS features of the EMG signal. On the other hand, the regular HHMM performed slightly worse on average than the best classifiers, such as

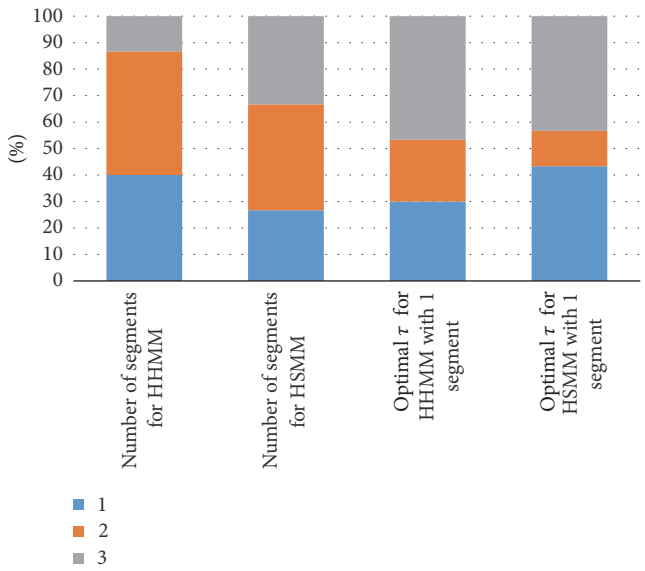

Figure 11: Optimization of the parameters. The chart shows that there is no clear advantage of using high number of segments per movement as in lot of cases even one segment is enough to achieve the highest classification accuracy. The same conclusion could be made for the number of AR samples as having only one previous sample available for making prediction could lead to high accuracy.

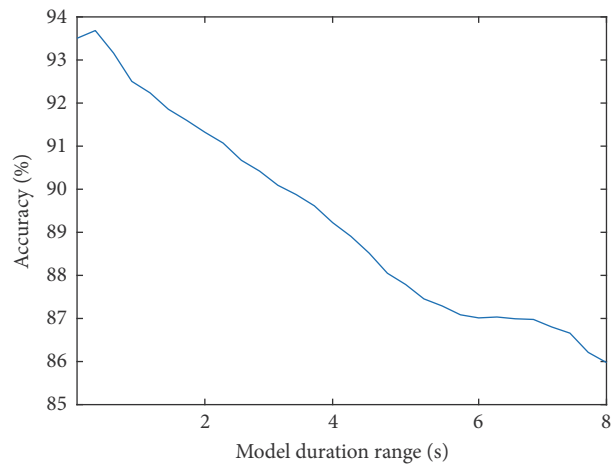

Figure 12: Dependence of the distribution range to the accuracy of the HSHMM classifier. The graph is showing that the accuracy decreases almost linearly with the increase of the movement duration range.

LDA, SVM ECOC, L ECOC, and LDA ECOC. Similar to HSMM, reducing number of segments per movement for the HHMM does not result in significant drop in performance related to MS and MC times.

We also analyzed another parameter, namely, the optimal number of segments per movement that results from the optimization procedure. For both HHMM and HSMM algorithms, two segments per movement most frequently produced the highest accuracy score (Figure 11). Another interesting parameter that was optimized and analyzed is the order of the vector autoregressive process (τ) in the HHMM and HSMM models with one segment per movement. The highest accuracy was achieved with 3 successive points, but what was not expected was relatively good accuracy with only one autoregressive sample (prediction relies only on the previous observation).

As the performance of HSMM algorithm depends on the predefined distribution of possible movement durations, analyzing this parameter was of great importance. During the measurements, the duration of movements was governed by the visual cues that were presented in automated manner. This way, the resulting movements have roughly the same duration of 5 s. To artificially introduce expected movement duration variability, we expanded the uniform duration distribution around central point of 5 s. With the extension of the expected movement duration, we evaluated classification accuracy. As presented in Figure 12, the dependency between classification accuracy and the range of permitted movement duration is almost linear in the mid-range. This finding is valuable for defining expected movement duration, while taking into account the tradeoff between accuracy and flexibility of the classifier to adapt to free movements by a user.

4. Discussion

In this paper, we presented novel algorithms for classifying features from surface EMG signals. Both of the proposed algorithms (HHMM and HSMM) are variations of the VARHHMM algorithm which combines vector autoregression, hidden Markov models, and Bayesian inference. The main focus of the presented results is the comparison between different EMG classifiers, including some of the most commonly used ones and VARHHMM variants. The results presented in Table 1 indicate that the HSMM algorithm with a priori fixed movement duration outperforms other classifiers. It should be also noted that the results of HSMM algorithm presented in this table are with the ad hoc uniform movement durations distribution between 3 s and 5 s. It is envisioned that, in the prolonged prosthesis use with this control algorithm, the movement duration distribution would be the parameter updated with each correctly executed movement. Thus, as the time of use increases, the distribution should become optimal and result in increased movement classification accuracy. The other derived algorithm (HHMM) was ranked overall just behind the SVM ECOC, mostly because of low accuracy when frequency related time-based features were used as inputs.

The results also reveal that reducing number of segments per movement to one does not result in considerable drop in accuracy scores for the derived algorithms (with the exception of VAR feature). This fact has significant impact on the possible implementation of the algorithms as the optimization, even in the case of large time series, for example, tens of minutes, could be executed in a matter of seconds. As the illustration, optimization of algorithm variants with free parameter of segments per movement takes up to 10 minutes per movement (Python 3.6 and Intel i7 processor). Depending on the embedded platform, our estimate is that optimization with one segment per movement could be still done in less than a minute. The other fact that contributes to

low processing during optimization and real-time application is that algorithm does not need high order autoregressive models. As presented in Figure 11, using even only one previous sample point could result in the highest accuracy score.

As this study was also aiming at finding out which feature extraction method works the best when coupled with the proposed algorithms and commonly used ones, we carried out a systematic test that included all features and subjects. With the EMG signals that we acquired, using MAV feature as the first step in the classification chain produced the highest accuracy scores among classifiers. The performance of MAV was closely matched by RMS, while WA produced the best results among the frequency related time-based features.

When compared with the reported results of Li et al. [38], the obtained MS and MC times calculated with our data and algorithms show some deviations. This is mostly present in MS values that represent the delay of the first properly classified sample. In the case of Li et al., MS values were in range 0.16–0.33 s, while in our simulations, only HSMM with MAV, RMS, and WA achieved similar performance. This behavior is the result of the difference in the ground truth choice: Li et al. used actual onset of the EMG activity, while we selected visual cue onset. With this in mind, it is expected that the MS times in our case have the superimposed lag of approximately 200–400 ms resulting from the latency between the cue and the muscle activation. That practically means that the HSMM would outperform reported classifiers if used in similar conditions. The same rationale goes for the MC times. Although classifiers tested in this study produced longer MC times on average, if reduced by the visual cue to muscle activity offset, the results would show that HSMM manages to correctly detect 40 samples (which correspond to 10 samples in paper of Li et al.) faster than the classifiers reported by Li et al.

5. Conclusion

The study performed on our set of multichannel surface EMG indicates that using MAV feature coupled with HSMM algorithm leads to movement decoding accuracy higher than other combinations of features and classifiers. This combination also guaranties the shortest MS and MC times, influencing a response of a prosthetic hand to a user intent.

The main advantages inherent to our algorithms compared to the existing methods are the following. (1) Low computation complexity for the execution of the algorithm: following the optimization procedure, which is computationally demanding but executed only once per model, the implementation of our algorithm comes down to the basic algebraic operations that could be implemented even on low-end microcontrollers. This feature also permits true real-time execution with the delay only related to EMG feature extraction and AR depth. Additionally, we tested even faster variations of developed algorithms that have only one segment per movement. With the small drop in performances, these algorithms, especially HSMM with one segment per movement, significantly decreased optimization time and further decreased execution load. (2) Easy expansion: once optimized, models could be stored, and in the case of introducing a new movement class, the optimization could be performed only on the newly added movement class. (3) Noise resilient: in comparison with some weak classifiers and threshold centered rule-based algorithms, the VARHHMM approach implicitly takes into account possible sources of stochastic noise.

The method proposed in this paper is intended for decoding individual finger movements for directly controlling actuated fingers of a prosthetic hand. Although desirable, this approach is not common as the prosthesis use during activities of daily living mostly consists of synergistic movements (grasps). Thus, as the alternative control paradigm, the proposed method could be implemented as the state machine classifier-controller. In this approach, the separable classes might be used to initiate fixed grasps (pinch/power/lateral/open) as this is what most commercial hands support.

Conflicts of Interest

The authors declare that there are no conflicts of interest regarding the publication of this paper.

Acknowledgments

This research is supported by the EU-Funded DeTOP Poject (EIT-ICT-24-2015, GA no. 687905) and the Swedish Research Council (637-2013-444).

References

[1] M. Zecca, S. Micera, M. C. Carrozza, and P. Dario, "Control of multifunctional prosthetic hands by processing the electromyographic signal," *Critical Reviews in Biomedical Engineering*, vol. 30, no. 4–6, pp. 459–485, 2002.

[2] N. Jiang, S. Dosen, K.-R. Muller, and D. Farina, "Myoelectric control of artificial limbs—is there a need to change focus? [In the Spotlight]," *IEEE Signal Processing Magazine*, vol. 29, no. 5, pp. 148–152, 2012.

[3] A. Fougner, O. Stavdahl, P. J. Kyberd, Y. G. Losier, and P. A. Parker, "Control of upper limb prostheses: Terminology and proportional myoelectric controla review," *IEEE Transactions on Neural Systems and Rehabilitation Engineering*, vol. 20, no. 5, pp. 663–677, 2012.

[4] C. Connolly, "Prosthetic hands from touch bionics," *Industrial Robot*, vol. 35, no. 4, pp. 290–293, 2008.

[5] S. Došen, C. Cipriani, M. Kostić, M. Controzzi, M. C. Carrozza, and D. B. Popovič, "Cognitive vision system for control of dexterous prosthetic hands: experimental evaluation," *Journal of NeuroEngineering and Rehabilitation*, vol. 7, no. 1, article 42, 2010.

[6] M. Controzzi, F. Clemente, D. Barone, A. Ghionzoli, and C. Cipriani, "The SSSA-MyHand: A dexterous lightweight myoelectric hand prosthesis," *IEEE Transactions on Neural Systems and Rehabilitation Engineering*, vol. 25, no. 5, pp. 459–468, 2017.

[7] *Touchbionics*, http://www.touchbionics.com/.

[8] *bebionic*, http://bebionic.com/.

[9] *Michelangelo*, http://www.ottobockus.com/prosthetics/upper-limb-prosthetics/solution-overview/michelangelo-prosthetic-hand/.

[10] *Vincent hand*, http://vincentsystems.de/en/.

[11] M. Ortiz-Catalan, R. Brånemark, B. Håkansson, and J. Delbeke, "On the viability of implantable electrodes for the natural control of artificial limbs: review and discussion," *Biomedical Engineering Online*, vol. 11, article 33, 2012.

[12] S. Muceli and D. Farina, "Simultaneous and proportional estimation of hand kinematics from EMG during mirrored movements at multiple degrees-of-freedom," *IEEE Transactions on Neural Systems and Rehabilitation Engineering*, vol. 20, no. 3, pp. 371–378, 2012.

[13] A. Phinyomark, C. Limsakul, and P. Phukpattaranont, "A novel feature extraction for robust EMG pattern recognition," *Journal of Computing*, vol. 1, no. 1, pp. 71–80, 2009.

[14] M. A. Oskoei and H. Hu, "Myoelectric control systems—a survey," *Biomedical Signal Processing and Control*, vol. 2, no. 4, pp. 275–294, 2007.

[15] M. Ortiz-Catalan, B. Håkansson, and R. Brånemark, "An osseointegrated human-machine gateway for long-term sensory feedback and motor control of artificial limbs," *Science Translational Medicine*, vol. 6, no. 257, Article ID 257re6, 2014.

[16] A. Ameri, E. N. Kamavuako, E. J. Scheme, K. B. Englehart, and P. A. Parker, "Support vector regression for improved real-time, simultaneous myoelectric control," *IEEE Transactions on Neural Systems and Rehabilitation Engineering*, vol. 22, no. 6, pp. 1198–1209, 2014.

[17] F. Sebelius, L. Eriksson, C. Balkenius, and T. Laurell, "Myoelectric control of a computer animated hand: a new concept based on the combined use of a tree-structured artificial neural network and a data glove," *Journal of Medical Engineering & Technology*, vol. 30, no. 1, pp. 2–10, 2006.

[18] S. Bitzer and P. Van Der Smagt, "Learning EMG control of a robotic hand: towards active prostheses," in *Proceedings of the IEEE International Conference on Robotics and Automation (ICRA '06)*, pp. 2819–2823, IEEE, May 2006.

[19] G. R. Naik, A. H. Al-Timemy, and H. T. Nguyen, "Transradial amputee gesture classification using an optimal number of sEMG sensors: an approach using ICA clustering," *IEEE Transactions on Neural Systems and Rehabilitation Engineering*, vol. 24, no. 8, pp. 837–846, 2016.

[20] A. D. C. Chan and K. B. Englehart, "Continuous myoelectric control for powered prostheses using hidden Markov models," *IEEE Transactions on Biomedical Engineering*, vol. 52, no. 1, pp. 121–124, 2005.

[21] C. Huang, X. Chen, S. Cao, B. Qiu, and X. Zhang, "An isometric muscle force estimation framework based on a high-density surface EMG array and an NMF algorithm," *Journal of Neural Engineering*, vol. 14, no. 4, Article ID 046005, 2017.

[22] R. N. Khushaba, A. H. Al-Timemy, A. Al-Ani, and A. Al-Jumaily, "A framework of temporal-spatial descriptors-based feature extraction for improved myoelectric pattern recognition," *IEEE Transactions on Neural Systems and Rehabilitation Engineering*, vol. 25, no. 10, pp. 1821–1831, 2017.

[23] A. A. Adewuyi, L. J. Hargrove, and T. A. Kuiken, "An analysis of intrinsic and extrinsic hand muscle EMG for improved pattern recognition control," *IEEE Transactions on Neural Systems and Rehabilitation Engineering*, vol. 24, no. 4, pp. 485–494, 2016.

[24] N. Celadon, S. Došen, I. Binder, P. Ariano, and D. Farina, "Proportional estimation of finger movements from high-density surface electromyography," *Journal of NeuroEngineering and Rehabilitation*, vol. 13, no. 1, article 73, 2016.

[25] C. Cipriani, C. Antfolk, M. Controzzi et al., "Online myoelectric control of a dexterous hand prosthesis by transradial amputees," *IEEE Transactions on Neural Systems and Rehabilitation Engineering*, vol. 19, no. 3, pp. 260–270, 2011.

[26] M. Yang, "Some properties of vector autoregressive processes with Markov-switching coefficients," *Econometric Theory*, vol. 16, no. 1, pp. 23–43, 2000.

[27] M. Dong and D. He, "Hidden semi-Markov model-based methodology for multi-sensor equipment health diagnosis and prognosis," *European Journal of Operational Research*, vol. 178, no. 3, pp. 858–878, 2007.

[28] S.-Z. Yu, "Hidden semi-Markov models," *Artificial Intelligence*, vol. 174, no. 2, pp. 215–243, 2010.

[29] N. Malešević, D. Marković, G. Kanitz, M. Controzzi, C. Cipriani, and C. Antfolk, "Decoding of individual finger movements from surface EMG signals using vector autoregressive hierarchical hidden Markov models (VARHHMM)," in *Proceedings of the International Conference on Rehabilitation Robotics (ICORR '17)*, pp. 1518–1523, IEEE, July 2017.

[30] H. Huang, T. Li, C. Bruschini et al., "EMG pattern recognition using decomposition techniques for constructing multiclass classifiers," in *Proceedings of the 6th IEEE RAS/EMBS International Conference on Biomedical Robotics and Biomechatronics (BioRob '16)*, pp. 1296–1301, IEEE, June 2016.

[31] C. Antfolk, C. Cipriani, M. Controzzi et al., "Using EMG for real-time prediction of joint angles to control a prosthetic hand equipped with a sensory feedback system," *Journal of Medical and Biological Engineering*, vol. 30, no. 6, pp. 399–406, 2010.

[32] N. Alves, E. Sejdić, B. Sahota, and T. Chau, "The effect of accelerometer location on the classification of single-site forearm mechanomyograms," *Biomedical Engineering Online*, vol. 9, article 23, 2010.

[33] B. Hudgins, P. Parker, and R. N. Scott, "A new strategy for multifunction myoelectric control," *IEEE Transactions on Biomedical Engineering*, vol. 40, no. 1, pp. 82–94, 1993.

[34] G. D. Forney, "The viterbi algorithm," *Proceedings of the IEEE*, vol. 61, no. 3, pp. 268–278, 1973.

[35] A. Logothetis and V. Krishnamurthy, "Expectation maximization algorithms for MAP estimation of jump Markov linear systems," *IEEE Transactions on Signal Processing*, vol. 47, no. 8, pp. 2139–2156, 1999.

[36] M. Johnson, *pyhsmm-autoregresive*, https://github.com/mattjj/pyhsmm-autoregressive.

[37] B. North and A. Blake, "Learning dynamical models using expectation-maximisation," in *Proceedings of the IEEE 6th International Conference on Computer Vision*, pp. 384–389, IEEE, 1998.

[38] G. Li, A. E. Schultz, and T. A. Kuiken, "Quantifying pattern recognition—based myoelectric control of multifunctional transradial prostheses," *IEEE Transactions on Neural Systems and Rehabilitation Engineering*, vol. 18, no. 2, pp. 185–192, 2010.

[39] M. Ortiz-Catalan, B. Håkansson, and R. Brånemark, "Real-time and simultaneous control of artificial limbs based on pattern recognition algorithms," *IEEE Transactions on Neural Systems and Rehabilitation Engineering*, vol. 22, no. 4, pp. 756–764, 2014.

Hindawi
Complexity
Volume 2017, Article ID 7120691, 11 pages
https://doi.org/10.1155/2017/7120691

Research Article

Sparse Learning of the Disease Severity Score for High-Dimensional Data

Ivan Stojkovic[1,2] and Zoran Obradovic[2]

[1]*Signals and Systems Department, School of Electrical Engineering, University of Belgrade, Bulevar Kralja Aleksandra 73, 11120 Belgrade, Serbia*
[2]*Center for Data Analytics and Biomedical Informatics, College of Science and Technology, Temple University, 1925 North 12th Street, Philadelphia, PA 19122, USA*

Correspondence should be addressed to Zoran Obradovic; zoran.obradovic@temple.edu

Received 11 May 2017; Revised 6 November 2017; Accepted 27 November 2017; Published 18 December 2017

Academic Editor: Sergio Gómez

Copyright © 2017 Ivan Stojkovic and Zoran Obradovic. This is an open access article distributed under the Creative Commons Attribution License, which permits unrestricted use, distribution, and reproduction in any medium, provided the original work is properly cited.

Learning disease severity scores automatically from collected measurements may aid in the quality of both healthcare and scientific understanding. Some steps in that direction have been taken and machine learning algorithms for extracting scoring functions from data have been proposed. Given the rapid increase in both quantity and diversity of data measured and stored, the large amount of information is becoming one of the challenges for learning algorithms. In this work, we investigated the direction of the problem where the dimensionality of measured variables is large. Learning the severity score in such cases brings the issue of which of measured features are relevant. We have proposed a novel approach by combining desirable properties of existing formulations, which compares favorably to alternatives in accuracy and especially in the robustness of the learned scoring function. The proposed formulation has a nonsmooth penalty that induces sparsity. This problem is solved by addressing a dual formulation which is smooth and allows an efficient optimization. The proposed approach might be used as an effective and reliable tool for both scoring function learning and biomarker discovery, as demonstrated by identifying a stable set of genes related to influenza symptoms' severity, which are enriched in immune-related processes.

1. Introduction

Diseases and other health conditions require continuous monitoring and assessment of the subject's state. The severity of the condition needs to be quantified, such that it can be used to guide medical decisions and allow appropriate and timely interventions. Disease severity scoring functions are typically used to quantify a patient's condition. However, disease severity and health are often difficult to quantify. That is because they are essentially latent concepts and are not directly accessible or observable. In an absence of a direct measurement of health, the severity of a condition is estimated based on values of some surrogate variables that are observable and hopefully informative about the condition of interest. In clinical practice, commonly tracked variables include temperature, heart rate, blood pressure, and responsiveness, to name a few out of a myriad of possible other variables. A severity score is subsequently calculated from such observable quantities using some heuristic rules. Prominent examples of such rules are SOFA [1] score for sepsis, or more general ICU scoring systems like APACHE II [2]. Both relevant variables and associated heuristic rules are established in a consensus of expert bodies and relevant institutions based on experience and current understanding of a condition. That process is long and tedious and often results in extensively coarse scoring rules and a nonoptimal set of relevant observable variables.

Although utilizing data was always part of this process, recently it was acknowledged that it might be improved/complemented by using machine learning methods that can automatically extract both rules and relevant variables directly from the data. There are already a number of approaches for automatic learning of severity scores/rules from data. One way is to use discrete class labels

for building classifiers and subsequently use the probability of a sample belonging to a certain class as a quantification measure of severity [3]. Another supervised approach is to learn the severity score function in a regression manner [4] from some surrogate of severity highly associated with undesired outcomes down the stream. A downside is that it already requires a good candidate for scoring function. An additional issue is that it might be sensitive to censoring due to treatment, where the severity of state is not acknowledged because treatment prevented undesired outcomes from happening. Some of the mentioned drawbacks are addressed in a more recent approach [5, 6] that is based on a clever observation that comparing two cases according to severity is easier to assess than to directly quantify the severity of a particular case. It was built upon the existing work on learning scoring functions for information retrieval tasks [7]. However, even this approach might be inappropriate in some cases, since it learns the severity score as a function of all measured variables, which will affect its performance when there are irrelevant features or when the number of features is much higher than the number of samples [8]. In essence, features unrelated to severity will be present even in small sets of measured variables, and, in high-throughput measurements like gene expression, this might be an even larger obstacle.

In this paper, we present an approach to the problem of learning disease severity scores in presence of irrelevant or high-dimensional measurements. We build on top of existing efforts by simultaneously performing feature selections that are most relevant for severity score learning. In particular, we are introducing the L_1 norm in the formulation of ranking SVM [7] along with the temporal smoothness constraint [6]. Attractive regularization properties of L_1 norm are already well acknowledged and exploited in a number of statistical learning methods since its introduction [9]. The proposed formulation of sparse severity score learning forces weights of (most of) the features to be exactly zero, therefore effectively performing feature selection by learning the sparse linear scoring function. This novel severity score objective function is convex and nonsmooth and it precludes the direct use of convenient optimization tools like gradient-based methods. Therefore, in this work, we are also providing the reformulation of the problem into its dual that is smooth and that allows efficient optimization. Other than learning the severity score from the data, which is an important instrument for assessing severity, the methodology may also be used to discover the most relevant variables/features for the disease severity phenotype. Such findings might be further used to suggest novel (testable) hypotheses about causal relations leading to disease manifestation and also to inspire novel therapeutic approaches.

The rest of the article is structured as follows: Methods begins with the introduction to related work and continues with new formulation and derivation of its solution. Results begins with evaluation on intuitive synthetic examples where the advantages of sparse severity score framework over the nonsparse one are apparent. Results continues with the assessment on a gene expression dataset of H3N2 viral infection responses. Efficacy and the robustness of the proposed method are compared favorably against multiple alternative methods. Results is concluded with gene ontology overrepresentation analysis of the discovered subset of genes most useful for the scoring function.

2. Methods

2.1. Previous and Related Work. As mentioned in Introduction, some of the first proposed severity score learning methods are supervised approaches that solve classification or regression tasks and whose solution provides a way to calculate a severity score.

For example, in [4] Alzheimer's Disease severity, as measured by cognitive scores, was modeled as (temporal) multitask regression using the fused sparse group lasso approach. The approach was more concerned with the progression of the disease, hence the multitask formulation. However, as we are mostly interested in severity score mapping from a single time-point set of measurements, here we are presenting its more influential ancestor, the LASSO model [9]:

$$\underset{w}{\operatorname{argmin}} \quad \mathrm{LASSO}(w) = \frac{1}{2} \|Y - Xw\|_2^2 + \lambda \|w\|_1 . \tag{1}$$

Here, Y is column vector of n given numeric scores, associated with d dimensional measurement matrix $X_{n\times d}$, while w denotes the solution in form of a d-dimensional column weight vector. We will use this model as one of the baselines for comparison as it is one of the main workhorses of biomarker selection [10] and even statistical learning in general.

Another approach used sparsity-inducing L_1 norm in combination with classical loss function for learning disease severity scoring function [3]. They proposed using L_1 regularized Logistic Regression model (among others), to model the severity scores for the abnormality of the skull in craniosynostosis cases:

$$\begin{aligned} \underset{w}{\operatorname{argmin}} \quad & L_1\mathrm{LogReg}(w) \\ & = \sum_{i=1}^{n} \log\left(1 + \exp\left(-Y_i\left(X_i w\right)\right)\right) + \lambda \|w\|_1 . \end{aligned} \tag{2}$$

This Sparse Logistic Regression formulation is another related model, as it also results in a sparse vector of feature weights w that essentially regress the decision boundary between the severity classes and might be used as a mapping function for severity scores. In (2), $Y_i \in \{-1, 1\}$ is a binary label for ith row of data matrix X.

As outlined previously, these forms of supervision where estimates of severity score functions (or severity classes) are needed might be hard to obtain in order to be utilized for training the severity score automatically. On the other hand, obtaining the pairs of comparisons is an easier task. Seminal work of learning the scoring functions from the comparison labels is proposed in [7]. In that work, the ranking SVM formulation (see (3)) is developed to learn better document retrieval from click-through data. This great insight came from noticing that the clicked links automatically have greater

ranks compared to the ones not clicked. And such kind of data is much more abundant than the user provided rankings.

$$\begin{aligned}\underset{w}{\operatorname{argmin}} \quad & \operatorname{rankingSVM}(w) \\ &= \frac{1}{2}\|w\|_2^2 \\ &\quad + c\sum_{\{p,q\}\in O}\max\left(0, 1-\left(X_p - X_q\right)w\right).\end{aligned} \tag{3}$$

Set O is composed of comparison of ordered pairs $\{p, q\}$, where p has a higher rank than q and which corresponds to rows of measurement matrix X_p and X_q, respectively. More recently the approach was adopted for learning the Sepsis Disease Severity Score [5]. In it (see (4)), the constraint that scoring function should gradually evolve over the time was introduced and hence a temporal smoothness term is added. In addition, nonsmooth Hinge loss ($\max(0, 1 - Xw)$) is replaced with its smooth approximation, Huber loss (L_h), to obtain the formulation of (linear) Disease Severity Score Learning (DSSL) framework:

$$\begin{aligned}\underset{w}{\operatorname{argmin}} \quad & \operatorname{DSSL}(w) \\ &= \frac{1}{2}\|w\|_2^2 + c\sum_{\{p,q\}\in O} L_h\left(1-\left(X_p - X_q\right)w\right) \\ &\quad + b\sum_{\{i,i+1\}_s\in S}\left(\frac{\left(X_{i+1}^s - X_i^s\right)w}{\left(t_{i+1}^s - t_i^s\right)}\right)^2.\end{aligned} \tag{4}$$

Temporal smoothness term in (4) penalizes high rates of change in severity in consecutive time steps t_i and t_{i+1} of a single subject s. Set of all consecutive pairs in all subjects is denoted by S and constants c and b are hyperparameters determining the cost of respective loss terms.

DSSL framework was adopted and extended in different ways. A multitask DSSL was proposed in [11], which utilizes matrix norm regularization to couple multiple distinct tasks. Nonlinear version of DSSL framework, as well as its solution in form of gradient boosted regression trees, was also proposed in [6]. Nevertheless, mentioned DSSL approaches are dense in a sense that they operate on all variables (in case of a linear version, all coefficients are typically nonzero). The approach in [11] is based on expensive proximal gradient optimization algorithm, which makes it unsuitable for high-dimensional problems. The utility of the approaches in [6] was presented on an application with a moderately small number of different pieces of clinical information, vitals, and laboratory analysis variables and it is not clear how the approach would perform in situations with high-dimensional data common in high-throughput techniques like genetic, genomic, epigenetic, proteomic, and so on.

Yet, high-throughput data is also a very rich source of useful biomarkers that could be used for diagnostic and prognostic purposes, as well as for obtaining insight into causal relations [12]. Therefore we are proposing an approach that is able to learn a (temporally smooth) scoring function from comparison data while simultaneously performing the selection of most relevant (important) variables.

2.2. Proposed Model Formulation. In our Sparse Learning of Disease Severity Score (SLDSS) formulation, we combine attractive properties (and terms) of previously mentioned approaches, ranking SVM (see (3)) [7], temporal smoothness constraint (see (4)) [6], and L_1 norm from sparse methods (see (1) and (2)) [3, 9]:

$$\begin{aligned}\underset{w}{\min} \quad & \operatorname{SLDSS}(w) \\ &= \frac{1}{2}\|w\|_2^2 + c\sum_{\{p,q\}\in O}\max\left(0, 1-\left(X_p - X_q\right)w\right) \\ &\quad + b\sum_{\{i,i+1\}_s\in S}\left(\frac{\left(X_{i+1}^s - X_i^s\right)w}{\left(t_{i+1}^s - t_i^s\right)}\right)^2 + \lambda\|w\|_1.\end{aligned} \tag{5}$$

In fact, since the model imposes both L_1 and L_2 norms on the feature vector w, it resembles the elastic net regularization [13], which has an advantage of achieving higher stability with respect to random sampling [14].

The solution w^* of the optimization objective defined in (5) serves as a sparse linear function $f(X) = Xw^*$ that may be applied on measurements from the new patient, to obtain a scalar value of severity that might be compared to previously assessed cases and inform further actions. The sparse vector w^* may also serve as an indicator of which features are the most influential for pairwise comparison. The formulation contains two nonsmooth terms, L_1 and Hinge loss, and therefore it is not directly solvable using off-the-shelf gradient methods. In DSSL formulation, the (nondifferentiable) Hinge loss is approximated with twice differentiable Huber loss, thus making the optimization criterion solvable using the second-order gradient methods (e.g., Newton and Quasi-Newton). In order to provide an efficient solution for the proposed nonsmooth objective, we will solve the smooth dual problem instead of relying on smooth approximation or nonsmooth optimization tools.

First we rewrite (5) into a more suitable form for which we will later provide the smooth dual problem. We aggregate the differences of measurements into single data matrix $D_{k\times d}$, where k is a number of pairs in the comparison set O. Similarly, we express measurement and temporal difference ratios as matrix $R_{l\times d}$, where rows are $R_i = (X_{i+1}^s - X_i^s)/(t_{i+1}^s - t_i^s)$ and l is a number of pairs in the consecutive measurements set S. We aggregate the L_2 norm and temporal smoothness terms (they are essentially weighting the square of optimization parameters) into a single weighted quadratic term $(1/2)w^TQw$, where $Q = I + 2bR^TR$, I being d-dimensional identity matrix. The first two terms, weighted quadratic norm and Hinge loss, resemble the well-known SVM criterion function that we will rewrite in its "soft" form with additional slack variables z_i and their associated constraints. Additional set of "dummy variables" y is introduced in L_1 term, with trivial constraints $w = y$. The equation of the rewritten SLDSS now reads

$$\begin{aligned}\underset{w}{\min} \quad & \operatorname{SLDSS}(w, z, y) = \frac{1}{2}w^TQw + c\sum_{i=1}^{k} z_i + \lambda\|y\|_1 \\ \text{s.t.} \quad & D_i w \geq 1 - z_i,\end{aligned}$$

$$z_i \geq 0,$$
$$\forall i \in \{1, \ldots, k\},$$
$$w = y. \tag{6}$$

Now we turn this constrained problem with inequalities and equalities into its Lagrangian dual. Constraints are moved to the criterion function as penal terms weighted by Lagrangian multipliers α, β, and γ. The equation of the SLDSS dual problem is

$$\begin{aligned} \min_{w,y,z\geq 0} \max_{\alpha\geq 0,\beta\geq 0} \quad & \text{Dual}(w, y, z, \alpha, \beta, \gamma) \\ & = \frac{1}{2} w^T Q w + c\mathbf{1}^T z + \alpha^T (\mathbf{1} - z - Dw) \\ & \quad - \beta^T z + \lambda \|y\|_1 + \gamma^T (w - y). \end{aligned} \tag{7}$$

Given that optimization criterion is convex and feasible (Slater's condition holds [15]), strong duality allows switching the order of maximization and minimization in (7), and minimization in primal variables can be safely performed first. Now we analyze the expression according to primal variables w, y, and z and find the minimizing conditions for each of them.

The dual formulation is the quadratic function of parameters w and we can find its optimal form as a function of new free parameters introduced in dual (by equating its gradient with zero):

$$\begin{aligned} \min_{w} \quad & \text{DUAL}(w) = \min_{w} \frac{1}{2} \left(w^T Q - \alpha^T D + \gamma^T \right) w \\ & \nabla_w \text{DUAL}(w) = w^T Q - \alpha^T D + \gamma^T = \mathbf{0} \\ & \Downarrow \\ & w^* = Q^{-1} \left(\alpha^T D - \gamma^T \right). \end{aligned} \tag{8}$$

Similarly, the expression for slack variables z is a linear combination of dual variables and it is minimal when the directional gradient is equated to zero vector, giving the optimality condition in a form of an equality constraint:

$$\begin{aligned} \min_{z} \quad & \text{DUAL}(z) = \min_{z} \frac{1}{2} \left(c\mathbf{1}^T - \alpha^T - \beta^T \right) z \\ & \nabla_z \text{DUAL}(z) = c\mathbf{1}^T - \alpha^T - \beta^T = \mathbf{0} \\ & \Downarrow \\ & \beta = c\mathbf{1} - \alpha. \end{aligned} \tag{9}$$

Resulting equality constraint $\beta = c\mathbf{1} - \alpha$ in combination with inequality $\beta \geq \mathbf{0}$ can be reduced to just one constraint $\alpha \leq c\mathbf{1}$, which removes β from further consideration.

For minimization over dummy variables y, we use the convex (Fenchel) conjugate function of the expression [15] and obtain optimality condition as inequality constraint over the infinity norm of the dual variable:

$$\begin{aligned} \min_{y} \quad & \text{DUAL}(y) = \min_{y} \lambda \|y\|_1 - \gamma^T y \\ & = -\max_{y} \gamma^T y - \lambda \|y\|_1 \\ & = 0 \quad \text{if} \ \|\gamma\|_\infty \leq \lambda, \\ & \text{or} = -\infty \quad \text{otherwise} \\ & \Downarrow \\ & \|\gamma\|_\infty \leq \lambda. \end{aligned} \tag{10}$$

When optimal (minimizing) conditions (see (8), (9), and (10)) are replaced in dual formulation (7), it becomes

$$\begin{aligned} \max_{\alpha\geq 0, \alpha\leq c\mathbf{1}, \|\gamma\|_\infty \leq \lambda} \quad & \text{Dual}(\alpha, \gamma) \\ & = \frac{1}{2} \left(D^T \alpha - \gamma \right)^T Q^{-1} Q Q^{-1} \left(D^T \alpha - \gamma \right) \\ & \quad - \alpha^T D Q^{-1} \left(D^T \alpha - \gamma \right) \\ & \quad + \gamma^T Q^{-1} \left(D^T \alpha - \gamma \right) + \mathbf{1}^T \alpha. \end{aligned} \tag{11}$$

After negating (11) to turn it into minimization problem and after simplification of the expression, final problem formulation is

$$\begin{aligned} \min \quad & \frac{1}{2} \left(D^T \alpha - \gamma \right)^T Q^{-1} \left(D^T \alpha - \gamma \right) - \mathbf{1}^T \alpha \\ \text{s.t.} \quad & \mathbf{0} \leq \alpha \leq c\mathbf{1}, \\ & -\lambda\mathbf{1} \leq \gamma \leq \lambda\mathbf{1}. \end{aligned} \tag{12}$$

The original nonsmooth problem is turned into the smooth dual problem, which can be solved for its two sets of parameters α and γ. Since the strong duality holds, a solution to dual is a solution to the original problem, and optimal weight vector w^* can be retrieved after plugging the solution of dual, α^* and γ^*, into (8).

Similar dual formulation, just without the dummy variables y and associated multipliers γ, might be used for DSSL with the exact Hinge loss, instead of the originally proposed DSSL which uses Huber loss approximation [6].

2.3. Optimization Algorithm. The differentiable dual from (12) is, in fact, a quadratic optimization problem with box constraints:

$$\begin{aligned} \min_{x} \quad & \frac{1}{2} x^T H x + \mathbf{f}^T x \\ \text{s.t.} \quad & \mathbf{lb} \leq x \leq \mathbf{ub}, \end{aligned} \tag{13}$$

$$x = \begin{bmatrix} \alpha \\ \gamma \end{bmatrix},$$

$$\mathbf{f} = \begin{bmatrix} \mathbf{1}_{k\times 1} \\ \mathbf{0}_{d\times 1} \end{bmatrix},$$

$$\mathbf{lb} = \begin{bmatrix} \mathbf{0}_{k\times 1} \\ -\lambda \mathbf{1}_{d\times 1} \end{bmatrix}, \tag{14}$$

$$\mathbf{ub} = \begin{bmatrix} c\mathbf{1}_{k\times 1} \\ \lambda \mathbf{1}_{d\times 1} \end{bmatrix},$$

$$H = \begin{bmatrix} D & \mathbf{0}_{k\times d} \\ \mathbf{0}_{d\times d} & -I \end{bmatrix} \begin{bmatrix} Q^{-1} & Q^{-1} \\ Q^{-1} & Q^{-1} \end{bmatrix} \begin{bmatrix} D^T & \mathbf{0}_{d\times d} \\ \mathbf{0}_{d\times k} & -I \end{bmatrix}.$$

There are ready-to-use tools for solving the problem in (13), and we utilized the built-in Matlab "quadprog" solver, which is implemented as a projection method with the active set.

3. Results

3.1. Severity Score Characterization on Synthetic Data. For the initial assessment of the proposed framework, we have generated a synthetic example with properties that motivated the approach. If a large number of variables are measured, many are expected to be irrelevant for the assessment of severity.

We defined the severity score as a linear combination of intensities of the first 10 features after initiating a set of 100. In addition, we set the coefficients to have different magnitudes, as it is expected that contribution of different variables is of various levels (Figure 1(a)). The remaining ninety features do not affect severity score at all; they are irrelevant and only introduce uncertainty into the problem. For training purposes, values of all features are randomly sampled from a uniform distribution for 10 fictitious subjects with 10 different measurements each. Severity scores are associated based on a linear function with weights depicted in Figure 1. Comparison labels (pairs) were generated as all possible pairs in which the first element (sample) has substantially higher severity score as compared to the second element. This requirement of substantial gap in severity between pairs serves to mimic the case where a doctor could claim, with high confidence, that one patient is in more severe condition than another. Such generated training data was utilized to fit Sparse LDSS, (dense) DSSL, and DSSL model trained on the exact 10 features that are relevant, which we named Ideal DSSL in Table 1.

All models were tested on comparison pairs from an additional 50 test subjects with 10 measurements each. Testing data was generated by the same protocol as explained for training, except the threshold for the required difference of scores was set several times lower, in order to see how learned

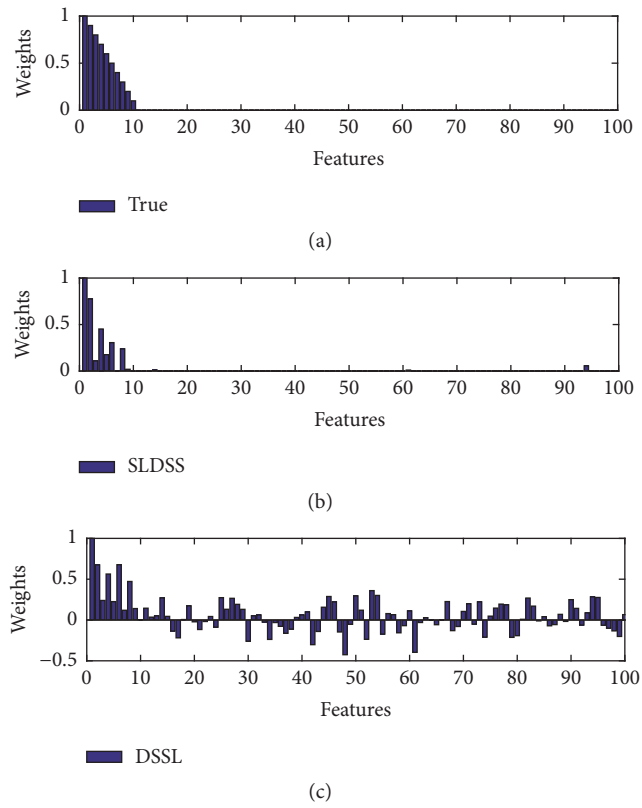

Figure 1: Synthetic example. Comparison of learned weight vectors (normalized) of sparse SLDSS method and dense DSSL method with the ground truth.

Table 1: Performance on synthetic data as measured by correctly ordered pairs, accuracy, and by aggregated error (magnitude of difference in wrongly ordered pairs), Hinge loss.

Approach	SLDSS	DSSL	Ideal DSSL
Accuracy	0.9397	0.8373	0.9558
Hinge loss	176.06	3110.20	180.65

functions generalize to more subtle differences between the cases.

$$\begin{aligned} \text{Accuracy} &= \frac{\#\ \text{Correctly Ranked}}{\#\ \text{Total Examples}} \\ &= 1 - \frac{\#\ \text{Incorrectly Ranked}}{\#\ \text{Total Examples}}. \end{aligned} \tag{15}$$

The predictive performance was measured as "Accuracy" (see (15)), that is, the fraction of the total examples that are correctly ordered, meaning that a linear function assigned a higher score to the first component of a pair. The results presented in Table 1 show that learning a dense weight vector impairs the predictive accuracy of the model, while learning a sparse vector, using the SLDSS, approaches the accuracy of the Ideal model, obtained by learning a disease severity score from relevant features known in advance. Figure 1 shows the

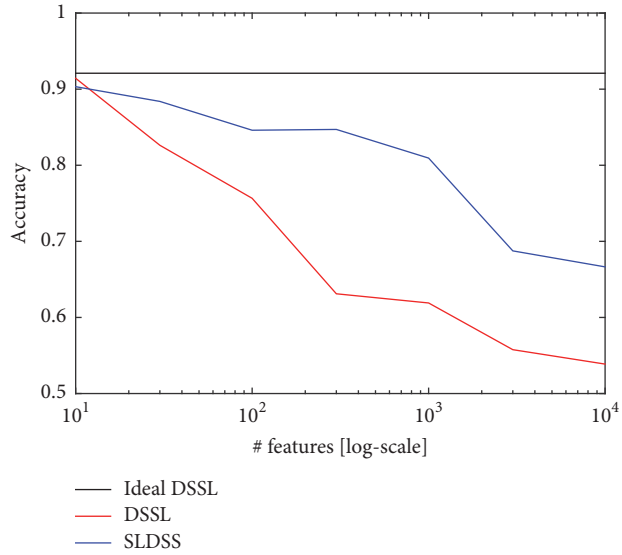

Figure 2: Synthetic experiment. Influence of the problem dimensionality (number of features) on the accuracy of ranking methods.

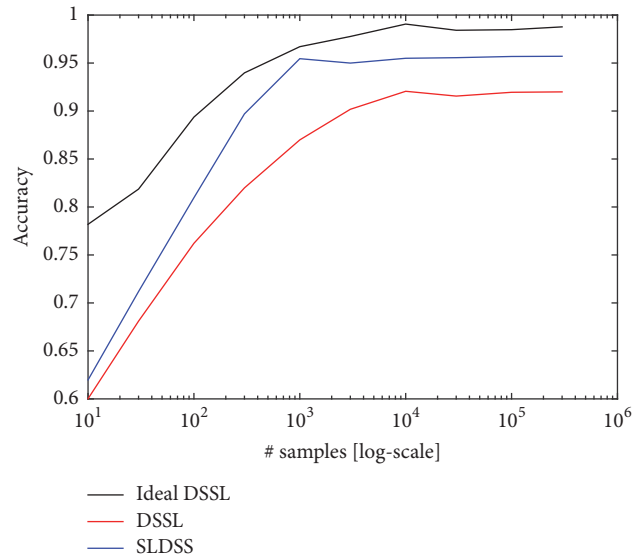

Figure 3: Synthetic experiment. Influence of the sample size (number of sample pairs) on the accuracy of ranking methods.

weights of learned severity functions, and it might be seen that reason for the reduced testing accuracy of the dense DSSL method (Figure 1(c)) is because it assigned nonzero weights to (by design) completely irrelevant features.

3.2. Feature Size Analysis. We have explored how the number of irrelevant features affects the model performance. This time we sampled 100 subjects (with 10 time-step samples each), with 10,000 features, where only the first 10 contribute to the true score. We varied the number of features from 10 (all features informative) up to 10,000 in exponentially progressive increments [10; 30; 100; 300; 1,000; 3,000; 10,000]. Results presented in Figure 2 show that when all features are informative (10 out of 10) DSSL is slightly better than SLDSS. However, as soon as irrelevant features are added, the SLDSS approach becomes more accurate than DSSL. As more irrelevant dimensions are added, both approaches' performance decreases, however SLDSS at a slower pace.

3.3. Sample Size Analysis. We also investigated how the number of training samples affects the predictive performance of the ranking approaches. We generated another synthetic set of 100 subjects (10 samples each). All samples had 100 features, where the first 10 were relevant for the ground truth score. From such generated examples, we constructed 357,355 comparison pairs for training. We varied the number of sample pairs, by randomly sampling from 10 up to 300,000 in exponentially progressive increments [10; 30; 100; 300; 1,000; 3,000; 10,000; 30,000; 100,000; 300,000]. From the results on holdout testing set, presented in Figure 3, it can be seen that accuracy increases with the number of training pairs and that SLDSS is always more accurate than DSSL. The Ideal DSSL, which is always trained only on the 10 relevant features, is consistently the most accurate.

3.4. Severity Score for Influenza A Virus. To further assess the proposed approach, we applied it to learning the severity of H3N2 influenza symptoms. The utilized dataset (http://people.ee.duke.edu/~lcarin/reproduce.html) contains temporally collected gene expression measurements of human subjects infected with H3N2 virus [16]. The samples were collected on multiple occasions (approximately every eight hours) during the period of one week after the virus was inoculated in subjects. Concurrently, the severity of their symptoms was tracked (approximately twice a day) and clinically assessed using the modified Jackson score [17]. When measurement time points were not perfectly aligned with severity score estimates, the temporally nearest estimate was associated with the gene expression vector. Having high dimensionality of the measurements (12,032 genes), temporally collected samples, and associated severity score estimates, this dataset was suited for testing the proposed severity score learning framework. In addition to direct assessments of severity scores, which could be used for regression, the data samples are also accompanied with class labels "symptomatic" and "asymptomatic" [18], based on the values of modified Jackson scores. Our comparison pairs generation process follows the guidelines proposed in [6]. Ideally, an expert would be presented with example pairs and would assess which one appears more intense (with respect to a property of interest), based on visual inspection, clinical report, or arbitrary convenient source. The alternative is to use an existing scoring system to generate comparison pairs, and for this application we utilized the Jackson score. We generated a third label type by extracting all possible pairs of samples where the first component is associated with a score that is substantially larger than the second. In our experiments, the "substantial" is defined by setting a threshold to 5 for training and 1 for testing.

Table 2: Performance on H3N2 influenza gene expression dataset as measured by the fraction of correctly ordered pairs (accuracy).

Approach	SLDSS	DSSL	LASSO	L_1 Logistic Regression
Accuracy	0.8097	0.7689	0.9490	0.7815

On the described dataset containing 267 samples (17 subjects with about 16 temporal samples each), we have compared the predictive performances of 4 methods:

(1) Sparse Learning of Disease Severity Score (SLDSS) from comparison pairs

(2) "Dense" Disease Severity Score Learning (DSSL) from comparison pairs

(3) LASSO regression on direct values of severity scores

(4) L_1-regularized Logistic Regression fitted on binary classification labels of symptom severity.

All enumerated methods result in a vector of feature weights that can be used as a scoring function. Except for the DSSL which results in a dense vector of weights, all other approaches typically only have a small number of nonzero weights, while all others are exactly equal to zero.

We compared the mentioned methods in a 10-fold cross-validation procedure (where all samples belonging to one subject are either all in training or all in testing folds) and the results are shown in Table 2.

In conducted experiments, the nonsparse method (DSSL) has the lowest accuracy, which provides evidence that sparse approaches were beneficial. LASSO was the most accurate, due to its direct access to the ground truth values (of the underlying scores), while other methods only had access to partial information. The Logistic Regression only had information if the score was larger than a certain threshold, while the DSSL and SLDSS only knew, for a list of pairs, which element in a given pair had a higher score. This, on the other hand, limits the application of LASSO to cases where scoring function already exists, thus reducing the necessity for learning it from the data. Among the approaches which learn from indirect information about underlying values of scores (comparison pairs and severity classes), our SLDSS is the most accurate.

3.5. Robustness of Selected Features. We were also interested in using SLDSS for feature selection to discover the most relevant variables for the condition. Therefore, we have performed additional analysis regarding the robustness (stability) of the selected features. Robustness of selected features is a very important aspect of the feature selection algorithms that was relatively neglected up until recently [19]. Various fields aim at finding the right subset of variables that would allow reliable prediction, and the more there are candidates to search from, the harder it is to find the right subset. Feature selection methods play a crucial role there, but when the dimensionality of data is much higher than the number of samples, the expectation of consistently finding high-quality solution decreases [20]. On the other side, L_1 regularized models have far fewer requirements for sample size as compared to rotation invariant models (L_2 regularized models, Support Vector Machines, Artificial Neural Networks, and DSSL, whose sample complexity grows at least linearly in the number of irrelevant features), as their sample size requirement grows logarithmically in the dimension of (irrelevant) features [21], so they are an attractive tool for such tasks.

Robustness is a metric that quantifies how different training sets affect the affinity of the algorithm towards the particular features and there are different measures proposed [22]. Here we used the common three:

(1) Pearson coefficient (see (16)), which measures the correlation between the weight vectors w and w' learned on different data (sub)sets and tells magnitude stability of the weights. In the case when the weight vector is used as a linear function, it also tells how stable the learned function is.

$$C_P\left(w, w'\right) = \frac{\sum_i \left(w_i - \mu_w\right)\left(w_i' - \mu_{w'}\right)}{\sqrt{\sum_i \left(w_i - \mu_w\right)^2 \sum_i \left(w_i' - \mu_{w'}\right)^2}}. \quad (16)$$

(2) Spearman rho metric (see (17)), which measures how well the orders (ranks) r and r' of weights' w and w' magnitudes are preserved between different training sets. It is important, for example, in the dense methods where features are selected as some top number of features according to the magnitude of weights.

$$C_S\left(r, r'\right) = \frac{\sum_i \left(r_i - \mu_r\right)\left(r_i' - \mu_{r'}\right)}{\sqrt{\sum_i \left(r_i - \mu_r\right)^2 \sum_i \left(r_i' - \mu_{r'}\right)^2}}. \quad (17)$$

(3) Jaccard index (see (18)), which measures the overlap between two discrete sets s and s' of nonzero features in w and w', normalized with their union ($|\cdot|$ is cardinality operator). Jaccard index is the most relevant measure (out of the three mentioned) regarding the stability of selected features, as studied frameworks select features in the form of a discrete set of nonzero features.

$$C_J\left(s, s'\right) = \frac{\left|s \cap s'\right|}{\left|s \cup s'\right|} = \frac{\left|s \cap s'\right|}{|s| + \left|s'\right| - \left|s \cap s'\right|}. \quad (18)$$

All four severity score learning methods are assessed for consistency/robustness based on each of the three stability measures (see (16)–(18)), through a 10-fold cross-validation procedure on H3N2 data. The sparsity level was tuned with free parameters (for sparse methods) so as to produce the average number (over tenfold) of nonzero features of about 100 out of 12,032 possible (SLDSS 97.1±16.7; LASSO 99.9±8.8; L_1LogReg 101.7 ± 22.7), with results presented in Figure 4 and summarized in Table 3. The dense method, DSSL, was compared to others, according to Jaccard index, by taking only the top 100 features according to the largest magnitudes

Table 3: Stability of selected feature subsets summarized as an average pairwise similarity over ten training folds.

Measure	SLDSS	DSSL	LASSO	L_1 Logistic Regression
Pearson coefficient	**0.8656**	0.7402	0.7362	0.5562
Spearman rank	**0.8163**	0.7204	0.5162	0.3988
Jaccard index	**0.6916**	0.2946	0.3595	0.2474

in each of the folds separately. The results show that here proposed SLDSS method is the most stable one according to each of the three measures. This means that it learns the most stable severity score function (according to Pearson correlation), as well as the most stable set of nonzero features (according to Jaccard index). This evidence is suggesting that SLDSS is finding the most reliable signal in the data, out of all the tested approaches. Nevertheless, there are no guarantees that the selected set of features is free of false positives, as previously it was theoretically concluded that LASSO-like approaches select a superset of the true features [23].

3.6. Gene Ontology Overrepresentation Analysis. To further check the appropriateness of SLDSS method as a biomarker discovery tool, we performed gene ontology overrepresentation analysis to assess the relevance of a set of features extracted from the influenza dataset. In the robustness analysis section, we found that more than two-thirds (0.6916) of the nonzero features are, on average, shared between the different folds of data. In fact, 50 genes were nonzero in all of the folds, so we took that set of genes and submitted it for overrepresentation analysis in the PANTHER [24] online tool.

We analyzed the list of 50 selected genes given in Table 4, against all the 12,032 genes in the dataset. Some of the 12,032 genes were duplicates, and some symbols were not recognized by the database (annotation version and release date: GO Ontology database, released 2016-03-25) resulting in the comparison of the 50 selected genes against the reference list of 10,792 genes using the PANTHER Overrepresentation Test (released 2016-03-21) with Bonferroni correction. Bonferroni correction [25] is a simple and common method for multiple testing correction of significance value indicators. It is well acknowledged that it might be substantially conservative, especially when multiple tests are not independent. In multiple gene ontology process testing, it might be extremely conservative because descendants of a process are completely dependent on their parents. Nevertheless, even after overly conservative adjustments, a number of processes are found statistically significantly overrepresented with the cutoff value of 0.05 for P value. Significantly overrepresented GO biological processes (listed in Table 5) are related almost exclusively to immune response and a reaction of the host body to the virus. This is consistent with the fact that the dataset is about the response to viral infection, suggesting that the discovered set of features is indeed relevant for the studied process.

Table 4: Genes selected by the Sparse Disease Severity Score Learning method, listed in alphabetical order.

Gene symbols
AIM2
ALDH1A1
ATF3
BLVRA
C3AR1
CASP5
CASP7
CCL2
CCL8
CDKN1C
CXCL10
EIF2AK2
EPB41L3
ETV7
GBP1
HERC5
IFI35
IFI44
IFI44L
IFI6
IFIH1
IFIT1
IFIT2
IFIT3
IL18RAP
ISG15
LAMP3
LAP3
LILRA5
MAFB
MS4A4A
MX1
MYOF
OAS1
OAS2
OAS3
OASL
RIN2
RSAD2
RTP4
S100A12
SERPING1
SIGLEC1
STAT1
TFEC
TLR7
TNFSF10
TYMP
XAF1
ZBP1

4. Conclusion

We assessed multiple approaches to learning the severity scores in high-dimensional applications. Our results point

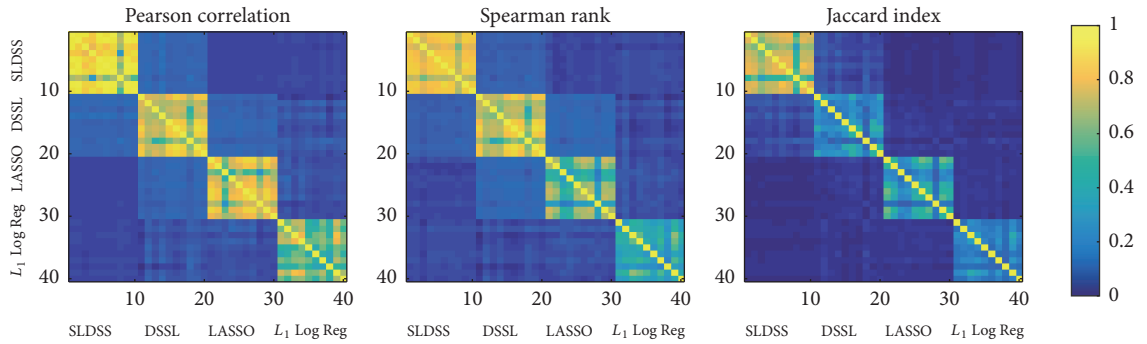

Figure 4: Similarity matrices. Similarity matrices between weight vectors learned over all 10 folds of data and all four methods. Warmer colors correspond to higher similarity (stability) and cooler tones to lower similarity. SLDSS (upper left squares) has the highest similarities among all methods.

Table 5: PANTHER overrepresentation analysis results. No.: number of associated genes; Exp.: expected number of genes by chance; Fold: number of times enriched.

GO biological process complete	GOID	No.	Exp.	Fold	P value
Defense response to virus	(GO:0051607)	18	.62	29.21	$4.00E-18$
Response to virus	(GO:0009615)	20	.96	20.75	$1.01E-17$
Type I interferon signaling pathway	(GO:0060337)	14	.28	49.54	$1.97E-16$
Cellular response to type I interferon	(GO:0071357)	14	.28	49.54	$1.97E-16$
Response to type I interferon	(GO:0034340)	14	.29	47.96	$3.08E-16$
Immune response	(GO:0006955)	32	5.42	5.91	$2.37E-15$
Immune system process	(GO:0002376)	35	8.20	4.27	$4.07E-13$
Innate immune response	(GO:0045087)	26	3.79	6.87	$1.07E-12$
Defense response	(GO:0006952)	31	6.12	5.07	$1.07E-12$
Defense response to other organisms	(GO:0098542)	19	1.73	10.97	$1.46E-11$
Immune effector process	(GO:0002252)	19	1.75	10.85	$1.76E-11$
Cytokine-mediated signaling pathway	(GO:0019221)	20	2.13	9.40	$3.84E-11$
Cellular response to cytokine stimulus	(GO:0071345)	21	2.72	7.72	$3.01E-10$
Response to cytokine	(GO:0034097)	22	3.16	6.96	$4.80E-10$
Response to other organisms	(GO:0051707)	22	3.23	6.81	$7.44E-10$
Response to external biotic stimulus	(GO:0043207)	22	3.23	6.81	$7.44E-10$
Response to biotic stimulus	(GO:0009607)	22	3.31	6.65	$1.21E-09$
Negative regulation of viral genome replication	(GO:0045071)	8	.19	41.11	$1.83E-07$
Negative regulation of viral process	(GO:0048525)	9	.36	24.90	$7.74E-07$
Regulation of viral genome replication	(GO:0045069)	8	.30	26.56	$5.56E-06$
Negative regulation of viral life cycle	(GO:1903901)	8	.35	23.02	$1.69E-05$
Response to stress	(GO:0006950)	34	14.20	2.40	$5.49E-05$
Negative regulation of multiorganism process	(GO:0043901)	9	.60	15.06	$6.01E-05$
Response to external stimulus	(GO:0009605)	26	8.48	3.06	$1.19E-04$
Cellular response to interferon-gamma	(GO:0071346)	8	.50	16.14	$2.59E-04$
Regulation of viral process	(GO:0050792)	9	.79	11.43	$6.26E-04$
Response to interferon-gamma	(GO:0034341)	8	.57	13.93	$7.95E-04$
Regulation of symbiosis	(GO:0043903)	9	.88	10.17	$1.66E-03$
Regulation of viral life cycle	(GO:1903900)	8	.74	10.86	$5.14E-03$
Interferon-gamma-mediated signaling pathway	(GO:0060333)	6	.31	19.33	$5.39E-03$
Response to stimulus	(GO:0050896)	43	26.53	1.62	$6.68E-03$
Regulation of defense response	(GO:0031347)	14	3.03	4.61	$8.01E-03$
Regulation of cytokine production	(GO:0001817)	12	2.19	5.48	$9.59E-03$
Cellular response to organic substance	(GO:0071310)	23	8.36	2.75	$1.01E-02$
Regulation of multiorganism process	(GO:0043900)	11	1.81	6.07	$1.07E-02$
Response to interferon-alpha	(GO:0035455)	4	.09	45.44	$1.55E-02$
Cellular response to chemical stimulus	(GO:0070887)	25	10.06	2.49	$1.75E-02$
Cell surface receptor signaling pathway	(GO:0007166)	23	9.04	2.54	$4.07E-02$
Multiorganism process	(GO:0051704)	22	8.40	2.62	$4.59E-02$

to the utility and maybe even necessity of reducing the dimensionality of the problem through sparse learning techniques. Combination of the advantages of existing solutions turned out to be beneficial for the performance of the formulation proposed in this study. The robustness of the learned disease severity score function, as well as features selected by our approach, compares very favorably to the alternatives. Conducted gene ontology overrepresentation analysis supports the relevance of the genes identified by the SLDSS approach. Additional studies are possible to further characterize selected genes and the processes they are involved in, in order to provide further insight into causal relations underlining the influenza infection. These are all mounting evidence that our approach could be used as a discovery tool for both disease severity scores and related informative variables, which could further motivate novel hypotheses. The method we proposed in this article is appropriate for learning severity score from a relatively small number of high-dimensional cases. More efficient optimization tools would be needed for applications where the number of cases is also large since in such applications a quadratic number of comparisons in the number of samples can be a challenge.

Abbreviations

SOFA:	Sequential Organ Failure Assessment
ICU:	Intensive Care Unit
APACHE:	Acute Physiology and Chronic Health Evaluation
SVM:	Support Vector Machine
LASSO:	Least Absolute Shrinkage and Selection Operator
SLDSS:	Sparse Linear Disease Severity Score
DSSL:	Disease Severity Score Learning.

Disclosure

The funding bodies had no role in the design, collection, analysis, or interpretation of this study, and any opinions, findings, conclusion, or recommendations expressed in this material are those of the authors and do not necessarily reflect the view of the DARPA, ARO, or the US Government.

Conflicts of Interest

The authors declare that there are no conflicts of interest regarding the publication of this article.

Authors' Contributions

Ivan Stojkovic developed and implemented the computational methods and conducted the experiments, supervised by Zoran Obradovic. Ivan Stojkovic and Zoran Obradovic discussed and analyzed the results and wrote the manuscript. All authors read and approved the final manuscript.

Acknowledgments

The authors wish to thank Aleksandar Obradovic for proofreading and editing the language of the manuscript. This material is based upon work partially supported by the Defense Advanced Research Projects Agency (DARPA) and the Army Research Office (ARO) under Contract no. W911NF-16-C-0050 and partially supported by DARPA Grant no. 66001-11-1-4183 negotiated by SSC Pacific grant.

References

[1] J.-L. Vincent, R. Moreno, J. Takala et al., "The SOFA (Sepsis-related Organ Failure Assessment) score to describe organ dysfunction/failure," *Intensive Care Medicine*, vol. 22, no. 7, pp. 707–710, 1996.

[2] W. A. Knaus, E. A. Draper, D. P. Wagner, and J. E. Zimmerman, "APACHE II: a severity of disease classification system," *Critical Care Medicine*, vol. 13, no. 10, pp. 818–829, 1985.

[3] S. Yang, L. Shapiro, M. Cunningham et al., "Skull retrieval for craniosynostosis using sparse logistic regression models," in *Medical Content-Based Retrieval for Clinical Decision Support*, pp. 33–44, Springer, 2012.

[4] J. Zhou, J. Liu, V. A. Narayan, and J. Ye, "Modeling disease progression via fused sparse group lasso," in *Proceedings of the 18th ACM SIGKDD International Conference on Knowledge Discovery and Data Mining (KDD '12)*, pp. 1095–1103, August 2012.

[5] K. Dyagilev and S. Saria, "Learning severity score for sepsis: a novel approach based on clinical comparisons," in *Proceedings of the in. AMIA Annual Symposium Proceedings*, pp. 1890–1898, 2015.

[6] K. Dyagilev and S. Saria, "Learning (predictive) risk scores in the presence of censoring due to interventions," *Machine Learning*, vol. 102, no. 3, pp. 323–348, 2016.

[7] T. Joachims, "Optimizing search engines using clickthrough data," in *Proceedings of the Eighth ACM SIGKDD International Conference on Knowledge Discovery and Data Mining*, pp. 133–142, July 2002.

[8] I. M. Johnstone and D. M. Titterington, "Statistical challenges of high-dimensional data," *Philosophical Transactions of the Royal Society A: Mathematical, Physical & Engineering Sciences*, vol. 367, no. 1906, pp. 4237–4253, 2009.

[9] R. Tibshirani, "Regression shrinkage and selection via the lasso: a retrospective," *Journal of the Royal Statistical Society: Series B (Statistical Methodology)*, vol. 73, no. 3, pp. 273–282, 2011.

[10] D. Ghosh and A. M. Chinnaiyan, "Classification and selection of biomarkers in genomic data using LASSO," *Journal of Biomedicine and Biotechnology*, vol. 2005, no. 2, pp. 147–154, 2005.

[11] I. Stojkovic, M. F. Ghalwash, and Z. Obradovic, "Ranking based multitask learning of scoring functions," in *Proceedings of the European Conference on Machine Learning and Principles and Practice of Knowledge Discovery in Databases*, 2017.

[12] A. J. Atkinson Jr., W. A. Colburn, V. G. DeGruttola et al., "Biomarkers and surrogate endpoints: preferred definitions and conceptual framework," *Clinical Pharmacology & Therapeutics*, vol. 69, no. 3, pp. 89–95, 2001.

[13] H. Zou and T. Hastie, "Regularization and variable selection via the elastic net," *Journal of the Royal Statistical Society: Series B (Statistical Methodology)*, vol. 67, no. 2, pp. 301–320, 2005.

[14] C. De Mol, E. De Vito, and L. Rosasco, "Elastic-net regularization in learning theory," *Journal of Complexity*, vol. 25, no. 2, pp. 201–230, 2009.

[15] S. Boyd and L. Vandenberghe, *Convex Optimization*, Cambridge University Press, Cambridge, UK, 2004.

[16] A. K. Zaas, M. Chen, J. Varkey et al., "Gene expression signatures diagnose influenza and other symptomatic respiratory viral infections in humans," *Cell Host & Microbe*, vol. 6, no. 3, pp. 207–217, 2009.

[17] G. G. Jackson, H. F. Dowling, I. G. Spiesman, and A. V. Boand, "Transmission of the common cold to volunteers under controlled conditions: I. The common cold as a clinical entity," *A.M.A Archives of Internal Medicine*, vol. 101, no. 2, pp. 267–278, 1958.

[18] C. W. Woods, M. T. McClain, and M. Chen, "A host transcriptional signature for presymptomatic detection of infection in humans exposed to influenza H1N1 or H3N2," *PLoS ONE*, vol. 8, no. 1, Article ID e52198, 2013.

[19] Y. Saeys, I. Inza, and P. Larrañaga, "A review of feature selection techniques in bioinformatics," *Bioinformatics*, vol. 23, no. 19, pp. 2507–2517, 2007.

[20] C. Sima and E. R. Dougherty, "What should be expected from feature selection in small-sample settings," *Bioinformatics*, vol. 22, no. 19, pp. 2430–2436, 2006.

[21] A. Y. Ng, "Feature selection, L 1 vs. L 2 regularization, and rotational invariance," in *Proceedings of The Twenty-First International Conference on Machine Learning*, Banff, Alberta, Canada, July 2004.

[22] A. Kalousis, J. Prados, and M. Hilario, "Stability of feature selection algorithms: a study on high-dimensional spaces," *Knowledge and Information Systems*, vol. 12, no. 1, pp. 95–116, 2007.

[23] P. Bühlmann and S. van de Geer, *Statistics for High-dimensional Data: Methods, Theory and Applications*, Springer Series in Statistics, Springer, New York, NY, USA, 2011.

[24] H. Mi, S. Poudel, A. Muruganujan, J. T. Casagrande, and P. D. Thomas, "PANTHER version 10: expanded protein families and functions, and analysis tools," *Nucleic Acids Research*, vol. 44, no. D1, pp. D336–D342, 2016.

[25] W. Haynes, "Bonferroni Correction," in *Encyclopedia of Systems Biology*, W. Dubitzky, O. Wolkenhauer, K.-H. Cho, and H. Yokota, Eds., pp. 154-154, Springer, New York, NY, USA, 2013.

Hindawi
Complexity
Volume 2017, Article ID 1232868, 12 pages
https://doi.org/10.1155/2017/1232868

Research Article

HSimulator: Hybrid Stochastic/Deterministic Simulation of Biochemical Reaction Networks

Luca Marchetti,[1] Rosario Lombardo,[1] and Corrado Priami[1,2]

[1]*The Microsoft Research–University of Trento Centre for Computational and Systems Biology (COSBI), Piazza Manifattura, No. 1, 38068 Rovereto, Italy*
[2]*Department of Computer Science, University of Pisa, Pisa, Italy*

Correspondence should be addressed to Luca Marchetti; marchetti@cosbi.eu

Received 12 May 2017; Revised 18 August 2017; Accepted 19 November 2017; Published 13 December 2017

Academic Editor: Valeri Mladenov

Copyright © 2017 Luca Marchetti et al. This is an open access article distributed under the Creative Commons Attribution License, which permits unrestricted use, distribution, and reproduction in any medium, provided the original work is properly cited.

HSimulator is a multithread simulator for mass-action biochemical reaction systems placed in a well-mixed environment. HSimulator provides optimized implementation of a set of widespread state-of-the-art stochastic, deterministic, and hybrid simulation strategies including the first publicly available implementation of the Hybrid Rejection-based Stochastic Simulation Algorithm (HRSSA). HRSSA, the fastest hybrid algorithm to date, allows for an efficient simulation of the models while ensuring the exact simulation of a subset of the reaction network modeling slow reactions. Benchmarks show that HSimulator is often considerably faster than the other considered simulators. The software, running on Java v6.0 or higher, offers a simulation GUI for modeling and visually exploring biological processes and a Javadoc-documented Java library to support the development of custom applications. HSimulator is released under the COSBI Shared Source license agreement (COSBI-SSLA).

1. Introduction

Computational systems biology is becoming a fundamental tool of life-science research, which aims at developing *models* representing biological phenomena and reliable *computational techniques* for their simulation [1–7].

We introduce *HSimulator*, a Java hybrid stochastic/deterministic simulator for mass-action biochemical reaction systems placed in a well-mixed environment, where position and speed of molecular species are randomized and therefore they do not affect reaction executions. Species $S_1, \ldots, S_n$ are represented in terms of *abundances* (number of molecules) and reactions $R_1, \ldots, R_m$ are defined as

$$R_j : \nu_{1j} S_1 + \cdots + \nu_{nj} S_n \longrightarrow \nu'_{1j} S_1 + \cdots + \nu'_{nj} S_n, \; c_j, \qquad (1)$$

where the species on the left of the arrow are *reactants* and the ones on the right are *products*. The stoichiometric coefficients ν_{ij} and ν'_{ij} indicate how many molecules of reactant are consumed and how many molecules of product are produced, respectively. The constant c_j at the end of the reaction is the *stochastic reaction constant* introduced by Gillespie [8] for computing reaction firing according to the definition of *mass-action propensities*.

From the milestone work of Gillespie [8], where the *Direct Method* (DM) has been defined, *exact stochastic simulation* is the most accurate simulation approach. Its drawback is the high computational complexity arising from the need of separately simulating each reaction firing. Several algorithms have been introduced to decrease simulation runtime, such as the *Next Reaction Method* (NRM, [9]) and later the *Rejection-based Stochastic Simulation Algorithm* (RSSA, [10]). The latter is tailored for complex biochemical reactions with time-consuming propensity functions and it constitutes the state of the art of exact stochastic simulation.

Despite the improvements, the problem of simulation complexity remains. In fact, the investigation of complex diseases or disorders is often concerned with extended biomolecular networks involving genes, proteins, metabolites, and signal transduction cascades. This justifies the introduction of *approximate* simulation strategies, which sacrifice accuracy to decrease runtime. Such strategies progressively reduce the stochasticity of the dynamics [11, 12] until reaching a *deterministic* simulation, where the model is translated to a

system of *ordinary differential equations* (ODEs, [7, 13]) and the dynamics provides an averaged behavior.

A drawback of an approximate simulation is that *all* reactions in the model are simulated according to the same approximate strategy. This is an issue when exact simulation is required at least for a small part of the reaction network, for example, when slow reactions are considered to model rare stochastic events. In such a case, a *hybrid* simulation strategy is able to partition reactions into subsets that are simulated by different algorithms [7, 14, 15]. Hybrid simulation therefore needs to *synchronize* the progress of different simulation strategies in order to guarantee the exactness of the simulation of slow reactions. This requires considering *time-varying transition propensities*, which in turn require the computation of integrals to calculate the exact firing time of slow reactions [7, 14, 16–20] (see also Section 2.5 and (19)). This step is computationally demanding and practical implementation necessarily approximates the integral computation by a numerical method that affects the accuracy of the simulation of slow reactions.

The *Hybrid Rejection-based Stochastic Simulation Algorithm* (HRSSA) has been recently introduced in [21] to avoid approximations in simulating slow reactions. HRSSA exploits some computational advantages introduced in RSSA to exactly simulate slow reactions and to apply an efficient and accurate dynamic partitioning of reactions, which constitute the two most significant bottlenecks of hybrid simulation.

HSimulator herein presented fills a gap in the current literature of stochastic and hybrid simulation by providing a suite of published state-of-the-art simulation algorithms including, in the same package, the exact algorithm RSSA and the first publicly available implementation of its hybrid version HRSSA. The benchmarks in the paper show that the HSimulator implementation is often faster than the state-of-the-art simulator COPASI [22]. HSimulator is released under the COSBI Shared Source license agreement (COSBI-SSLA) and it is available for download at the COSBI website at http://www.cosbi.eu/research/prototypes/hsimulator.

2. Materials and Methods

HSimulator provides an implementation of five state-of-the-art simulation strategies covering exact stochastic simulation (DM and RSSA), deterministic simulation (Forward Euler and the Runge-Kutta-Fehlberg RK45 adaptive algorithm), and hybrid simulation (HRSSA). For deterministic and hybrid simulations, the simulator automatically translates the mass-action reaction network into a set of ordinary differential equations (ODEs, see Section 2.3). In the following some insights about the implemented simulation algorithms are provided as well as their pseudocodes, which can be used as a reference to better understand the functionalities implemented in the simulator (for additional details, the reader is invited to refer to the user guide of HSimulator available at http://www.cosbi.eu/research/prototypes/hsimulator). Readers already familiar with the topic can skip this section and going directly to Section 3.

2.1. Direct Method (DM). The Direct Method constitutes the first practical implementation of an exact stochastic simulator [8]. The simulation of an exact algorithm is based on the concept of *reaction probability density function* (pdf):

$$P\left(\tau, j \mid \mathbf{x}, t\right) = a_j\left(\mathbf{x}\right) e^{-a_0(\mathbf{x})\tau}, \tag{2}$$

which provides the probability $P(\tau, j \mid \mathbf{x}, t)d\tau$ that the next reaction to apply will be R_j in the infinitesimal time interval $[t + \tau; t + \tau + d\tau]$, given the system state $\mathbf{x}$ at time t.

The *state of the system* at time t is represented by the column vector

$$\mathbf{X}\left(t\right) = \left(X_1\left(t\right), \ldots, X_n\left(t\right)\right)^T, \tag{3}$$

where $X_i(t)$ is the number of molecules of species S_i in the system at time t. In the following we will often write $\mathbf{x}$ for $\mathbf{X}(t)$ and x_i for $X_i(t)$ to improve the readability of formulas.

The term $a_j(\mathbf{x})$ in (2) is the *propensity* of R_j in the state $\mathbf{x}$, while the *total propensity* $a_0(\mathbf{x})$ is the sum of the propensities of all reactions:

$$a_0\left(\mathbf{x}\right) = \sum_{j=1}^{m} a_j\left(\mathbf{x}\right). \tag{4}$$

The reaction propensities $a_j(\mathbf{x})$ are computed from the stochastic reaction rate c_j:

$$a_j\left(\mathbf{x}\right) = \begin{cases} c_j, & \text{if } h_j\left(\mathbf{x}\right) = 0 \\ h_j\left(\mathbf{x}\right) c_j, & \text{otherwise,} \end{cases} \tag{5}$$

where $h_j(\mathbf{x})$ is the number of distinct reactant combinations for R_j in the state $\mathbf{x}$ [8]. For standard mass-action kinetics, as considered here, it is

$$h_j\left(\mathbf{x}\right) = \prod_i \binom{x_i}{\nu_{ij}} = \prod_i \frac{x_i!}{\nu_{ij}!\left(x_i - \nu_{ij}\right)!}, \tag{6}$$

where ν_{ij} are the stoichiometric coefficients of R_j according to (1).

Equation (2) shows that the next reaction R_j fires with a discrete probability $a_j(\mathbf{x})/a_0(\mathbf{x})$ and its firing time τ has an exponential distribution with rate $a_0(\mathbf{x})$. Gillespie introduced the *Direct Method* (DM) for exactly sampling the pdf $P(\tau, j \mid \mathbf{x}, t)$ by applying the inverse transformation:

$$\begin{aligned} \tau &= -\frac{\ln\left(r_1\right)}{a_0\left(\mathbf{x}\right)}, \\ j &= \text{the smallest index s.t. } \sum_{i=1}^{j} \frac{a_i\left(\mathbf{x}\right)}{a_0\left(\mathbf{x}\right)} \geq r_2, \end{aligned} \tag{7}$$

where r_1 and r_2 are random numbers drawn from a uniform distribution $U(0, 1)$. The pseudocode of the DM algorithm is in Algorithm 1.

Input: a reaction system with n species and m reactions as the one in (1), with a stochastic reaction constant c_j associated with each reaction R_j; an initial state $\mathbf{X}(t_0)$ defining molecule abundances at time t_0; the last time instant t_{end} to be simulated.
Output: a time series of states $\mathbf{X}(t)$, $t \in [t_0; t_{\text{end}}]$, providing the dynamics of the system.
Pseudocode:

(0) $t \coloneqq t_0$;
(1) `while` $t < t_{\text{end}}$ `do`
  (2) For each reaction R_i, $i = 1, \ldots, m$, compute reaction propensities $a_i(\mathbf{x})$ according to (5);
  (3) Compute $a_0(\mathbf{x})$ according to (4);
  (4) Generate two random numbers r_1, r_2 in $U(0, 1)$;
  (5) $\tau \coloneqq -\ln(r_1)/a_0(\mathbf{x})$;
  (6) Select R_j such that j satisfies
$$\sum_{i=1}^{j-1} \frac{a_i(\mathbf{x})}{a_0(\mathbf{x})} < r_2 \leq \sum_{i=1}^{j} \frac{a_i(\mathbf{x})}{a_0(\mathbf{x})};$$
  (7) Compute $\mathbf{X}(t + \tau)$ by applying R_j to $\mathbf{x}$;
  (8) $t \coloneqq t + \tau$;
(9) `end while`

Algorithm 1: Gillespie's Direct Method (DM).

Input: The same as DM (Algorithm 1) together with a simulation parameter $0 < \delta < 1$ for calculating the fluctuation interval of the system state.
Output: a time series of states $\mathbf{X}(t)$, $t \in [t_0; t_{\text{end}}]$, providing the dynamics of the system.
Pseudocode:

(0) $t \coloneqq t_0$;
(1) `while` $t < t_{\text{end}}$ `do`
  (2) Define the fluctuation interval $\mathbb{X} = [\underline{\mathbf{x}}; \overline{\mathbf{x}}]$ according to (8);
  (3) For each reaction R_i, $i = 1, \ldots, m$, compute propensity bounds $a_i(\underline{\mathbf{x}})$, $a_i(\overline{\mathbf{x}})$ and the total propensity $a_0(\overline{\mathbf{x}})$;
  (4) `while` $(t < t_{\text{end}} \wedge \mathbf{x} \in \mathbb{X})$ `do`
    (5) Generate three random numbers r_1, r_2, r_3 in $U(0, 1)$;
    (6) $\tau \coloneqq -\ln(r_1)/a_0(\overline{\mathbf{x}})$;
    (7) Select R_j such that j satisfies
$$\sum_{i=1}^{j-1} \frac{a_i(\overline{\mathbf{x}})}{a_0(\overline{\mathbf{x}})} < r_2 \leq \sum_{i=1}^{j} \frac{a_i(\overline{\mathbf{x}})}{a_0(\overline{\mathbf{x}})};$$
    (8) accepted $\coloneqq$ false;
    (9) `if` $(r_3 \leq a_j(\underline{\mathbf{x}})/a_j(\overline{\mathbf{x}}))$ `then`
      (10) accepted $\coloneqq$ true;
    (11) `else`
      (12) Compute $a_j(\mathbf{x})$ according to (5);
      (13) `if` $r_3 \leq a_j(\mathbf{x})/a_j(\overline{\mathbf{x}})$ `then` accepted $\coloneqq$ true;
    (14) `end if`
    (15) `if` (accepted) `then`
      (16) Compute $\mathbf{X}(t + \tau)$ by applying R_j to $\mathbf{x}$;
    (17) `end if`
    (18) $t \coloneqq t + \tau$;
  (19) `end while`
(20) `end while`

Algorithm 2: Rejection-based Stochastic Simulation Algorithm (RSSA).

2.2. The Rejection-Based Stochastic Simulation Algorithm (RSSA). The Rejection-based Stochastic Simulation Algorithm (RSSA) is a novel exact stochastic simulation algorithm introduced in [10] and further improved in [7, 24–26]. RSSA constitutes the state of the art of exact stochastic simulation tailored for complex biochemical reactions with time-consuming propensity functions. The pseudocode of RSSA is provided in Algorithm 2.

RSSA computes for each reaction a lower bound and an upper bound of the propensity, which encompass all possible

values of reaction propensities over the fluctuation interval. Such bounds are derived by defining a *fluctuation interval* $\mathbb{X} = [\underline{\mathbf{x}}; \overline{\mathbf{x}}]$ for the system state $\mathbf{x}$ (step (2)), where

$$\begin{aligned} \underline{\mathbf{x}} &= \lfloor \mathbf{x} - \delta \mathbf{x} \rfloor, \\ \overline{\mathbf{x}} &= \lceil \mathbf{x} + \delta \mathbf{x} \rceil \end{aligned} \tag{8}$$

and $0 < \delta < 1$ is a simulation parameter whose value is usually between 0.1 and 0.2 (10–20% of the system state). Because reaction propensities with mass-action kinetics are monotonic functions, the propensity bounds of reaction R_i, for $i = 1, \ldots, m$, correspond to the interval $[a_i(\underline{\mathbf{x}}), a_i(\overline{\mathbf{x}})]$ (step (3)). These propensity bounds are recomputed only when the current system state is not anymore inside its fluctuation interval ($\mathbf{x} \notin \mathbb{X}$).

The selection of reaction firing in RSSA is composed of two steps. First, it selects a candidate reaction R_j with probability $a_j(\overline{\mathbf{x}})/a_0(\overline{\mathbf{x}})$ (step (7)), where $a_0(\overline{\mathbf{x}}) = \sum_{j=1}^{m} a_j(\overline{\mathbf{x}})$. The candidate reaction is then validated according to a rejection-based procedure that implements the toss of a biased coin with success probability $a_j(\mathbf{x})/a_j(\overline{\mathbf{x}})$ (steps (8)–(14)). To do this, the algorithm generates a random number r in $U(0, 1)$ and moves in one of the following three cases:

(1) If $r \leq a_j(\underline{\mathbf{x}})/a_j(\overline{\mathbf{x}})$, then R_j is accepted without computing its propensity $a_j(\mathbf{x})$ because $a_j(\underline{\mathbf{x}})/a_j(\overline{\mathbf{x}}) \leq a_j(\mathbf{x})/a_j(\overline{\mathbf{x}})$ (*quick accept*);

(2) If $r > a_j(\underline{\mathbf{x}})/a_j(\overline{\mathbf{x}})$, then reaction propensity $a_j(\mathbf{x})$ is computed and R_j is accepted if $r \leq a_j(\mathbf{x})/a_j(\overline{\mathbf{x}})$ (*slow accept*);

(3) If $r > a_j(\mathbf{x})/a_j(\overline{\mathbf{x}})$, then R_j is rejected (rejection).

After a reaction is accepted to fire, the state is updated and the algorithm moves to the next simulation iteration without updating the propensity bounds. Only for uncommon cases when state $\mathbf{x}$ moves out of its fluctuation interval does RSSA have to define a new fluctuation interval and update the propensity bounds. Numerical experiments show that propensity updates in RSSA are infrequent; hence their impact is very low during the computation [10]. This advantage is mitigated by the penalty paid to prepare a potential advancement of the system for a candidate reaction that is finally rejected to fire, but the overall performance is still considerably better than DM and other stochastic simulation algorithms.

2.3. The Forward Euler Algorithm. The forward Euler algorithm is the simplest example of *deterministic* simulation algorithm. Here the mass-action model is translated to a system of *ordinary differential equations* (ODEs, [7, 13]) and the dynamics provides an averaged behavior of the system.

Consider a biochemical reaction system with $S_1, \ldots, S_N$ species, $R_1, \ldots, R_M$ reactions defined according to (1). The mass-action deterministic rate constant k_j of R_j can be obtained from the stochastic one c_j as

$$k_j = \frac{c_j \left(N_A V\right)^{\text{Order}_j - 1}}{\prod_{i=1}^{N} \nu_{ij}!}, \tag{9}$$

where N_A indicates Avogadro's number, V is the volume where the reaction is taking place, and Order_j is the overall order of reaction R_j, which in mass-action is defined as the sum of the stoichiometric coefficients of reaction reactants. Finally, the ODE describing the evolution in terms of molar concentrations of species S_i, $i = 1, \ldots, N$, is

$$\frac{d\left[S_i\right]}{dt} = \sum_{j=1}^{M} \left(k_j \left(\nu'_{ij} - \nu_{ij} \right) \prod_{l=1}^{N} \left[S_l\right]^{\nu_{lj}} \right), \quad i = 1, \ldots, N, \tag{10}$$

where squared brackets are used to indicate molar concentration of species ($[S_i] = S_i/(N_A V)$, $i = 1, \ldots, N$). Once the model has been translated to a system of ODEs

$$\frac{d\left[\mathbf{X}\right]}{dt} = \mathbf{F}\left(t, \left[\mathbf{X}\right]\right), \tag{11}$$

a first-order approximation of the next system state can be computed by

$$\left[\mathbf{X}_{n+1}\right] = \left[\mathbf{X}_n\right] + h \cdot \mathbf{F}\left(t_n, \left[\mathbf{X}_n\right]\right), \tag{12}$$

where h is a user-defined discretization stepsize. The pseudocode of the Forward Euler algorithm is provided in Algorithm 3.

2.4. Runge-Kutta-Fehlberg Algorithm (RK45). The forward Euler algorithm introduced in the previous section is a first-order numerical method provided for didactic purposes. Several numerical methods have been introduced to increase the accuracy of deterministic simulations and to decrease simulation runtime. A popular algorithm is the *Runge-Kutta-Fehlberg algorithm (RK45)*. This algorithm represents the standard choice of several numerical integrators when the model does not exhibit stiffness. It is also often used in hybrid simulation strategies for the simulation of the fast part of the network. The reader can find a comprehensive guide to numerical methods of ODEs in [7, 13].

The Runge-Kutta Fehlberg method of fourth-order, also known as the RK45 method, updates the system state by

$$\left[\mathbf{X}_{n+1}\right] = \left[\mathbf{X}_n\right] + \frac{25}{216}K_1 + \frac{1408}{2565}K_3 + \frac{2197}{4104}K_4 - \frac{1}{5}K_5 \tag{13}$$

coupled with a fifth-order RK method

$$\left[\widetilde{\mathbf{X}}_{n+1}\right] = \left[\mathbf{X}_n\right] + \frac{16}{135}K_1 + \frac{6656}{12825}K_3 + \frac{28561}{56430}K_4 - \frac{9}{50}K_5 + \frac{2}{55}K_6. \tag{14}$$

Input: a system of ODEs $d[\mathbf{X}]/dt = \mathbf{F}(t, [\mathbf{X}])$ corresponding to a biochemical reaction system, the initial state $[\mathbf{X}(t_0)]$ of the system with species concentrations at time 0, the last time instant t_{end} to be simulated and the discretization stepsize h.
Output: a time series of states $[\mathbf{X}(t)]$, $t \in [t_0; t_{\text{end}}]$, providing the dynamics of the system in terms of molar concentrations with discretization stepsize h.
Pseudocode:
(0) initialize time $t = 0$ and state $[\mathbf{X}] = [\mathbf{X}(t_0)]$;
(1) `while` $t < t_{\text{end}}$ `do`
  (2) update $[\mathbf{X}] = [\mathbf{X}] + h \cdot \mathbf{F}(t, [\mathbf{X}])$;
  (3) update $t = t + h$;
(4) `end while`

Algorithm 3: Forward Euler method.

Given a system of ODEs as in (11) and a discretization stepsize h, the values of $K_1, \ldots, K_6$ are shared between (13) and (14) and they can be computed as

$$
\begin{aligned}
K_1 &= h \cdot \mathbf{F}\left(t_n, [\mathbf{X}_n]\right) \\
K_2 &= h \cdot \mathbf{F}\left(t_n + \frac{h}{4}, [\mathbf{X}_n] + \frac{1}{4}K_1\right) \\
K_3 &= h \cdot \mathbf{F}\left(t_n + \frac{3h}{8}, [\mathbf{X}_n] + \frac{3}{32}K_1 + \frac{9}{32}K_2\right) \\
K_4 &= h \cdot \mathbf{F}\left(t_n + \frac{12h}{13}, [\mathbf{X}_n] + \frac{1932}{2197}K_1 - \frac{7200}{2197}K_2 \right. \\
&\quad \left. + \frac{7296}{2197}K_3\right) \\
K_5 &= h \cdot \mathbf{F}\left(t_n + h, [\mathbf{X}_n] + \frac{439}{216}K_1 - 8K_2 + \frac{3680}{513}K_3 \right. \\
&\quad \left. - \frac{845}{4104}K_4\right) \\
K_6 &= h \cdot \mathbf{F}\left(t_n + \frac{h}{2}, [\mathbf{X}_n] - \frac{8}{27}K_1 + 2K_2 - \frac{3544}{2565}K_3 \right. \\
&\quad \left. + \frac{1859}{4104}K_4 - \frac{11}{40}K_5\right).
\end{aligned}
\tag{15}
$$

The fourth-order version of the algorithm provided in (13) is used to compute the dynamics of the system. The fifth-order scheme of (14), instead, is used to estimate the maximum local truncation error introduced in the simulated step:

$$
\Delta_{n+1} = \max\left(\frac{\left|\left[\widetilde{\mathbf{X}}_{n+1}\right] - \left[\mathbf{X}_{n+1}\right]\right|}{h}\right), \tag{16}
$$

where max provides the maximum value along the vector of truncation errors. The error estimate Δ_{n+1} is then compared to the error threshold ϵ_t specified by the user. When $\Delta_{n+1} \leq \epsilon_t$, the local truncation error is assumed to be smaller than the threshold, the state $[\mathbf{X}_{n+1}]$ is accepted, and the algorithm moves one step forward. Otherwise, the new state is not accepted and the next state is evaluated again using a different (smaller) value of h. In both cases, the value of h is updated as

$$
h_{n+1} = h_n \sigma \tag{17}
$$

$$
\sigma = \left(\frac{\epsilon_t}{2\Delta_{n+1}}\right)^{1/4} \approx 0.84\left(\frac{\epsilon_t}{\Delta_{n+1}}\right)^{1/4}. \tag{18}
$$

When the estimations $[\mathbf{X}_{n+1}]$ and $[\widetilde{\mathbf{X}}_{n+1}]$ agree to more significant digits than required, then σ becomes greater than 1 and h is increased. Equation (18) is derived from the general formula $\sigma = (\epsilon_t/\Delta_{n+1})^{1/p}$, which defines how to update the value of h of an adaptive one-step numerical method of order p, by considering the error estimate Δ_{n+1} and the user-defined threshold ϵ_t. The additional multiplicative factor of 0.84 is an empirical number commonly added in RK45 implementation to reduce the variability of h, because very high values of the stepsize increase the probability of repeating the next computed step.

The implementation of the algorithm is in Algorithm 4. The value of h is updated at each step starting from an user-provided initial value h_0. The next computed state of the system is accepted only when the estimate of the local truncation error Δ remains below the user-provided threshold ϵ_t. Steps (16)–(21) are additional steps added to the implementation in order to avoid very large modifications of h in a single step.

Even if the computation of a simulation iteration of the RK45 algorithm is more computational demanding than other nonadaptive Runge-Kutta implementation, the possibility of changing the value of h often dramatically decreases the simulation runtime.

2.5. Hybrid Rejection-Based Stochastic Simulation Algorithm (HRSSA). A drawback of approximate simulation is that *all* the model reactions are simulated according to the same approximate strategy. This is an issue when exact simulation is required at least for a small part of the reaction network, for example, when slow reactions are considered to model rare stochastic events. In such a case, a *hybrid* simulation strategy can be applied, which divides reactions into subsets that are simulated by different strategies at the same time [7, 14, 15].

An issue of this approach is the *synchronization* between the employed simulation strategies in order to guarantee the

Input: a system of ODEs $d[\mathbf{X}]/dt = \mathbf{F}(t, [\mathbf{X}])$ corresponding to a biochemical reaction system, the initial state $[\mathbf{X}(t_0)]$ of the system with species concentrations at time 0, the last time instant t_{end} to be simulated, an initial value for the discretization stepsize h_0 and a threshold for the maximum local truncation error ϵ_t.
Output: a time series of states $[\mathbf{X}(t)]$, $t \in [t_0; t_{\text{end}}]$, providing the dynamics of the system in terms of molar concentrations.
Pseudocode:

(0) initialize time $t = 0$, state $[\mathbf{X}] = [\mathbf{X}(t_0)]$ and discretization stepsize $h = h_0$;
(1) `while` $t < t_{\text{end}}$ `do`
  (2) compute $K_1 = h \cdot \mathbf{F}(t, [\mathbf{X}])$;
  (3) compute $K_2 = h \cdot \mathbf{F}(t + h/4, [\mathbf{X}] + (1/4)K_1)$;
  (4) compute $K_3 = h \cdot \mathbf{F}(t + 3h/8, [\mathbf{X}] + (3/32)K_1 + (9/32)K_2)$;
  (5) compute $K_4 = h \cdot \mathbf{F}(t + 12h/13, [\mathbf{X}] + (1932/2197)K_1 - (7200/2197)K_2 + (7296/2197)K_3)$;
  (6) compute $K_5 = h \cdot \mathbf{F}(t + h, [\mathbf{X}] + (439/216)K_1 - 8K_2 + (3680/513)K_3 - (845/4104)K_4)$;
  (7) compute $K_6 = h \cdot \mathbf{F}(t + h/2, [\mathbf{X}] - (8/27)\mathrm{K}_1 + 2K_2 - (3544/2565)K_3 + (1859/4104)K_4 - (11/40)K_5)$;
  (8) compute $[\mathbf{X}_{\text{new}}] = [\mathbf{X}] + (25/216)K_1 + (1408/2565)K_3 + (2197/4104)K_4 - (1/5)K_5$;
  (9) compute $[\widetilde{\mathbf{X}}_{\text{new}}] = [\mathbf{X}] + (16/135)K_1 + (6656/12825)K_3 + (28561/56430)K_4 - (9/50)K_5 + (2/55)K_6$;
  (10) compute $\Delta = \max(|[\widetilde{\mathbf{X}}_{\text{new}}] - [\mathbf{X}_{\text{new}}]|/h)$ according to (16);
  (11) `if` $(\Delta \leq \epsilon_t)$ `then`
    (12) update $[\mathbf{X}] = [\mathbf{X}_{\text{new}}]$;
    (13) update $t = t + h$;
  (14) `end if`
  (15) compute $\sigma = 0.84(\epsilon_t/\Delta)^{1/4}$;
  (16) `if` $(\sigma < 0.1)$ `then`
    (17) update $\sigma = 0.1$;
  (18) `end if`
  (19) `if` $(\sigma > 4)$ `then`
    (20) update $\sigma = 4$;
  (21) `end if`
  (22) update $h = h \cdot \sigma$;
(23) `end while`

Algorithm 4: The Runge-Kutta Fehlberg (RK45) algorithm.

exactness of the simulation of slow reactions. This is a fundamental aspect of hybrid simulation relying on the definition of the probability density function (pdf) of slow reactions. In fact, even though fast reactions can be safely simulated across slow reaction events, it is not always the case that slow reactions can be simulated regardless of what fast reactions are changing in the system. Actually the reaction propensity a_j of a slow reaction $R_j \in \mathscr{R}^{\text{slow}}$ may depend on species whose quantities are changed by fast reactions. For this reason, the reaction probability density function of (2) is not suitable to simulate the reaction subnetwork made of only the slow reactions of the system and it has to be extended to consider *time-varying transition propensities* [7, 14], which account for the fact that reaction propensities of slow reactions may change over time by the simulation of fast reactions.

According to [7, 14, 16–20], the pdf of the next firing of a slow reaction $R_j \in \mathscr{R}^{\text{slow}}$ finally becomes

$$P^{\text{slow}}(\tau, j \mid \mathbf{x}, t) = a_j(\mathbf{X}(t+\tau))\, e^{-\int_t^{t+\tau} a_0^{\text{slow}}(\mathbf{X}(t'))dt'}, \quad (19)$$

where

$$a_0^{\text{slow}}(\mathbf{x}) = \sum_{R_j \in \mathscr{R}^{\text{slow}}} a_j(\mathbf{x}). \quad (20)$$

The firing time τ of the next slow reaction R_j is thus obtained by solving the equation

$$\int_t^{t+\tau} a_0^{\text{slow}}\left(\mathbf{X}\left(t'\right)\right) dt' = -\ln(r), \quad (21)$$

where r is a random number from $U(0, 1)$. Solving (21) is computationally challenging because the state $X(t)$ is changed by fast reactions during time interval $[t, t + \tau]$. Therefore, the hybrid simulation has to evaluate the integral simultaneously with the simulation of fast reactions in order to correctly generate the next slow reaction event. Moreover, in practical implementation this step has to be necessarily approximated by a numerical method relying on an error threshold that introduces an additional approximation in the simulation of slow reactions. This step is so critical that the standard choice of several implementation available in literature, such as the hybrid algorithms implemented in COPASI [22], intentionally avoids the computation of the integral during the simulation by accepting some approximation also in the simulation of slow reactions.

The hybrid algorithm HRSSA is a novel hybrid simulation algorithm introduced in [21] to solve this problem. HRSSA is built on top of RSSA introduced in Section 2.2. In particular, the RSSA concept of fluctuation interval of the system

Input: The same as RSSA (Algorithm 2) together with the time granularity τ_{fast} used for the (approximate) simulation of fast reactions; the minimum amount $\gamma \in \mathbb{N}$ of molecules that has to be available for fast reactions; the minimum number of times $\theta \in \mathbb{N}$ that a fast reaction has to be applied, in average, within the time range of size τ_{fast}.
Output: the sets $\mathscr{R}^{\text{slow}}$ and $\mathscr{R}^{\text{fast}}$ of slow and fast reactions, respectively.
Pseudocode:

(0) $\mathscr{R}^{\text{slow}} := \emptyset$; $\mathscr{R}^{\text{fast}} := \emptyset$;
(1) `for each` reaction R_j
  (2) `if` $(a_j(\underline{\mathbf{x}})\tau_{\text{fast}} < \theta)$ `then`
    (3) Put reaction R_j in the set $\mathscr{R}^{\text{slow}}$;
  (4) `else if` ($\exists S_i$, modified by R_j with stoichiometric coefficient ν_{ij}, such that $\underline{x}_i < \gamma \cdot \nu_{ij}$) `then`
    (5) Put reaction R_j in the set $\mathscr{R}^{\text{slow}}$;
  (6) `else`
    (7) Put reaction R_j in the set $\mathscr{R}^{\text{fast}}$;
  (8) `end if`
(9) `end for`

Algorithm 5: The dynamic reaction partitioning of HRSSA (please refer to [21] for details).

state is widely used to provide an important computational advantage. HRSSA synchronizes the simulation of slow and fast reactions by avoiding the computation of the integral of (21) and applies an accurate dynamic partitioning of reactions without updating reaction classification at each simulation step.

HRSSA updates reaction partitioning only when the current system state does not fit anymore in its fluctuation interval (see (8)). This permits reducing the computational overhead without losing the accuracy of the classification. HRSSA considers both reaction propensities and the number of transformed molecules for reaction partitioning, by replacing real propensities with their lower bounds. The adoption of bounds instead of real propensities does not affect the accuracy of the classification. Conversely, the usage of lower bounds imposes more stringent constraints that tend to increase the number of reactions that are classified as slow (and therefore simulated without approximations). The pseudocode of the dynamic reaction partitioning of HRSSA is in Algorithm 5. The if clauses of steps (2) and (4) implement the two conditions on reaction propensities and number of transformed molecules, respectively.

After reaction partitioning in the two sets of slow and fast reactions, HRSSA computes the sum of upper propensity bounds $a_0^{\text{slow}}(\overline{\mathbf{x}})$ of slow reactions as defined in (20). The firing time of a candidate slow reaction is then computed as

$$\tau = -\frac{\ln(r)}{a_0^{\text{slow}}(\overline{\mathbf{x}})}, \tag{22}$$

where r is a random number in $U(0,1)$.

Under the hypothesis that the system state will remain inside its fluctuation interval in $[t, t+\tau]$, we can consider $a_0^{\text{slow}}(\overline{\mathbf{x}})$ not dependent on time over $[t, t+\tau]$ and this allows us to simulate fast reactions over this interval without taking any side effect on the application of slow reactions into account. This is because (22) remains valid, regardless of the action of fast reactions, as long as the current system state respects its bounds.

After the simulation of fast reactions for the time interval $[t, t+\tau]$, a slow reaction is chosen and validated to fire by a rejection test, according to the RSSA simulation strategy. To guarantee the exact simulation of slow reactions (the proof is in [21]), the simulation of fast reactions is required to happen in a feasible system state. Therefore, every time the system state exits from its bounds the simulation is stopped and the fluctuation interval is updated. The pseudocode of HRSSA is provided in Algorithm 6.

3. Results and Discussion

HSimulator is a cross-platform simulation software written in Java, offering a suite of state-of-the-art stochastic, deterministic, and hybrid simulation strategies for mass-action well-stirred biochemical reaction systems. Multi-compartmental modeling is natively supported allowing the definition of nested reaction volumes via a customary text-based representation of reactions and compartments. The multithreading implementation allows scaling very well when computing averaged model dynamics obtained by running multiple stochastic simulations in parallel. The software has been designed to run in three user-scenarios: (i) via command-line, for example, as batch jobs or as part of wider modeling terminal scripts; (ii) programmatically embedded via its API in custom applications [27] or within MATLAB/Octave/R/Mathematica projects; (iii) as a self-standing simulation environment with a graphical user interface (GUI) for biomedical system modeling. For the three usage scenarios extensive documentation is available at the software web page (http://www.cosbi.eu/research/prototypes/hsimulator.). The GUI assists the modeler while defining the reactions with syntax highlighting of the typed entities and quick graphical access to simulation parameters. The simulation environment

Input: The same as RSSA (Algorithm 2) together with the time granularity τ_{fast} used for the (approximate) simulation of fast reactions; the minimum amount $\gamma \in \mathbb{N}$ of molecules that has to be available for fast reactions; the minimum number of times $\theta \in \mathbb{N}$ that a fast reaction has to be applied, in average, within the time range of size τ_{fast}.
Output: a time series of states $\mathbf{X}(t)$, $t \in [t_0; t_{\text{end}}]$, providing the dynamics of the system.
Pseudocode:

(0) $t \coloneqq t_0$;
(1) `while` $t < t_{\text{end}}$ `do`
  (2) Define the fluctuation interval $\mathbb{X} = [\underline{\mathbf{x}}; \overline{\mathbf{x}}]$ according to (8);
  (3) For each reaction R_i, $i = 1, \ldots, m$, compute propensity bounds $a_i(\underline{\mathbf{x}})$ and $a_i(\overline{\mathbf{x}})$;
  (4) Update reaction partitioning (sets $\mathscr{R}^{\text{slow}}$ and $\mathscr{R}^{\text{fast}}$) by applying the algorithm in Algorithm 5 according to input parameters γ, θ and τ_{fast};
  (5) Compute $a_0^{\text{slow}}(\overline{\mathbf{x}})$ according to (20);
  (6) updateNeeded $\coloneqq$ false;
  (7) `while` $(t < t_{\text{end}} \wedge \neg$updateNeeded$)$ `do`
    (8) $\tau \coloneqq -\ln(r)/a_0^{\text{slow}}(\overline{\mathbf{x}})$, where r is a random number in $U(0, 1)$;
    (9) Compute $\mathbf{X}(t + \tau')$ by simulating fast reactions ($\mathscr{R}^{\text{fast}}$), at time steps of maximum length τ_{fast}, according to an approximate algorithm (either stochastic or deterministic), where τ' is a value $\tau' \leq \tau$ such that $\mathbf{X}(t + \tau') \in \mathbb{X}$;
    (10) `if` $(\tau' = \tau)$ `then`
      (11) Select a candidate slow reaction $R_j \in \mathscr{R}^{\text{slow}}$ by applying RSSA steps (7)–(14) in Algorithm 2;
      (12) `if` R_j is accepted by RSSA `then` update $\mathbf{X}(t + \tau')$ computed at step (9) by applying R_j;
      (13) `if` $(\mathbf{X}(t + \tau') \notin \mathbb{X})$ `then` updateNeeded $\coloneqq$ true;
    (14) `else`
      (15) updateNeeded $\coloneqq$ true;
    (16) `end if`
    (17) $t \coloneqq t + \tau'$;
  (18) `end while`
(19) `end while`

Algorithm 6: The hybrid rejection-based stochastic simulation algorithm (HRSSA, please refer to [21] for details). In HSimulator, step (9) is implemented by a deterministic Runge-Kutta numerical method.

is completed by an interactive viewport to explore and understand the modeled system dynamics (see Figure 1) which can be then exported as Excel spreadsheets.

To evaluate the performance of the HSimulator implementation, a set of benchmarks have been carried out considering the state-of-the-art simulator COPASI [22], version 4.19 (build 140). All the simulations have been run in the same conditions on a 64 bit macOS Sierra MacBook Pro, with 16 GB of RAM. Six models have been simulated according to 6 different algorithms covering all the simulation strategies (stochastic, deterministic, and hybrid). Namely, we considered the Direct Method (implemented in both COPASI and HSimulator) and RSSA (only implemented in HSimulator) for exact stochastic simulation, LSODA (implemented in COPASI) and RK45 (implemented in HSimulator) for deterministic simulation, and Hybrid Runge-Kutta (implemented in COPASI) and HRSSA (implemented in HSimulator) for hybrid simulation. Benchmarks have been computed by averaging the runtime of 20 simulations. The simulation parameters for each algorithm are in Table 1 and they have been chosen to preserve as much as possible the reliability of comparisons.

The Hybrid Runge-Kutta algorithm provided by COPASI combines two fast simulation strategies available in literature to simulate slow and fast reactions (NRM combined with the 4th order Runge-Kutta method [7, 13]). Reaction partitioning is computed dynamically during the simulation according to a threshold which provides the maximum number of reactant molecules of a slow reaction. Moreover, the simulation of slow and fast reactions is synchronized without computing the integral of (21) by approximating reaction probabilities of slow reactions as constant during one stochastic step. This solution introduces an error in the simulation of slow reactions, but makes the computation faster. HRSSA resulted to be faster than this algorithm in all the simulation cases we considered, even if HRSSA does not apply such approximation in simulating slow reactions.

We note that the latest version of COPASI (version 4.19 build 140) considered in our benchmarks provides other two implementation cases of hybrid simulation algorithms (Hybrid LSODA and Hybrid RK45). Here we considered Hybrid Runge-Kutta because its implementation is closer to the one of HRSSA. However, we obtained very similar simulation runtimes also by running our benchmarks with

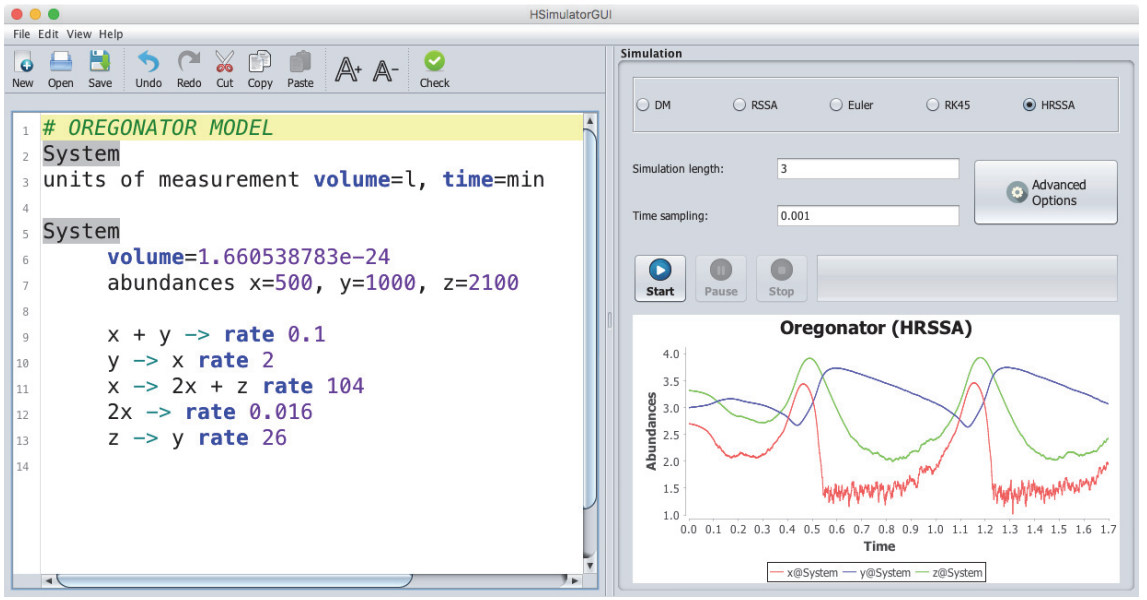

Figure 1: The HSimulator graphical user interface allows easily defining, even complex, biological models in terms of customary text-based reactions. The appropriate simulation strategy can be selected and parameterised as well according to the model, although the HRSSA method offers the best hybrid simulator. The figure shows the Oregonator model [8] simulated by the HRSSA algorithm [21]. The plot shows variable abundances in logarithmic scale to illustrate the switch between the deterministic simulation of fast reactions (high abundances) and the exact stochastic simulation of slow reactions (low abundances).

Table 1: Simulation parameters used for the benchmarks of the compared tools.

Algorithm	Software	Parameters
DM	HSimulator	No parameters needed
DM	COPASI	No parameters needed
RSSA	HSimulator	$\delta = 0.1$
LSODA	COPASI	Relative and absolute thresholds: 10^{-3}
RK45	HSimulator	Initial stepsize: 10^{-2} Error threshold: 10^{-3}
Hybrid Runge-Kutta	COPASI	Maximum number of reactant molecules for slow reactions: 100 RK4 stepsize: 10^{-2}
HRSSA	HSimulator	$\delta = 0.1$; $\tau_{\text{fast}} = 10^{-2}$; $\gamma = 100$; $\theta = 10$

Hybrid LSODA (data not shown). Hybrid RK45 has been not considered here, because this simulation strategy uses a static reaction partitioning whereas HSimulator and the compared methods use a dynamical approach allowing for a fair benchmark between strategies. We also have to acknowledge that COPASI is not the only simulation software available in the literature. In the present work we considered COPASI due to its high popularity and to allow, as much as possible, a fair comparison with HSimulator. In fact, COPASI provides a way of specifying the biochemical system that is very close to the one of HSimulator. Snoopy [28] is another promising simulation software that provides different simulation strategies for hybrid models, including a reinterpretation of HRSSA.

Simulation benchmarks are provided in Table 2. To allow the reproducibility of the presented results, all the considered models are provided with HSimulator both implemented for HSimulator and for COPASI. Simulation benchmarks comprehend two biological models (the MAPK cascade and the Gemcitabine mechanism of action) to test simulation strategies in real modeling applications plus two theoretical models (the fully connected model and the multiscale model) considered with two different parameterisations each, to evaluate the performance of simulation algorithms under specific conditions. The fully connected model has been considered to evaluate the performance of simulation algorithms when a mass-action biochemical reaction network of reactions that are all slow (MCM $i = 20$) or fast (MCM $i = 2000$) is simulated. Conversely, the multiscale model allowed testing the intermediate condition, where the biochemical network can be divided into two subnetworks working at different time scales. This scenario has been specifically considered to test hybrid simulation strategies. The biochemical network of the multiscale model has been generated two times to test the scalability of simulation algorithms (MSM $(10, 50)$, network of 60 species and 140 reactions; MSM $(20, 100)$, network of 120 species and 480 reactions, see Section 3.4

Table 2: Simulation running times of HSimulator and of the state-of-the-art simulator COPASI. Except for the deterministic simulation, HSimulator is demonstrated to be faster in all the considered scenarios (FCM indicates the fully connected model; MSM indicates the multiscaled model). The considered models were simulated for 150 time units (MAPK and fully connected model), 12 time units (Gemcitabine), and 10 time units (multiscaled model).

Algorithm	MAPK	Gemcitabine	FCM $i = 20$	FCM $i = 2000$	MSM (10, 50)	MSM (20, 100)
COPASI - DM	2.39 sec.	0.88 sec.	5.09 sec.	415.04 sec.	28.87 sec.	262.1 sec.
HSimulator - DM	2.23 sec. (−6%)	0.7 sec. (−12%)	1.61 sec. (−68%)	168.75 sec. (−59%)	11.0 sec. (−62%)	120.84 sec. (−54%)
HSimulator - RSSA	2.03 sec. (−15%)	0.66 sec. (−25%)	1.10 sec. (−78%)	77.46 sec. (−81%)	4.25 sec. (−85%)	37.23 sec. (−86%)
COPASI - LSODA	0.06 sec.	0.02 sec.	0.56 sec.	0.08 sec.	0.08 sec.	0.21 sec.
HSimulator - RK45	0.06 sec. (+0%)	0.04 sec. (+100%)	0.001 sec. (−99%)	0.001 sec. (−99%)	0.13 sec. (+63%)	0.52 sec. (+148%)
COPASI - Hyb. RK	0.21 sec	0.54 sec.	26.74 sec.	14.67 sec.	1.93 sec.	35.49 sec.
HSimulator - HRSSA	0.1 sec. (−52%)	0.38 sec. (−30%)	1.10 sec. (−96%)	0.8 sec. (−95%)	2.53 sec. (−31%)	5.89 sec. (−83%)

for details). The provided benchmarks seem to indicate that HSimulator is more scalable than COPASI with respect to the growing complexity of the model. This result is interesting, especially from an implementer's point of view, showing how a recent Java-based implementation (HSimulator), in the given conditions, may compare favourably with respect to C++ (COPASI).

3.1. The MAPK Cascade. The *Mitogen-Activated Protein Kinase cascade (MAPK cascade)* is one of the most important and intensively studied signaling pathways [29]. The MAPK cascade is at the heart of a molecular-signaling network that governs the growth, proliferation, differentiation, and survival of many cell types. Moreover, the MAPK pathway is deregulated in various diseases, ranging from cancer to immunological, inflammatory, and degenerative syndromes, and thus represents also an important drug target [30].

The MAPK cascade is a series of three protein kinases that are responsible for cell response to growth factors. The signal $E1$ activates MAPKKK by phosphorylation, which in turn activates MAPKK. Once activated, MAPKK activates MAPK. When $E1$ is added to the system, the output of activated MAPK increases rapidly. By removing the signal $E1$, the output level of activated MAPK reverts back to zero. Reverse reactions are triggered by the signal $E2$ and by the MAPK phosphatases KKpase and Kpase. The reaction-based representation is

$$\begin{aligned}
R_1 &: \mathrm{KKK} + E1 \longrightarrow \mathrm{KKKp} + E1\\
R_2 &: \mathrm{KKKp} + E2 \longrightarrow \mathrm{KKK} + E2\\
R_3 &: \mathrm{KK} + \mathrm{KKKp} \longrightarrow \mathrm{KKp} + \mathrm{KKKp}\\
R_4 &: \mathrm{KKp} + \mathrm{KKpase} \longrightarrow \mathrm{KK} + \mathrm{KKpase}\\
R_5 &: \mathrm{KKp} + \mathrm{KKKp} \longrightarrow \mathrm{KKpp} + \mathrm{KKKp}\\
R_6 &: \mathrm{KKpp} + \mathrm{KKpase} \longrightarrow \mathrm{KKp} + \mathrm{KKpase}\\
R_7 &: \mathrm{K} + \mathrm{KKpp} \longrightarrow \mathrm{Kp} + \mathrm{KKpp}\\
R_8 &: \mathrm{Kp} + \mathrm{Kpase} \longrightarrow \mathrm{K} + \mathrm{Kpase}\\
R_9 &: \mathrm{Kp} + \mathrm{KKpp} \longrightarrow \mathrm{Kpp} + \mathrm{KKpp}\\
R_{10} &: \mathrm{Kpp} + \mathrm{Kpase} \longrightarrow \mathrm{Kp} + \mathrm{Kpase},
\end{aligned} \tag{23}$$

where KKK denotes MAPKKK, KK denotes MAPKK, and K denotes MAPK and tags p and pp indicate phosphorylation and double phosphorylation, respectively.

A simulation benchmark of the MAPK cascade is in Table 2 (first column). In the computed benchmark, the model has been simulated for 150 time units with all stochastic reaction constants equal to 0.001. The initial abundances have been set to $E1 = 2000$, $E2 = 2000$, $\mathrm{K} = 200000$, $\mathrm{KK} = 200000$, and $\mathrm{KKK} = 20000$. All the other species are initialized with 0 molecules.

3.2. The Gemcitabine Model. Gemcitabine is a drug for non-small-cell lung cancer, pancreatic cancer, bladder cancer, and breast cancer. Here we will consider a simplified model of its mechanism of action according to [23].

Gemcitabine (dFdC, see Box 1) is transported from plasma into the cell through the cell membrane ($\mathrm{dFdC_{out}} \rightarrow$ dFdC). Gemcitabine can be deaminated by CDA in the cytoplasm and in the extracellular environment leading to dFdU. Both dFdC and dFdU can be phosphorylated by dCK. Monophosphorylated Gemcitabine can be deaminated by dCMPD, whereas dCMPD is inhibited by $\mathrm{dFdC_{TP}}$. Alternatively, it is further phosphorylated. The Gemcitabine triphosphates $\mathrm{dFdC_{TP}}$ and $\mathrm{dFdU_{TP}}$ compete with the natural nucleoside triphosphate dCTP for incorporation into nascent DNA chain and inhibit DNA synthesis, thus blocking cell proliferation in the early DNA synthesis phase.

A simulation benchmark of the Gemcitabine model is in Table 2 (second column, simulation length 12 time units). In the computed benchmark, stochastic reaction constants are [23]: $c_1 = 9.97$, $c_2 = 2.61e^{-4}$, $c_3 = 4.72e^{-6}$, $c_4 = 0.05$, $c_5 = 0$, $c_6 = 0.001$, $c_7 = 0.087$, $c_8 = 2.37$, $c_9 = 0.21$, $c_{10} = 2.52$, $c_{11} = 1.45$, $c_{12} = 9.68e^{-4}$, $c_{13} = 5.6e^{-5}$, $c_{14} = 0.078$, $c_{15} = 0.004$, $c_{16} = 0.16$, $c_{17} = 9.05e^{-5}$, $c_{18} = 4.76e^{-4}$, $c_{19} = 4.559e^{-6}$, $c_{20} = 1000$, $c_{21} = 0.05$, $c_{22} = 25.20$, $c_{23} = 1e^{-5}$, $c_{24} = 0.1$, $c_{25} = 1e^{-5}$, $c_{26} = 0.1$, $c_{27} = 1e^{-7}$, $c_{28} = 0.1$, $c_{29} = 0.05$, $c_{30} = 7.37e^{-4}$, and $c_{31} = 0.5$. Initially all the variables have been set to 0 except for $\mathrm{dFdC_{out}} = 100000$, $\mathrm{dCK} = 1000$, $\mathrm{RR} = 1000$, $\mathrm{dCMPD} = 1000$, and $\mathrm{CDP} = 2000$.

3.3. The Fully Connected Model. The fully connected model is a theoretical model that consists of n species $S_1, S_2, \ldots, S_n$

R_1 : $dFdC_{out} \longrightarrow dFdC$
R_2 : $dFdC \longrightarrow dFdC_{out}$
R_3 : $dFdC_{out} \longrightarrow dFdU$
R_4 : $dFdU \longrightarrow dFdU_{out}$
R_5 : $dFdC \longrightarrow dFdU$
R_6 : $dFdC + dCK \longrightarrow dFdC_{MP} + dCK$
R_7 : $dFdC_{MP} \longrightarrow dFdC$
R_8 : $dFdC_{MP} \longrightarrow dFdC_{DP}$
R_9 : $dFdC_{DP} \longrightarrow dFdC_{MP}$
R_{10} : $dFdC_{DP} \longrightarrow dFdC_{TP}$
R_{11} : $dFdC_{TP} \longrightarrow dFdC_{DP}$
R_{12} : $dFdU + dCK \longrightarrow dFdU_{MP} + dCK$
R_{13} : $dFdU_{MP} \longrightarrow dFdU$
R_{14} : $dFdU_{MP} \longrightarrow dFdU_{DP}$
R_{15} : $dFdU_{DP} \longrightarrow dFdU_{MP}$
R_{16} : $dFdU_{DP} \longrightarrow dFdU_{TP}$
R_{17} : $dFdU_{TP} \longrightarrow dFdU_{DP}$
R_{18} : $dFdC \longrightarrow dFdU$
R_{19} : $dFdC_{MP} + dCMPD \longrightarrow dFdU_{MP} + dCMPD$
R_{20} : $\emptyset \longrightarrow CDP$
R_{21} : $CDP + RR \longrightarrow dCDP + RR$
R_{22} : $dCDP \longrightarrow dCTP$
R_{23} : $dFdC_{DP} + RR \longrightarrow dFdC_{DP} : RR$
R_{24} : $dFdC_{DP} : RR \longrightarrow dFdC_{DP} + RR$
R_{25} : $dCTP + dCK \longrightarrow dCTP : dCK$
R_{26} : $dCTP : dCK \longrightarrow dCTP + dCK$
R_{27} : $dFdC_{TP} + dCMPD \longrightarrow dFdC_{TP} : dCMPD$
R_{28} : $dFdC_{TP} : dCMPD \longrightarrow dFdC_{TP} + dCMPD$
R_{29} : $dFdC_{TP} \longrightarrow dFdC_{TP} : DNA$
R_{30} : $dFdU_{TP} \longrightarrow dFdU_{TP} : DNA$
R_{31} : $dCTP \longrightarrow dCTP : DNA$

Box 1: Reactions of the Gemcitabine model [23].

and a set of reactions that reversibly convert each species into each other of the form

$$S_i \longleftrightarrow S_j, \quad i, j = 1, \ldots, n, \; i \neq j. \tag{24}$$

The fully connected model is useful to evaluate the scalability of algorithms (variation in runtime with growing values of n). Moreover, if we fix initial values of the species and stochastic reaction constants, then we can evaluate the performance of a simulation algorithm when it simulates a system that remains in a steady state condition for the entire length of the simulation.

Here we use the fully connected model starting from two different steady state conditions to quantify simulation runtime of a reaction network composed by only slow or fast reactions. These benchmarks are provided in Table 2, third and fourth columns. In both cases, the model has been generated with $n = 20$, that is, with 20 variables and 380 reactions. All stochastic reaction constants have been set to 1. In the first benchmark (MCM $i = 20$), the initial state of all model variables has been set to 20 in order to create a network of slow reactions. In the second one (MCM $i = 2000$), instead, the initial state of all model variables has been set to 2000 in order to create a network of fast reactions. In both conditions, simulation algorithms implemented in HSimulator were the fastest (simulation length 150 time units).

3.4. The Multiscaled Model. The multiscaled model is a theoretical model with a reaction network that can be divided into two subnetworks working at different time scales. It has been specifically considered to test hybrid simulation strategies because it allows testing the intermediate condition (network made of both fast and slow reactions) between the two scenarios previously considered with the fully connected model (network made of only slow or fast reactions). The first subnetwork of the model is given by a fully connected model of n_{fast} species $S_1, \ldots, S_{n_{\text{fast}}}$ modified by a set of fast reactions. The model is then extended with n_{slow} species $s_1, \ldots, s_{n_{\text{slow}}}$ modified by a set of n_{slow} reactions of the form

$$S_i + s_j \longrightarrow s_k, \quad j = 1, 2, \ldots, n_{\text{slow}}, \tag{25}$$

where S_i and s_k are random species such that $S_i \in \{S_1, \ldots, S_{n_{\text{fast}}}\}$ and $s_k \in \{s_1, \ldots, s_{n_{\text{slow}}}\}$. The stochastic constant rates of fast reactions are some order of magnitude bigger than the rates of the slow reactions to emphasize the difference of speed between the two subnetworks.

The fully connected model has been considered to evaluate the performance of simulation algorithms when a mass-action biochemical reaction network of reactions that are all slow (MCM $i = 20$) or fast (MCM $i = 2000$) is simulated. Conversely, the multiscale model allowed testing the intermediate condition, where the biochemical network can be divided into two subnetworks working at different time scales.

In Table 2 two benchmarks related to this model are provided. The first one (fifth column, MSM (10, 50)) is related to a model with $n_{\text{fast}} = 10$ and $n_{\text{slow}} = 50$ (60 species and 140 reactions), stochastic reaction constants equal to 10.0 (fast reactions) and 0.001 (slow reactions), initial values of fast species set to 2000, and initial values of slow species set to 20. The second benchmark (last column of the table, MSM (20, 100)) uses the same parameters of the first one except for $n_{\text{fast}} = 20$ and $n_{\text{slow}} = 100$ (120 species and 480 reactions). The provided benchmarks show that the gain in simulation runtime provided by HSimulator is scalable with respect to the complexity of the model (simulation length 10 time units).

4. Conclusions

We presented HSimulator, a state-of-the-art multithread Java simulator for mass-action well-stirred biochemical reaction systems. HSimulator provides a suite of published state-of-the-art simulation algorithms including, in the same package, the exact algorithm RSSA and the first publicly available implementation of its hybrid version HRSSA. The benchmarks in the paper show that the HSimulator implementation is often faster than the state-of-the-art simulator COPASI [22]. This could open new perspectives in computational systems biology, where often scientists have to balance the accuracy of their simulations with the need of considering large reaction networks modeling complex diseases or disorders.

Conflicts of Interest

The authors declare that they have no conflicts of interest.

Acknowledgments

The authors acknowledge Alessandro Pozzer for technical assistance and Dr. Giuditta Franco (Department of Computer Science, University of Verona, Italy) for her helpful suggestions and discussions. This work was partially supported by the PAT (Provincia Autonoma di Trento) Project S503/2015/664730 Zoomer.

References

[1] H. Kitano, "Computational systems biology," *Nature*, vol. 420, no. 6912, pp. 206–210, 2002.

[2] H. Kitano, "Systems biology: a brief overview," *Science*, vol. 295, no. 5560, pp. 1662–1664, 2002.

[3] L. Hood and D. Galas, "The digital code of DNA," *Nature*, vol. 421, no. 6921, pp. 444–448, 2003.

[4] A. P. Heath and L. E. Kavraki, "Computational challenges in systems biology," *Computer Science Review*, vol. 3, no. 1, pp. 1–17, 2009.

[5] C. Priami, "Algorithmic systems biology," *Communications of the ACM*, vol. 52, no. 5, pp. 80–88, 2009.

[6] C. Priami and M. J. Morine, *Analysis of Biological Systems*, Imperial College Press, London, UK, 2015.

[7] L. Marchetti, C. Priami, and V. H. Thanh, *Simulation Algorithms for Computational Systems Biology*, Springer International Publishing, Berlin, Germany, 2017.

[8] D. T. Gillespie, "Exact stochastic simulation of coupled chemical reactions," *The Journal of Physical Chemistry C*, vol. 81, no. 25, pp. 2340–2361, 1977.

[9] M. A. Gibson and J. Bruck, "Efficient exact stochastic simulation of chemical systems with many species and many channels," *The Journal of Physical Chemistry A*, vol. 104, no. 9, pp. 1876–1889, 2000.

[10] V. H. Thanh, C. Priami, and R. Zunino, "Efficient rejection-based simulation of biochemical reactions with stochastic noise and delays," *The Journal of Chemical Physics*, vol. 141, no. 13, Article ID 134116, 2014.

[11] D. T. Gillespie, "The Chemical Langevin equation," *The Journal of Chemical Physics*, vol. 113, no. 1, pp. 297–306, 2000.

[12] D. T. Gillespie, "Approximate accelerated stochastic simulation of chemically reacting systems," *The Journal of Chemical Physics*, vol. 115, no. 4, pp. 1716–1733, 2001.

[13] J. C. Butcher, *Numerical Methods for Ordinary Differential Equations*, John Wiley & Sons, New York, NY, USA, 2nd edition, 2008.

[14] J. Pahle, "Biochemical simulations: stochastic, approximate stochastic and hybrid approaches," *Briefings in Bioinformatics*, vol. 10, no. 1, pp. 53–64, 2009.

[15] M. Bentele and R. Eils, "General stochastic hybrid method for the simulation of chemical reaction processes in cells," in *Computational Methods in Systems Biology*, V. Danos and V. Schachter, Eds., vol. 3082 of *Lecture Notes in Computer Science*, Springer, Berlin, Germany, 2005.

[16] M. Herajy and M. Heiner, "Hybrid representation and simulation of stiff biochemical networks," *Nonlinear Analysis: Hybrid Systems*, vol. 6, no. 4, pp. 942–959, 2012.

[17] R. Irizarry, "Stochastic simulation of population balance models with disparate time scales: hybrid strategies," *Chemical Engineering Science*, vol. 66, no. 18, pp. 4059–4069, 2011.

[18] M. Griffith, T. Courtney, J. Peccoud, and W. H. Sanders, "Dynamic partitioning for hybrid simulation of the bistable HIV-1 transactivation network," *Bioinformatics*, vol. 22, no. 22, pp. 2782–2789, 2006.

[19] H. Salis and Y. Kaznessis, "Accurate hybrid stochastic simulation of a system of coupled chemical or biochemical reactions," *The Journal of Chemical Physics*, vol. 122, no. 5, Article ID 054103, 2005.

[20] E. L. Haseltine and J. B. Rawlings, "On the origins of approximations for stochastic chemical kinetics," *The Journal of Chemical Physics*, vol. 123, no. 16, Article ID 164115, 2005.

[21] L. Marchetti, C. Priami, and V. H. Thanh, "HRSSA—efficient hybrid stochastic simulation for spatially homogeneous biochemical reaction networks," *Journal of Computational Physics*, vol. 317, pp. 301–317, 2016.

[22] S. Hoops, R. Gauges, C. Lee et al., "COPASI—a COmplex PAthway SImulator," *Bioinformatics*, vol. 22, no. 24, pp. 3067–3074, 2006.

[23] O. Kahramanoğullari, G. Fantaccini, P. Lecca, D. Morpurgo, and C. Priami, "Algorithmic modeling quantifies the complementary contribution of metabolic inhibitions to gemcitabine efficacy," *PLoS ONE*, vol. 7, no. 12, Article ID e50176, 2012.

[24] V. H. Thanh, R. Zunino, and C. Priami, "On the rejection-based algorithm for simulation and analysis of large-scale reaction networks," *The Journal of Chemical Physics*, vol. 142, no. 24, Article ID 244106, 2015.

[25] V. H. Thanh and C. Priami, "Simulation of biochemical reactions with time-dependent rates by the rejection-based algorithm," *The Journal of Chemical Physics*, vol. 143, no. 5, Article ID 054104, 2015.

[26] V. H. Thanh, R. Zunino, and C. Priami, "Efficient constant-time complexity algorithm for stochastic simulation of large reaction networks," *IEEE/ACM Transactions on Computational Biology and Bioinformatics*, vol. 14, no. 3, pp. 657–667, 2017.

[27] R. Lombardo and C. Priami, "Graphical modeling meets systems pharmacology," *Gene Regulation and Systems Biology*, vol. 11, pp. 1–10, 2017.

[28] M. Herajy, F. Liu, C. Rohr, and M. Heiner, "Snoopy's hybrid simulator: a tool to construct and simulate hybrid biological models," *BMC Systems Biology*, vol. 11, no. 71, 2017.

[29] L. Chang and M. Karin, "Mammalian MAP kinase signalling cascades," *Nature*, vol. 410, no. 6824, pp. 37–40, 2001.

[30] R. J. Orton, O. E. Sturm, V. Vyshemirsky, M. Calder, D. R. Gilbert, and W. Kolch, "Computational modelling of the receptor-tyrosine-kinase-activated MAPK pathway," *Biochemical Journal*, vol. 392, no. 2, pp. 249–261, 2005.

Hindawi
Complexity
Volume 2017, Article ID 1580414, 9 pages
https://doi.org/10.1155/2017/1580414

Research Article

Identification of S1 and S2 Heart Sound Patterns Based on Fractal Theory and Shape Context

Ana Gavrovska,[1] Goran Zajić,[1,2] Vesna Bogdanović,[3] Irini Reljin,[1] and Branimir Reljin[1]

[1]*School of Electrical Engineering, University of Belgrade, Bulevar kralja Aleksandra 73, 11120 Belgrade, Serbia*
[2]*ICT College of Vocational Studies, Zdravka Čelara 16, 11000 Belgrade, Serbia*
[3]*Health Center "Zvezdara", Olge Jovanovic 11, 11000 Belgrade, Serbia*

Correspondence should be addressed to Ana Gavrovska; anaga777@gmail.com

Received 10 June 2017; Accepted 23 October 2017; Published 13 November 2017

Academic Editor: Roberto Tonelli

Copyright © 2017 Ana Gavrovska et al. This is an open access article distributed under the Creative Commons Attribution License, which permits unrestricted use, distribution, and reproduction in any medium, provided the original work is properly cited.

There has been a sustained effort in the research community over the recent years to develop algorithms that automatically analyze heart sounds. One of the major challenges is identifying primary heart sounds, S1 and S2, as they represent reference events for the analysis. The study presented in this paper analyzes the possibility of improving the structure characterization based on shape context and structure assessment using a small number of descriptors. Particularly, for the primary sound characterization, an adaptive waveform filtering is applied based on blanket fractal dimension for each preprocessed sound candidate belonging to pediatric subjects. This is followed by applying the shape based methods selected for the structure assessment of primary heart sounds. Different methods, such as the fractal ones, are used for the comparison. The analysis of heart sound patterns is performed using support vector machine classifier showing promising results (above 95% accuracy). The obtained results suggest that it is possible to improve the identification process using the shape related methods which are rarely applied. This can be helpful for applications involving automatic heart sound analysis.

1. Introduction

Auscultation is widely used for evaluation of cardiac function. Since the heart sound analysis mostly depends on the individual skills of the clinician, there is a growing demand for automatic heart sound interpretation methods and systems [1]. Phonocardiography is a cost-effective noninvasive method which enables both hearing and visualizing the content of heart sound signals. It is considered to be helpful in avoiding complex and expensive imaging equipment [2].

One of the major concerns in heart sound analysis is to identify the first (S1) and the second (S2) heart sound [3]. Their proper identification is of key importance for interpretation of other signal's components, such as extra sounds and murmurs found between the fundamental sounds, in systole (S1-S2) and diastole (S2-S1) intervals. The closure of mitral and tricuspid valves forms S1, where S2 sound is produced by the closure of aortic and pulmonary valves. With the use of electrocardiogram reference, the identification of S1 is easy to perform due to the localization of QRS complex. More often, there is a need to identify the sounds without the use of any synchronously recorded reference. This is a challenging task since these sounds are found as components of relatively high energy in the same low frequency range having similar morphology [4]. Thus, characterizing the typical heart sounds, such as S1 and S2, has acquired great popularity over the years [5–8].

The existing methods for characterization of the sounds often apply the calculation of envelograms to introduce the energy aspect, such as the Shannon energy based one, where higher energy is usually associated with S1 [5, 6, 9]. Similar auxiliary envelopes are applied using different joint time-frequency representations [8, 10, 11]. The identification methods for the primary heart sounds usually consider signal/envelope characteristics (e.g., maximum, variance, frequency, and positive/negative area [6, 9, 12]). It is noticed that the labels S1 and S2 are traditionally assigned without taking into account varying energy of the sounds [8, 10], where

the improved characterization is needed regardless of the assumptions concerning the intervals between the candidates (e.g., recurring sequence of S1-S2 pairs, no excitement, and neither missed candidates nor misinterpreted systoles as intervals of short duration [9, 10]).

On the other hand, shape descriptors for the structure characterization are considered to be valuable for the identification, even though they are rarely applied. Skewness of the envelope waveform as a measure of high order statistics is used in [4] to characterize the structure, where the asymmetrical energy distribution of S2 is assumed due to closure of valves. Another shape related method is based on the kurtosis calculation to characterize the peakedness of the sounds [8]. The advantages of fractal framework are also recognized for the heart sounds, where different fractal dimension (FD) methods related to variation and structure of the waveforms are applied. Typical heart sounds S1 and S2, of short duration (20–200 ms) and low frequencies (20–200 Hz), can be considered fractal in nature [2, 11].

So far, fractal complexity is used for heart rate variability [13, 14], as well as for the auscultatory recording classification [15], where FD is shown as a satisfying tool in comparison to the other time-frequency features. As a measure of fractal complexity, for S1 and S2 heart sound identification, variance FD (VFD) is applied in [16]. For lung sounds belonging to pediatric patients, Katz FD (KFD) [17] is applied in identification of crackles and swallowing in [18, 19]. In [20], blanket method (BFD) is used for the tidal volume estimation using tracheal sounds. In the previous work of our group, initial examination of blanket method is shown as a possible tool for primary heart sounds as well [21]. Moreover, in our previous works [11, 12], novel methods are proposed for efficient classification of the auscultatory recordings without the primary heart sound detection using a few multifractal spectrum related features.

This study makes a contribution to research on methods for heart sound analysis using advantages of fractal theory and shape context, using relatively small number of descriptors. In Section 2, the description of fractal concepts in identification of primary heart sounds is briefly presented. For the waveform pattern analysis, new shape related methods are proposed, which are based on adaptive filtering and modified blanket approach bearing in mind the most extreme points within the heart sound signals. The new method is tested over real heart sounds belonging to pediatric subjects and compared with other methods known from literature. The results of the study are presented in Section 3. In Section 4, some concluding remarks are presented.

2. Materials and Methods

The fundamental cardiac sounds S1 (heard as a "lub" sound) and S2 (heard as a "dub" sound) are usually found in an auscultatory recording as characteristic components of relatively high energy. Each beat consists of four parts: S1 sound, systole, S2 sound, and diastole [3]. Other extra sounds found in a heart sound signal (clicks, snaps, murmurs, etc.) may convey valuable information, but an interpretation of any extra sound depends on the identification of S1 and S2.

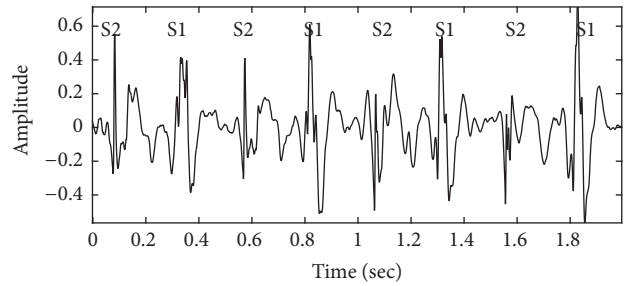

Figure 1: An auscultatory recording.

Figure 1 shows a part of a record (duration of two seconds) belonging to a pediatric subject. The labels S1 and S2 are given by physician as the fundamental heart sounds.

In order to examine the patterns of structures found in auscultatory recordings, the dataset of over a thousand sequences belonging to pediatric subjects is gathered. Particularly, heart sounds are collected in compliance with the ethical standards from the apex area. The acquisition of heart sounds is performed at the Health Center "Zvezdara" and additional echocardiography examination at the University Children's Hospital in Belgrade, Serbia. The sounds are initially recorded with 8 kHz and downsampled to 1 kHz for the analysis since the basic structure of the waveforms is not degraded after downsampling. Littman 4100WS stethoscope is used for the acquisition.

2.1. Fractal Concept in the Pattern Characterization. Self-similarity property of the waveforms is based on the existence of similar patterns across different scales. Namely, the similar shape may arise when observing a structure across the scales, where these structures (fractals) can be described by their fractal dimension [17]. The fractal approaches were found as efficient tools for characterization of complex structures, where different covering techniques and extensions from the envelopes to measuring area can be used [12, 13, 17, 18].

In order to clarify the basic mathematical concept applied in FD calculation, a brief explanation is given for better understanding. The principle for calculating box-counting FD (BCFD), as one of the most frequently used methods, is based on covering a waveform x with boxes of size ε by appropriate grid, defined by evenly spaced squares, where the number of boxes, $N(\varepsilon)$, needed to cover a signal is calculated [12]. The size of squares, $1/\varepsilon$, changes with scale. When ε tends to zero, the dimension can be estimated via the power law:

$$D_{\mathrm{BCFD}} = -\lim_{\varepsilon \to 0} \left(\frac{\log (N(\varepsilon))}{\log (\varepsilon)} \right). \quad (1)$$

The algorithms for FD estimation are mostly defined to be easy to calculate, where a waveform can be described by a single fractal measure. When applied to specific sound structures of relatively short duration, they may be valuable in their identification. There are many different methods, where some of them are directly related to the structure analyzed. It is worth mentioning that the KFD is one of the most

often applied, related to the pattern characterization [17, 22], which considers the length of a curve, $L(d)$, calculated as a sum of Euclidean distances between the successive samples. The KFD is computed by averaging the distance between the successive samples $\overline{a}$ as

$$D_{\mathrm{KFD}} = \frac{\log(n)}{\left(\log(n) + \log(d/L)\right)}, \tag{2}$$

where $n = L/\overline{a}$ and d is the planar diameter of a waveform defined as a maximum of distances between the first and any other point of the waveform.

Envelopes can be applied in measuring area, as used in BFD method. By defining the blankets for structure covering, it is possible to define adequate covering areas and perform the fitting in a log-log domain

$$D_{\mathrm{BFD1/2}} = \frac{\log(A(\varepsilon))}{\log(\varepsilon)}, \tag{3}$$

where $A(\varepsilon)$ can be described as follows:

(i) The area change between the adjacent ε as in [23] (here denoted as BFD1) or

(ii) The curve length estimation as in [24] (here denoted as BFD2).

2.2. Multiscale Heart Sound Identification. Even though the higher number of components is expected in S1, the interpretation of each of the primary heart sound waveforms for the identification purpose is not an easy task [7]. The structure of the S1 and S2 heart sounds produced by cardiac contractions and valve closures can be considered to be similar across different scales. By assuming the importance of the most abrupt change of a waveform's magnitude for the identification, we propose an adapting technique as follows:

$$u_{\varepsilon,\mathrm{new}} = \max_i\left(u_\varepsilon(i)\right) - u_\varepsilon(i) + x(i), \tag{4a}$$

where

$$u_\varepsilon(i) = \max_{[k-i\le 1]}\left\{u_{\varepsilon-1}(k)\right\}, \tag{4b}$$

$$b_{\varepsilon,\mathrm{new}}(i) = x(i) - b_\varepsilon(i), \tag{5a}$$

where

$$b_\varepsilon(i) = \min_{[k-i\le 1]}\left\{b_{\varepsilon-1}(k)\right\}. \tag{5b}$$

Initially, $u_0 = b_0 = x$ and $i, k = 1, \ldots, N$. The proposed technique calculates the upper $u_{\varepsilon,\mathrm{new}}$ ("above") and lower $b_{\varepsilon,\mathrm{new}}$ ("below") envelopes starting from the maximum and minimum points, respectively. The envelopes are formed according to the most prominent extreme points. The curves are adapting to the original waveform structure and the extreme points in each iteration ε. The information related to the extremes is extracted by the adaptive structure filtering (4a), (4b), (5a), and (5b), so that the local maxima affect variation of the lower envelopes, while the local minima affect the upper ones. Moreover, it is assumed that the most abrupt waveform change is relevant for the classification by clamping the curves using the maximum and the minimum of a structure. In Figure 2, the envelopes are presented for BFD1 and the new covering method based on (4a), (4b), (5a), and (5b). Ability of extremes to affect variation of the envelopes can be noticed in Figure 2(b).

In order to describe the primary heart sounds, the covering area is divided into two parts: the area when viewing the structure from "above" (V_ε^+) and the area when viewing the structure from "below" (V_ε^-), similarly as in [23]. The upper and lower areas are calculated as

$$\begin{aligned} V_\varepsilon^+ &= \sum_i\left(u_{\varepsilon,\mathrm{new}}(i) + x(i)\right), \\ V_\varepsilon^- &= \sum_i\left(x(i) - b_{\varepsilon,\mathrm{new}}(i)\right). \end{aligned} \tag{6}$$

The applied filtering decreases the difference between the curves and the original structure. This enables the strip-like estimation of the waveform until the difference between the positive upper and lower areas becomes negligible ($V_\varepsilon^+ \ge V_\varepsilon^-$, $\varepsilon = 1, \ldots, m$). An extension to measuring area is made from the adaptive filtering in order to assess each structure.

After the adaptive filtering, three different methods for characterization of the primary sounds are proposed. The proposed methods are based on the structure assessment using the difference between the covering areas. As noticed in FD calculation and texture/pattern estimation [25], the first few iterations are mainly sensitive to the structure, that is, to the most noticeable notches. Thus, the adaptive technique in the first iterations seems to be useful in the identification. Waveform is bounded around the most abrupt change of a waveform's magnitude using a threshold T. The threshold is determined empirically as $T = 0.2 * \max(d_\varepsilon)$, where d_ε denotes the maximum of difference between upper and lower envelopes: $d_\varepsilon = |u_\varepsilon - b_\varepsilon|$. By testing, it is found that smaller threshold values can lead to misinterpretation, that is, the detection of local extremes which are not dominant.

In the first method, the value A_1 is calculated as

$$A_1 = A_1(\varepsilon) = \frac{\left(V_\varepsilon^+ - V_\varepsilon^-\right)}{2\varepsilon}. \tag{7}$$

For each scale, it can be interpreted as difference between slopes of the covering area values. After intensive experiments, we found the third iteration as appropriate for characterizing S1 and S2 sounds.

The second method calculates the total area in the multiscale structure estimation as

$$A_2 = \sum_\varepsilon A_2(\varepsilon) = \sum_\varepsilon V_\varepsilon^+ - \sum_\varepsilon V_\varepsilon^-, \tag{8a}$$

where

$$A_2(\varepsilon) = 2\varepsilon \cdot A_1(\varepsilon) = V_\varepsilon^+ - V_\varepsilon^-. \tag{8b}$$

The value $A_2(\varepsilon)$ decreases in each subsequent iteration.

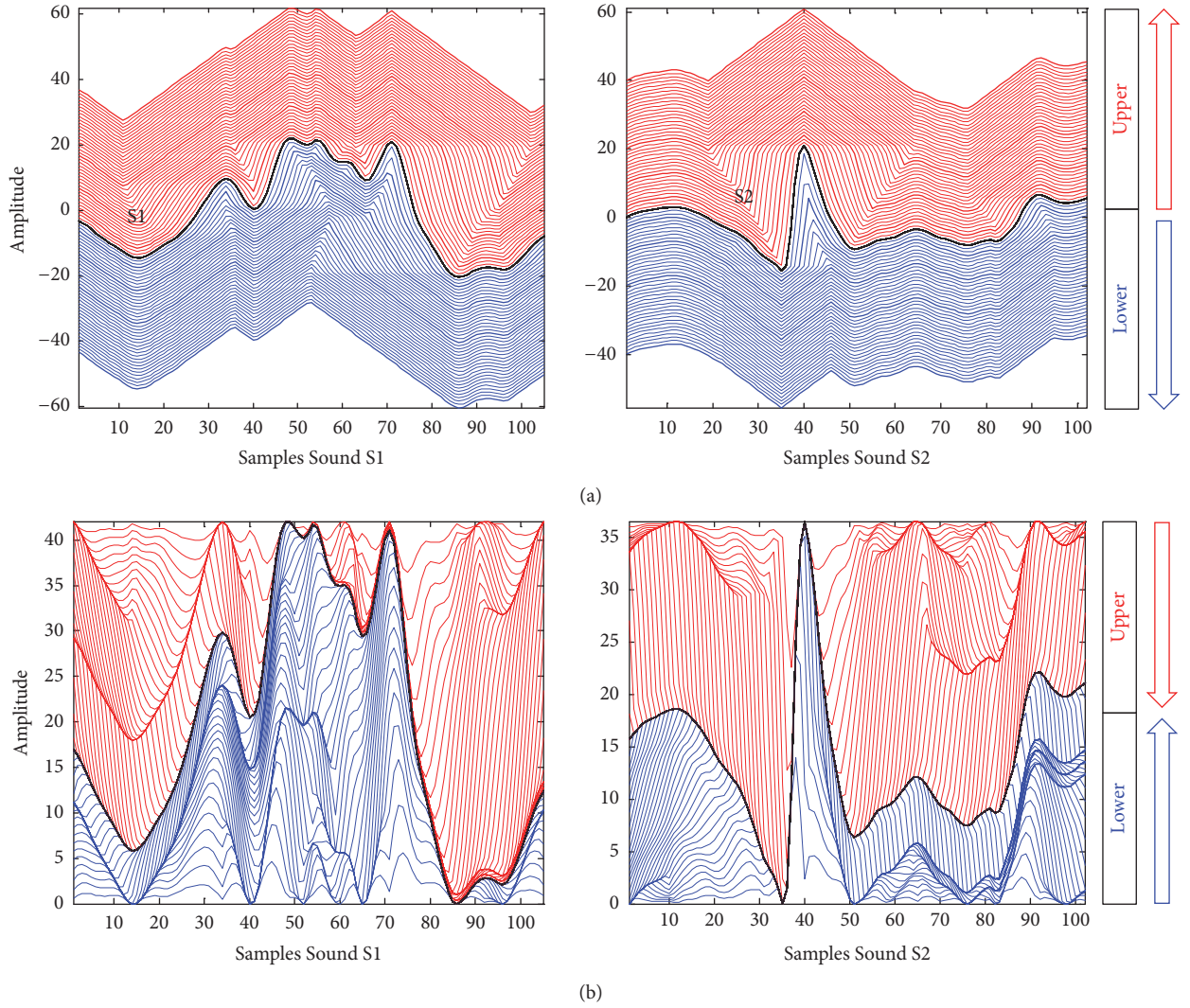

FIGURE 2: The upper and lower envelopes: (a) moving from the original structure used in BFD1, with forty iterations presented; (b) moving towards the structures according to the adapting technique: (4a), (4b), (5a), and (5b).

The third method is based on the slope-difference. It is applied to assess the structure as

$$A_3 = \sum_{\varepsilon} A_3(\varepsilon) = \sum_{\varepsilon} \frac{A_2(\varepsilon)}{\varepsilon} = \sum_{\varepsilon} t_{\varepsilon}^{+} - \sum_{\varepsilon} t_{\varepsilon}^{-}, \quad (9a)$$

where

$$A_3(\varepsilon) = \frac{A_2(\varepsilon)}{\varepsilon} = \frac{\left(V_{\varepsilon}^{+} - V_{\varepsilon}^{-}\right)}{\varepsilon} = t_{\varepsilon}^{+} - t_{\varepsilon}^{-}. \quad (9b)$$

The slope vectors are calculated for covering area values across scales ($t_{\varepsilon}^{+} = V_{\varepsilon}^{+}/\varepsilon$, $t_{\varepsilon}^{-} = V_{\varepsilon}^{-}/\varepsilon$). After the estimation, the local directions are summed, forming the result which yields the information related to the structure of primary heart sounds. Similar approaches based on summing the local directions are used in image processing for different structures in the shape context methods [26, 27]. In our approach, the sum of local directions, described by (9a) and (9b), is applied for heart sound identification.

Each of the methods (7), (8a), (8b), (9a), and (9b) can give insight into the content and shape of the structures. Computation error in the multiscale structure estimation does not produce significant consequences on the proposed methods suitability. The computation error, such as an error of the roundoff noise nature, affects the upper and lower areas, V_{ε}^{+} and V_{ε}^{-} in a similar way; thus the overall impact is negligible.

2.3. Classification and Evaluation. The classification method is based on support vector machine (SVM) classifier, which is considered as a suitable tool for discrimination tasks [28–30]. Namely, SVM is applied as a classifier which distinguishes the data by finding a separating hyperplane with a maximal margin between the classes. When applied to the waveforms,

it is described by the kernel function and regularization parameter, based on the trade-off having large normalized margin and less constraint violation. The kernel function is used to train the SVM, where the most common kernel types are the linear and the Gaussian radial basis function (RBF) described by its squared bandwidth [21, 30].

SVM based classification is performed using fivefold cross-validation [28], where nine hundred sound sequences are used. The separation of the candidates is made during the cross-validation to properly estimate the overall performance, where the classification is performed without any prior knowledge, meaning that the sequences used in the training phase are not a part of the dataset used for testing. The recursive feature elimination technique is used to improve the classification accuracy by eliminating the least significant descriptors [29, 30].

The evaluation results are obtained using the Receiver Operating Characteristic (ROC) curve. The ROC curve presents true positive rate versus false positive rate for different decision thresholds, where as a performance measure the Area Under the Curve (AUC) is calculated. Moreover, the classification accuracy and F-measure are calculated as

$$\begin{aligned} \text{Acc} &= \frac{\text{TP} + \text{TN}}{\text{TP} + \text{FP} + \text{TN} + \text{FN}}, \\ F &= \frac{2\text{TP}}{2\text{TP} + \text{FN} + \text{FP}}, \end{aligned} \tag{10}$$

respectively, where TP are the true positives (S1 hits), TN are the true negatives (S2 hits), FP are the false positives (missed S2), and FN are the false negatives (missed S1). The F-measure describes the class imbalance.

3. Results and Discussion

The three proposed methods, described in Section 2.2, are firstly tested individually for the structure assessment of the heart sounds, according to their AUC performance. They are compared to additional methods from the literature. We considered standard methods based on signal or its Shannon energy based envelope [5] (such as variance, highest amplitude/envelope value, signal/envelope area, and positive/negative signal area [6, 10, 11]) and different fractal methods: BCFD, KFD, BFD1, and BFD2 (described by expressions (1)–(3)), VFD [16], Sevcik (SFD) [31], and Higuchi (HFD) [22]. Five of FD methods can be considered highly shape related (KFD, BFD1, BFD2, SFD, and HFD). To the authors' knowledge, some of them have not been examined so far for the primary sound identification, like SFD or BFD2. We also considered statistical and shape related methods, based on kurtosis and skewness [4, 8].

3.1. Results. The AUC performance of the proposed methods is compared to other methods, where only the methods having AUC values higher than 60% are presented in Figure 3. In Figure 3, the positive area and the negative area are calculated in accordance with the sound amplitude, while the total area 1 and the total area 2 are calculated using the sound

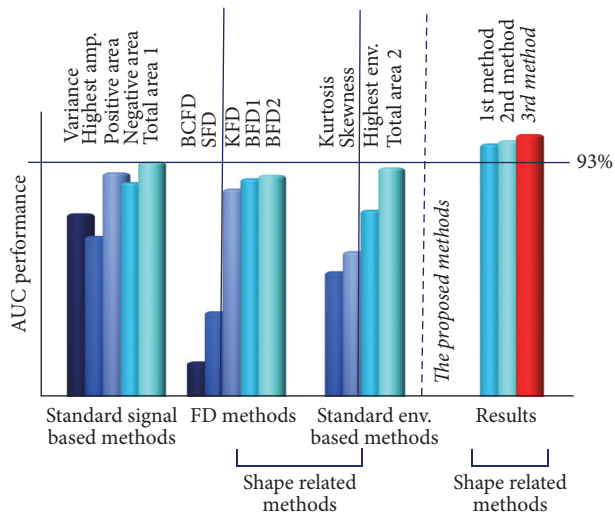

Figure 3: AUC performance of the proposed methods and other tested methods which are characterized by AUC > 60%.

amplitude and the Shannon energy based envelope, respectively. The results presented in Figure 3 show that all three methods proposed in Section 2.2 gave better performance in comparison to the other tested methods.

Note that our proposed methods are related to shape characterization. By testing other shape related methods, we found the BFD2 as a best choice for S1 versus S2 classification (AUC > 90%). It is expected that the KFD may show promising results (here AUC > 85%) since the method is considered highly consistent for shape characterization in different applications (e.g., for electroencephalogram analysis [22]). Examples of some hits and missed candidates for a set of waveforms using the third proposed method, described by (9a) and (9b), are presented in Figure 4, where only a few candidates are misinterpreted due to their structures.

The tests with AUC performance are followed by SVM based classification and cross-validation, where the selection of methods is made using the feature elimination and the grid search technique [28–30]. In order to obtain robust results in sound characterization, the accuracies are calculated after five repetitions dividing the recordings in a random manner. For SVM based classification, we analyzed all previous methods which had been tested individually. For the classification, different number N ($N = 2, \ldots, 19$) of descriptors is used in the feature elimination technique.

For the case $N = 2$, the best result is obtained for the two proposed shape context methods A_1 and A_3, where a decision boundary is presented in Figure 5(a). For different values of N, the obtained accuracy and AUC values are presented in Figure 5(b) showing the noticeable changes in accuracy in comparison to AUC performance. This is mainly due to the third method which is shown as the most significant one among the tested methods for the waveform characterization. The best performance is found for $N = 4$, where the selected descriptors are the proposed shape context values A_3 and A_1, BFD2, and the total area calculated as $A_s = \sum_i x(i)$. In this case the best accuracy results are obtained

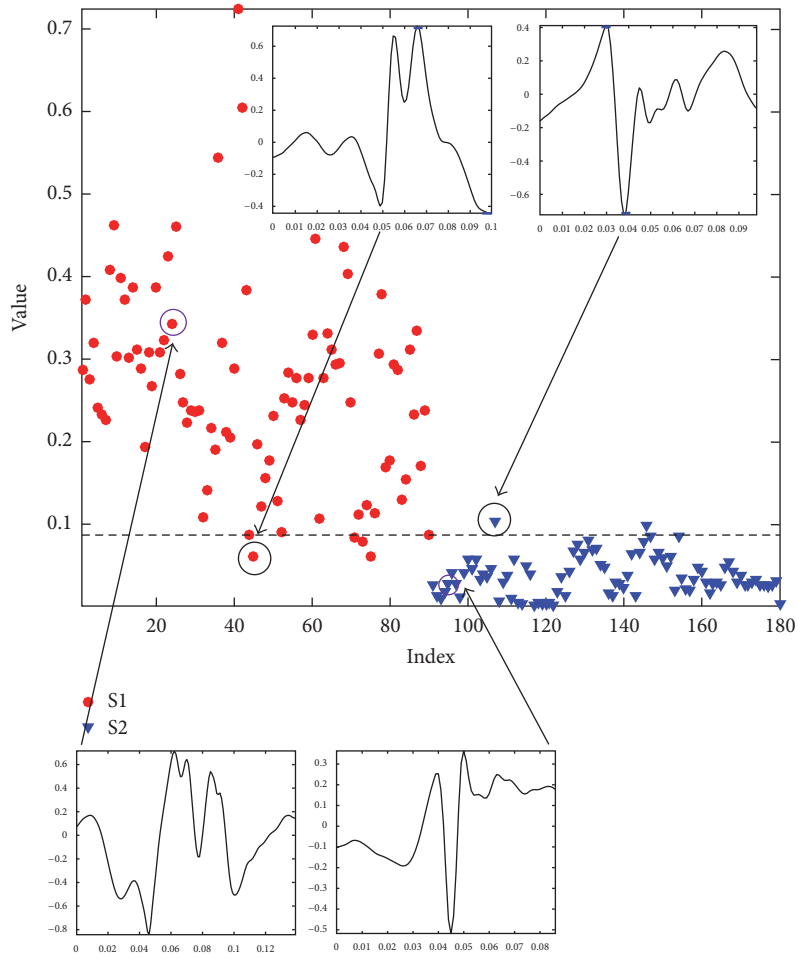

Figure 4: Calculated values obtained using the third proposed method for a set of waveforms. Examples of hits and missed candidates are presented in the lower and the upper part of the figure, respectively.

Table 1: The SVM based classification results after the cross-validation.

Classification	Accuracy [%]	F-measure	AUC [%]
RBF-SVM based	95.1	0.95	98.3
Linear SVM based	91.2	0.91	96.7

and presented in Table 1. In Table 1, the results represent the obtained average values showing above 95% accuracy for each of the classes and AUC higher than 98% for the classification. Approximately, 4% higher accuracy results are obtained using RBF kernel in comparison to the linear one.

The proposed SVM based classification utilizes the adaptive filtering and the measuring areas for the sound classification. In this paper, the cross-validation is performed only according to the healthy pediatric subjects. An additional validation of the model is performed on the waveforms belonging to ten patients which were not included in the cross-validation procedure, where the proposed structure assessment methodology showed excellent results with AUC of 97.6% and accuracy of 90.6% (F-measure of 0.91).

3.2. Discussion and Comparison. The study in this paper is applied and tested for the primary heart sound identification process on the basis of shape related characterization for pediatric subjects. The advantage of the proposed methodology relies on the applied adaptive filtering and the selected structure assessment. The high accuracy results for the classification are obtained efficiently, without time-consuming characterization methods, by employing the shape context characterization and keeping a small number of descriptors. In comparison to the state-of-the-art methods that employ FD methods, the structure assessment characterization methods do not use averaging/fitting estimations, like the least-squares in log-log domain used in (3). The applied method also overcomes high iterations for the calculation. Particularly, the high iterations found for BFD1/2 seem not to bring new relevant information regarding the structure and may prevent FD to reflect the sound type with high accuracy

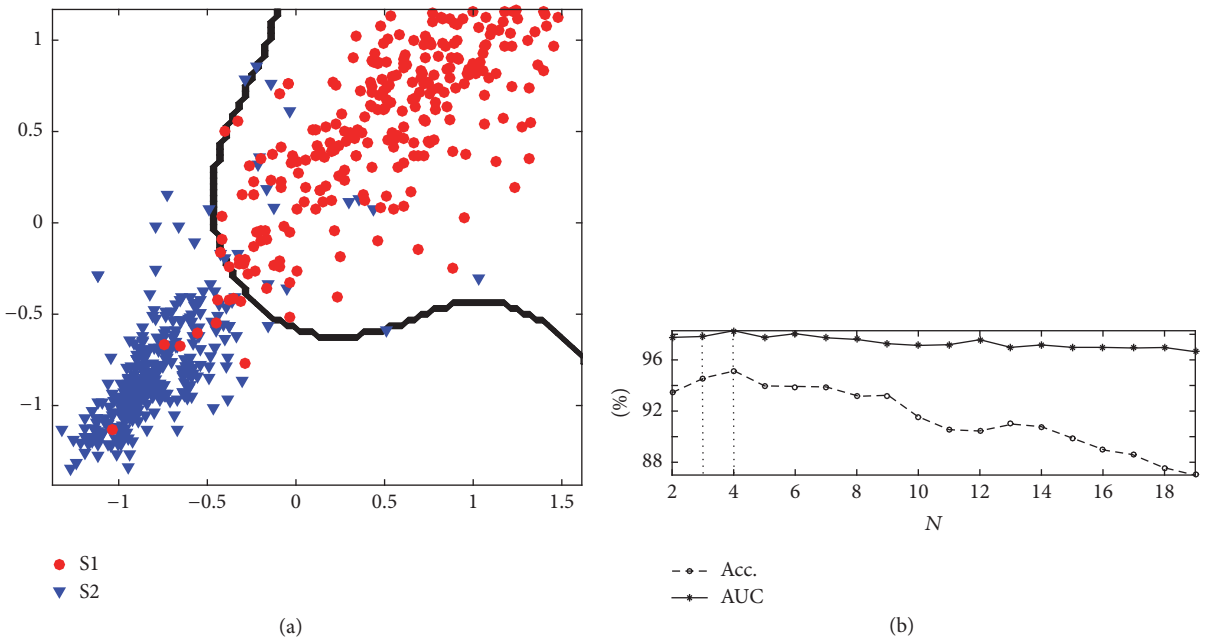

FIGURE 5: (a) Decision boundary for the two proposed shape context methods, $N = 2$. (b) The calculated validation accuracy and AUC values for different number of descriptors.

(Figure 2). Thus, applying the filtering towards the structure enables adapting to the most prominent extreme points. It can be noticed that the S1 adapting to the structure encounters the higher number of the prominent local extremes than in S2. The limitations of the proposed methodology are directly related to the sound characterization. In particular, the misclassified sounds are found among the missed examples presented in Figure 4. These are the limitations related to the found positions of the most prominent maximum and minimum used for clamping the envelopes, where some side details may produce the misinterpretation. The proposed model is adjusted to the healthy individuals. The additional experiment for nonhealthy group using a set of 180 waveforms is performed under the same circumstances providing high accuracy results.

The study is based on the shape context characterization and can be considered valuable for automatic heart sound analysis. High accuracy (above 95%) is obtained for the classification and labeling of the primary sounds regardless of the intersound relationships. In comparison to the identification from [5, 11], where highest envelope value (E) is applied for S1-systole and S2-diastole differentiation, the structure assessment overcomes the errors found due to varying energy in a signal, as presented in Figure 6(a). Recurring sounds are not assumed for the classification model, and thus the methodology may overcome errors found due to nondetected candidates and similar misinterpretations. Finally, the methodology shows significant improvement of 6% higher accuracy in comparison to the methodology from [21], as presented in Table 2. The obtained ROC curves are presented in Figure 6(b) with 6.5% higher AUC value and 0.08 higher F-measure.

TABLE 2: The comparison results.

Classification	Obtained results, accuracy [%]	Methodology from [21], accuracy [%]
RBF-SVM based	95.1	89.1
Linear SVM based	91.2	90.5

4. Conclusions

The study in this paper analyzes the possibility of using the shape context and fractal theory in the S1 and S2 pattern characterization. The obtained results show that the proposed method is able to significantly improve the accuracy (higher than 95%) by avoiding averaging and fitting procedures across the scales. The fractal theory based approaches enable developing new methods keeping a small number of descriptors in the identification of the primary sounds.

The study shows the significance of the shape context and ability to differentiate the sounds regardless of the variable energy values without even considering intersound relationships. Moreover, the obtained results indicate that the shape related approaches are valuable for further improvements in the identification of the heart sounds.

Conflicts of Interest

The authors declare that there are no conflicts of interest regarding the publication of this article.

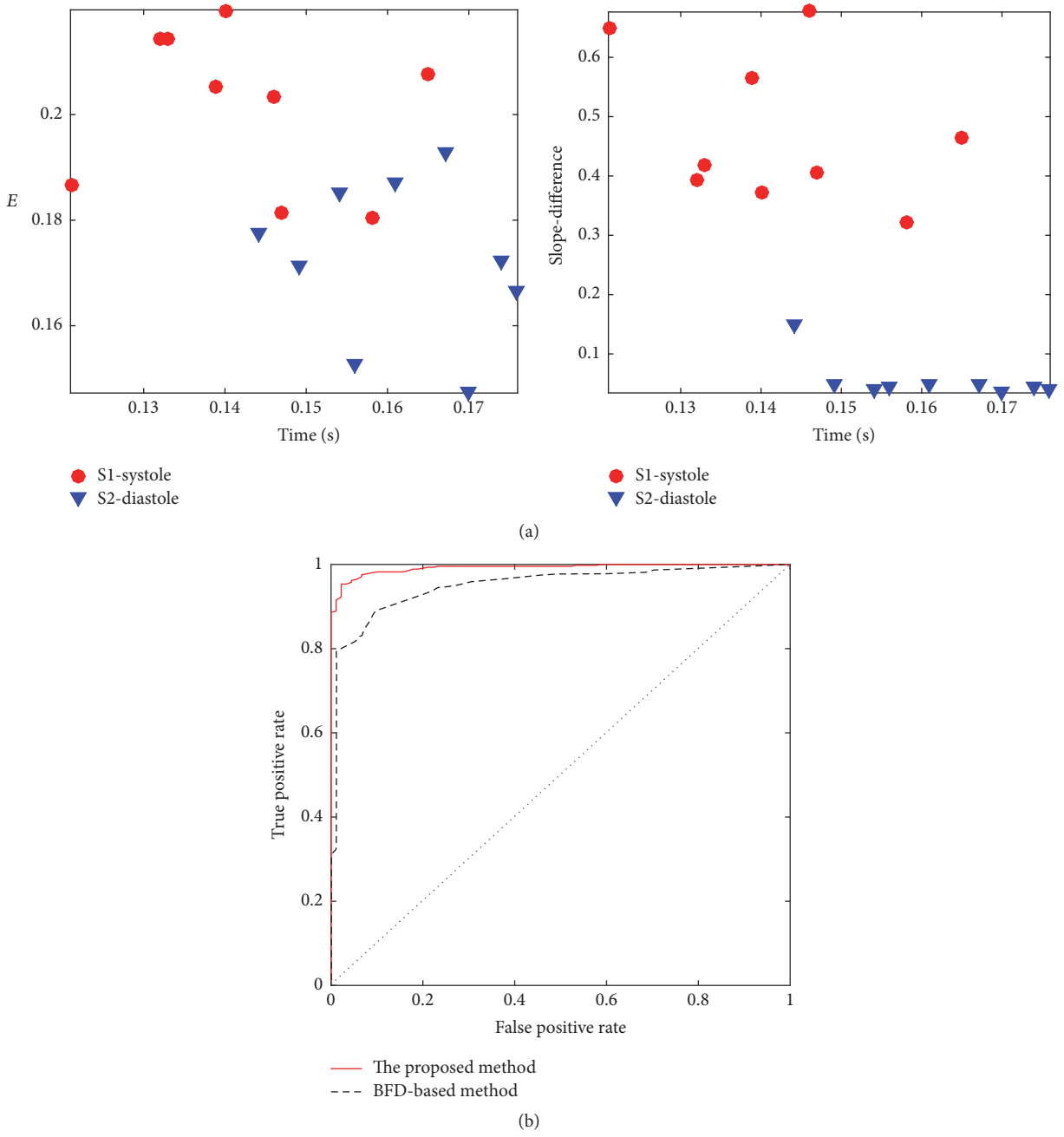

FIGURE 6: (a) S1-systole and S2-diastole differentiation using the standard and the slope-difference approach. (b) ROC curves of the proposed and fractal based methodology.

Acknowledgments

This research has been partially supported by the Ministry of Education, Science and Technological Development of the Republic of Serbia under Grant no. III44009.

References

[1] M. E. Tavel, "Cardiac auscultation: a glorious past - But does it have a future?" *Circulation, Journal of the American Heart Association*, vol. 93, no. 6, pp. 1250–1253, 1996.

[2] F. Safara, "Cumulant-based trapezoidal basis selection for heart sound classification," *Medical & Biological Engineering & Computing*, vol. 53, no. 11, pp. 1153–1164, 2015.

[3] M. A. Chizner, "Cardiac Auscultation: Rediscovering the Lost Art," *Current Problems in Cardiology*, vol. 33, no. 7, pp. 326–408, 2008.

[4] J. Hebden and J. N. Tony, "Neural network and conventional classifiers to distinguish between first and second heart sounds," in *Proceedings of the IEE Colloquium on Artificial Intelligence Methods for Biomedical Data Processing*, pp. 3-3, London, UK.

[5] L. Huiying, L. Sakari, and H. Iiro, "Heart sound segmentation algorithm based on heart sound envelogram," *Computers in Cardiology*, vol. 24, pp. 105–108, 1997.

[6] D. Kumar, P. Carvalho, M. Antunes et al., "Detection of S1 and S2 Heart Sounds by High Frequency Signatures," in *Proceedings of the Conference Proceedings. Annual International Conference of the IEEE Engineering in Medicine and Biology Society*, pp. 1410–1416, New York, NY, USA, August 2006.

[7] S. M. Debbal and F. Bereksi-Reguig, "Computerized heart sounds analysis," *Computers in Biology and Medicine*, vol. 38, no. 2, pp. 263–280, 2008.

[8] A. Moukadem, S. Schmidt, and A. Dieterlen, "High order statistics and time-frequency domain to classify heart sounds for subjects under cardiac stress test," *Computational and Mathematical Methods in Medicine*, vol. 2015, Article ID 157825, 15 pages, 2015.

[9] S. Rajan, E. Budd, M. Stevenson, and R. Doraiswami, "Unsupervised and uncued segmentation of the fundamental heart sounds in phonocardiograms using a time-scale representation," in *Proceedings of the Proceedings of the 28th IEEE/EMBS Annual International Conference*, pp. 3732–3735, New York, NY, USA, August 2006.

[10] A. M. Amiri and G. Armano, "A decision support system to diagnose heart diseases in newborns," in *Proceedings of the In The 3rd International Conference on Health Science and Biomedical Systems (HSBS'14)*, pp. 16–21, 2014.

[11] A. Gavrovska, V. Bogdanović, I. Reljin, and B. Reljin, "Automatic heart sound detection in pediatric patients without electrocardiogram reference via pseudo-affine Wigner-Ville distribution and Haar wavelet lifting," *Computer Methods and Programs in Biomedicine*, vol. 113, no. 2, pp. 515–528, 2014.

[12] A. Gavrovska, G. Zajić, I. Reljin, and B. Reljin, "Classification of prolapsed mitral valve versus healthy heart from phonocardiograms by multifractal analysis," *Computational and Mathematical Methods in Medicine*, vol. 2013, Article ID 376152, 10 pages, 2013.

[13] P. C. Ivanov, L. A. Nunes Amaral, A. L. Goldberger et al., "Multifractality in human heartbeat dynamics," *Nature*, vol. 399, no. 6735, pp. 461–465, 1999.

[14] U. R. Acharya, K. P. Joseph, N. Kannathal, C. M. Lim, and J. S. Suri, "Heart rate variability: a review," *Medical & Biological Engineering & Computing*, vol. 44, no. 12, pp. 1031–1051, 2006.

[15] C. Ahlstrom, P. Hult, P. Rask et al., "Feature extraction for systolic heart murmur classification," *Annals of Biomedical Engineering*, vol. 34, no. 11, pp. 1666–1677, 2006.

[16] P. Carvalho, P. Gil, J. Henriques, L. Eugenio, and M. Antunes, "Low complexity algorithm for heart sound segmentation using the variance fractal dimension," in *Proceedings of the IEEE International Workshop on Intelligent Signal Processing*, pp. 194–199, IEEE, 2005.

[17] M. J. Katz, "Fractals and the analysis of waveforms," *Computers in Biology and Medicine*, vol. 18, no. 3, pp. 145–156, 1988.

[18] J. Gnitecki and Z. Moussavi, "The fractality of lung sounds: A comparison of three waveform fractal dimension algorithms," *Chaos, Solitons & Fractals*, vol. 26, no. 4, pp. 1065–1072, 2005.

[19] L. J. Hadjileontiadis, "Wavelet-based enhancement of lung and bowel sounds using fractal dimension thresholding - Part I: Methodology," *IEEE Transactions on Biomedical Engineering*, vol. 52, no. 6, pp. 1143–1148, 2005.

[20] N. Reljin, B. A. Reyes, and K. H. Chon, "Tidal volume estimation using the blanket fractal dimension of the tracheal sounds acquired by smartphone," *Sensors*, vol. 15, no. 5, pp. 9773–9790, 2015.

[21] M. P. Paskaš, A. M. Gavrovska, and N. B. Reljin, "Identification of fundamental heart sounds from PCG using blanket fractal dimension," in *Proceedings of the 2014 8th Conference of the European Study Group on Cardiovascular Oscillations, ESGCO 2014*, pp. 123-124, May 2014.

[22] R. Esteller, G. Vachtsevanos, J. Echauz, and B. Litt, "A Comparison of waveform fractal dimension algorithms," *IEEE Transactions on Circuits and Systems I: Fundamental Theory and Applications*, vol. 48, no. 2, pp. 177–183, 2001.

[23] S. Peleg, J. Naor, R. Hartley, and D. Avnir, "Multiple resolution texture analysis and classification," *IEEE Transactions on Pattern Analysis and Machine Intelligence*, vol. 6, no. 4, pp. 518–523, 1984.

[24] R. Lopes, P. Dubois, I. Bhouri, M. H. Bedoui, S. Maouche, and N. Betrouni, "Local fractal and multifractal features for volumic texture characterization," *Pattern Recognition*, vol. 44, no. 8, pp. 1690–1697, 2011.

[25] S. Novianto, Y. Suzuki, and J. Maeda, "Near optimum estimation of local fractal dimension for image segmentation," *Pattern Recognition Letters*, vol. 24, no. 1-3, pp. 365–374, 2003.

[26] S. Belongie and J. Malik, "Matching with shape contexts," in *Proceedings of the IEEE Workshop on Content-Based Access of Image and Video Libraries, CBAIVL 2000*, 2000, pp. 20–26.

[27] G. Mori and J. Malik, "Recovering 3D human body configurations using shape contexts," *IEEE Transactions on Pattern Analysis and Machine Intelligence*, vol. 28, no. 7, pp. 1052–1062, 2006.

[28] K. De Brabanter, P. Karsmakers, F. Ojeda et al., "Suykens, LS-SVMlab toolbox users guide," ESAT-SISTA 10 (146), 2011.

[29] T. Pereira, J. S. Paiva, C. Correia, and J. Cardoso, "An automatic method for arterial pulse waveform recognition using KNN and SVM classifiers," *Medical & Biological Engineering & Computing*, vol. 54, no. 7, pp. 1049–1059, 2016.

[30] Z. Yin, A. Sadok, H. Sailem et al., "A screen for morphological complexity identifies regulators of switch-like transitions between discrete cell shapes," *Nature Cell Biology*, vol. 15, no. 7, pp. 860–871, 2013.

[31] C. Sevcik, "A procedure to estimate the fractal dimension of waveforms," https://arxiv.org/abs/1003.5266v1.

Hindawi
Complexity
Volume 2017, Article ID 2647164, 15 pages
https://doi.org/10.1155/2017/2647164

Research Article

Interpolative Boolean Networks

Vladimir Dobrić, Pavle Milošević, Aleksandar Rakićević, Bratislav Petrović, and Ana Poledica

Faculty of Organizational Sciences, University of Belgrade, Jove Ilića 154, 11000 Belgrade, Serbia

Correspondence should be addressed to Vladimir Dobrić; vdobric@gmail.com

Received 8 June 2017; Accepted 21 August 2017; Published 29 October 2017

Academic Editor: Valeri Mladenov

Copyright © 2017 Vladimir Dobrić et al. This is an open access article distributed under the Creative Commons Attribution License, which permits unrestricted use, distribution, and reproduction in any medium, provided the original work is properly cited.

Boolean networks are used for modeling and analysis of complex systems of interacting entities. Classical Boolean networks are binary and they are relevant for modeling systems with complex switch-like causal interactions. More descriptive power can be provided by the introduction of gradation in this model. If this is accomplished by using conventional fuzzy logics, the generalized model cannot secure the Boolean frame. Consequently, the validity of the model's dynamics is not secured. The aim of this paper is to present the Boolean consistent generalization of Boolean networks, interpolative Boolean networks. The generalization is based on interpolative Boolean algebra, the $[0, 1]$-valued realization of Boolean algebra. The proposed model is adaptive with respect to the nature of input variables and it offers greater descriptive power as compared with traditional models. For illustrative purposes, IBN is compared to the models based on existing real-valued approaches. Due to the complexity of the most systems to be analyzed and the characteristics of interpolative Boolean algebra, the software support is developed to provide graphical and numerical tools for complex system modeling and analysis.

1. Introduction

Approaches based on logic are used for modeling systems with complex causal interactions between the components [1–3]. Obtained models usually have the form of directed graphs, with a logical state variable and a logical function assigned to each node. The state of a node evolves in continuous or discrete time, in accordance with the value realization of the logical function. In comparison to traditional models of dynamical systems, logical models are less detailed and requires less information about the process of interest. Determination of an appropriate level of detail is considered as the major challenge in modeling. If the model is very detailed, it might be extremely difficult to gain insight; thus, the essential nature of the system may be obscured. On the other hand, if too little detail is included, the model may not be a reliable representation of reality. The appropriate level of detail is determined with respect to the purpose of the model and the amount of information about the process of interest. The logical modeling is aimed at capturing the nonlinear dynamics of possibly large-scale systems. The modeling of such systems is typically hampered by the lack of information. According to the principle of incompatibility [4], as the complexity of a system increases our ability to obtain both relevant and precise model of the system diminishes, and, eventually, these two model characteristics become incompatible. In the logical approaches, the precision suffers for the relevance. This enables modeling of systems that are too complex for traditional approaches.

Boolean networks (BNs) are the common logical model for modeling complex systems based on binary logic. They may be seen as discrete dynamical systems where each node logical function works dynamically to compute the node state at the next time step depending on the input values coming from other nodes [5, 6]. Therefore, the research in this field mainly addresses the structural and dynamical aspect of BN. The BN structure can be specified by an expert [7], identified from the data [8] or randomly constructed [5, 9]. On the other hand, the validity of the dynamics is secured by the laws of Boolean algebra (BA). According to the principle of truth functionality, the values of logical functions in such models are calculated by the values of their arguments in parallel or serial manner [10]. Classical models are widely used in biology and medicine [11–14], geosciences [15–18], and social sciences [19–22].

BNs are relevant for modeling systems which exhibit threshold behavior. If more details are available, BNs can be generalized by the introduction of gradation. In this case, logical variables and functions are treated as $[0,1]$-valued. In [9, 23–28], BNs are generalized using conventional, truth functional fuzzy logics. Since such fuzzy logics are not a BA [29, 30], the generalized models cannot secure the Boolean frame. Consequently, the validity of the dynamics of the model cannot be secured.

In this paper, we proposed the Boolean consistent $[0,1]$-valued generalization of BN. This approach, called the interpolative Boolean networks (IBN), is based on interpolative Boolean algebra (IBA), the $[0,1]$-valued realization of BA [31]. Unlike conventional fuzzy logics which are based on the truth functionality principle, IBA is based on the structural functionality principle to secure Boolean consistent generalization. According to this principle, logical functions have vector nature, and thus, the Boolean consistent calculations of values can be accomplished by the immanent structure vectors. This enables IBA, and consequently the IBN, to be used for modeling and analysis of complex dynamical systems in a Boolean consistent manner. Further, IBN is the general $[0,1]$-valued approach, while Boolecube, Hillcube, and similar approaches may be seen as the special case of IBN. The validity of the dynamics of IBN is illustrated on two examples from the literature using a software support developed for this purpose.

The paper is organized as follows. In Section 2, we describe the classical binary BNs and the existing real-valued realizations of BNs. Section 3 provides the basic concepts of interpolative Boolean algebra. In Section 4, the proposed generalization of BN is introduced. Furthermore, the software for complex system modeling and analysis, implementing IBN, is presented. In Section 5, the proposed approach is illustrated on two examples. The obtained results are compared with both conventional fuzzy approach and the Boolecube/Hillcube approach. The main conclusions and directions for future work are given in Section 6.

2. Boolean Networks

Boolean networks are the least detailed mathematical models of causally interacting entities. The model has the form of a directed graph, whose nodes represent the entities, and the edges represent the interactions between the entities:

$$\mathrm{BN} = (N, E), \tag{1}$$

where $N = \{x_1, \ldots, x_m\}$ is a set of nodes and E is a set of direct edges [5].

2.1. Binary Boolean Networks. Dynamics of BN is introduced by assigning a Boolean state variable and a Boolean function to each node. It is assumed that all nodes change state at each time step, with a unit time-delay. The dynamics of a BN reflects the topology of the directed graph. The state of node x_i takes the value of its Boolean function whose arguments are the states of the node's predecessors in the previous time step:

$$x_i(t+1) = f_i\left(x_{i_1}(t), \ldots, x_{i_{K_i}}(t)\right), \tag{2}$$

where $x_i(t+1) \in \{0,1\}$ and $f_i : \{0,1\}^{K_i} \to \{0,1\}$ are the state and the Boolean function of node x_i, $x_{i_1}(t), \ldots, x_{i_{K_i}}(t) \in \{0,1\}$ are the states of node x_i predecessors in the previous time step, and K_i is the number of predecessors of the node x_i.

Dynamics of BN is defined by equations which update the state of all nodes in a system:

$$\begin{bmatrix} x_1(t+1) \\ \vdots \\ x_m(t+1) \end{bmatrix} = \begin{bmatrix} f_1\left(x_{1_1}(t), \ldots, x_{1_{K_1}}(t)\right) \\ \vdots \\ f_m\left(x_{m_1}(t), \ldots, N_{m_{K_m}}(t)\right) \end{bmatrix}, \tag{3}$$

where $x(t+1) = [x_i(t+1) \mid i = 1, \ldots, m]^T$, $x(t+1) \in \{0,1\}^m$, is the state of a Boolean network at time $t+1$, and m is the number of nodes.

Transition functions $f_i(\,)$ in a classic BN, as any binary logical function, follow the principle of truth functionality [32, 33]: the value of a complex formula is uniquely determined by the truth values of its subformulas [34]. In other words, the value of a logical function is calculated using the values of functions' arguments. Since the algebra of binary BNs is Boolean, the validity of the BN dynamics is secured. The global dynamics is characterized by the existence of one or more point or cycle attractors. This is a state or a set of states where the dynamic of the network stabilizes. For each attractor there is a basin of attraction which contains states that converge to the attractor. The dynamics of a BN depends on which basin of attraction the initial states are located. The number and size of attractors, and the corresponding basins of attraction, are the state space properties which reveal the global dynamics of BNs.

Classical Boolean networks are adequate for modeling systems with complex switch-like causal interactions. In such systems, cause and effect relationships between the components are governed by thresholds [35]. Below (or above) a certain level, a component has a little or no influence on the behavior of others, while above (or below) this level the influence saturates rapidly to a constant level. Such a switch-like causal relationships can be represented using sigmoid functions. Binary representation in the classical BNs is an idealization of such relationships.

2.2. Real-Valued Realization of Boolean Networks. When more detailed description of a system is required and/or possible, the Boolean networks can be generalized by the introduction of gradation. In this case, logical state variables and logical functions are realized as real-valued. This provides the drastic increases of the descriptive power of the model [36–38]. The behavior of a system can be quantified with much more precision, and thus, deeper insight into the system's dynamics is possible. In [9, 23–28], Gödel, product, and Lukasiewicz conventional fuzzy logics are proposed for

generalization of BNs. However, the validity of the dynamics of the proposed generalized models cannot be secured, since the Boolean laws of excluded middle and contradiction are not followed in fuzzy logic [29]. This implies that the behavior of complex systems may not be accurately predicted by such models.

The Boolecube/Hillcube model is able to predict and explain quantitative experimental data [3]. This approach is the generalization of BNs based on multilinear interpolation of Boolean functions. Boolean functions are replaced by their real-valued realizations called the Boolecubes or the Hillcubes. The Boolecube is defined by the following expression:

$$\overline{f}(\overline{x}_1,\ldots,\overline{x}_m) = \sum_{x_1=0}^{1}\sum_{x_2=0}^{1}\cdots\sum_{x_m=0}^{1}\left(f(x_1,\ldots,x_m)\prod_{i=1}^{m}(x_i\overline{x}_i+(1-x_i)(1-\overline{x}_i))\right), \quad (4)$$

where $x_i(t) \in \{0,1\}$, $\overline{x}_i \in [0,1]$, and $f(x_1,\ldots,x_m) \in \{0,1\}$ is a Boolean function that indicates the inclusion of the variables/functions in the Boolecube.

The Hillcube approach is the generalization of the Boolecube approach since it uses the sigmoid function for mapping variables. This function is called the Hill function and it is defined by the following expression:

$$h(\overline{x}_i) = \frac{(\overline{x}_i)^{n_i}}{(\overline{x}_i)^{n_i}+(k_i)^{n_i}}, \quad (5)$$

where n_i is the Hill coefficient which defines the steepness of the function and k_i is the threshold parameter. Therefore, the Hillcube is defined by the following expression:

$$\overline{f_h}(\overline{x}_1,\ldots,\overline{x}_m) = \sum_{x_1=0}^{1}\sum_{x_2=0}^{1}\cdots\sum_{x_m=0}^{1}\left(f(x_1,\ldots,x_m)\prod_{i=1}^{m}(x_ih(\overline{x}_i)+(1-x_i)(1-h(\overline{x}_i)))\right), \quad (6)$$

where $x_i(t) \in \{0,1\}$, $\overline{x}_i \in [0,1]$, $f(x_1,\ldots,x_m) \in \{0,1\}$ is a Boolean function, and $h(\overline{x}_i) \in [0,1]$ is the Hill function.

3. Interpolative Boolean Algebra

Interpolative Boolean algebra (IBA) is the Boolean consistent $[0,1]$-valued generalization of finite (atomic) Boolean algebra (BA) [30, 39]. Formally, IBA is based on the principle of structural functionality [39–41]. It implies the necessity to distinctly detach the structure of the logical function from its value realization. Therefore, IBA is two-leveled algebra consisting of symbolic and valued level. The structural transformation on a symbolic level enables us to evaluate any logical function in the Boolean consistent way. Once the transformations have been conducted, the value level is introduced. The values do not have an influence on the preservation of Boolean laws. Therefore, IBA is used as a natural frame for Boolean consistent fuzzy logic [42], logical aggregation [40], similarity measure [43], and computational cognition [44].

3.1. The Principle of Structural Functionality. Unlike the truth functional fuzzy logic and many-valued algebras, IBA is based on the principle of structural functionality [39–41]. This principle implies that the immanent structure of any logical function can be directly derived from the structures of the function's arguments. In other words, any element of finite Boolean algebra uniquely corresponds to its structure (content, relation of inclusion). Relying on the principle of structural functionality is essentially different from relying on the principle of truth functionality—the structure of the observed function is at the forefront rather than the values of its arguments [45].

The main motive of introducing the principle of structural functionality is that the principle of truth functionality is binary in its essence, that is, the truth value of an expression may be true or false. Therefore, the truth functionality principle is valid in the sense that it preserves all Boolean axioms and theorems for a two-valued realization of Boolean algebra, while it is not valid in many-valued case and fuzzy logic [29]. On the other hand, according to the principle of structure functionality, the structure of the logical expression and the intensity of variables should both be taken into account in $[0,1]$-valued case. The structure of an element determines which atomic elements of IBA are included in it and/or which are not included in it. An atomic element of IBA is the simplest elements of the Boolean algebra domain of attributes BA in the sense that they do not include in themselves anything except for a trivial Boolean constant 0. Atomic element expresses the intensities of variable within the observed structure. Detailed mathematical formalization of IBA structural functionality is given further in the text.

In [40], it is shown that the truth functional principle is a value realization of the structure functional principle which is valid (in the sense that it preserves all Boolean axioms and theorems) only for a two-valued realization of Boolean algebra. On the other hand, the structure functional principle is valid in general case [40]. Therefore, the principle of truth functionality is a special case of the principle of structural functionality from the aspect of the Boolean laws.

3.2. IBA Symbolic Level. From the mathematical point of view, any logical function on IBA symbolic level is represented in a vector form, structure vector. The value of any logical function can be defined as a scalar product of two vectors:

$$f^{\otimes}(x_1,\ldots,x_m) = \overrightarrow{\sigma}_f\overrightarrow{\alpha}, \quad (7)$$

where $\overrightarrow{\sigma}_f$ is the structure vector of $f(x_1,\ldots,x_m)$ and $\overrightarrow{\alpha}$ is atomic vector. The structure vector is binary and it represents

the shape/structure of the logical function, while the atomic vector expresses the intensities of variable. In classical binary case, the intensity of variables is {0, 1}, so it is clearly a special case of IBA approach.

The structure vector is a binary vector defined by the following expression [40]:

$$\overrightarrow{\sigma}_f = \left[\sigma_f(\alpha_S) \mid S \in P(\Omega)\right]^T, \tag{8}$$

where σ_f are the structure function of logical function $f(x_1, \ldots, x_m)$, α_S is an atom of $\mathrm{BA}(\Omega) = P(P(\Omega))$, and $P(\Omega)$ is the power set of a set of free variables $\Omega = \{x_1, \ldots, x_m\}$.

The structure vector $\overrightarrow{\sigma}_f$ contains information about which atoms are relevant/included in a logical function. Such information is given by the structural function σ_f, which is defined by the following expression [40]:

$$\sigma_f(\alpha_S) = \begin{cases} 1, & \alpha_S(x_1, \ldots, x_m) \wedge f(x_1, \ldots, x_m) = \alpha_S(x_1, \ldots, x_m) \\ 0, & \alpha_S(x_1, \ldots, x_m) \wedge f(x_1, \ldots, x_m) = \underline{0}. \end{cases} \tag{9}$$

An atom in IBA is defined by the following expression [40]:

$$\alpha_S(x_1, \ldots, x_m) = \bigwedge_{x_i \in S} x_i \bigwedge_{x_j \in \Omega \setminus S} \neg x_j, \tag{10}$$

where $S \in P(\Omega)$. For instance, atomic elements of BA generated by two attributes $\Omega = \{a, b\}$ are $a \wedge b$, $a \wedge \neg b$, $\neg a \wedge b$, and $\neg a \wedge \neg b$.

In accordance with the structural functionality principle, any logical function can be uniquely represented by the following disjunctive canonical form [39]:

$$f(x_1, \ldots, x_m) = \bigcup_{\sigma_f(\alpha_S)=1 \mid S \in P(\Omega)} \alpha_S(x_1, \ldots, x_m). \tag{11}$$

In order to obtain the real value realization of any logical function, IBA uses generalized Boolean polynomials (GBPs). GBP is a sum of the relevant atomic Boolean polynomials:

$$\begin{aligned} f^{\otimes}(x_1, \ldots, x_m) &= \sum_{\sigma_f(\alpha_S)=1 \mid S \in P(\Omega)} \alpha_S^{\otimes}(x_1, \ldots, x_m) \\ &= \sum_{\sigma_f(\alpha_S)=1 \mid S \in P(\Omega)} \left(\bigotimes_{x_i \in S} x_i \bigotimes_{x_j \in \Omega \setminus S} \left(1 - x_j\right) \right), \end{aligned} \tag{12}$$

where $x_i \in [0, 1]$ and $\otimes$ is a generalized product.

3.3. IBA Structural Transformation and Valued Level. IBA is technically based on the mapping procedure of logical function to GBP. Any Boolean function can be mapped into corresponding GBP using the following rules [40]:

$$\begin{aligned} &\left(f_i(x_1, \ldots, x_m) \wedge f_j(x_1, \ldots, x_m)\right)^{\otimes} \\ &\quad = f_i^{\otimes}(x_1, \ldots, x_m) \otimes f_j^{\otimes}(x_1, \ldots, x_m) \\ &\left(f_i(x_1, \ldots, x_m) \vee f_j(x_1, \ldots, x_m)\right)^{\otimes} \\ &\quad = f_i^{\otimes}(x_1, \ldots, x_m) + f_i^{\otimes}(x_1, \ldots, x_m) \\ &\qquad - f_i^{\otimes}(x_1, \ldots, x_m) \otimes f_j^{\otimes}(x_1, \ldots, x_m) \\ &\left(\neg f_i(x_1, \ldots, x_m)\right)^{\otimes} = 1 - f_i^{\otimes}(x_1, \ldots, x_m) \\ &\left(x_i \wedge x_j\right)^{\otimes} = \begin{cases} x_i \otimes x_j, & i \neq j \\ x_i, & i = j \end{cases} \\ &\left(x_i \vee x_j\right)^{\otimes} = x_i + x_j - x_i \otimes x_j \\ &\left(\neg x_i\right)^{\otimes} = 1 - x_i. \end{aligned} \tag{13}$$

The generalized product $\otimes$ is any function that maps $\otimes : [0, 1] \times [0, 1] \to [0, 1]$ and satisfies all four axioms of t-norms (commutativity, associativity, monotonicity, and boundary condition) and the condition which ensures that the values of atomic Boolean polynomials are nonnegative [39, 40]. Therefore, the generalized product $\otimes$ for $\Omega = \{x_1, x_2\}$ may be realized as any t-norm that produce the value from the following interval:

$$\max(x_1 + x_2 - 1, 0) \leq x_1 \otimes x_2 \leq \min(x_1, x_2). \tag{14}$$

Three cases may be distinguished as particularly important realizations of the generalized product: minimum function, ordinary product, and Lukasiewicz operator.

4. Interpolative Boolean Networks

In this section, we present the Boolean consistent $[0, 1]$-valued generalization of Boolean networks, interpolative Boolean network. In the proposed model, states of nodes take value from the unit interval, while the Boolean functions are mapped into generalized Boolean polynomials according to (13). Such polynomials are the $[0, 1]$-valued realizations of Boolean functions with respect to the structure functionality principle. The proposed generalization provides a drastic increase of the descriptive power of BNs. It allows the model to be used for gaining quantitative insight into the behavior of complex systems. For the purpose of this paper, we assumed that interpolative Boolean networks evolve in discrete time, although continuous time models can be generalized in the same way. Formally, in the IBN, the state of node x_i takes the value of its generalized Boolean polynomial whose arguments

are the states of node x_i predecessors in the previous time step:

$$x_i(t+1) = f_i^{\otimes}\left(x_{i_1}(t), \ldots, x_{i_{K_i}}(t)\right) = \sum_{\sigma_{f_i}(\alpha_S)=1 | S \in P(N)} \left(\bigotimes_{x_p \in S} x_p(t) \bigotimes_{x_q \in N \setminus S} \left(1 - x_q(t)\right) \right), \tag{15}$$

where $x_i(t+1) \in [0,1]$ and $f_i(x_{i_1}(t), \ldots, x_{i_{K_i}}(t)) \in \mathrm{BA}(N)$ are the state and the Boolean function of node $x_i \in N$, $x_{i_1}(t), \ldots, x_{i_{K_i}}(t) \in [0,1]$ are the states of node x_i predecessors in the previous time step, σ_{f_i} is the structure function of $f_i \in \mathrm{BA}(N)$, $x_i \otimes x_j : [0,1] \times [0,1] \to [0,1]$ is the generalized product, and K_i is the number of predecessors of the node x_i.

The state of node x_i can be defined as the scalar product of two vectors:

$$x_i(t+1) = \overrightarrow{\sigma}_{f_i} \overrightarrow{\alpha}(t), \tag{16}$$

where $\overrightarrow{\sigma}_{f_i}$ is the structure vector of $f_i \in \mathrm{BA}(N)$ and $\overrightarrow{\alpha}(t)$ is a vector of atomic Boolean polynomials of $\mathrm{BA}(N)$ at time t.

Dynamics of interpolative Boolean network is defined by the following equations:

$$\begin{bmatrix} x_1(t+1) \\ \vdots \\ x_m(t+1) \end{bmatrix} = \begin{bmatrix} f_1^{\otimes}\left(x_{1_1}(t), \ldots, x_{1_{K_1}}(t)\right) \\ \vdots \\ f_m^{\otimes}\left(x_{m_1}(t), \ldots, x_{m_{K_m}}(t)\right) \end{bmatrix} = \begin{bmatrix} \overrightarrow{\sigma}_{f_1} \overrightarrow{\alpha}(t) \\ \vdots \\ \overrightarrow{\sigma}_{f_m} \overrightarrow{\alpha}(t) \end{bmatrix}, \tag{17}$$

where $x(t+1) = [x_i(t+1) \mid i = 1, \ldots, m]^T$, $x(t+1) \in [0,1]^m$, is the state of IBN at time $t+1$ and m is the number of nodes.

The interpolative Boolean network evolves according to the principle of structure functionality. This secures the Boolean frame and the logical validity of the model's dynamics. The global dynamics is characterized by the existence of point, cycle, and/or chaotic attractors, with the corresponding basins of attraction. The behavior of IBN can be fundamentally different depending on which basin of attraction the initial states are located. If the initial state of each node is two-valued, IBN reduces to the classical model; that is, the structure functionality principle reduces to the truth functionality principle. IBN can be used for modeling complex systems which may or may not exhibit the threshold behavior.

The behavior of IBN depends on the way how generalized product operators are treated. The adequate generalized product operator for the two variables is determined with respect to the nature of the variables. Two logical variables $x_i(t) \in [0,1]$ and $x_j(t) \in [0,1]$ are of the same nature if they represent the same quality. If this is the case, the adequate generalized product operator is minimum function; that is, $x_i(t) \otimes x_j(t) = \min(x_i(t), x_j(t))$. If two variables are of the same nature, but negatively correlated, the Lukasiewicz operator is used; thus, $x_i(t) \otimes x_j(t) = \max(x_i(t) + x_j(t) - 1, 0)$. On the other hand, if two variables are not correlated, that is, these variables are of the different nature, the proper operator is ordinary product, and thus, $x_i(t) \otimes x_j(t) = x_i(t) \cdot x_j(t)$.

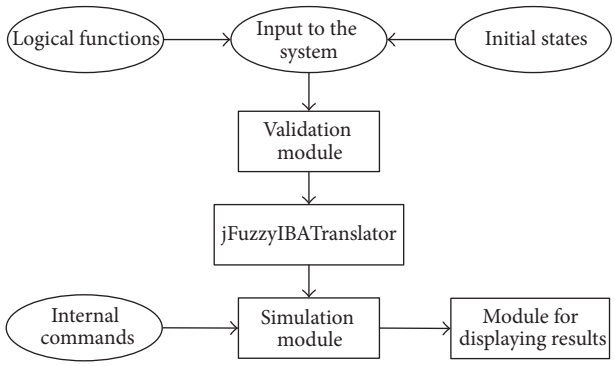

Figure 1: Software support tool architecture.

In IBN, different operators for generalized product can be used for any pair of variables. In this way, the nature of the variables can be fully taken into consideration. Comparing to the Boolecube/Hillcube approach, in which it is assumed that all variables are of the different nature, IBN offers more descriptive power. The Boolecube/Hillcube implicitly take into account the structure of elements; its Boolean indicator functions have the role of IBN structure vector, but the only ordinary product is applied as the t-norm. In other words, if each generalized product operator in IBN is treated as ordinary product, the proposed approach reduces to the Boolecube/Hillcube approach (see (4), (6), and (15)). Further, IBN utilize comprehensible and direct IBA transformation procedure from logical function to GBP given in (13), which provides an easier interpretation of the model.

4.1. Software Support. For the task of modeling and analysis of complex dynamical systems, the software tool implementing interpolative Boolean networks is developed. The architecture of the software is shown in Figure 1. The software is based on jFuzzyIBATranslator, the very first software realization of IBA, which can also process conventional fuzzy expressions [45]. jFuzzyIBATranslator is an application written in the Java programming language using NetBeans 6.9 development environment. The task of jFuzzyIBATranslator is to transform logical functions into corresponding generalized Boolean polynomials according to the transformation rules given in (13). Logical functions are validated (syntax validation, nested parentheses, etc.) and then forwarded to jFuzzyIBATranslator. The minimal GBPs are obtained after application of the distributivity law and the rule of idempotency. The developed software tool is covered by jUnit tests, a popular testing framework for Java [46], to verify software correctness.

The procedure for complex systems modeling and analysis using the software tool is the following. The input to the software is the number of nodes of IBN, where each node

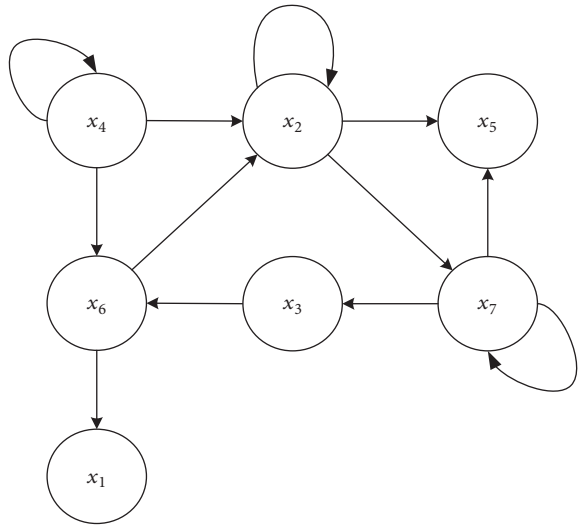

Figure 2: Structure of WNT5A gene regulatory network.

represents a system's component, and an initial state and a logical function for each node. The states take initial values from the unit interval. Logical functions are validated and transformed into GBPs. The nodes evolve in discrete time, governed by the GBPs. Since the initial states and the GBPs for each node are obtained, IBN can be simulated. The software tool predicts the future behavior of a complex system. After a number of iterations, an attractor is reached, while the dynamics of each node are presented in the graphical form. The software can be used for analysis of classical Boolean networks. In this case, it is sufficient to enter the binary initial states for each node.

5. Illustrative Examples

To illustrate the proposed approach, two classical BN models are taken from the literature as examples and generalized using IBA. The obtained IBN models are then simulated with the software tool presented in Section 4.1. Further, the obtained IBN results are compared to the results of conventional fuzzy BN and Boolecube approach.

5.1. Comparing the IBN Approach to the Conventional Fuzzy BN Approach. To compare the proposed IBN approach with the conventional fuzzy BN approach, the example of WNT5A gene regulatory network (Figure 2) is used. The WNT5A gene regulatory network is related to melanoma and thoroughly studied as BN in [47, 48]. First, the basic model is generalized to obtain both fuzzy BN and IBN models. Further, these real-valued networks are simulated using two t-norms: minimum and ordinary product. Finally, the obtained results are compared and discussed.

The basic WNT5A gene regulatory network dynamics is described with the following logical expressions [48]:

$$\begin{aligned}
x_1(t+1) &= \neg x_6(t)\\
x_2(t+1) &= \left(\neg x_2(t) \wedge x_4(t) \wedge x_6(t)\right)\\
&\quad \vee \left(x_2(t) \wedge \left(x_4(t) \vee x_6(t)\right)\right)\\
x_3(t+1) &= \neg x_7(t)\\
x_4(t+1) &= x_4(t)\\
x_5(t+1) &= x_2(t) \wedge \neg x_7(t)\\
x_6(t+1) &= x_3(t) \vee x_4(t)\\
x_7(t+1) &= \neg x_2(t) \vee x_7(t),
\end{aligned} \tag{18}$$

where $x(t+1) = [x_i(t+1) \mid i = 1, \ldots, 7]^T$, $x(t+1) \in \{0,1\}^7$.

The corresponding IBN model, presented in (A.1) of Appendix A, is obtained by mapping Boolean functions from (18) into the generalized Boolean polynomials. To translate the obtained GBPs, two operators of generalized product are used and their results are compared. In the first case scenario, a minimum function is used as an operator of generalized product; that is, $x_i \otimes x_j = \min(x_i, x_j)$, where $i, j = 1, \ldots, 7$. In the second case scenario, generalized product is replaced with an ordinary product, $x_i \otimes x_j = x_i \cdot x_j$, where $i, j = 1, \ldots, 7$. For both of selected operators, the proposed IBN model is reduced to the classical fuzzy network model and results are compared.

Case 1. In the first case scenario, we investigate the differences between IBN and classical fuzzy BN approach in the case of the Gödel (minimum) t-norm. The following equations (19) and (20) present, respectively, IBN and conventional fuzzy BN generalizations of the classical BN given in (18), obtained with minimum operator.

IBN model with minimum operator ($\otimes := \min$) for WNT5A gene regulation is defined with the following set of equations:

$$\begin{aligned}
x_1(t+1) &= 1 - x_6(t)\\
x_2(t+1) &= \min\left(x_4(t), x_6(t)\right) - 2\\
&\quad \cdot \min\left(x_2(t), x_4(t), x_6(t)\right)\\
&\quad + \min\left(x_2(t), x_4(t)\right)\\
&\quad + \min\left(x_2(t), x_6(t)\right)\\
x_3(t+1) &= 1 - x_7(t)\\
x_4(t+1) &= x_4(t)\\
x_5(t+1) &= x_2(t) - \min\left(x_2(t), x_7(t)\right)\\
x_6(t+1) &= x_3(t) + x_4(t) - \min\left(x_3(t), x_4(t)\right)\\
x_7(t+1) &= 1 - x_2(t) + \min\left(x_2(t), x_7(t)\right),
\end{aligned} \tag{19}$$

where $x(t) = [x_i(t) \mid i = 1, \ldots, 7]^T$ and $x(t) \in [0,1]^7$.

Table 1: Final state values for WNT5A gene regulation network nodes in IBN and fuzzy BN models obtained with minimum operator.

	x_1	x_2	x_3	x_4	x_5	x_6	x_7
Initial states	0	0.6	0	0.6	0	0	0
Final states (IBN)	0.4	0.6	**0**	0.6	**0**	0.6	**1**
Final states (fuzzy BN)	0.4	0.6	**0.6**	0.6	**0.6**	0.6	**0.4**

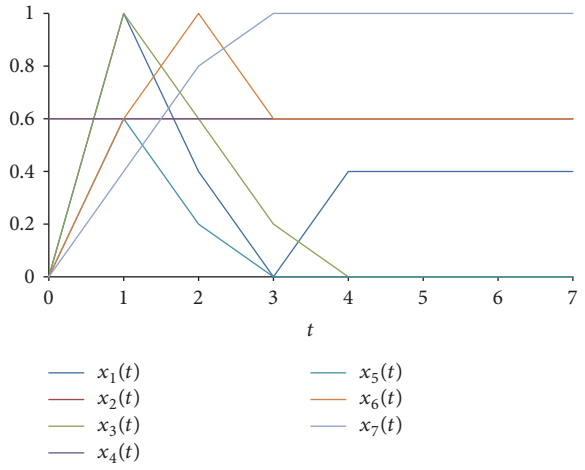

Figure 3: Dynamics of the IBN model for WNT5A gene regulation with initial state conditions $X(0) = [0; 0.6; 0; 0.6; 0; 0; 0]$ and minimum operator used as t-norm. The IBN model reaches the point attractor in 4th iteration $X(4) = [0.4; 0.6; 0; 0.6; 0; 0.6; 1]$.

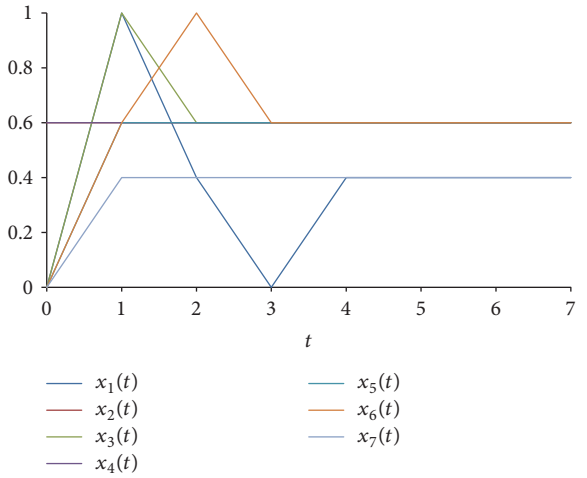

Figure 4: Dynamics of the fuzzy BN model for WNT5A gene regulation with initial state conditions $X(0) = [0; 0.6; 0; 0.6; 0; 0; 0]$ and minimum operator used as t-norm. The fuzzy BN model reaches the point attractor in 4th iteration $X(4) = [0.4; 0.6; 0.6; 0.6; 0.6; 0.6; 0.4]$.

The conventional fuzzy BN model with minimum operator for WNT5A gene regulation is defined with the following set of equations:

$$\begin{aligned}
x_1(t+1) &= 1 - x_6(t) \\
x_2(t+1) &= \max\left(\min\left(1 - x_2(t), x_4(t), x_6(t)\right),\right. \\
&\quad \left.\min\left(x_2(t), \max\left(x_4(t), x_6(t)\right)\right)\right) \\
x_3(t+1) &= 1 - x_7(t) \\
x_4(t+1) &= x_4(t) \\
x_5(t+1) &= \min\left(x_2(t), 1 - x_7(t)\right) \\
x_6(t+1) &= \max\left(x_3(t), x_4(t)\right) \\
x_7(t+1) &= \max\left(1 - x_2(t), x_7(t)\right).
\end{aligned} \tag{20}$$

Both IBN and fuzzy BN models are simulated for the same initial conditions. The obtained dynamics are presented in Figures 3 and 4.

The final results of the experiment are presented in Table 1.

Although the dynamics of the state variables are similar in two approaches, state variables $x_3(t)$, $x_5(t)$, and $x_7(t)$ reach significantly different point attractors in IBN model as compared with fuzzy BN model (values are bold in Table 1). These differences are due to inconsistency (in a Boolean sense) of the conventional fuzzy logic approach.

Case 2. In the second case scenario, we investigate the differences between IBN and classical fuzzy BN approach in the case of the ordinary product t-norm. The following equations (21) and (22) present, respectively, IBN and conventional fuzzy BN generalizations of the classical BN given in (18), obtained with product operator.

The IBN model with product operator ($\otimes := \cdot$) for WNT5A gene regulation is defined by the following set of equations:

$$\begin{aligned}
x_1(t+1) &= 1 - x_6(t) \\
x_2(t+1) &= x_4(t) \cdot x_6(t) - 2 \cdot x_2(t) \cdot x_4(t) \cdot x_6(t) \\
&\quad + x_2(t-1) \cdot x_4(t) + x_2(t) \cdot x_6(t) \\
x_3(t+1) &= 1 - x_7(t) \\
x_4(t+1) &= x_4(t) \\
x_5(t+1) &= x_2(t) - x_2(t) \cdot x_7(t) \\
x_6(t+1) &= x_3(t) + x_4(t) - x_3(t) \cdot x_4(t) \\
x_7(t+1) &= 1 - x_2(t) + x_2(t) \cdot x_7(t),
\end{aligned} \tag{21}$$

where $x(t) = [x_i(t) \mid i = 1, \ldots, 7]^T$ and $x(t) \in [0, 1]^7$.

Table 2: Final state values for WNT5A gene regulation network nodes in IBN and fuzzy BN models obtained with product operator.

	x_1	x_2	x_3	x_4	x_5	x_6	x_7
Initial states	0	0.6	0	0.6	0	0	0
Final states (IBN)	0.4	**0.69**	0	0.6	0	0.6	1
Final states (fuzzy BN)	0.4	**0.55**	0	0.6	0	0.6	1

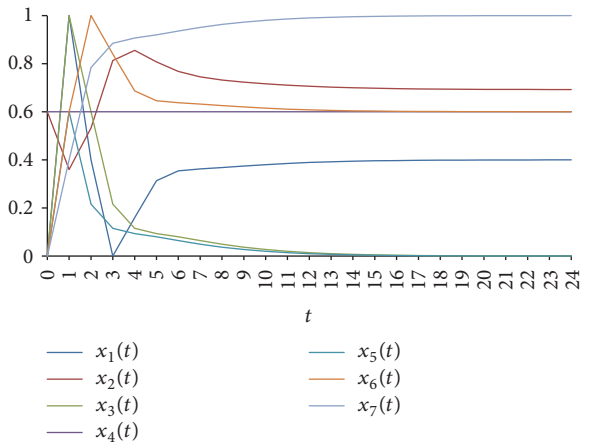

Figure 5: Dynamics of the IBN model for WNT5A gene regulation with initial state conditions $X(0) = [0; 0.6; 0; 0.6; 0; 0; 0]$ and product operator used as t-norm. The IBN model reaches the point attractor in 22nd iteration $X(22) = [0.4; 0.69; 0; 0.6; 0; 0.6; 1]$.

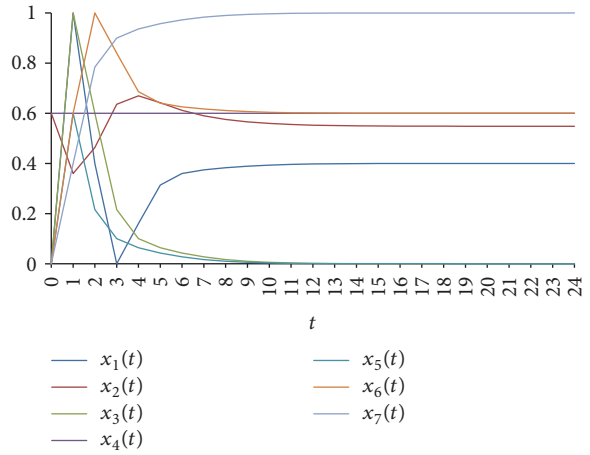

Figure 6: Dynamics of the fuzzy BN model for WNT5A gene regulation with initial state conditions $X(0) = [0; 0.6; 0; 0.6; 0; 0; 0]$ and product operator used as t-norm. The fuzzy BN model reaches the point attractor in 22nd iteration $X(22) = [0.4; 0.55; 0; 0.6; 0; 0.6; 1]$.

On the other hand, the conventional fuzzy BN model with the same product operator for WNT5A gene regulation is defined as

$$\begin{aligned}
x_1(t+1) &= 1 - x_6(t)\\
x_2(t+1) &= x_4(t)\cdot x_6(t) - 2\cdot x_2(t)\cdot x_4(t)\cdot x_6(t)\\
&\quad + x_2(t)\cdot x_4(t) + x_2(t)\cdot x_6(t) - \big((1 - x_2(t))\\
&\quad \cdot x_2(t)\cdot x_4(t)\cdot x_6(t)\\
&\quad \cdot \big(x_4(t) + x_6(t) - x_4(t)\cdot x_6(t)\big)\big)\\
x_3(t+1) &= 1 - x_7(t)\\
x_4(t+1) &= x_4(t)\\
x_5(t+1) &= x_2(t) - x_2(t)\cdot x_7(t)\\
x_6(t+1) &= x_3(t) + x_4(t) - x_3(t)\cdot x_4(t)\\
x_7(t+1) &= 1 - x_2(t) + x_2(t)\cdot x_7(t).
\end{aligned} \tag{22}$$

Notice that in this case the only difference between the two models is in the second equation. The Boolean function for state variable $x_2(t)$ from (18) is too complex to be generalized in the Boolean consistent way with the conventional fuzzy approach.

Models are simulated for the same initial conditions, and obtained dynamics are presented in Figures 5 and 6.

The final results of the experiment are presented in Table 2.

In this case scenario, the dynamics of the state variables of the two models are much more similar than in the previous case. There is only one state that significantly differs in the value of the point attractor reached, and it is $x_2(t)$. It is a direct consequence of the difference between IBN and fuzzy BN model for x_2 state space equations. However, this difference is important since it indicates inconsistency in the classical fuzzy BNs. It is also important to mention that the presented WNT5A gene regulation models based on product operator need more time to reach its point attractors comparing to the previous models based on minimum operator. This is due to the characteristics of the operator itself.

5.2. Comparing the IBN Approach to the Boolecube Approach. To compare the proposed IBN approach with the Boolecube approach, the example of modeling gene interaction is used. The starting point is the classical BN model used in [7] to describe interactions between the *Drosophila* segment polarity genes. The following equations specify its dynamic:

$$\mathrm{SLP}_i(t+1) = \begin{cases} 0, & i \in \{1,2\} \\ 1, & i \in \{3,4\} \end{cases}$$

$$\mathrm{wg}_i(t+1) = \big(\mathrm{CIA}_i(t) \wedge \mathrm{SLP}_i(t) \wedge \neg \mathrm{CIR}_i(t)\big)$$

Table 3: Final state values for *Drosophila* segment polarity genes model variables in IBN approach and Boolecube approach.

	SLP_i	wq_i	WG_i	en_i	EN_i	hh_i	HH_i	ptc_i	PTC_i	ci_i	CI_i	CIA_i	CIR_i
Initial states	0.5	0.7	0.7	0.7	0.7	0.7	0.7	0.7	0.7	0.7	0.7	0.7	0.7
Final states (IBN)	0.5	0	0	**0.35**	**0.35**	**0.12**	**0.12**	0	0	**0.65**	**0.65**	0	**0.65**
Final states (Boolecube)	0.5	0	0	**0.45**	**0.45**	**0.2**	**0.2**	0	0	**0.55**	**0.55**	0	**0.55**

$$\begin{aligned}
&\vee \left(wg_i\left(t\right) \wedge \left(CIA_i\left(t\right) \vee SLP_i\left(t\right)\right) \wedge \neg CIR_i\left(t\right)\right)\\
&WG_i\left(t+1\right) = wg_i\left(t\right)\\
&en_i\left(t+1\right) = \left(WG_{i-1}\left(t\right) \vee WG_{i+1}\left(t\right)\right) \wedge \neg SLP_i\left(t\right)\\
&EN_i\left(t+1\right) = en_i\left(t\right)\\
&hh_i\left(t+1\right) = EN_i\left(t\right) \wedge \neg CIR_i\left(t\right)\\
&HH_i\left(t+1\right) = hh_i\left(t\right)\\
&ptc_i\left(t+1\right) = CIA_i\left(t\right) \wedge \neg EN_i\left(t\right) \wedge \neg CIR_i\left(t\right)\\
&PTC_i\left(t+1\right) = ptc_i\left(t\right) \vee \left(PTC_i\left(t\right) \wedge \neg HH_{i-1}\left(t\right)\right.\\
&\quad \left.\wedge \neg HH_{i+1}\left(t\right)\right)\\
&ci_i\left(t+1\right) = \neg EN_i\left(t\right)\\
&CI_i\left(t+1\right) = ci_i\left(t\right)\\
&CIA_i\left(t+1\right) = CI_i\left(t\right) \wedge \left(\neg PTC_i\left(t\right) \vee HH_{i-1}\left(t\right)\right.\\
&\quad \left.\vee HH_{i+1}\left(t\right) \vee hh_{i-1}\left(t\right) \vee hh_{i+1}\left(t\right)\right)\\
&CIR_i\left(t+1\right) = CI_i\left(t\right) \wedge PTC_i\left(t\right) \wedge \neg HH_{i-1}\left(t\right)\\
&\quad \wedge \neg HH_{i+1}\left(t\right) \wedge \neg hh_{i-1}\left(t\right) \wedge \neg hh_{i+1}\left(t\right),
\end{aligned} \tag{23}$$

where $(t) = [SLP_i(t), wg_i(t), WG_i(t), en_i(t), EN_i(t), hh_i(t), HH_i(t), ptc_i(t), PTC_i(t), ci_i(t), CI_i(t), CIA_i(t), CIR_i(t)]^T$ is the network state at time t, and $x(t) \in \{0,1\}^{13}$.

The IBN model, presented in (B.1) of Appendix B, is obtained by mapping the Boolean functions into generalized Boolean polynomials. Operators of generalized product in this model are treated in the following way. Since the variables $WG_{i-1}(t)$ and $WG_{i+1}(t)$, $HH_{i-1}(t)$ and $HH_{i+1}(t)$, $hh_{i-1}(t)$ and $hh_{i+1}(t)$ are of the same nature, the adequate generalized product operator for these pairs of variables is minimum function. Thus,

$$\begin{aligned}
&WG_{i-1}\left(t\right) \otimes WG_{i+1}\left(t\right)\\
&\quad = \min\left(WG_{i-1}\left(t\right), WG_{i+1}\left(t\right)\right),\\
&HH_{i-1}\left(t\right) \otimes HH_{i+1}\left(t\right) = \min\left(HH_{i-1}\left(t\right), HH_{i+1}\left(t\right)\right),\\
&hh_{i-1}\left(t\right) \otimes hh_{i+1}\left(t\right) = \min\left(hh_{i-1}\left(t\right), hh_{i+1}\left(t\right)\right).
\end{aligned} \tag{24}$$

The remaining variables are of different nature and, therefore, the adequate operator of generalized product is the ordinary product. The final IBN model is presented in (B.2) of Appendix B.

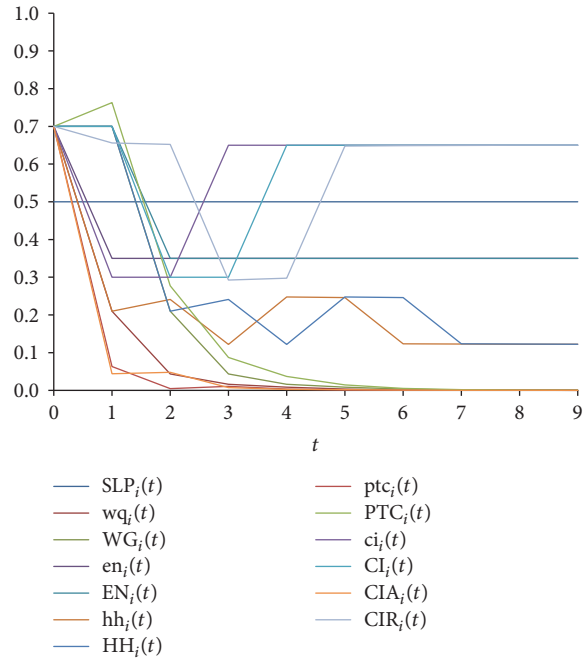

Figure 7: Dynamics of the IBN model of *Drosophila* segment polarity genes interactions with initial state conditions $X(0) = [0.5; 0.7; 0.7; 0.7; 0.7; 0.7; 0.7; 0.7; 0.7; 0.7; 0.7; 0.7; 0.7]$. The IBN model reaches the point attractor in 7th iteration $X(7) = [0.5; 0; 0; 0.35; 0.35; 0.12; 0.12; 0; 0; 0.65; 0.65; 0; 0.65]$.

On the other hand, in the Boolecube/Hillcube approach, each generalized product in (B.1) is replaced with an ordinary product. The final Boolecube/Hillcube model is presented in (B.3).

Both IBN and Boolecube/Hillcube models are simulated using the following initial conditions $(0) = [0.5, 0.7, 0.7, 0.7, 0.7, 0.7, 0.7, 0.7, 0.7, 0.7, 0.7, 0.7, 0.7]$. The obtained models' dynamics are presented in Figures 7 and 8.

The final results of the experiment are presented in Table 3.

It is easy to see differences in IBN and Boolecube models dynamics and their point attractors reached. This difference is a direct consequence of the nature of the model variables that is taken into account when selecting an appropriate operator in the IBN approach, unlike the Boolecube/Hillcube approach. For this reason, the IBN offers superior descriptive power and it is adaptive with respect to nature of inputs. In fact, the IBN approach can be considered as the generalization of the Boolecube/Hillcube approach since it can be reduced to it when only the product t-norm is used as an operator of the generalized product.

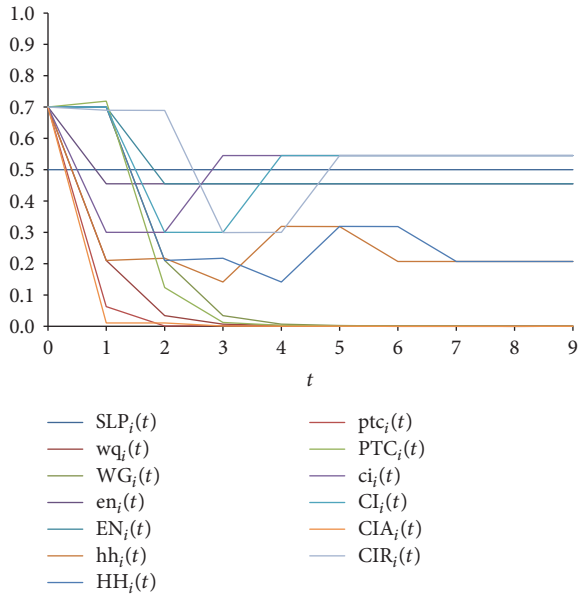

FIGURE 8: Dynamics of the Boolecube model of *Drosophila* segment polarity genes interactions with initial state conditions $X(0) = [0.5; 0.7; 0.7; 0.7; 0.7; 0.7; 0.7; 0.7; 0.7; 0.7; 0.7; 0.7; 0.7]$. The Boolecube model reaches the point attractor in 7th iteration $X(7) = [0.5; 0; 0; 0.45; 0.45; 0.2; 0.2; 0; 0; 0.55; 0.55; 0; 0.55]$.

6. Conclusion

Logical approaches are widely used for modeling and analysis of complex dynamical systems. Classical models are within the Boolean frame, which secures the validity of their dynamics. Such models are adequate for modeling system which exhibit threshold behavior. If more detail is required, the Boolean networks should be generalized to include real-valued case.

In this paper, interpolative Boolean networks are proposed. They are based on interpolative Boolean algebra and represent a Boolean consistent real-valued generalization of classical Boolean networks. The validity of their dynamics is secured thanks to the principle of structure functionality. Furthermore, the proposed approach is a generalization of the current state-of-the-art approaches (e.g., Boolecube/Hillcube) and offers a guideline for the appropriate realization of generalized product. Also, IBN utilizes comprehensible and direct IBA transformation procedure from logical function to GBP.

Interpolative Boolean networks can be used to predict behavior of complex systems. For the purpose of their practical application, a simple software support tool is developed. The proposed approach is applied on two examples from the literature and compared against other real-valued logical approaches. Interpolative Boolean networks offer superior descriptive power compared to other approaches. This approach facilitates modeling and analysis of systems too complex for quantitative mathematical approaches.

Appendix

A. WNT5A Gene Regulatory Network Realized Using IBN

The WNT5A gene regulatory network realized as IBN is defined by the following equations:

$$\begin{aligned}
x_1(t+1) &= 1 - x_6(t)\\
x_2(t+1) &= x_4(t) \otimes x_6(t) - 2x_2(t) \otimes x_4(t) \otimes x_6(t)\\
&\quad + x_2(t) \otimes x_4(t) + x_2(t) \otimes x_6(t)\\
x_3(t+1) &= 1 - x_7(t)\\
x_4(t+1) &= x_4(t)\\
x_5(t+1) &= x_2(t) - x_2(t) \otimes x_7(t)\\
x_6(t+1) &= x_3(t) + x_4(t) - x_3(t) \otimes x_4(t)\\
x_7(t+1) &= 1 - x_2(t) + x_2(t) \otimes x_7(t),
\end{aligned} \tag{A.1}$$

where $x(t) = [x_i(t) \mid i = 1, \ldots, 7]^T$ and $x(t) \in [0, 1]^7$.

B. *Drosophila* Segment Polarity Genes Regulatory Network Realized Using IBN

The *Drosophila* segment polarity genes network realized as IBN is defined by the following equations:

$$\begin{aligned}
&\text{SLP}_i(t+1) = \text{SLP}_i(t)\\
&\text{wg}_i(t+1) = \left(\text{CIA}_i(t) \wedge \text{SLP}_i(t) \wedge \neg\text{CIR}_i(t)\right)\\
&\quad \vee \left(\text{wg}_i(t) \wedge \left(\text{CIA}_i(t) \vee \text{SLP}_i(t)\right) \wedge \neg\text{CIR}_i(t)\right)\\
&\quad = \text{CIA}_i(t) \otimes \text{SLP}_i(t) - \text{CIA}_i(t) \otimes \text{SLP}_i(t)\\
&\quad \otimes \text{CIR}_i(t) + \text{CIA}_i(t) \otimes \text{wg}_i(t) + \text{SLP}_i(t) \otimes \text{wg}_i(t)\\
&\quad - 2 * \text{CIA}_i(t) \otimes \text{SLP}_i(t) \otimes \text{wg}_i(t) - \text{CIA}_i(t)\\
&\quad \otimes \text{CIR}_i(t) \otimes \text{wg}_i(t) - \text{CIA}_i(t) \otimes \text{CIR}_i(t) \otimes \text{wg}_i(t)\\
&\quad + 2 * \text{CIA}_i(t) \otimes \text{SLP}_i(t) \otimes \text{CIR}_i(t) \otimes \text{wg}_i(t)\\
&\text{WG}_i(t+1) = \text{wg}_i(t)\\
&\text{en}_i(t+1) = \left(\text{WG}_{i-1}(t) \vee \text{WG}_{i+1}(t)\right) \wedge \neg\text{SLP}_i(t)\\
&\quad = \text{WG}_{i-1}(t) + \text{WG}_{i+1}(t) - \text{WG}_{i-1}(t) \otimes \text{WG}_{i+1}(t)\\
&\quad - \text{WG}_{i-1}(t) \otimes \text{SLP}_i(t) - \text{WG}_{i+1}(t) \otimes \text{SLP}_i(t)\\
&\quad + \text{WG}_{i-1}(t) \otimes \text{WG}_{i+1}(t) \otimes \text{SLP}_i(t)\\
&\text{EN}_i(t+1) = \text{en}_i(t)\\
&\text{hh}_i(t+1) = \text{EN}_i(t) \wedge \neg\text{CIR}_i(t) = \text{EN}_i(t) - \text{EN}_i(t)\\
&\quad \otimes \text{CIR}_i(t)\\
&\text{HH}_i(t+1) = \text{hh}_i(t)
\end{aligned}$$

$$
\begin{aligned}
\mathrm{ptc}_i(t+1) &= \mathrm{CIA}_i(t) \wedge \neg \mathrm{EN}_i(t) \wedge \neg \mathrm{CIR}_i(t) \\
&= \mathrm{CIA}_i(t) - \mathrm{CIA}_i(t) \otimes \mathrm{EN}_i(t) - \mathrm{CIA}_i(t) \\
&\otimes \mathrm{CIR}_i(t) + \mathrm{CIA}_i(t) \otimes \mathrm{EN}_i(t) \otimes \mathrm{CIR}_i(t) \\
\mathrm{PTC}_i(t+1) &= \mathrm{ptc}_i(t) \vee \left(\mathrm{PTC}_i(t) \wedge \neg \mathrm{HH}_{i-1}(t)\right. \\
&\left. \wedge \neg \mathrm{HH}_{i+1}(t)\right) = \mathrm{ptc}_i(t) + \mathrm{PTC}_i(t) - \mathrm{PTC}_i(t) \\
&\otimes \mathrm{HH}_{i-1}(t) - \mathrm{PTC}_i(t) \otimes \mathrm{HH}_{i+1}(t) + \mathrm{PTC}_i(t) \\
&\otimes \mathrm{HH}_{i-1}(t) \otimes \mathrm{HH}_{i+1}(t) - \mathrm{ptc}_i(t) \otimes \mathrm{PTC}_i(t) \\
&+ \mathrm{ptc}_i(t) \otimes \mathrm{PTC}_i(t) \otimes \mathrm{HH}_{i-1}(t) + \mathrm{ptc}_i(t) \\
&\otimes \mathrm{PTC}_i(t) \otimes \mathrm{HH}_{i+1}(t) - \mathrm{ptc}_i(t) \otimes \mathrm{PTC}_i(t) \\
&\otimes \mathrm{HH}_{i-1}(t) \otimes \mathrm{HH}_{i+1}(t) \\
\mathrm{ci}_i(t+1) &= \neg \mathrm{EN}_i(t) = 1 - \mathrm{EN}_i(t) \\
\mathrm{CI}_i(t+1) &= \mathrm{ci}_i(t) \\
\mathrm{CIA}_i(t+1) &= \mathrm{CI}_i(t) \wedge \left(\neg \mathrm{PTC}_i(t) \vee \mathrm{HH}_{i-1}(t)\right. \\
&\left. \vee \mathrm{HH}_{i+1}(t) \vee \mathrm{hh}_{i-1}(t) \vee \mathrm{hh}_{i+1}(t)\right) = \mathrm{CI}_i(t) \\
&- \mathrm{CI}_i(t) \otimes \mathrm{PTC}_i(t) + \mathrm{CI}_i(t) \otimes \mathrm{PTC}_i(t) \\
&\otimes \mathrm{HH}_{i-1}(t) + \mathrm{CI}_i(t) \otimes \mathrm{PTC}_i(t) \otimes \mathrm{HH}_{i+1}(t) \\
&+ \mathrm{CI}_i(t) \otimes \mathrm{PTC}_i(t) \otimes \mathrm{hh}_{i-1}(t) + \mathrm{CI}_i(t) \\
&\otimes \mathrm{PTC}_i(t) \otimes \mathrm{hh}_{i+1}(t) - \mathrm{CI}_i(t) \otimes \mathrm{PTC}_i(t) \\
&\otimes \mathrm{HH}_{i-1}(t) \otimes \mathrm{HH}_{i+1}(t) - \mathrm{CI}_i(t) \otimes \mathrm{PTC}_i(t) \\
&\otimes \mathrm{HH}_{i-1}(t) \otimes \mathrm{hh}_{i-1}(t) - \mathrm{CI}_i(t) \otimes \mathrm{PTC}_i(t) \\
&\otimes \mathrm{HH}_{i-1}(t) \otimes \mathrm{hh}_{i+1}(t) - \mathrm{CI}_i(t) \otimes \mathrm{PTC}_i(t) \\
&\otimes \mathrm{HH}_{i+1}(t) \otimes \mathrm{hh}_{i-1}(t) - \mathrm{CI}_i(t) \otimes \mathrm{PTC}_i(t) \\
&\otimes \mathrm{HH}_{i+1}(t) \otimes \mathrm{hh}_{i+1}(t) - \mathrm{CI}_i(t) \otimes \mathrm{PTC}_i(t) \\
&\otimes \mathrm{hh}_{i-1}(t) \otimes \mathrm{hh}_{i+1}(t) + \mathrm{CI}_i(t) \otimes \mathrm{PTC}_i(t) \\
&\otimes \mathrm{HH}_{i-1}(t) \otimes \mathrm{HH}_{i+1}(t) \otimes \mathrm{hh}_{i-1}(t) + \mathrm{CI}_i(t) \\
&\otimes \mathrm{PTC}_i(t) \otimes \mathrm{HH}_{i-1}(t) \otimes \mathrm{HH}_{i+1}(t) \otimes \mathrm{hh}_{i+1}(t) \\
&+ \mathrm{CI}_i(t) \otimes \mathrm{PTC}_i(t) \otimes \mathrm{HH}_{i-1}(t) \otimes \mathrm{hh}_{i-1}(t) \\
&\otimes \mathrm{hh}_{i+1}(t) + \mathrm{CI}_i(t) \otimes \mathrm{PTC}_i(t) \otimes \mathrm{HH}_{i+1}(t) \\
&\otimes \mathrm{hh}_{i-1}(t) \otimes \mathrm{hh}_{i+1}(t) - \mathrm{CI}_i(t) \otimes \mathrm{PTC}_i(t) \\
&\otimes \mathrm{HH}_{i-1}(t) \otimes \mathrm{HH}_{i+1}(t) \otimes \mathrm{hh}_{i-1}(t) \otimes \mathrm{hh}_{i+1}(t) \\
\mathrm{CIR}_i(t+1) &= \mathrm{CI}_i(t) \wedge \mathrm{PTC}_i(t) \wedge \neg \mathrm{HH}_{i-1}(t) \\
&\wedge \neg \mathrm{HH}_{i+1}(t) \wedge \neg \mathrm{hh}_{i-1}(t) \wedge \neg \mathrm{hh}_{i+1}(t) = \mathrm{CI}_i(t) \\
&\otimes \mathrm{PTC}_i(t) - \mathrm{CI}_i(t) \otimes \mathrm{PTC}_i(t) \otimes \mathrm{HH}_{i-1}(t) \\
&- \mathrm{CI}_i(t) \otimes \mathrm{PTC}_i(t) \otimes \mathrm{HH}_{i+1}(t) - \mathrm{CI}_i(t) \\
&\otimes \mathrm{PTC}_i(t) \otimes \mathrm{hh}_{i-1}(t) - \mathrm{CI}_i(t) \otimes \mathrm{PTC}_i(t) \\
&\otimes \mathrm{hh}_{i+1}(t) + \mathrm{CI}_i(t) \otimes \mathrm{PTC}_i(t) \otimes \mathrm{HH}_{i-1}(t) \\
&\otimes \mathrm{HH}_{i+1}(t) + \mathrm{CI}_i(t) \otimes \mathrm{PTC}_i(t) \otimes \mathrm{HH}_{i-1}(t) \\
&\otimes \mathrm{hh}_{i-1}(t) + \mathrm{CI}_i(t) \otimes \mathrm{PTC}_i(t) \otimes \mathrm{HH}_{i-1}(t) \\
&\otimes \mathrm{hh}_{i-1}(t) + \mathrm{CI}_i(t) \otimes \mathrm{PTC}_i(t) \otimes \mathrm{HH}_{i+1}(t) \\
&\otimes \mathrm{hh}_{i-1}(t) + \mathrm{CI}_i(t) \otimes \mathrm{PTC}_i(t) \otimes \mathrm{HH}_{i+1}(t) \\
&\otimes \mathrm{hh}_{i+1}(t) + \mathrm{CI}_i(t) \otimes \mathrm{PTC}_i(t) \otimes \mathrm{hh}_{i-1}(t) \\
&\otimes \mathrm{hh}_{i+1}(t) - \mathrm{CI}_i(t) \otimes \mathrm{PTC}_i(t) \otimes \mathrm{HH}_{i-1}(t) \\
&\otimes \mathrm{HH}_{i+1}(t) \otimes \mathrm{hh}_{i-1}(t) - \mathrm{CI}_i(t) \otimes \mathrm{PTC}_i(t) \\
&\otimes \mathrm{HH}_{i-1}(t) \otimes \mathrm{HH}_{i+1}(t) \otimes \mathrm{hh}_{i+1}(t) - \mathrm{CI}_i(t) \\
&\otimes \mathrm{PTC}_i(t) \otimes \mathrm{HH}_{i-1}(t) \otimes \mathrm{hh}_{i-1}(t) \otimes \mathrm{hh}_{i+1}(t) \\
&- \mathrm{CI}_i(t) \otimes \mathrm{PTC}_i(t) \otimes \mathrm{HH}_{i+1}(t) \otimes \mathrm{hh}_{i-1}(t) \\
&\otimes \mathrm{hh}_{i+1}(t) + \mathrm{CI}_i(t) \otimes \mathrm{PTC}_i(t) \otimes \mathrm{HH}_{i-1}(t) \\
&\otimes \mathrm{HH}_{i+1}(t) \otimes \mathrm{hh}_{i-1}(t) \otimes \mathrm{hh}_{i+1}(t),
\end{aligned}
\tag{B.1}
$$

where $x(t) = [\mathrm{SLP}_i(t), \mathrm{wg}_i(t), \mathrm{WG}_i(t), \mathrm{en}_i(t), \mathrm{EN}_i(t), \mathrm{hh}_i(t), \mathrm{HH}_i(t), \mathrm{ptc}_i(t), \mathrm{PTC}_i(t), \mathrm{ci}_i(t), \mathrm{CI}_i(t), \mathrm{CIA}_i(t), \mathrm{CIR}_i(t)]^T$ is the network state at time t, and $x(t) \in [0,1]^{13}$.

Taking into account the nature of the variables, this IBN is realized as follows:

$$
\begin{aligned}
\mathrm{SLP}_i(t+1) &= \mathrm{SLP}_i(t) \\
\mathrm{wg}_i(t+1) &= \left(\mathrm{CIA}_i(t) \wedge \mathrm{SLP}_i(t) \wedge \neg \mathrm{CIR}_i(t)\right) \\
&\vee \left(\mathrm{wg}_i(t) \wedge \left(\mathrm{CIA}_i(t) \vee \mathrm{SLP}_i(t)\right) \wedge \neg \mathrm{CIR}_i(t)\right) \\
&= \mathrm{CIA}_i(t) * \mathrm{SLP}_i(t) - \mathrm{CIA}_i(t) * \mathrm{SLP}_i(t) \\
&* \mathrm{CIR}_i(t) + \mathrm{CIA}_i(t) * \mathrm{wg}_i(t) + \mathrm{SLP}_i(t) * \mathrm{wg}_i(t) \\
&- 2 * \mathrm{CIA}_i(t) * \mathrm{SLP}_i(t) * \mathrm{wg}_i(t) - \mathrm{CIA}_i(t) \\
&* \mathrm{CIR}_i(t) * \mathrm{wg}_i(t) - \mathrm{CIA}_i(t) * \mathrm{CIR}_i(t) \\
&* \mathrm{wg}_i(t) + 2 * \mathrm{CIA}_i(t) * \mathrm{SLP}_i(t) * \mathrm{CIR}_i(t) \\
&* \mathrm{wg}_i(t) \\
\mathrm{WG}_i(t+1) &= \mathrm{wg}_i(t) \\
\mathrm{en}_i(t+1) &= \left(\mathrm{WG}_{i-1}(t) \vee \mathrm{WG}_{i+1}(t)\right) \wedge \neg \mathrm{SLP}_i(t) \\
&= \mathrm{WG}_{i-1}(t) + \mathrm{WG}_{i+1}(t) \\
&- \min\left(\mathrm{WG}_{i-1}(t), \mathrm{WG}_{i+1}(t)\right) - \mathrm{WG}_{i-1}(t) \\
&* \mathrm{SLP}_i(t) - \mathrm{WG}_{i+1}(t) * \mathrm{SLP}_i(t) \\
&+ \min\left(\mathrm{WG}_{i-1}(t), \mathrm{WG}_{i+1}(t)\right) * \mathrm{SLP}_i(t) \\
\mathrm{EN}_i(t+1) &= \mathrm{en}_i(t) \\
\mathrm{hh}_i(t+1) &= \mathrm{EN}_i(t) \wedge \neg \mathrm{CIR}_i(t) = \mathrm{EN}_i(t) - \mathrm{EN}_i(t)
\end{aligned}
$$

$$
\begin{aligned}
&* \mathrm{CIR}_i(t)\\
&\mathrm{HH}_i(t+1) = \mathrm{hh}_i(t)\\
&\mathrm{ptc}_i(t+1) = \mathrm{CIA}_i(t) \wedge \neg \mathrm{EN}_i(t) \wedge \neg \mathrm{CIR}_i(t)\\
&= \mathrm{CIA}_i(t) - \mathrm{CIA}_i(t) * \mathrm{EN}_i(t) - \mathrm{CIA}_i(t)\\
&* \mathrm{CIA}_i(t) + \mathrm{CIA}_i(t) * \mathrm{EN}_i(t) * \mathrm{CIR}_i(t)\\
&\mathrm{PTC}_i(t+1) = \mathrm{ptc}_i(t) \vee \left(\mathrm{PTC}_i(t) \wedge \neg \mathrm{HH}_{i-1}(t)\right.\\
&\left.\wedge \neg \mathrm{HH}_{i+1}(t)\right) = \mathrm{ptc}_i(t) + \mathrm{PTC}_i(t) - \mathrm{PTC}_i(t)\\
&* \mathrm{HH}_{i-1}(t) - \mathrm{PTC}_i(t) * \mathrm{HH}_{i+1}(t) + \mathrm{PTC}_i(t)\\
&* \min\left(\mathrm{HH}_{i-1}(t), \mathrm{HH}_{i+1}(t)\right) - \mathrm{ptc}_i(t) * \mathrm{PTC}_i(t)\\
&+ \mathrm{ptc}_i(t) * \mathrm{PTC}_i(t) * \mathrm{HH}_{i-1}(t) + \mathrm{ptc}_i(t)\\
&* \mathrm{PTC}_i(t) * \mathrm{HH}_{i+1}(t) - \mathrm{ptc}_i(t) * \mathrm{PTC}_i(t)\\
&* \min\left(\mathrm{HH}_{i-1}(t), \mathrm{HH}_{i+1}(t)\right)\\
&\mathrm{ci}_i(t+1) = \neg \mathrm{EN}_i(t) = 1 - \mathrm{EN}_i(t)\\
&\mathrm{CI}_i(t+1) = \mathrm{ci}_i(t)\\
&\mathrm{CIA}_i(t+1) = \mathrm{CI}_i(t) \wedge \left(\neg \mathrm{PTC}_i(t) \vee \mathrm{HH}_{i-1}(t)\right.\\
&\left.\vee \mathrm{HH}_{i+1}(t) \vee \mathrm{hh}_{i-1}(t) \vee \mathrm{hh}_{i+1}(t)\right) = \mathrm{CI}_i(t)\\
&- \mathrm{CI}_i(t) * \mathrm{PTC}_i(t) + \mathrm{CI}_i(t) * \mathrm{PTC}_i(t)\\
&* \mathrm{HH}_{i-1}(t) + \mathrm{CI}_i(t) * \mathrm{PTC}_i(t) * \mathrm{HH}_{i+1}(t)\\
&+ \mathrm{CI}_i(t) * \mathrm{PTC}_i(t) * \mathrm{hh}_{i-1}(t) + \mathrm{CI}_i(t)\\
&* \mathrm{PTC}_i(t) * \mathrm{hh}_{i+1}(t) - \mathrm{CI}_i(t) * \mathrm{PTC}_i(t)\\
&* \min\left(\mathrm{HH}_{i-1}(t), \mathrm{HH}_{i+1}(t)\right) - \mathrm{CI}_i(t) * \mathrm{PTC}_i(t)\\
&* \mathrm{HH}_{i-1}(t) * \mathrm{hh}_{i-1}(t) - \mathrm{CI}_i(t) * \mathrm{PTC}_i(t)\\
&* \mathrm{HH}_{i-1}(t) * \mathrm{hh}_{i+1}(t) - \mathrm{CI}_i(t) * \mathrm{PTC}_i(t)\\
&* \mathrm{HH}_{i+1}(t) * \mathrm{hh}_{i-1}(t) - \mathrm{CI}_i(t) * \mathrm{PTC}_i(t)\\
&* \mathrm{HH}_{i+1}(t) * \mathrm{hh}_{i+1}(t) - \mathrm{CI}_i(t) * \mathrm{PTC}_i(t)\\
&* \min\left(\mathrm{hh}_{i-1}(t), \mathrm{hh}_{i+1}(t)\right) + \mathrm{CI}_i(t) * \mathrm{PTC}_i(t)\\
&* \min\left(\mathrm{HH}_{i-1}(t), \mathrm{HH}_{i+1}(t)\right) * \mathrm{hh}_{i-1}(t) + \mathrm{CI}_i(t)\\
&* \mathrm{PTC}_i(t) * \min\left(\mathrm{HH}_{i-1}(t), \mathrm{HH}_{i+1}(t)\right)\\
&* \mathrm{hh}_{i+1}(t) + \mathrm{CI}_i(t) * \mathrm{PTC}_i(t) * \mathrm{HH}_{i-1}(t)\\
&* \min\left(\mathrm{hh}_{i-1}(t), \mathrm{hh}_{i+1}(t)\right) + \mathrm{CI}_i(t) * \mathrm{PTC}_i(t)\\
&* \mathrm{HH}_{i+1}(t) * \min\left(\mathrm{hh}_{i-1}(t), \mathrm{hh}_{i+1}(t)\right) - \mathrm{CI}_i(t)\\
&* \mathrm{PTC}_i(t) * \min\left(\mathrm{HH}_{i-1}(t), \mathrm{HH}_{i+1}(t)\right)\\
&* \min\left(\mathrm{hh}_{i-1}(t), \mathrm{hh}_{i+1}(t)\right)\\
&\mathrm{CIR}_i(t+1) = \mathrm{CI}_i(t) \wedge \mathrm{PTC}_i(t) \wedge \neg \mathrm{HH}_{i-1}(t)\\
&\wedge \neg \mathrm{HH}_{i+1}(t) \wedge \neg \mathrm{hh}_{i-1}(t) \wedge \neg \mathrm{hh}_{i+1}(t) = \mathrm{CI}_i(t)\\
&* \mathrm{PTC}_i(t) - \mathrm{CI}_i(t) * \mathrm{PTC}_i(t) * \mathrm{HH}_{i-1}(t)\\
&- \mathrm{CI}_i(t) * \mathrm{PTC}_i(t) * \mathrm{HH}_{i+1}(t) - \mathrm{CI}_i(t)\\
&* \mathrm{PTC}_i(t) * \mathrm{hh}_{i-1}(t) - \mathrm{CI}_i(t) * \mathrm{PTC}_i(t)\\
&* \mathrm{hh}_{i+1}(t) + \mathrm{CI}_i(t) * \mathrm{PTC}_i(t)\\
&* \min\left(\mathrm{HH}_{i-1}(t), \mathrm{HH}_{i+1}(t)\right) + \mathrm{CI}_i(t) * \mathrm{PTC}_i(t)\\
&* \mathrm{HH}_{i-1}(t) * \mathrm{hh}_{i-1}(t) + \mathrm{CI}_i(t) * \mathrm{PTC}_i(t)\\
&* \mathrm{HH}_{i-1}(t) * \mathrm{hh}_{i-1}(t) + \mathrm{CI}_i(t) * \mathrm{PTC}_i(t)\\
&* \mathrm{HH}_{i+1}(t) * \mathrm{hh}_{i-1}(t) + \mathrm{CI}_i(t) * \mathrm{PTC}_i(t)\\
&* \mathrm{HH}_{i+1}(t) * \mathrm{hh}_{i+1}(t) + \mathrm{CI}_i(t) * \mathrm{PTC}_i(t)\\
&* \min\left(\mathrm{hh}_{i-1}(t), \mathrm{hh}_{i+1}(t)\right) - \mathrm{CI}_i(t) * \mathrm{PTC}_i(t)\\
&* \min\left(\mathrm{HH}_{i-1}(t), \mathrm{HH}_{i+1}(t)\right) * \mathrm{hh}_{i-1}(t) - \mathrm{CI}_i(t)\\
&* \mathrm{PTC}_i(t) * \min\left(\mathrm{HH}_{i-1}(t), \mathrm{HH}_{i+1}(t)\right)\\
&* \mathrm{hh}_{i+1}(t) - \mathrm{CI}_i(t) * \mathrm{PTC}_i(t) * \mathrm{HH}_{i-1}(t)\\
&* \min\left(\mathrm{hh}_{i-1}(t), \mathrm{hh}_{i+1}(t)\right) - \mathrm{CI}_i(t) * \mathrm{PTC}_i(t)\\
&* \mathrm{HH}_{i+1}(t) * \min\left(\mathrm{hh}_{i-1}(t), \mathrm{hh}_{i+1}(t)\right) + \mathrm{CI}_i(t)\\
&* \mathrm{PTC}_i(t) * \min\left(\mathrm{HH}_{i-1}(t), \mathrm{HH}_{i+1}(t)\right)\\
&* \min\left(\mathrm{hh}_{i-1}(t), \mathrm{hh}_{i+1}(t)\right),
\end{aligned}
\tag{B.2}
$$

where $x(t) = [\mathrm{SLP}_i(t), \mathrm{wg}_i(t), \mathrm{WG}_i(t), \mathrm{en}_i(t), \mathrm{EN}_i(t), \mathrm{hh}_i(t), \mathrm{HH}_i(t), \mathrm{ptc}_i(t), \mathrm{PTC}_i(t), \mathrm{ci}_i(t), \mathrm{CI}_i(t), \mathrm{CIA}_i(t), \mathrm{CIR}_i(t)]^T$ is the network state at time t, and $x(t) \in [0,1]$[13].

The final Boolecube model of the *Drosophila* segment polarity genes network is defined by the following equations:

$$
\begin{aligned}
&\mathrm{SLP}_i(t+1) = \mathrm{SLP}_i(t)\\
&\mathrm{wg}_i(t+1) = \left(\mathrm{CIA}_i(t) \wedge \mathrm{SLP}_i(t) \wedge \neg \mathrm{CIR}_i(t)\right)\\
&\vee \left(\mathrm{wg}_i(t) \wedge \left(\mathrm{CIA}_i(t) \vee \mathrm{SLP}_i(t)\right) \wedge \neg \mathrm{CIR}_i(t)\right)\\
&= \mathrm{CIA}_i(t) * \mathrm{SLP}_i(t) - \mathrm{CIA}_i(t) * \mathrm{SLP}_i(t)\\
&* \mathrm{CIR}_i(t) + \mathrm{CIA}_i(t) * \mathrm{wg}_i(t) + \mathrm{SLP}_i(t) * \mathrm{wg}_i(t)\\
&- 2 * \mathrm{CIA}_i(t) * \mathrm{SLP}_i(t) * \mathrm{wg}_i(t) - \mathrm{CIA}_i(t)\\
&* \mathrm{CIR}_i(t) * \mathrm{wg}_i(t) - \mathrm{CIA}_i(t) * \mathrm{CIR}_i(t) * \mathrm{wg}_i(t)\\
&+ 2 * \mathrm{CIA}_i(t) * \mathrm{SLP}_i(t) * \mathrm{CIR}_i(t) * \mathrm{wg}_i(t)\\
&\mathrm{WG}_i(t+1) = \mathrm{wg}_i(t)\\
&\mathrm{en}_i(t+1) = \left(\mathrm{WG}_{i-1}(t) \vee \mathrm{WG}_{i+1}(t)\right) \wedge \neg \mathrm{SLP}_i(t)\\
&= \mathrm{WG}_{i-1}(t) + \mathrm{WG}_{i+1}(t) - \mathrm{WG}_{i-1}(t)\\
&* \mathrm{WG}_{i+1}(t) - \mathrm{WG}_{i-1}(t) * \mathrm{SLP}_i(t) - \mathrm{WG}_{i+1}(t)
\end{aligned}
$$

$$
\begin{aligned}
&* \mathrm{SLP}_i(t) + \mathrm{WG}_{i-1}(t) * \mathrm{WG}_{i+1}(t) * \mathrm{SLP}_i(t)\\
&\mathrm{EN}_i(t+1) = \mathrm{en}_i(t)\\
&\mathrm{hh}_i(t+1) = \mathrm{EN}_i(t) \wedge \neg \mathrm{CIR}_i(t) = \mathrm{EN}_i(t) - \mathrm{EN}_i(t)\\
&* \mathrm{CIR}_i(t)\\
&\mathrm{HH}_i(t+1) = \mathrm{hh}_i(t)\\
&\mathrm{ptc}_i(t+1) = \mathrm{CIA}_i(t) \wedge \neg \mathrm{EN}_i(t) \wedge \neg \mathrm{CIR}_i(t)\\
&= \mathrm{CIA}_i(t) - \mathrm{CIA}_i(t) * \mathrm{EN}_i(t) - \mathrm{CIA}_i(t)\\
&* \mathrm{CIR}_i(t) + \mathrm{CIA}_i(t) * \mathrm{EN}_i(t) * \mathrm{CIR}_i(t)\\
&\mathrm{PTC}_i(t+1) = \mathrm{ptc}_i(t) \vee \left(\mathrm{PTC}_i(t) \wedge \neg \mathrm{HH}_{i-1}(t)\right.\\
&\left.\wedge \neg \mathrm{HH}_{i+1}(t)\right) = \mathrm{ptc}_i(t) + \mathrm{PTC}_i(t) - \mathrm{PTC}_i(t)\\
&* \mathrm{HH}_{i-1}(t) - \mathrm{PTC}_i(t) * \mathrm{HH}_{i+1}(t) + \mathrm{PTC}_i(t)\\
&* \mathrm{HH}_{i-1}(t) * \mathrm{HH}_{i+1}(t) - \mathrm{ptc}_i(t) * \mathrm{PTC}_i(t)\\
&+ \mathrm{ptc}_i(t) * \mathrm{PTC}_i(t) * \mathrm{HH}_{i-1}(t) + \mathrm{ptc}_i(t)\\
&* \mathrm{PTC}_i(t) * \mathrm{HH}_{i+1}(t) - \mathrm{ptc}_i(t) * \mathrm{PTC}_i(t)\\
&* \mathrm{HH}_{i-1}(t) * \mathrm{HH}_{i+1}(t)\\
&\mathrm{ci}_i(t+1) = \neg \mathrm{EN}_i(t) = 1 - \mathrm{EN}_i(t)\\
&\mathrm{CI}_i(t+1) = \mathrm{ci}_i(t)\\
&\mathrm{CIA}_i(t+1) = \mathrm{CI}_i(t) \wedge \left(\neg \mathrm{PTC}_i(t) \vee \mathrm{HH}_{i-1}(t)\right.\\
&\left.\vee \mathrm{HH}_{i+1}(t) \vee \mathrm{hh}_{i-1}(t) \vee \mathrm{hh}_{i+1}(t)\right) = \mathrm{CI}_i(t)\\
&- \mathrm{CI}_i(t) * \mathrm{PTC}_i(t) + \mathrm{CI}_i(t) * \mathrm{PTC}_i(t)\\
&* \mathrm{HH}_{i-1}(t) + \mathrm{CI}_i(t) * \mathrm{PTC}_i(t) * \mathrm{HH}_{i+1}(t)\\
&+ \mathrm{CI}_i(t) * \mathrm{PTC}_i(t) * \mathrm{hh}_{i-1}(t) + \mathrm{CI}_i(t)\\
&* \mathrm{PTC}_i(t) * \mathrm{hh}_{i+1}(t) - \mathrm{CI}_i(t) * \mathrm{PTC}_i(t)\\
&* \mathrm{HH}_{i-1}(t) * \mathrm{HH}_{i+1}(t) - \mathrm{CI}_i(t) * \mathrm{PTC}_i(t)\\
&* \mathrm{HH}_{i-1}(t) * \mathrm{hh}_{i-1}(t) - \mathrm{CI}_i(t) * \mathrm{PTC}_i(t)\\
&* \mathrm{HH}_{i-1}(t) * \mathrm{hh}_{i+1}(t) - \mathrm{CI}_i(t) * \mathrm{PTC}_i(t)\\
&* \mathrm{HH}_{i+1}(t) * \mathrm{hh}_{i-1}(t) - \mathrm{CI}_i(t) * \mathrm{PTC}_i(t)\\
&* \mathrm{HH}_{i+1}(t) * \mathrm{hh}_{i+1}(t) - \mathrm{CI}_i(t) * \mathrm{PTC}_i(t)\\
&* \mathrm{hh}_{i-1}(t) * \mathrm{hh}_{i+1}(t) + \mathrm{CI}_i(t) * \mathrm{PTC}_i(t)\\
&* \mathrm{HH}_{i-1}(t) * \mathrm{HH}_{i+1}(t) * \mathrm{hh}_{i-1}(t) + \mathrm{CI}_i(t)\\
&* \mathrm{PTC}_i(t) * \mathrm{HH}_{i-1}(t) * \mathrm{HH}_{i+1}(t) * \mathrm{hh}_{i+1}(t)\\
&+ \mathrm{CI}_i(t) * \mathrm{PTC}_i(t) * \mathrm{HH}_{i-1}(t) * \mathrm{hh}_{i-1}(t)\\
&* \mathrm{hh}_{i+1}(t) + \mathrm{CI}_i(t) * \mathrm{PTC}_i(t) * \mathrm{HH}_{i+1}(t)\\
&* \mathrm{hh}_{i-1}(t) * \mathrm{hh}_{i+1}(t) - \mathrm{CI}_i(t) * \mathrm{PTC}_i(t)\\
&* \mathrm{HH}_{i-1}(t) * \mathrm{HH}_{i+1}(t) * \mathrm{hh}_{i-1}(t) * \mathrm{hh}_{i+1}(t)
\end{aligned}
$$

$$
\begin{aligned}
&\mathrm{CIR}_i(t+1) = \mathrm{CI}_i(t) \wedge \mathrm{PTC}_i(t) \wedge \neg \mathrm{HH}_{i-1}(t)\\
&\wedge \neg \mathrm{HH}_{i+1}(t) \wedge \neg \mathrm{hh}_{i-1}(t) \wedge \neg \mathrm{hh}_{i+1}(t) = \mathrm{CI}_i(t)\\
&* \mathrm{PTC}_i(t) - \mathrm{CI}_i(t) * \mathrm{PTC}_i(t) * \mathrm{HH}_{i-1}(t)\\
&- \mathrm{CI}_i(t) * \mathrm{PTC}_i(t) * \mathrm{HH}_{i+1}(t) - \mathrm{CI}_i(t)\\
&* \mathrm{PTC}_i(t) * \mathrm{hh}_{i-1}(t) - \mathrm{CI}_i(t) * \mathrm{PTC}_i(t)\\
&* \mathrm{hh}_{i+1}(t) + \mathrm{CI}_i(t) * \mathrm{PTC}_i(t) * \mathrm{HH}_{i-1}(t)\\
&* \mathrm{HH}_{i+1}(t) + \mathrm{CI}_i(t) * \mathrm{PTC}_i(t) * \mathrm{HH}_{i-1}(t)\\
&* \mathrm{hh}_{i-1}(t) + \mathrm{CI}_i(t) * \mathrm{PTC}_i(t) * \mathrm{HH}_{i-1}(t)\\
&* \mathrm{hh}_{i-1}(t) + \mathrm{CI}_i(t) * \mathrm{PTC}_i(t) * \mathrm{HH}_{i+1}(t)\\
&* \mathrm{hh}_{i-1}(t) + \mathrm{CI}_i(t) * \mathrm{PTC}_i(t) * \mathrm{HH}_{i+1}(t)\\
&* \mathrm{hh}_{i+1}(t) + \mathrm{CI}_i(t) * \mathrm{PTC}_i(t) * \mathrm{hh}_{i-1}(t)\\
&* \mathrm{hh}_{i+1}(t) - \mathrm{CI}_i(t) * \mathrm{PTC}_i(t) * \mathrm{HH}_{i-1}(t)\\
&* \mathrm{HH}_{i+1}(t) * \mathrm{hh}_{i-1}(t) - \mathrm{CI}_i(t) * \mathrm{PTC}_i(t)\\
&* \mathrm{HH}_{i-1}(t) * \mathrm{HH}_{i+1}(t) * \mathrm{hh}_{i+1}(t) - \mathrm{CI}_i(t)\\
&* \mathrm{PTC}_i(t) * \mathrm{HH}_{i-1}(t) * \mathrm{hh}_{i-1}(t) * \mathrm{hh}_{i+1}(t)\\
&- \mathrm{CI}_i(t) * \mathrm{PTC}_i(t) * \mathrm{HH}_{i+1}(t) * \mathrm{hh}_{i-1}(t)\\
&* \mathrm{hh}_{i+1}(t) + \mathrm{CI}_i(t) * \mathrm{PTC}_i(t) * \mathrm{HH}_{i-1}(t)\\
&* \mathrm{HH}_{i+1}(t) * \mathrm{hh}_{i-1}(t) * \mathrm{hh}_{i+1}(t),
\end{aligned}
\tag{B.3}
$$

where $x(t) = [\mathrm{SLP}_i(t), \mathrm{wg}_i(t), \mathrm{WG}_i(t), \mathrm{en}_i(t), \mathrm{EN}_i(t), \mathrm{hh}_i(t), \mathrm{HH}_i(t), \mathrm{ptc}_i(t), \mathrm{PTC}_i(t), \mathrm{ci}_i(t), \mathrm{CI}_i(t), \mathrm{CIA}_i(t), \mathrm{CIR}_i(t)]^T$ is the network state at time t, and $x(t) \in [0,1]^{13}$.

Disclosure

Short version of this paper was presented at "1st International Conference on Decision Support System Technology: Big Data Analytics for Decision Making," Belgrade, Serbia, 2015.

Conflicts of Interest

The authors declare that there are no conflicts of interest regarding the publication of this paper.

References

[1] R. Thomas, "Regulatory networks seen as asynchronous automata: a logical description," *Journal of Theoretical Biology*, vol. 153, no. 1, pp. 1–23, 1991.

[2] M. Ghil, I. Zaliapin, and B. Coluzzi, "Boolean delay equations: a simple way of looking at complex systems," *Physica D: Nonlinear Phenomena*, vol. 237, no. 23, pp. 2967–2986, 2008.

[3] D. M. Wittmann, J. Krumsiek, J. Saez-Rodriguez, D. A. Lauffenburger, S. Klamt, and F. J. Theis, "Transforming Boolean models to continuous models: methodology and application to T-cell receptor signaling," *BMC Systems Biology*, vol. 3, article 98, 2009.

[4] L. A. Zadeh, "Outline of a new approach to the analysis of complex systems and decision processes," *IEEE Transactions on Systems, Man, and Cybernetics*, vol. 3, no. 1, pp. 28–44, 1973.

[5] S. A. Kauffman, "Metabolic stability and epigenesis in randomly constructed genetic nets," *Journal of Theoretical Biology*, vol. 22, no. 3, pp. 437–467, 1969.

[6] J. A. Tomé and J. P. Carvalho, "Fuzzy Boolean nets—a nature inspired model for learning and reasoning," *Fuzzy Sets and Systems*, vol. 253, pp. 1–27, 2014.

[7] A. Saadatpour and R. Albert, "Boolean modeling of biological regulatory networks: a methodology tutorial," *Methods*, vol. 62, no. 1, pp. 3–12, 2013.

[8] S. Videla, C. Guziolowski, F. Eduati et al., "Learning Boolean logic models of signaling networks with ASP," *Theoretical Computer Science*, vol. 599, pp. 79–101, 2015.

[9] D. M. Wittmann and F. J. Theis, "Dynamic regimes of random fuzzy logic networks," *New Journal of Physics*, vol. 13, Article ID 013041, 2011.

[10] E. Goles and L. Salinas, "Comparison between parallel and serial dynamics of Boolean networks," *Theoretical Computer Science*, vol. 396, no. 1-3, pp. 247–253, 2008.

[11] R. Thomas, "Boolean formalization of genetic control circuits," *Journal of Theoretical Biology*, vol. 42, no. 3, pp. 563–585, 1973.

[12] R.-S. Wang, A. Saadatpour, and R. Albert, "Boolean modeling in systems biology: an overview of methodology and applications," *Physical Biology*, vol. 9, no. 5, Article ID 055001, 2012.

[13] M. Chaves, R. Albert, and E. D. Sontag, "Robustness and fragility of Boolean models for genetic regulatory networks," *Journal of Theoretical Biology*, vol. 235, no. 3, pp. 431–449, 2005.

[14] M. Chaves and A. Carta, "Attractor computation using interconnected Boolean networks: testing growth rate models in *E. Coli*," *Theoretical Computer Science*, vol. 599, pp. 47–63, 2015.

[15] D. G. Wright, T. F. Stocker, and L. A. Mysak, "A note on quaternary climate modelling using Boolean delay equations," *Climate Dynamics*, vol. 4, no. 4, pp. 263–267, 1990.

[16] A. Saunders and M. Ghil, "A Boolean delay equation model of ENSO variability," *Physica D: Nonlinear Phenomena*, vol. 160, no. 1-2, pp. 54–78, 2001.

[17] I. Zaliapin, V. Keilis-Borok, and M. Ghil, "A boolean delay equation model of colliding cascades. Part I: multiple seismic regimes," *Journal of Statistical Physics*, vol. 111, no. 3-4, pp. 815–837, 2003.

[18] I. Zaliapin, V. Keilis-Borok, and M. Ghil, "A boolean delay equation model of colliding cascades. Part II: prediction of critical transitions," *Journal of Statistical Physics*, vol. 111, no. 3-4, pp. 839–861, 2003.

[19] G. Easton, R. J. Brooks, K. Georgieva, and I. Wilkinson, "Understanding the dynamics of industrial networks using Kauffman Boolean networks," *Advances in Complex Systems. A Multidisciplinary Journal*, vol. 11, no. 1, pp. 139–164, 2008.

[20] B. Coluzzi, M. Ghil, S. Hallegatte, and G. Weisbuch, "Boolean delay equations on networks in economics and the geosciences," *International Journal of Bifurcation and Chaos*, vol. 21, no. 12, pp. 3511–3548, 2011.

[21] J.-W. Gu, T.-K. Siu, and H. Zheng, "On modeling credit defaults: a probabilistic Boolean network approach," *Risk and Decision Analysis*, vol. 4, no. 2, pp. 119–129, 2013.

[22] K. Kobayashi and K. Hiraishi, "A probabilistic approach to control of complex systems and its application to real-time pricing," *Mathematical Problems in Engineering*, vol. 2014, Article ID 906717, 8 pages, 2014.

[23] T. Kok and P. Wang, "A study of 3-gene regulation networks using NK-boolean network model and fuzzy logic networking," in *Fuzzy Applications in Industrial Engineering*, vol. 201 of *Studies in Fuzziness and Soft Computing*, pp. 119–151, Springer, Berlin, Germany, 2006.

[24] Y. Cao, P. P. Wang, and A. Tokuta, "Gene regulatory network modeling: a data driven approach," in *Fuzzy Logic*, vol. 215 of *Studies in Fuzziness and Soft Computing*, pp. 247–281, Springer, Berlin, Germany, 2007.

[25] M. K. Morris, J. Saez-Rodriguez, D. C. Clarke, P. K. Sorger, and D. A. Lauffenburger, "Training signaling pathway maps to biochemical data with constrained fuzzy logic: quantitative analysis of liver cell responses to inflammatory stimuli," *PLoS Computational Biology*, vol. 7, no. 3, Article ID e1001099, 2011.

[26] J. L. Salmeron and E. I. Papageorgiou, "A Fuzzy Grey Cognitive Maps-based Decision Support System for radiotherapy treatment planning," *Knowledge-Based Systems*, vol. 30, pp. 151–160, 2012.

[27] A. Poret, C. M. Sousa, and J. P. Boissel, "A logic-based modeling derived from boolean networks: adding fuzzy logic and edge tuning," *Simulation*, vol. 1, article 10, 2014.

[28] M. Grieb, A. Burkovski, J. E. Sträng et al., "Predicting variabilities in cardiac gene expression with a boolean network incorporating uncertainty," *PLoS ONE*, vol. 10, no. 7, Article ID e0131832, 2015.

[29] P. Hájek, *Metamathematics of Fuzzy Logic*, Kluwer Academic, Dordrecht, The Netherlands, 1998.

[30] S. Jenei, "A more efficient method for defining fuzzy connectives," *Fuzzy Sets and Systems*, vol. 90, no. 1, pp. 25–35, 1997.

[31] D. Radojevic, "New [0, 1]-valued logic: a natural generalization of Boolean logic," *Yugoslav Journal of Operations Research*, vol. 10, no. 2, pp. 185–216, 2000.

[32] H. Lähdesmäki, I. Shmulevich, and O. Yli-Harja, "On learning gene regulatory networks under the Boolean network model," *Machine Learning*, vol. 52, no. 1-2, pp. 147–167, 2003.

[33] R. Sharan and R. M. Karp, "Reconstructing Boolean models of signaling," *Journal of Computational Biology*, vol. 20, no. 3, pp. 249–257, 2013.

[34] D. M. Gabbay and F. Guenthner, *Handbook of Philosophical Logic*, Springer-Verlag, Berlin, Germany, 2nd edition, 2011.

[35] M. I. Davidich and S. Bornholdt, "Boolean Network Model Predicts Knockout Mutant Phenotypes of Fission Yeast," *PLoS ONE*, vol. 8, no. 9, Article ID e71786, 2013.

[36] V. Dobric, "Fuzzification of boolean networks," in *Decision Making and Soft Computing—Proceedings of the 11th International FLINS Conference*, R. M. De Moraes, E. E. Kerre, L. Dos Santos Machado, and J. Lu, Eds., pp. 276–281, World Scientific, Singapore.

[37] V. D. Dobrić, *Concepts modelling using consistent fuzzy logic [PhD, thesis]*, Faculty of Organisational Sciences, University of Belgrade, Belgrade, Serbia, 2016.

[38] V. Dobrić, P. Milošević, and B. Petrović, "Modelling Complex Systems using Interpolative Boolean algebra," in *Proceedings of the 1st EWG-DSS International Conference on Decision Support System Technology: Big Data Analytics for Decision Making (ICDSST '15)*, B. Delibašić and et al., Eds., Belgrade, Serbia, May 2015.

[39] D. Radojevic, "Fuzzy set theory in the Boolean frame," *International Journal of Computers Communications & Control*, vol. 3, no. 3, pp. 121–131, 2008.

[40] D. Radojević, "Logical aggregation based on interpolative Boolean algebra," *Mathware & Soft Computing*, vol. 15, no. 1, pp. 125–141, 2008.

[41] D. Radojević, "Real sets as consistent Boolean generalization of classical sets," in *From Natural Language to Soft Computing: New Paradigms in Artificial Intelligence*, pp. 150–171, Editing House of Romanian Academy, Bucharest, Romania, 2008.

[42] D. Radojevic, "Real-valued realizations of boolean algebras are a natural frame for consistent fuzzy logic," in *On Fuzziness*, vol. 299 of *Studies in Fuzziness and Soft Computing*, pp. 559–565, 2013.

[43] A. Poledica, P. Milošević, I. Dragović, B. Petrović, and D. Radojević, "Modeling consensus using logic-based similarity measures," *Soft Computing*, vol. 19, no. 11, pp. 3209–3219, 2015.

[44] V. Dobrić, D. Kovačević, B. Petrović, D. Radojević, and P. Milošević, "Formalization of human categorization process using interpolative Boolean algebra," *Mathematical Problems in Engineering*, vol. 2015, Article ID 620797, 8 pages, 2015.

[45] P. Milošević, B. Petrović, D. Radojević, and D. Kovačević, "A software tool for uncertainty modeling using Interpolative Boolean algebra," *Knowledge-Based Systems*, vol. 62, pp. 1–10, 2014.

[46] J. Baumeister, "Advanced empirical testing," *Knowledge-Based Systems*, vol. 24, no. 1, pp. 83–94, 2011.

[47] A. T. Weeraratna, Y. Jiang, G. Hostetter et al., "Wnt5a signaling directly affects cell motility and invasion of metastatic melanoma," *Cancer Cell*, vol. 1, no. 3, pp. 279–288, 2002.

[48] K. Kobayashi and K. Hiraishi, "Verification and optimal control of context-sensitive probabilistic Boolean networks using model checking and polynomial optimization," *The Scientific World Journal*, vol. 2014, Article ID 968341, 8 pages, 2014.

Hindawi
Complexity
Volume 2017, Article ID 4327175, 17 pages
https://doi.org/10.1155/2017/4327175

Research Article

New Perspectives for Computer-Aided Discrimination of Parkinson's Disease and Essential Tremor

P. Povalej Bržan,[1,2] J. A. Gallego,[3] J. P. Romero,[4,5] V. Glaser,[1] E. Rocon,[3] J. Benito-León,[6,7,8] F. Bermejo-Pareja,[8,9] I. J. Posada,[6,7,8] and A. Holobar[1]

[1] *Faculty of Electrical Engineering and Computer Science, University of Maribor, Maribor, Slovenia*
[2] *Faculty of Health Sciences, University of Maribor, Maribor, Slovenia*
[3] *Centre for Automation and Robotics, CSIC-UPM, 28500 Madrid, Spain*
[4] *Neurorehabilitation and Brain Damage Research Group, Experimental Sciences School, Universidad Francisco de Vitoria, Madrid, Spain*
[5] *Brain Damage Unit, Hospital Beata María Ana, Madrid, Spain*
[6] *Department of Neurology, University Hospital 12 de Octubre, Madrid, Spain*
[7] *Center of Biomedical Network Research on Neurodegenerative Diseases (CIBERNED), Madrid, Spain*
[8] *Department of Medicine, Faculty of Medicine, Complutense University, Madrid, Spain*
[9] *Clinical Research Unit, University Hospital 12 de Octubre, Madrid, Spain*

Correspondence should be addressed to A. Holobar; ales.holobar@um.si

Received 12 May 2017; Revised 31 July 2017; Accepted 12 September 2017; Published 19 October 2017

Academic Editor: Valeri Mladenov

Copyright © 2017 P. Povalej Bržan et al. This is an open access article distributed under the Creative Commons Attribution License, which permits unrestricted use, distribution, and reproduction in any medium, provided the original work is properly cited.

Pathological tremor is a common but highly complex movement disorder, affecting ~5% of population older than 65 years. Different methodologies have been proposed for its quantification. Nevertheless, the discrimination between Parkinson's disease tremor and essential tremor remains a daunting clinical challenge, greatly impacting patient treatment and basic research. Here, we propose and compare several movement-based and electromyography-based tremor quantification metrics. For the latter, we identified individual motor unit discharge patterns from high-density surface electromyograms and characterized the neural drive to a single muscle and how it relates to other affected muscles in 27 Parkinson's disease and 27 essential tremor patients. We also computed several metrics from the literature. The most discriminative metrics were the symmetry of the neural drive to muscles, motor unit synchronization, and the mean log power of the tremor harmonics in movement recordings. Noteworthily, the first two most discriminative metrics were proposed in this study. We then used decision tree modelling to find the most discriminative combinations of individual metrics, which increased the accuracy of tremor type discrimination to 94%. In summary, the proposed neural drive-based metrics were the most accurate at discriminating and characterizing the two most common pathological tremor types.

1. Introduction

Pathological tremor is the most common movement disorder and is strongly increasing in incidence and prevalence with ageing. About ~4% of the elderly (>65 years) suffer from essential tremor (ET), whereas ~1% of the population of age >50 years suffer from Parkinson's disease (PD) [1].

The central origin of ET and PD tremor is widely accepted but not fully understood. ET is believed to originate at the cerebellothalamocortical pathways [2, 3], although the involvement of the inferior olive has also been suggested due to its rhythmic properties [4, 5]. In PD patients, the loss of dopaminergic nigrostriatal neurons is believed to cause abnormal oscillations in the loop linking the cortex, basal ganglia, and thalamus [6]. Despite their potentially different origins, ET and PD frequently demonstrate similar symptoms and are often difficult to discriminate, especially at early stages. Up to 20% of patients with ET develop the signs typical for PD, whereas 30 to 50% of patients diagnosed with ET do not have ET [2, 7, 8].

Current methods for clinical tremor diagnosis and quantification are based on the mechanical demonstration of tremor (the tremulous movement), mainly with the help of movement disorder scales, such as the Fahn-Tolosa-Marin [9] and the UPDRSIII scale [10]. Some of the key clinical features for diagnosing ET and PD are that ET tends to increase in postural and kinetic tasks, whereas PD tremor is frequently present at rest. However, 20–30% of the ET patients also have clinically noticeable rest tremor [11], an observation that highlights the complexity of diagnosing these two tremor types. As to the tremors themselves, the mechanisms behind the observed differences (and similarities) between ET and PD are not well understood. In addition, tremor diagnosis is mainly based on the subjective clinical assessment of the tremulous movement (i.e., without quantifying its characteristics), whereas the pathophysiology of the underlying tremor is not fully understood, mainly due to the highly complex interactions between the central and peripheral structures of the nervous system [12].

Different computer-aided methods for tremor diagnosis have already been proposed [13–18]. Among them, the difference in the energy of the higher tremor harmonics in movement recordings, typically performed with inertial sensors, best discriminates ET and PD patients [17, 18]. These harmonics are usually computed after using relatively simple frequency filtering techniques which separate the higher tremor frequencies from the relatively low frequencies of voluntary movement [14, 15, 17, 19]. However, the tremulous movement is nonlinearly related to the underlying muscle activation and results from complicated interactions among the many muscles that control the same joint. These interactions between muscles are also yet not fully understood. For example, it has been recently demonstrated that not all the muscles are equally affected by ET [20] and that the interaction between antagonist muscles is different across conditions and patients, and intrinsically nonstationary [21].

In this study, we applied a sophisticated blind source separation algorithm [22–24] to the surface electromyograms (EMG) of PD and ET patients to estimate the neural drive that reflects the net input from the nervous system [25] to the wrist flexors and extensors. Our rationale was that by using a more detailed measurement of nervous system function than the classically used rectified EMG or resultant movement, we could develop better metrics for tremor characterization and discrimination. We systematically analyzed the properties of the neural drive in these two groups of patients, proposed novel pathological tremor characterization metrics, and analyzed their power to discriminate between ET and PD tremor. Finally, we compared the discriminative power of the proposed methodologies to that of previously proposed methods and demonstrated that our new metrics largely outperform them.

The manuscript is organized as follows. Section 2 justifies multichannel EMG recordings and the estimation of the neural drive to muscle using blind source separation of these signals in pathological tremor. Section 3 describes the experimental protocol and our novel methodology for quantifying and classifying pathological tremor types. Section 4 systematically analyzes the statistical power of the described metrics in discrimination of ET and PD patients. Section 5 discusses the main results and limitations and concludes the manuscript.

2. Neural Drive to Skeletal Muscles and Tremor Demonstration in Surface Electromyograms

The central nervous system causes movement by modulating the firing patterns of the motoneurons that innervate task-relevant muscles. The net output from all the motoneurons is referred to as neural drive to the muscle [26] and is the ultimate control signal mediating movement generation [27]. In heathy muscles, each motoneuron firing causes a motor unit action potential (MUAP) that makes the innervated fibers contract. MUAPs can be measured by surface EMG [28]. Subcutaneous tissue progressively filters electrical potentials with increasing distance from the muscle fibers, inducing spatial variability of MUAPs across the skin surface [28].

In pathological tremor, the neural drive to muscle has classically been estimated from bipolar surface EMG recordings [14, 15, 17]. In this procedure, the EMG signals are first rectified and their power spectrum is calculated to estimate the power at the main tremor frequency and its higher harmonics. While appropriate for coarse tremor assessment and for many pioneering tremor studies (e.g., [29]), this procedure of computing the power spectrum of the rectified EMG did not provide the most accurate insight into the complex and nonstationary neural drive underlying tremulous muscle dynamics in our study (see Results in Section 4). There are a number of reasons that support this statement as well as our results. First, not all the motor units are active during pathological tremor, and the muscle activation pattern, estimated from bipolar EMG recordings, depends significantly on the electrode position (Figure 1) and on motor unit distribution within the muscle tissue [27]. Second, in dynamic conditions as tremor, muscle fibers move relative to the skin, causing unpredictable changes in the detected MUAPs [25, 27, 28]. Third, the spatial distribution of the motor units varies significantly among subjects, and there is no universally optimal position for bipolar EMG recordings [28]. Fourth, the algebraic summation of biphasic MUAP trains causes EMG amplitude cancellation, which leads to an unpredictable underestimation of the effective neural drive [30–32]. For these reasons, the neural drive to muscle is better characterized using two-dimensional high-density (2D hdEMG) arrays of surface EMG electrodes, with several tens of surface electrodes placed over a substantial portion of the skin above the investigated muscle [25, 27]. This, however, generates large quantities of recorded data.

Different methodologies have been proposed to cope with this challenge [28]. Given that the neural drive to muscle is the net activity of all the innervating motoneurons, the best estimate of the neural drive is derived from the motoneuron (and, consequently, motor unit) spike trains themselves [25]. For this purpose, the highly variable MUAPs that mask the changes in the neural drive need to be separated from the motor unit spike trains. This is accomplished by

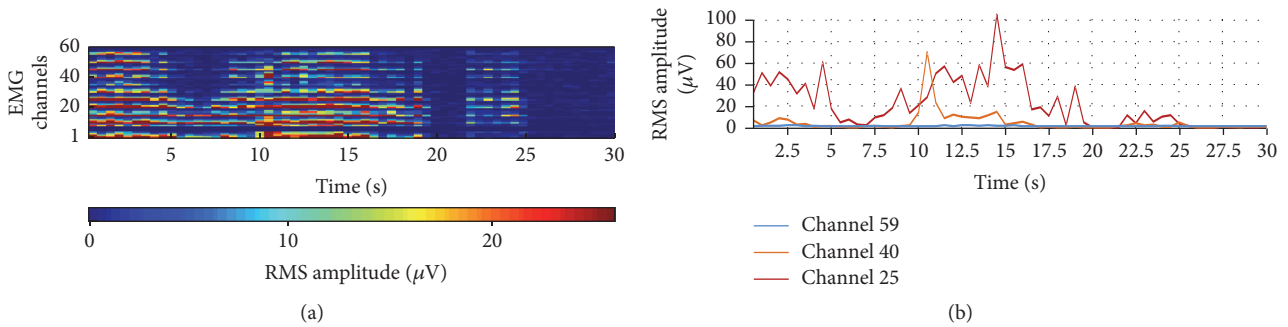

Figure 1: Surface EMG amplitude of the wrist extensors in a PD patient during rest condition. Electrode location greatly influences the EMG characterization of tremor. Tremor amplitude computed from the surface EMG using standard methods was highly variable across 60 bipolar channels of single-differential EMG (recorded with an array of 5×13 electrodes with interelectrode distance of 8 mm); for example, it ranged from severe tremor in channel 25 to no tremor in channel 59.

using advanced signal decomposition algorithms [23, 24, 32–34]. However, not all of these algorithms are applicable to hdEMG data in pathological tremor; in pathological tremor, motor unit firings tend to be significantly more synchronized than in healthy conditions [21, 23], causing bursts of EMG activity (Figure 2) that are very difficult to decompose into the contributions of individual motor units. The Convolution Kernel Compensation (CKC) technique has been recently demonstrated to successfully solve this problem [23], providing a solid ground for fully automatic and highly accurate assessment of the tremulous neural drive to muscles.

3. Methodology

3.1. Experimental Protocol. Fifty-four subjects (27 ET and 27 PD patients), all suffering from mild to severe tremor, were recruited at Hospital Universitario 12 de Octubre, Madrid, Spain. The ET patients were 12 females and 15 males with mean age of 70 ± 9 years (range 43–80 years). The PD patients were 10 females and 17 males with mean age of 66 ± 10 years (range 44–80 years). Tremor severity in the most affected limb ranged from 10 to 56 (mean ± SD: 31.6 ± 11.3) according to the Fahn-Tolosa-Marin scale in ET patients and from 5 to 51 (mean ± SD: 14.9±9.1) according to the UPDRS scale in PD patients. The mean disease duration was 19 ± 15 years (range 2–65 years) for the ET patients and 5 ± 3 years (range 1–13 years) for the PD patients. Seventeen ET patients were taking antitremor drugs, which in all cases were withheld for at least 12 h before the recordings. Sixteen PD patients were taking antitremor drugs and continued their medications during the recordings. This is the group of patients that was included into the induction of the decision model and its tenfold cross-validation.

Based on the method we devised to objectively identify tremor, 27 ET and 27 PD patients exhibited tremor in both rest and postural tasks studied, and 27 ET and 22 PD patients exhibited bilateral tremor. Our tremor identification method consisted in computing the power spectrum of the signal of interest (the summed motor unit spike trains, the rectified surface EMG, or wrist movement) and summing the peaks at the basic tremor frequency and its first two higher harmonics. If this sum was ≥50% of the total power of the signal, we considered that recording to exhibit tremor.

To further test the performance of our decision tree model, we recruited six additional ET and PD patients, which were blindly diagnosed by the proposed model and three expert clinicians. Importantly, both diagnoses were completely independent, and no data from these six patients were included into decision model induction. The ET patients were 1 female and 2 males, with mean age 65 ± 17 years (range 47–80 years); their mean disease duration was 20 ± 9 years (range 10–27 years). The PD patients were 2 females and 1 male, with mean age 68 ± 10 years (range 62–80 years); their mean disease duration was 9 ± 5 years (range 5–14 years). Tremor severity in the most affected limb ranged from 10 to 34 (mean ± SD: 25.3 ± 13.3) according to the Fahn-Tolosa-Marin scale for the ET patients and from 15 to 23 (19.3 ± 4.0) according to the UPDRS scale for the PD patients. These patients formed the test group.

All patients received a detailed explanation of the study and gave written informed consent prior to participation. The study was conducted in accordance with the Declaration of Helsinki and approved by the local ethics committee. The experimental protocol comprised measuring the inertial and EMG data from both forearms during standard tremor triggering tasks (see, e.g., [2, 6, 11, 14, 16–18, 21]). Each patient performed three repetitions of the following 30 s long standard tasks:

(i) *Rest task (RE)*: the patient was sitting relaxed, with both arms supported in elbow and wrist region. The patient's wrists were relaxed with no noticeable voluntary activity throughout the entire duration of the task.

(ii) *Arms outstretched against gravity (AO)*: after 5 seconds of rest, the patient outstretched his/her arms and maintained them parallel to the ground until the end of the task. The fingers were separated and the hands were held at the same height as the shoulders.

(iii) *Arms outstretched against gravity with weight (WE)*: it is the same as the AO task with additional weight load of 1 kg applied to both hands. The patient had the fingers outstretched.

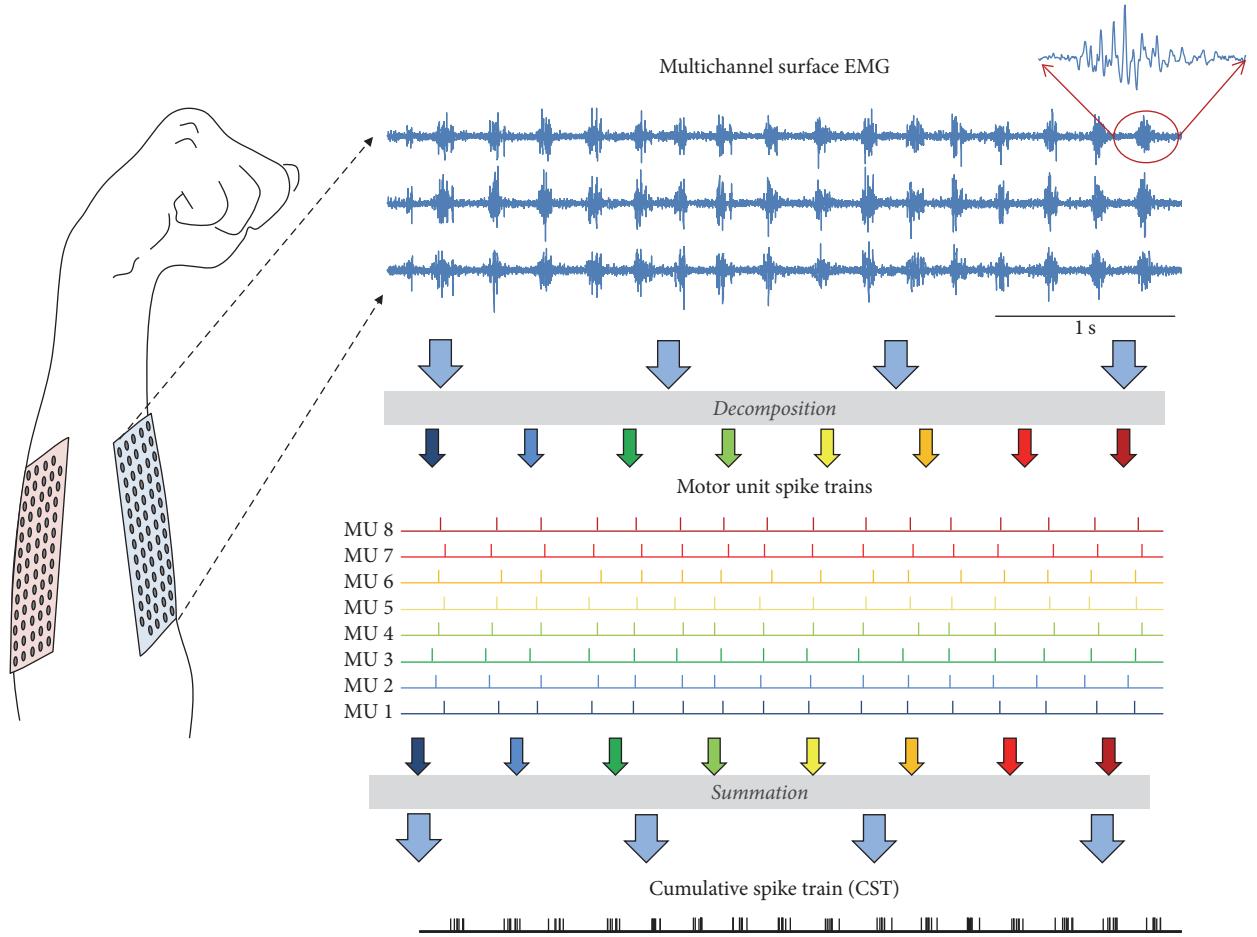

Figure 2: Experimental methods and estimation of the neural drive to muscle. Left: schematic of two 64-channel electrode arrays placed on the wrist flexors and extensors. Right: multichannel surface EMG in pathological tremor (upper panel) and its decomposition into constituent motor unit spike trains (lower panel). Decomposition allows for the identification of motor unit firing patterns and thus of the neural drive to muscles. Each vertical line in the lower right panel denotes an individual motor unit firing, whereas different motor units are depicted by different colors. Motor unit firing patterns are highly synchronized and have been identified using the Convolution Kernel Compensation (CKC) method [24]. Summed MU spike trains form cumulative spike train (CST; bottom-most panel).

(iv) *Arms supported + postural tremor elicited (PO)*: it is the same as RE task, but with both wrists held extended against gravity.

Wrist movement was assessed as the difference between the measured acceleration values in the axis parallel to the forearm [19]. Accelerometers (Tech MCS, Technaid S.L., Madrid, Spain) were fixed with surgical tape over the hand dorsum and the distal third of the forearm (on the dorsal side, close to the wrist) on each hand. Data were sampled at 100 Hz by a 12-bit A/D converter and low-pass filter (cut-off frequency of 20 Hz).

Surface hdEMG signals were recorded from the wrist flexors and extensors with 5 × 13 electrode arrays (LISiN–OT Bioelettronica, Torino, Italy, 8 mm interelectrode distance). The electrode arrays were centred over flexor carpi radialis and extensor digitorum communis, respectively. Before electrode placement, the skin was lightly abraded using abrasive paste (Meditec–Every, Parma, Italy) and cleaned. In order to improve the electrode-skin contact, each of the electrode cavities in the array was filled with conductive gel (Meditec–Every, Parma, Italy). A soaked bracelet placed around one of the wrists was used as reference. The surface EMG signals were amplified as bipolar recordings along the direction of the fibers, band-pass filtered (3 dB bandwidth, 10–750 Hz), and sampled at 2048 Hz and 12-bit resolution (LISiN–OT Bioelettronica, Torino, Italy). EMG and movement recordings were resampled to 2048 Hz and synchronized offline, using a common clock signal.

The hdEMG signals were decomposed into motor unit spike trains using the CKC algorithm [24]. The pulse-to-noise ratio (PNR) metric [23] was used to assess motor unit identification accuracy and all the motor units with PNR < 30 dB (corresponding to accuracy <~90% [24]) were discarded.

3.2. Assessment of the Tremor in the Neural Drive to Muscles. As mentioned above, tremor results from the pathological activation of several synergistic muscles, and oftentimes, of

antagonists as well. Due to the central origin of tremor, the descending drives to nearby muscles will possibly exhibit a similar tremor component [35], or at least its delayed reflection via afferent feedback loops [20, 21]. However, the characteristics of the neural drive to different muscles have been rarely studied in pathological tremor [23].

In this study, the neural drive to muscle was assessed by summing up individual motor unit spike trains into cumulative spike train (CST) (see, e.g., [20, 21, 35]). Afterwards, the CSTs of the different muscles were low-pass filtered (cut-off frequency of 20 Hz). In order to emphasize the rhythmic motor unit activity related to tremor and minimize the asynchronous motor unit activity caused by the concurrent voluntary contraction, we calculated the auto- and cross-correlation functions among all pairs of filtered CSTs. Representative results from one ET patient and one PD patient are depicted in Figures 3 and 4. Note that, in Figure 3(a), the neural drive to the extensors of the right wrist exhibited both tremulous and voluntary motor unit activity. The proposed auto- and cross-correlation functions filtered out the voluntary activity and emphasized the tremulous neural drive (Figure 3(b)). Moreover, usage of the auto- and cross-correlation functions of the neural drive also circumvented the ambiguity of our hdEMG decomposition method when estimating the amplitude of the neural drive. This well-known ambiguity is common to all blind source separation algorithms [22, 24] and implies that the amplitude of the neural drive can only be determined up to an unknown scalar factor (Figures 3, 4, and 6). This prevents the assessment of the absolute tremor power in the neural drive; however its relative power (with respect to the voluntary drive) can be easily assessed. The cross-correlation functions assess the interactions between the neural drives to different muscles and are, thus, insensitive to this amplitude ambiguity [25].

We observed different neural drive patterns for the two groups, with the ET patients exhibiting a larger degree of shared neural drive across muscles than the PD patients. To quantify this phenomenon, we considered the following neural drive-based metrics for ET and PD discrimination:

(N1) *Tremor amplitude in the neural drive*: average difference between the maxima and minima of the autocorrelation function of the neural drive to each individual muscle, calculated over correlation lags from −1 to +1 s.

(N2) *Tremor frequency in neural drive*: dominant frequency in the power spectrum of the neural drive to each individual muscle.

(N3) *Dominant hand tremor symmetry*: absolute values of cross-correlation coefficients between the neural drive to the wrist extensors and the neural drive to the wrist flexors in the dominant tremor hand, averaged over correlation lags from −1 to +1 s (Figure 3(b), panel N3).

(N4) *Interlimb tremor symmetry in extensors*: absolute values of the cross-correlation coefficients between the neural drive to the extensors of the left and the right wrist, averaged over correlation lags from −1 to +1 s (Figure 3(b), panel N4).

(N5) *Interlimb tremor symmetry in flexors*: absolute values of the cross-correlation coefficients between the neural drive to the flexors of the left and the right wrist, averaged over correlation lags from −1 to +1 s (Figure 3(b), panel N5).

(N6) *Global tremor symmetry*: absolute values of the cross-correlation coefficients between the neural drives correlation lags, averaged over all the muscle pairs and over correlation lags from −1 to +1 s (all panels in Figures 3(b) and 4(b)).

(N7) *Normalized global tremor symmetry*: the global tremor symmetry for the postural task (AO, WE, or PO), divided by the global tremor symmetry for the RE task.

3.3. Assessment of the Spatial Distribution of the Neural Drive to a Muscle. CST captures the temporal variability of neural drive to a muscle, while averaging out the differences among identified motor units [36]. Thus, the CST ignores how the tremor input is distributed across the motoneurons innervating the muscle. The distribution of the tremor input across motor units may be studied by quantifying the pairwise motor unit synchronization. During voluntary contractions, motor units discharge asynchronously, supporting smooth modulation of force [28]. In contrast, during pathological tremor, the level of motor unit synchronization increases significantly [20, 21, 23]. This can be quantified by assessing the distribution of backward and forward motor unit recurrence times in pairs of simultaneously active motor units [37]. The forward (backward) recurrence time is defined as the distance from the current motor unit discharge to the first next (closest previous) discharge of another motor unit (Figure 5(a)). In normal conditions, the recurrence times are uniformly distributed over the observed time support, indicating low motor unit synchronization. In pathological tremor, the motor unit recurrence times are grouped together (Figure 5(b)), reflecting highly synchronous motor unit activity.

We analyzed the distributions of motor unit recurrence times by calculating their histogram. We computed the 99% confidence limit assuming a uniform distribution and then identified the peaks exceeding this limit [37]. We then defined the pairwise motor unit synchronization index as the ratio between the peak area and the sum of all the histogram bins (Figure 5(b)). Finally, we used this index to define the following metrics of spatial tremor variability:

(N8) *Coefficient of variation for the pairwise motor unit synchronization*: the standard deviation of the distribution of pairwise motor unit synchronization indexes divided by their mean value, calculated over all the pairs of identified motor units per muscle and per task.

(N9) *Normalized coefficient of variation for the pairwise motor unit synchronization*: the N8 metric in the AO task, divided by the N8 metric in RE task. The

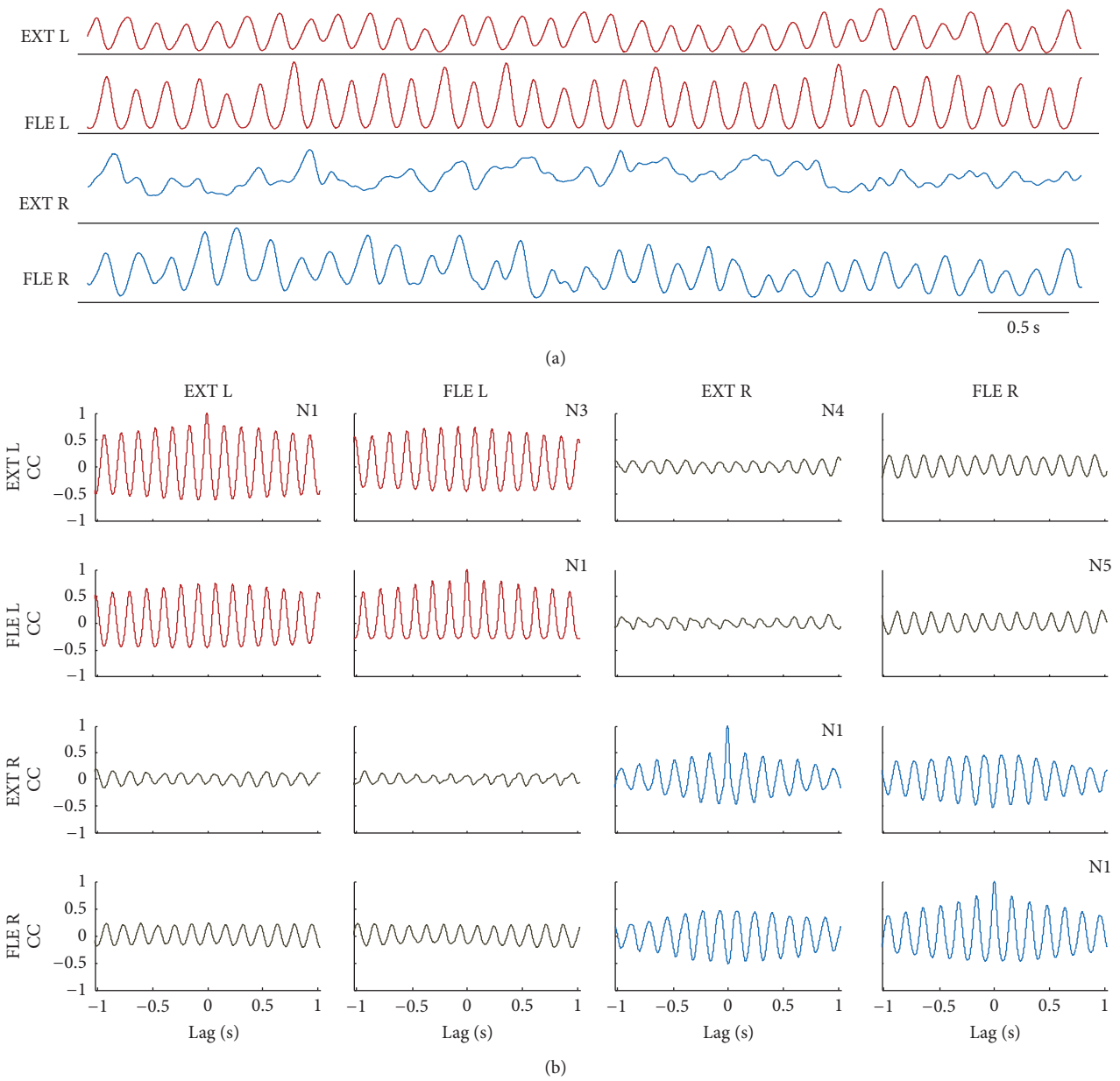

Figure 3: Neural drive to left and right wrist flexors and extensors in a representative ET patient during the arms outstretched task. (a) Neural drive as estimated by low-pass filtering of the cumulative motor unit spike train. All muscles exhibit tremulous drive, whereas voluntary drive is also present in the right extensor muscle. (b) Cross-correlations (CC) of neural drives; EXT L: left wrist extensors, FLE L: left wrist flexors, EXT R: right wrist extensors, and FLE R: right wrist flexors. The x-axis denotes the correlation lag in seconds. Voluntary drive is filtered out, whereas the tremulous drive is enhanced by the correlation function. Data from panels N1, N3, N4, and N5 are included into the calculation of the N1, N3, N4, and N5 tremor symmetry metrics (see text for details).

normalized coefficient of variability was averaged over all four investigated muscles for each patient.

3.4. Assessment of Tremor in Wrist Movements. Tremor characterization with inertial sensor recordings is very appealing due to the simplicity, robustness, and cost-effectiveness of these sensors [38]. Inertial sensor data have been used in many tremor diagnosis studies, demonstrating promising results in terms of ET and PD discrimination [13, 16, 18]. However, movement data reveal very limited information on the underlying tremor mechanisms. It then follows that the ability to discriminate between complicated ET and PD cases with metrics extracted from movement data is likely to be limited. To verify this hypothesis, we computed, separately for the dominant and nondominant tremor hands in each recorded task, the following metrics [18]: the basic tremor frequency and its power, the number of spectral peaks at the higher harmonics of the basic tremor frequency, and

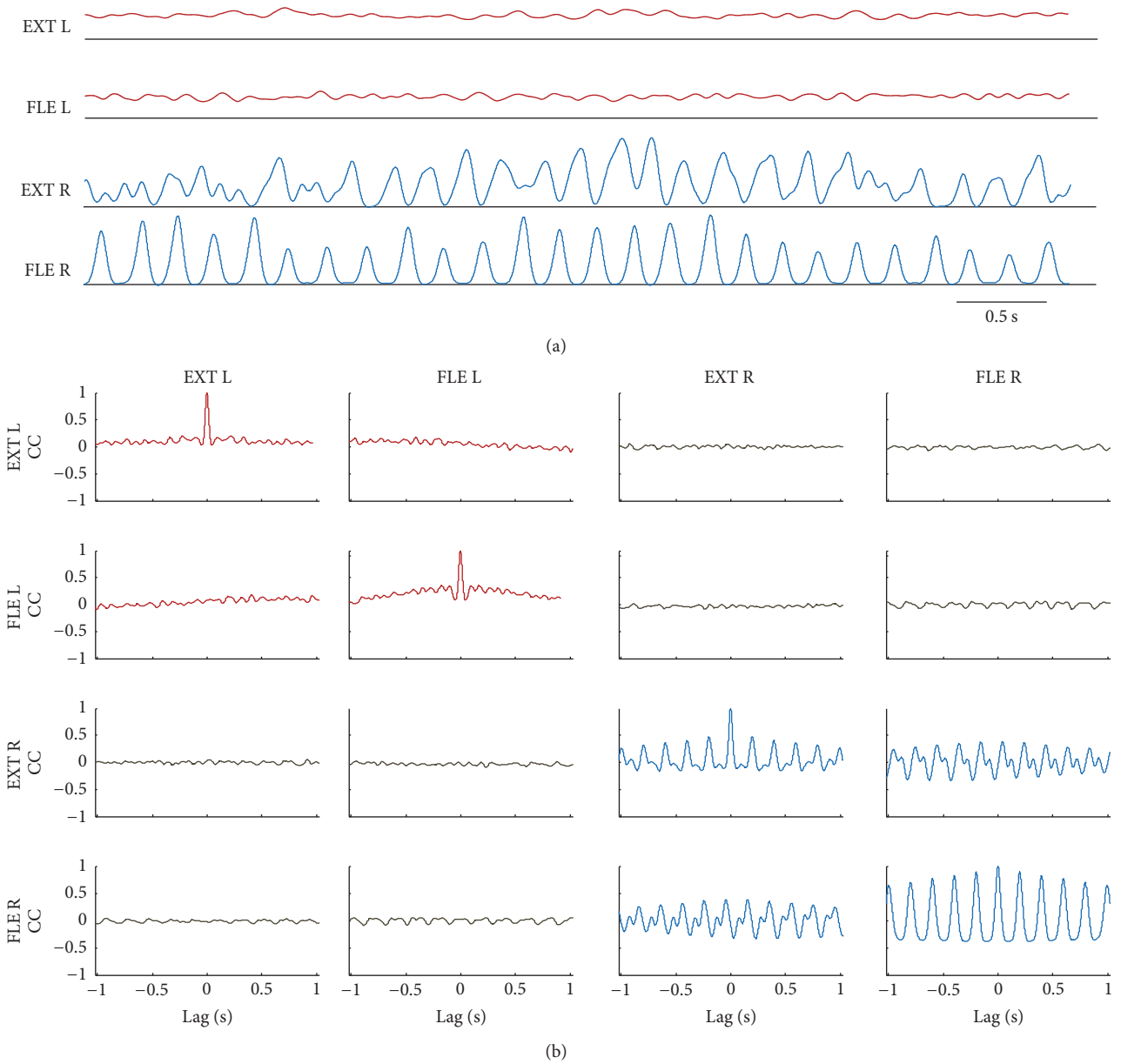

Figure 4: Neural drive to left and right wrist flexors and extensors in representative PD patient during arms outstretched task. (a) Neural drive as estimated by low-pass filtering of cumulative motor unit spike train. Left wrist extensors and flexors exhibit voluntary drive; right wrist extensors and flexors exhibit tremulous drive; (b) cross-correlations (CC) of neural drives; EXT L: left wrist extensors, FLE L: left wrist flexors, EXT R: right wrist extensors, and FLE R: right wrist flexors. The x-axis denotes the correlation lag in seconds.

their mean power. We also computed the asymmetry of the autocorrelation function [13], along with the statistical signal characterization (SSC) metric proposed in [16].

We also defined the following new movement-related metrics, calculated using the base 10 logarithm of the harmonic peak powers in the data from the dominant and nondominant tremor hand, respectively:

(M1) *Mean log power of all harmonics*: the mean of the logarithmic power of all the tremor harmonic peaks in the power spectrum of the movement recordings during a single task.

(M2) *Average of mean log power of all the harmonics*: the average of the mean of the logarithmic power of all the harmonic peaks across different tasks.

In order to make the differences between ET and PD patients most evident, and to further improve the patient classification performance, the values of all the movement metrics in the postural tasks (AO, WE, and PO) of individual patient were normalized by their corresponding values during the RE task. In this normalization, we subtracted the metric in the RE task from the corresponding values in the AO, WE, and PO tasks, respectively. We chose the repetition with the highest tremor

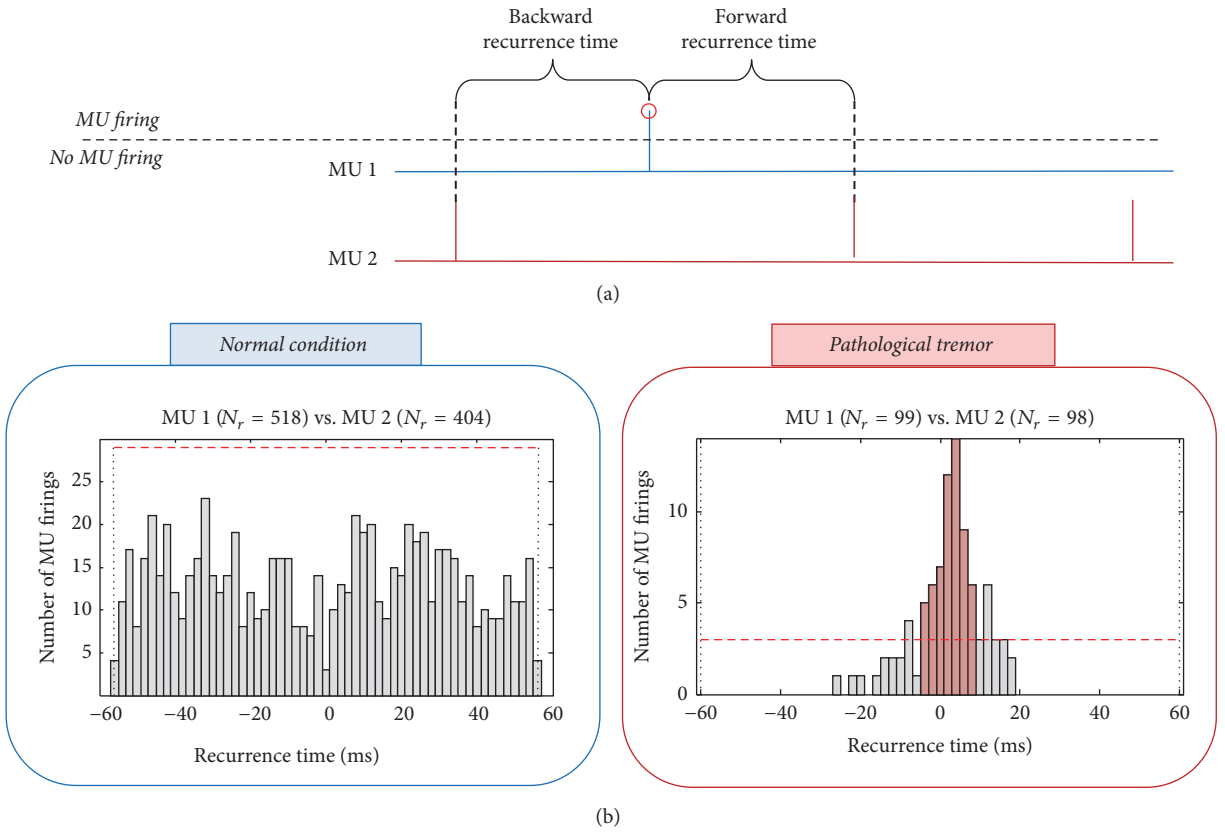

Figure 5: Definition of backward and forward motor unit (MU) recurrence times (a) and representative histograms of recurrence times in a healthy young control ((b), left panel) and a patient with pathological tremor ((b), right panel). The 99% confidence limit is depicted by red dashed line. For the peaks exceeding the 99% confidence limit, the peak area (red filling in (b), right panel) was calculated. N_r denotes the number of motor unit discharges.

amplitude for each of the AO, WE, and PO tasks, respectively, and the repetition with the lowest tremor amplitude for the RE task. This yielded one value for each type of task (AO, WE, and PO) for each patient.

3.5. Assessing the Discriminative Power of the Tremor Metrics. The presented metrics were combined with metrics describing the patient's demographics (age, gender) and tremor etiology (tremor onset, tremor duration, tremor severity, results on UPDRS/Fahn-Tolosa scale, family history, medications, and predominance). In total, 194 tremor metrics were analyzed. The discriminatory power of each extracted metric was evaluated using the receiver operating characteristics (ROC) curve. In particular, we used the following metrics: area under the ROC curve (AUC) with its corresponding 95% confidence interval (95% CI); specificity (Sp); sensitivity (Se); positive predictive value (PPV); and negative predictive value (NPV). The ROC curve describes the performance of different models based on varying threshold values, and thus allows selecting the optimal operating point [39]. In our study, the optimal operating point was the best trade-off between sensitivity and specificity. Sensitivity denotes the ability of a prediction model to correctly classify all positive cases and specificity is the ability to correctly classify negative cases. In our study, ET patients were indicated as positive cases and PD patients as negative cases. PPV and NPV values provide additional insight into the robustness of the generated prediction models. PPV or precision is the proportion of true positives (ETs) among all the patients classified as positive. Analogously, NPV or false discovery rate is the proportion of true negatives (PDs) among all the patients classified as negatives. Additionally, a Mann–Whitney U test was used to compare the extracted metrics between PD and ET patients. The basic level of statistical significance was set at $p < 0.05$.

Finally, the aforementioned movement and neural drive metrics were tested against their discriminative power in decision support systems. We were interested in methods that provide a symbolic representation of the extracted knowledge and that implement a simple data mining model. Therefore, we gave preference to binary logistic regression and decision tree modeling algorithms instead of black-box approaches (e.g., neural networks, support vector machines). However, as in most of the statistical modeling methods, the drawback of logistic regression is that all the observations that contain missing values are ignored, resulting in a reduced data set. This can substantially weaken the predictive power of these models. This limitation is mitigated in decision tree algorithms, where surrogate splitting rules enable the use of other predictor variables to perform a split for observations

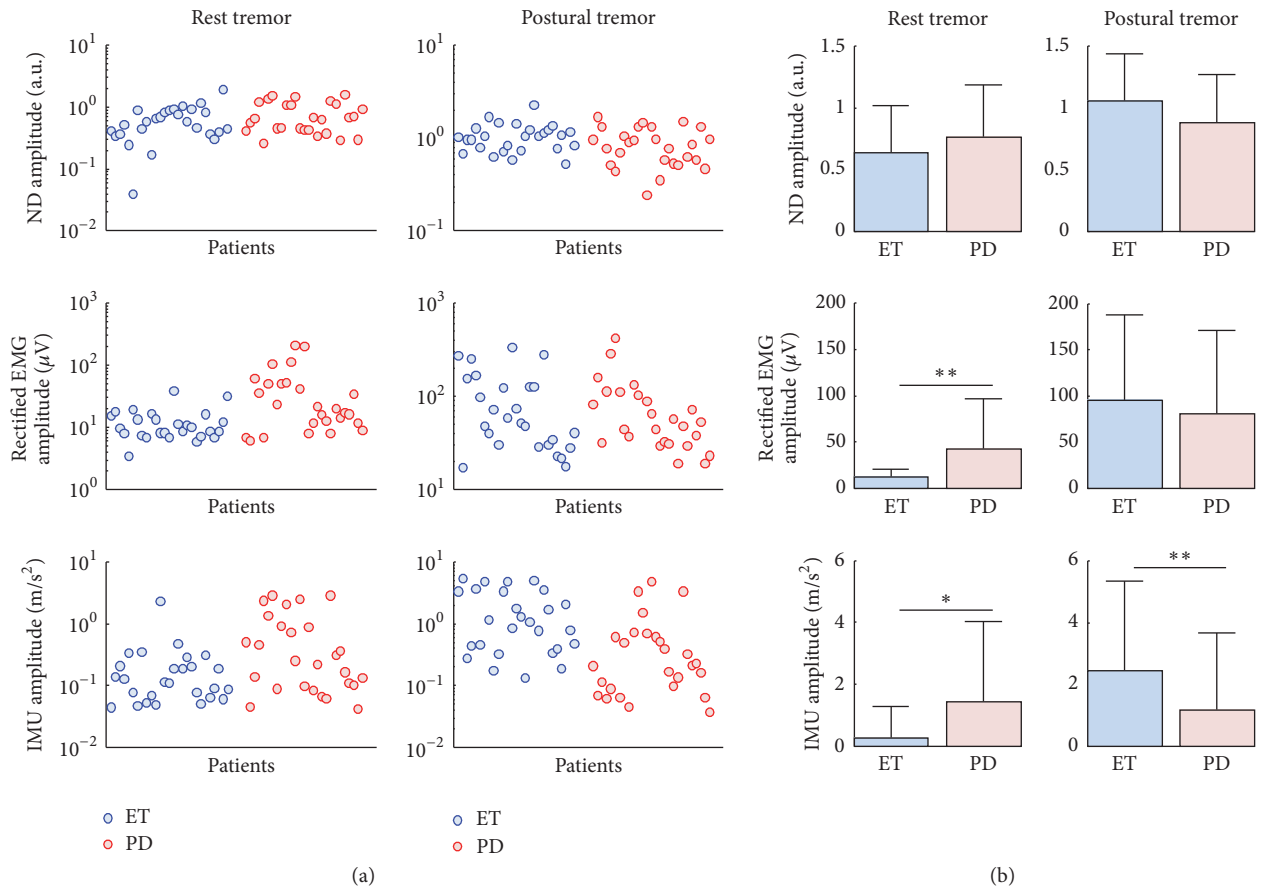

Figure 6: (a) Average amplitude of the rest and postural tremor in 54 ET and PD patients, as computed from the following: top: the neural drive (ND); middle: the spatial average of all the rectified EMG channels per muscle (EMG); and bottom: accelerometers (IMU). Tremor amplitude was assessed from the most affected muscle (ND and EMG) and from dominant tremor site (IMU). Each dot in the scatter plots represents one patient. The amplitude of the neural drive is expressed in arbitrary units (a.u.; see text). (b) Statistical comparison of the three different tremor amplitude estimates across ET and PD patients. $^{*}p < 0.05$ and $^{**}p < 0.01$ denote statistically significant difference as assessed by Kruskal-Wallis test.

with the missing values. We thus chose four different decision tree models, namely, CART [39], CHAID [40], C5.0 [41], and QUEST [42]. These four different algorithms differ basically in the splitting criteria. The CART (Classification and Regression Tree) algorithm uses the Gini index as splitting criterion [39]. The CHAID (Chi-Square Automatic Interaction Detector) algorithm uses chi-square tests of independence for evaluating an association between categorical variables [40]. The C5.0 algorithm, which is an improved version of the original Quinlan's C4.5 algorithm [41], defines each split based on the metric that provides the maximum information gain. In the QUEST (Quick, Unbiased, Efficient Statistical Tree) algorithm, the splits are determined by quadratic discriminant analysis using the selected input features on groups formed by the target categories [42].

The decision tree models were evaluated using tenfold cross-validation (see details in [43]). In this method, the original dataset is randomly partitioned into ten subsets. Then, in each of ten runs, a single subset is retained as testing set, while the remaining nine subsets are used as training data for computing the prediction model. Using this method, all the observations are used for both training and testing; each observation is used once for testing. The results from all ten models are then averaged to produce a single estimation of model performance.

4. Results

In total, ~20,500 motor units were identified with an accuracy above 90% according to the PNR metric [21]. The number of identified motor units did not depend significantly on the type of tremor triggering task (Kruskal-Wallis test, $p > 0.05$). A relatively large number of motor units was also identified in the rest condition in ET patients and during the postural tasks in PD patients. Figure 6 depicts the average rest and postural tremor amplitude in the 27 ET and 27 PD patients as derived from the neural drive, the spatially averaged rectified EMG and accelerometer data. Despite the statistically significant differences in tremor amplitude between ET and PD patients, none of these differences accurately discriminated ET and PD patients. This observation demonstrates the complexity of ET and PD tremor [2].

First we assessed the discriminative power of each of the metrics described above. Due to the large number of tested metrics, we only present the results for the tasks and metrics with highest discriminatory power (Tables 1 and 2). Tremor amplitude (N1) and tremor frequency (N2) in the neural drive did not significantly differ across ET and PD patients (Table 1, Figure 6). However, tremor symmetry in the dominant tremor hand (N3) was significantly different between ET and PD patients, especially during the AO and WE tasks. These differences further increased when we normalized the dominant tremor hand symmetry for the AO task with its corresponding value for the RE task (Table 1). The neural drive metric that best discriminated across tremor types was the normalized global tremor symmetry (N7) in the AO task (AUC = 0.94, Se = 85.2, Sp = 96.2), followed by the same tremor symmetry metric during the WE task (AUC = 0.90, Se = 85.2, Sp = 100.0). The second most discriminative metric was the normalized coefficient of variation of the pairwise motor unit synchronization (N9) during the AO task (Table 1). Notably, neural drive metric N7 outperformed all movement-related metrics at tremor discrimination (Table 2), as expected, because it captures more subtle aspects of the neural mechanisms of each condition. Figure 7 shows the N6, N7, N8, and N9 metrics for the AO and RE tasks. Note that the normalization of metrics during postural tremor triggering tasks with their values during the RE task significantly increased the discriminative power.

To test the added value of analyzing the neural drive via cumulative spike trains rather than EMG data, we compared the discriminative power of the normalized global tremor symmetry (N7) metric in the AO task as assessed from (1) the neural drive (low-pass filtered cumulative MU spike train); (2) a single rectified EMG channel (the channel with the maximal EMG energy per muscle); and (3) the spatial average of all the rectified EMG channels in the investigated muscle. We employed the same exact methodology in all three cases. The symmetry index computed from the channel with maximum EMG energy misclassified 8 ET and 10 PD patients (Se = 70.4, Sp = 63.0, PPV = 65.5, NPV = 68.0). The symmetry index obtained from all rectified EMG channels performed slightly better, but still misclassified 7 ET and 7 PD patients (Se = 74.1, Sp = 74.1, PPV = 74.1, NPV = 74.1). In clear contrast, the symmetry index calculated from the neural drive only misclassified 4 ET and 2 PD patients. These results support our statement that characterizing the neural drive to muscle based on the cumulative motor unit spike train outperforms other tested measures, likely because it provides the most precise characterization of the effective output of the innervating motoneurons.

Among the movement metrics, the highest AUC (AUC = 0.83, Se = 88.9, Sp = 70.4) was obtained with the M2 metric (mean log power of all the harmonics) of the nondominant tremor hand, averaged over the AO, WE, and PO tasks and normalized by the RE task (Table 2). The metric M1 during the AO (for the nondominant tremor hand) and WE tasks (for the dominant tremor hand) and normalized on RE task also achieved good performance (Table 2). Overall, the discriminative power of the movement metrics was slightly lower in the dominant than in nondominant tremor hand.

After testing the discriminative power of individual metrics, we compared the performance of the different decision tree algorithms. Among the tested decision tree algorithms (Section 3.5), the best predictive power was obtained using the CHAID algorithm (Figure 8). The overall accuracy of the induced model on the whole dataset was 94.4%. All the PD patients were correctly classified and only 3 ET patients were misclassified (AUC = 0.99 (0.98, 1.00), Se = 88.5, Sp = 100.00, PPV = 100.0, NPV = 90.0). The tenfold cross-validated risk estimate for the final tree was calculated as the average of the risks for all of the ten trees (Risk = 0.189, Std. Error = 0.054).

Only three metrics were automatically selected by the final CHAID model:

(i) The normalized global tremor symmetry for the AO task normalized by the same metric for the RE task (N7)

(ii) The normalized coefficient of variation for the motor unit synchronization index (N9) during the AO task in dominant tremor hand

(iii) The mean log power of all the movement harmonics, averaged over the AO, PO, WE, and RE tasks, for the nondominant tremor hand (M2).

Notably, these three metrics were proposed in this study, which highlights the potential impact of these novel methods. The most discriminative metric, the neural drive symmetry for the AO task normalized by the RE task (N7), was placed in the root of the decision tree. The cut-off point $T = 1.555$ clearly divided 25 PD patients, with parameter value lower or equal to T, from 23 ET patients (Figures 7 and 8). Thus, PD patients exhibited higher neural drive symmetry in the RE task than in the AO task, whereas the opposite was true for the ET patients (note that this result could not have been drawn from the rectified surface EMG). The other two metrics were used in the second level of the decision tree, thereby improving classification accuracy to accurately diagnose 2 additional PD patients. The ET patients exhibited lower variability in motor unit synchronization for the RE task than the PD patients (Figure 7). The interpretation of M2 splitting rules is more difficult, mainly due to the complex relationship between muscle activation dynamics and movement discussed above.

To further test the performance of our decision tree system for tremor diagnosis, we applied it on the data from the six additional patients (test group) that had not been included in the training datasets. Remarkably, all these six additional patients received the model-based diagnosis that matched the clinical diagnosis. This result highlights the potential of our model to generalize to new (unprocessed) patients.

5. Discussion

In this study we tested 194 tremor metrics (many of them proposed herein) with the goal of developing a computer-based system to diagnose ET and PD tremor. Despite this large number of metrics, the most successful data mining model relied only on three metrics we proposed: the global tremor symmetry in the AO task normalized to the RE

Table 1: Most discriminative tremor metrics, extracted from hdEMG recordings. The best cut-off value was selected as closest to upper left corner in the ROC curve. Normalization of values in postural condition to the ones in rest condition increased discriminative power of metrics. For informative reasons, the tremor amplitude and tremor frequency as assessed from the neural drive are also listed, though none of them adequately discriminated the ET and PD patients.

Symbol	Metric	Task	Hand	Cut-off	Sensitivity (%)*	Specificity (%)*	AUC (95% CI)	PPV (%)*	NPV (%)*	*U* value	*p* value
N1	Tremor amplitude in neural drive	AO	ND	0.630	59.3	51.9	0.54 (0.38, 0.70)	55.2	56.0	337.0	0.634
		WE	D	0.584	63.0	77.8	0.69 (0.54, 0.83)	73.9	67.7	228.0	0.018
N2	Tremor frequency in neural drive	AO	ND	6.248	40.7	63.0	0.41 (0.26, 0.57)	52.4	51.5	301.0	0.270
		WE	D	5.749	63.0	51.9	0.53 (0.37, 0.69)	56.7	58.3	345.0	0.734
N3	Dominant hand tremor symmetry	AO	ND	0.059	74.1	63.0	0.73 (0.59, 0.86)	66.7	70.8	199.0	0.004
		WE	D	0.079	85.2	74.1	0.79 (0.65, 0.92)	76.7	83.3	156.5	<0.001
N3	Normalized dominant tremor hand symmetry[1]	AO	D	1.446	85.2	74.1	0.89 (0.80, 0.98)	76.6	83.3	81.0	<0.001
N4, N5	Mean interlimb tremor symmetry in extensors and flexors[2]	AO	both	0.035	77.8	77.8	0.75 (0.61, 0.89)	77.8	77.8	185.0	0.002
		WE	both	0.033	81.5	59.3	0.71 (0.56, 0.85)	66.7	76.2	213.5	0.009
N7	Normalized global tremor symmetry[3]	AO	both	1.555	85.2	96.2	0.94 (0.86, 1.00)	95.8	86.7	45.0	<0.001
		WE	both	1.672	85.2	100	0.90 (0.79, 1.00)	100	87.1	76.5	<0.001
N9	Normalized coefficient of variability for motor unit synchronization[4]	AO	both	0.244	74.1	74.1	0.76 (0.63, 0.90)	74.1	74.1	172.0	0.001
		WE	both	0.253	55.6	81.5	0.67 (0.52, 0.82)	75.0	64.7	240.0	0.031

*ET patients: positive samples; PD patients: negative samples; [1]normalized to RE task; [2]mean value of metrics N4 and N5; [3]metric N7 represents N6, normalized to RE task; [4]metric N9 represents N8, normalized to RE task; D: dominant tremor hand; ND: nondominant tremor hand.

Table 2: Most discriminative tremor metrics, extracted from inertial recordings of ET and PD patients. The best cut-off value was selected as closest to upper left corner in the ROC curve. Normalization of values in postural condition to the ones in rest condition increased discriminative power of metrics.

Symbol	Metric	Task	Hand	Cut-off	Sensitivity (%)*	Specificity (%)*	AUC (95% CI)	PPV (%)*	NPV (%)*	*U* value	*p* value
M1	*Mean Log power of all harmonics*, modified from Muthuraman et al. [18]	AO	ND	−7.579	88.9	59.3	0.74 (0.60, 0.88)	68.6	84.2	190.0	0.003
		WE	D	−5.517	74.1	70.4	0.74 (0.60, 0.88)	71.4	73.1	189.0	0.002
		AO[1]	ND	0.983	77.8	85.2	0.82 (0.71, 0.94)	84.0	79.3	128.0	<0.001
		WE[1]	D	1.416	77.8	74.1	0.82 (0.71, 0.93)	75.0	76.9	129.0	<0.001
M2	*Average of mean Log power of all the harmonics*, modified from Muthuraman et al. [18]	AO, PO, WE, RE[2]	D	−6.770	74.1	51.9	0.60 (0.44, 0.76)	60.6	66.7	292.0	0.210
			ND	−7.246	81.5	55.6	0.68 (0.54, 0.83)	64.7	75.0	231.0	0.021
		AO, PO, WE, RE[2*]	D	0.872	74.1	74.1	0.76 (0.62, 0.90)	74.1	74.1	175.0	0.001
			N	0.659	85.2	70.4	0.83 (0.71, 0.95)	74.2	82.6	126.0	<0.001
		AO, PO, WE[3]	D	−6.251	77.8	63.0	0.72 (0.58, 0.86)	67.7	73.9	205.0	0.006
			ND	−6.669	77.8	66.7	0.75 (0.61, 0.88)	70.0	75.0	185.0	0.002
		AO, PO, WE[3*]	D	1.494	66.7	81.5	0.82 (0.71, 0.93)	78.3	71.0	133.0	<0.001
			ND	0.856	88.9	70.4	0.83 (0.71, 0.95)	75.0	86.4	123.0	<0.001
M3	*Basic tremor frequency power*, [18]	AO, PO, WE, RE[2]	D	0.019	66.7	59.3	0.64 (0.49, 0.79)	62.1	64.0	264.0	0.082
		AO, PO, WE, RE[2*]	D	12.770	66.7	92.6	0.82 (0.71, 0.93)	90.0	73.5	131.0	<0.001
		AO, PO, WE[3]	ND	0.011	74.1	66.7	0.74 (0.60, 0.87)	69.0	72.0	192.0	0.003
		AO, PO, WE[3*]	ND	12.820	74.1	81.5	0.78 (0.66, 0.92)	80.0	75.9	155.0	<0.001
M4	*Mean power of the tremor harmonics*, [18]	AO, PO, WE, RE[2]	D	0.005	77.8	55.6	0.65 (0.49, 0.80)	63.6	71.4	258.0	0.065
			ND	0.003	77.8	63.0	0.71 (0.57, 0.85)	67.8	73.9	212.0	0.008
		AO, PO, WE, RE[2*]	D	7.901	66.7	85.2	0.82 (0.71, 0.93)	81.8	71.9	133.0	<0.001
			ND	7.567	66.7	81.5	0.79 (0.66, 0.92)	78.3	71.0	154.0	<0.001
		AO, PO, WE[3]	D	0.013	66.7	85.2	0.74 (0.60, 0.88)	81.8	71.9	188.0	0.002
		AO, PO, WE[3*]	D	10.201	66.7	85.2	0.82 (0.71, 0.93)	81.8	71.9	131.0	<0.001

ET patients: positive cases; PD patients: negative cases; [1]normalized to RE task; [2]averaged through all tasks (not normalized to RE task); [2]averaged through all the tasks and normalized to RE task; [3]averaged on postural tasks (not normalized to RE task); [3*]averaged on postural tasks and normalized to RE task; D: dominant tremor hand; ND: nondominant tremor hand.

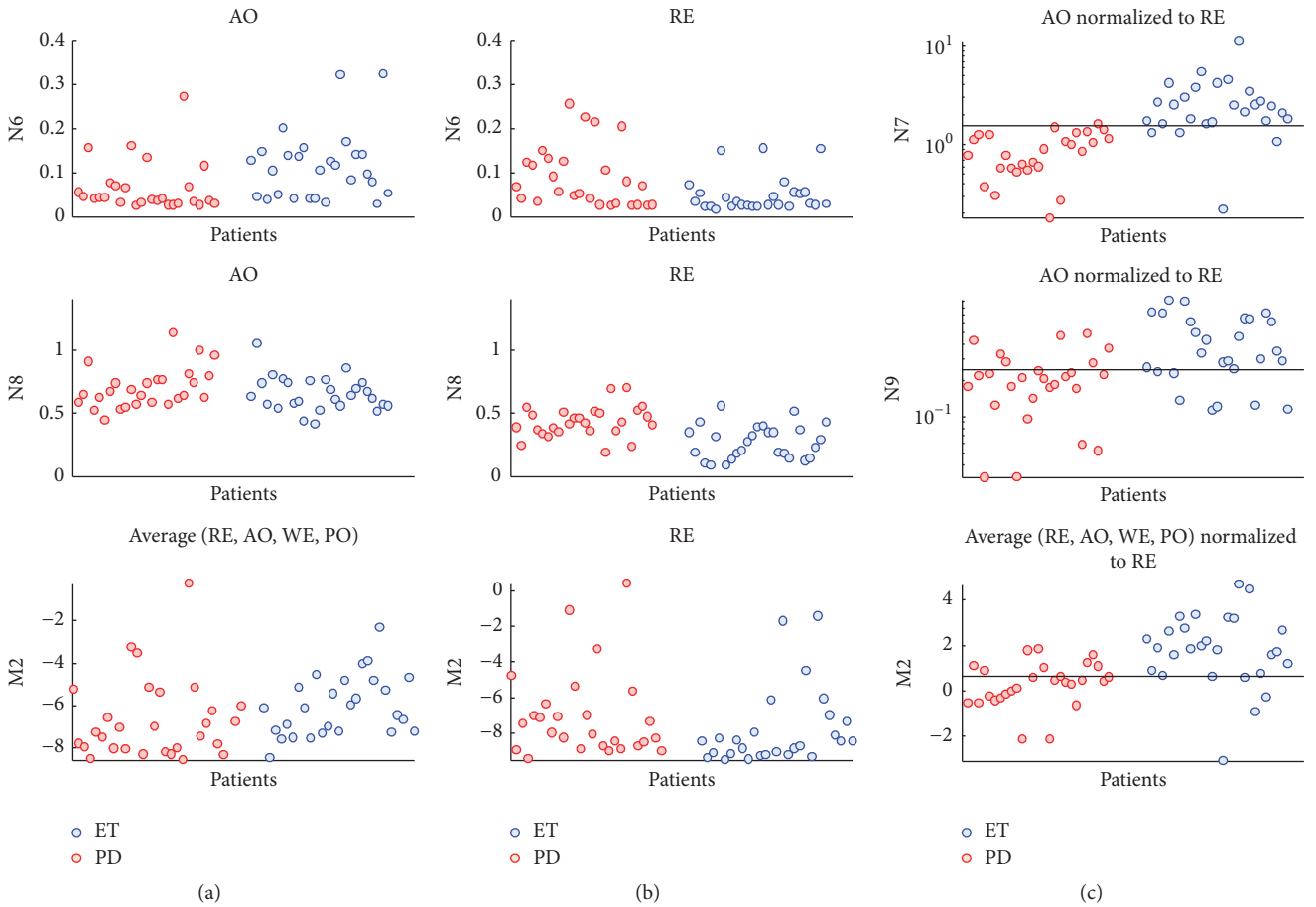

Figure 7: Values of the global tremor symmetry (N6 and N7), the coefficient of variation for pairwise motor unit synchronization (N8 and N9), and the mean log power of all the harmonics (M2) metrics in the postural (AO, WE, and PO) and rest (RE) conditions. Normalization of the metrics during postural tasks with respect to their values during the RE task significantly increased the power to discriminate between ET and PD patients (c). The black horizontal lines depict the best cut-off values as listed in Tables 1 and 2.

task (N7); the coefficient of variation for the pairwise motor unit synchronization (N9) in the AO task normalized to the RE task; and the mean log power of all the harmonics averaged over the AO, PO, WE, and RE tasks (M2) in the nondominant tremor hand. The same three tremor metrics were also proposed by logistic regression (results not shown). Critically, the two metrics that best discriminated tremor types were based on the analysis of motor unit activity. This indicates that accurate computer-aided tremor diagnosis benefits from examining fine aspects of neural control that are not detectable with raw surface EMG recordings.

There are several possible explanations why the neural drive metrics (especially tremor symmetry) are more informative than the wrist movement metrics. First of all, the tremulous neural drive may be subtle and obscured by substantial simultaneous voluntary and/or involuntary cocontraction of several antagonistic muscles, which may stabilize the controlled joint and, thus, mask the tremor component of movement. Second, due to the intrinsic complexity of the tremor dynamics [21], the tremor may shift from one muscle to another or may affect the whole group of muscles during the entire trial. When those muscles control the same joint, the changes of their net mechanical effect can be relatively small or relatively complex and, thus, difficult to interpret and quantify from movement measurements. Third, the interactions among synergistic and antagonistic muscles likely affect the harmonics of the wrist movement, but this effect is highly complex and difficult to interpret from wrist movements. Assessments of the neural drive to individual muscles provide more precise insight into the underlying neural mechanisms of tremor, which likely explains why it is the basis for the most discriminative metrics.

In pathological tremor, the motor unit firing patterns that ultimately cause the tremulous movement depend on the strength of the descending common tremor drive to the motoneuron pool; the concomitant voluntary drive, if present; afferent feedback from receptors within the same muscle and from other muscles; the intrinsic motoneuron properties; and the level of synaptic noise [20, 21]. By summing motor unit spike trains together into CST, the intrinsic noise components of many motoneurons average out, revealing their time-varying common input [21, 36, 44, 45]. Autocorrelation function of neural drive further emphasizes the rhythmic (synchronous) motor neuron activities

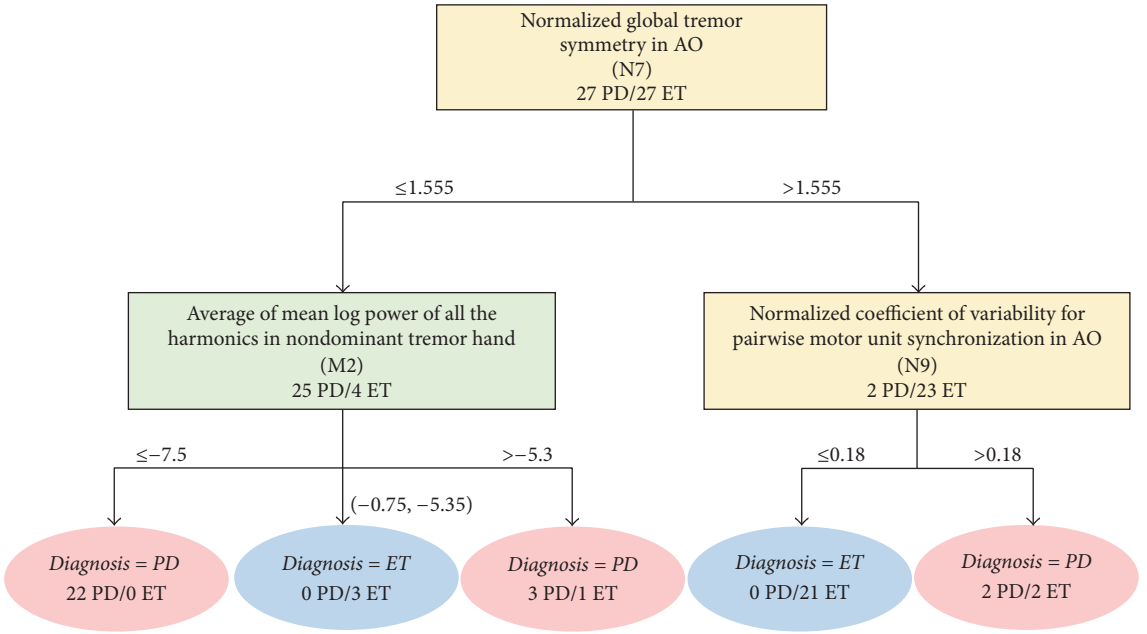

Figure 8: Decision tree, induced by CHAID algorithm on the data from 27 ET and 27 PD patients. Rectangles depict neural drive (yellow) and movement (green) metrics. Red and blue ellipses depict PD and ET diagnosis, as predicted by the model. "Normalized global tremor symmetry in AO" (N7) metric discriminated 25 PD and 23 ET patients. Additional 3 ET and 2 PD patients were discriminated by "average of mean log power of all the harmonics in non-dominant tremor hand" (M2) and "normalized coefficient of variability for pairwise motor unit synchronization in AO" (N9) metrics, respectively. Three ET patients were misdiagnosed by this model.

and suppresses the asynchronous ones. When extended to several muscles, this analysis of neural drive may provide also an insight into the tremor drive projections to neighboring muscles [35] or even compartments within the same muscle [46].

Critically, this detailed assessment of the neural drive is unlikely to come from classical EMG measures, such as the EMG power spectrum or the rectified EMG, because, contrary to CSTs, these measures reflect both the tremor-related input to the muscle and the undesired effects of muscle anatomy and geometry on the EMG [25, 28]. The latter aspects are not relevant for the neural control of movement and thus constitute "biological noise" from a data processing point of view. This "noise" is mostly due to the negative influence of the MUAP shapes (see, e.g., [25, 30–32, 47]), caused by the heterogeneity of subcutaneous tissues and the (close to) random motor unit distribution within the muscle tissue [27]. In fact, the EMG power spectrum can be directly expressed as the sum of the MUAP spectra, weighted by motor unit discharge rates [25]. The CSTs, analyzed in this study, are not sensitive to MUAP shapes (nor to muscle geometry and anatomy) and thus constitute much more appropriate means for characterizing the tremulous drive than the rectified EMG. In this regard, here we clearly demonstrated the negative effect that a single surface electrode placement has on the assessment of pathological tremor characteristics (Figure 1). We also showed that metrics based on the rectified EMG have less discriminative power than metrics based on the summed motor unit spike trains. This was true even when we minimized the impact of electrode location by averaging the rectified EMG over all 60 EMG channels in the electrode matrix whereat the electrode matrix covered most of the skin above the muscle of interest (see Section 4).

Possibly due to the aforementioned very high sensitivity of our tremor identification metrics, we found that all the tested ET and PD patients had tremor in the tested rest and postural conditions (Figures 6 and 7). In several cases, the tremor was subclinical and almost invisible to the naked eye. Thus, further studies of this observation are required. However, all the three selected metrics, namely, the global symmetry (N6), the coefficient of variation for pairwise motor unit synchronization metrics (N8), and the mean log power of all the movement harmonics (M2), increased significantly their discriminative power when we normalized their values in the postural tasks by their value in the rest task (Tables 1 and 2, Figure 7). Critically, this indicates that, while tremor properties (and thus the values of our metrics) are similar across PD and ET patients during an individual task (Figure 7), they have very different trends when switching from rest to posture. In our study, both the global tremor symmetry and the coefficient of variation for the pairwise motor unit synchronization increased in the ET patients, whereas the increase was much smaller (or there even was a decrease) in the PD patients. Similar trends were observed in the wrist movement metrics.

An interesting observation from all of the experiments is that none of the demographics/clinical parameters (age,

gender, tremor onset, tremor duration, severity of tremor, results on UPDRS/Fahn-Tolosa scale, family history, medications, and predominance) was included in the models built by stepwise algorithms. This suggests that the proposed tremor metrics complement clinical parameters in discriminating ET and PD, thereby demonstrating their potential to aid diagnosis in complicated cases.

We also want to note that one of the three ET patients that were misclassified by the CHAID decision tree model was rediagnosed as PD more than one year after he was originally diagnosed by his neurologist. Another misclassified ET patient was rediagnosed as dystonic tremor with ET. The third misclassified ET patient experienced very mild tremor in all of the investigated tasks. These observations further highlight the potential of the proposed tremor metrics and the proposed decision model to aid clinical diagnosis of tremors. Also, importantly, these objective measures open the door to deriving metrics of patient response to different treatments and to drawing objective comparisons among interventions. Even though clinical diagnosis will remain the gold standard for tremor diagnosis, our data suggest that neural drive-based metrics may identify patient-specific peculiarities that are otherwise hard to detect, especially during the early stage of the disease when misdiagnosis is most common [7, 8]. Furthermore, due to their objectiveness and precision, these metrics may help guide patient follow-up and treatment.

There are two practical limitations that make the clinical use of neural drive metrics less attractive than movement metrics. First, the acquisition of hdEMG signals is more cumbersome and time consuming than movement recordings, which can be easily performed using inertial measurement units. Second, several muscles need to be recorded to compute the proposed metrics. These limitations may be mitigated in the near future by recent developments of unobtrusive and wireless surface EMG sensors, such as epidermal electronics [48]. We further acknowledge that, in this study, we only measured each patient in a single session. Thus, we were not able to assess the test-retest reliability. For the same reason, we could not evaluate the long-term tracking of tremor characteristics. Finally, we focused on the discrimination of ET and PD patients because these are the most prevalent types of tremor [1, 49]. The analyses of other types of tremor such as dystonic tremor are left for future work.

In summary, here we have introduced novel metrics to quantify and discriminate PD and ET tremor. In particular, we proposed metrics that characterize the temporal (CSTs), spatial (the normalized coefficient of variation for the pairwise motor unit synchronization), and cross-muscle tremor variability (neural drive symmetry). We showed that these metrics provide highly accurate insight into the characteristics of ET and PD tremor, and that they outperform metrics based on the rectified EMG and movement data. By demonstrating the discriminative power of the neural drive-based metrics on 30 ET and 30 PD patients, we confirmed our hypothesis that neural drive assessment provides novel insight into these pathologies.

Conflicts of Interest

The authors declare that they have no conflicts of interest.

Acknowledgments

This study was supported by the Commission of the European Union (Grant agreement no. ICT-2011.5.1-287739 "NeuroTREMOR: A novel concept for support to diagnosis and remote management of tremor"), by the Slovenian Research Agency (research core funding no. P2-0041 and the Project J2-7357 "Exact quantification of muscle control strategies and co-activation patterns in robot-assisted rehabilitation of hemiparetic patients"), and by Spanish government, MINECO (Research Grant DPI2015-72638-EXP). J. A. Gallego received funding from the Commission of the European Union (FP7-PEOPLE-2013-IOF-627384).

References

[1] G. K. Wenning, S. Kiechl, K. Seppi et al., "Prevalence of movement disorders in men and women aged 50-89 years (Bruneck Study cohort): a population-based study," *The Lancet Neurology*, vol. 4, no. 12, pp. 815–820, 2005.

[2] J. Benito-León and E. D. Louis, "Essential tremor: emerging views of a common disorder," *Nature Clinical Practice Neurology*, vol. 2, no. 12, pp. 666–678, 2006.

[3] R. J. Elble, "Origins of tremor," *The Lancet*, vol. 355, no. 9210, pp. 1113-1114, 2000.

[4] Y.-G. Park, H.-Y. Park, C. J. Lee et al., "CaV3.1 is a tremor rhythm pacemaker in the inferior olive," *Proceedings of the National Acadamy of Sciences of the United States of America*, vol. 107, no. 23, pp. 10731–10736, 2010.

[5] H. Wilms, J. Sievers, and G. Deuschl, "Animal models of tremor," *Movement Disorders*, vol. 14, no. 4, pp. 557–571, 1999.

[6] R. J. Elble, "Tremor: clinical features, pathophysiology, and treatment," *Neurologic Clinics*, vol. 27, no. 3, pp. 679–695, 2009.

[7] M. A. Thenganatt and E. D. Louis, "Distinguishing essential tremor from Parkinson's disease: bedside tests and laboratory evaluations," *Expert Review of Neurotherapeutics*, vol. 12, no. 6, pp. 687–696, 2012.

[8] S. Jain, S. E. Lo, and E. D. Louis, "Common misdiagnosis of a common neurological disorder: How are we misdiagnosing essential tremor?" *JAMA Neurology*, vol. 63, no. 8, pp. 1100–1104, 2006.

[9] S. Fahn, E. Tolosa, and C. Marín, "Clinical rating scale for tremor," in *Parkinson's Disease And Movement Disorders*, pp. 271–280, Williams and Wilkins, Baltimore, 1993.

[10] P. Martinez-Martin, A. Gil-Nagel, L. M. Gracia et al., "Unified Parkinson's disease rating scale characteristics and structure," *Movement Disorders*, vol. 9, no. 1, pp. 76–83, 1994.

[11] O. Cohen, S. Pullman, E. Jurewicz, D. Watner, and E. D. Louis, "Rest tremor in patients with essential tremor: prevalence, clinical correlates, and electrophysiologic characteristics," *JAMA Neurology*, vol. 60, no. 3, pp. 405–410, 2003.

[12] R. C. Helmich, I. Toni, G. Deuschl, and B. R. Bloem, "The pathophysiology of essential tremor and Parkinson's tremor," *Current Neurology and Neuroscience Reports*, vol. 13, no. 9, article 378, 2013.

[13] G. Deuschl, M. Lauk, and J. Timmer, "Tremor classification and tremor time series analysis," *Chaos: An Interdisciplinary Journal of Nonlinear Science*, vol. 5, no. 1, pp. 48–51, 1995.

[14] B. Hellwig, S. Häußler, B. Schelter et al., "Tremor-correlated cortical activity in essential tremor," *The Lancet*, vol. 357, no. 9255, pp. 519–523, 2001.

[15] B. Hellwig, B. Schelter, B. Guschlbauer, J. Timmer, and C. H. Lücking, "Dynamic synchronisation of central oscillators in essential tremor," *Clinical Neurophysiology*, vol. 114, no. 8, pp. 1462–1467, 2003.

[16] A. Hossen, M. Muthuraman, Z. Al-Hakim, J. Raethjen, G. Deuschl, and U. Heute, "Discrimination of Parkinsonian tremor from essential tremor using statistical signal characterization of the spectrum of accelerometer signal," *Bio-Medical Materials and Engineering*, vol. 23, no. 6, pp. 513–531, 2013.

[17] M. Muthuraman, U. Heute, K. Arning et al., "Oscillating central motor networks in pathological tremors and voluntary movements. What makes the difference?" *NeuroImage*, vol. 60, no. 2, pp. 1331–1339, 2012.

[18] M. Muthuraman, A. Hossen, U. Heute, G. Deuschl, and J. Raethjen, "A new diagnostic test to distinguish tremulous Parkinson's disease from advanced essential tremor," *Movement Disorders*, vol. 26, no. 8, pp. 1548–1552, 2011.

[19] J. A. Gallego, E. Rocon, J. O. Roa, J. C. Moreno, and J. L. Pons, "Real-time estimation of pathological tremor parameters from gyroscope data," *Sensors*, vol. 10, no. 3, pp. 2129–2149, 2010.

[20] J. A. Gallego, J. L. Dideriksen, A. Holobar et al., "Influence of common synaptic input to motor neurons on the neural drive to muscle in essential tremor," *Journal of Neurophysiology*, vol. 113, no. 1, pp. 182–191, 2015.

[21] J. A. Gallego, J. L. Dideriksen, A. Holobar et al., "The phase difference between neural drives to antagonist muscles in essential tremor is associated with the relative strength of supraspinal and afferent input," *The Journal of Neuroscience*, vol. 35, no. 23, pp. 8925–8937, 2015.

[22] A. Holobar, D. Farina, M. Gazzoni, R. Merletti, and D. Zazula, "Estimating motor unit discharge patterns from high-density surface electromyogram," *Clinical Neurophysiology*, vol. 120, no. 3, pp. 551–562, 2009.

[23] A. Holobar, V. Glaser, J. A. Gallego, J. L. Dideriksen, and D. Farina, "Non-invasive characterization of motor unit behaviour in pathological tremor," *Journal of Neural Engineering*, vol. 9, no. 5, Article ID 056011, 2012.

[24] A. s. Holobar and D. Zazula, "Multichannel blind source separation using convolution kernel compensation," *IEEE Transactions on Signal Processing*, vol. 55, no. 9, pp. 4487–4496, 2007.

[25] D. Farina and A. Holobar, "Characterization of Human Motor Units from Surface EMG Decomposition," *Proceedings of the IEEE*, vol. 104, no. 2, pp. 353–373, 2016.

[26] D. Farina, A. Holobar, R. Merletti, and R. M. Enoka, "Decoding the neural drive to muscles from the surface electromyogram," *Clinical Neurophysiology*, vol. 121, no. 10, pp. 1616–1623, 2010.

[27] A. Holobar and D. Farina, "Blind source identification from the multichannel surface electromyogram," *Physiological Measurement*, vol. 35, no. 7, pp. R143–R165, 2014.

[28] R. Merletti and D. Farina, *Surface Electromyography: Physiology, Engineering and Applications*, John Wiley & Sons, 2016.

[29] R. J. Elble and J. E. Randall, "Motor unit activity responsible for 8- to 12-Hz component of human physiological finger tremor," *Journal of Neurophysiology*, vol. 39, no. 2, pp. 370–383, 1976.

[30] S. J. Day and M. Hulliger, "Experimental simulation of cat electromyogram: evidence for algebraic summation of motor-unit action-potential trains," *Journal of Neurophysiology*, vol. 86, no. 5, pp. 2144–2158, 2001.

[31] K. G. Keenan, D. Farina, K. S. Maluf, R. Merletti, and R. M. Enoka, "Influence of amplitude cancellation on the simulated surface electromyogram," *Journal of Applied Physiology*, vol. 98, no. 1, pp. 120–131, 2005.

[32] K. G. Keenan, D. Farina, R. Merletti, and R. M. Enoka, "Amplitude cancellation reduces the size of motor unit potentials averaged from the surface EMG," *Journal of Applied Physiology*, vol. 100, no. 6, pp. 1928–1937, 2006.

[33] M. Chen and P. Zhou, "A novel framework based on FastICA for high density surface EMG decomposition," *IEEE Transactions on Neural Systems and Rehabilitation Engineering*, vol. 24, no. 1, pp. 117–127, 2016.

[34] S. H. Nawab, S.-S. Chang, and C. J. De Luca, "High-yield decomposition of surface EMG signals," *Clinical Neurophysiology*, vol. 121, no. 10, pp. 1602–1615, 2010.

[35] J. Raethjen, M. Lindemann, H. Schmaljohann, R. Wenzelburger, G. Pfister, and G. Deuschl, "Multiple oscillators are causing parkinsonian and essential tremor," *Movement Disorders*, vol. 15, no. 1, pp. 84–94, 2000.

[36] D. Farina, R. Merletti, and R. M. Enoka, "The extraction of neural strategies from the surface EMG: an update," *Journal of Applied Physiology*, vol. 117, no. 11, pp. 1215–1230, 2014.

[37] C. J. De Luca, A. M. Roy, and Z. Erim, "Synchronization of motor-unit firings in several human muscles," *Journal of Neurophysiology*, vol. 70, no. 5, pp. 2010–2023, 1993.

[38] R. J. Elble and J. McNames, "Using portable transducers to measure tremor severity," *Tremor and Other Hyperkinetic Movements*, vol. 6, 2016.

[39] L. Breiman et al., *Classification and Regression Trees*, CRC press, 1984.

[40] G. V. Kass, "An exploratory technique for investigating large quantities of categorical data," *Journal of Applied Statistics*, vol. 29, no. 2, pp. 119–127, 1980.

[41] J. R. Quinlan, *C4. 5: Programs for Machine Learning*, Morgan Kaufmann, 1993.

[42] W.-Y. Loh and Y.-S. Shih, "Split selection methods for classification trees," *Statistica Sinica*, vol. 7, no. 4, pp. 815–840, 1997.

[43] M. Kuhn and K. Johnson, *Applied predictive modeling*, Springer, New York, 2013.

[44] F. Negro and D. Farina, "Linear transmission of cortical oscillations to the neural drive to muscles is mediated by common projections to populations of motoneurons in humans," *The Journal of Physiology*, vol. 589, no. 3, pp. 629–637, 2011.

[45] D. Farina, F. Negro, and J. L. Dideriksen, "The effective neural drive to muscles is the common synaptic input to motor neurons," *The Journal of Physiology*, vol. 592, no. 16, pp. 3427–3441, 2014.

[46] D. A. Keen and A. J. Fuglevand, "Common Input to Motor Neurons Innervating the Same and Different Compartments of the Human Extensor Digitorum Muscle," *Journal of Neurophysiology*, vol. 91, no. 1, pp. 57–62, 2004.

[47] D. Farina, C. Cescon, F. Negro, and R. M. Enoka, "Amplitude cancellation of motor-unit action potentials in the surface electromyogram can be estimated with spike-triggered averaging," *Journal of Neurophysiology*, vol. 100, no. 1, pp. 431–440, 2008.

[48] D.-H. Kim, N. Lu, R. Ma et al., "Epidermal electronics," *Science*, vol. 333, no. 6044, pp. 838–843, 2011.

[49] J.-P. Bach, U. Ziegler, G. Deuschl, R. Dodel, and G. Doblhammer-Reiter, "Projected numbers of people with movement disorders in the years 2030 and 2050," *Movement Disorders*, vol. 26, no. 12, pp. 2286–2290, 2011.

Hindawi
Complexity
Volume 2017, Article ID 9078541, 13 pages
https://doi.org/10.1155/2017/9078541

Research Article

Monitoring Effective Connectivity in the Preterm Brain: A Graph Approach to Study Maturation

M. Lavanga,[1,2] O. De Wel,[1,2] A. Caicedo,[1,2] K. Jansen,[3,4] A. Dereymaeker,[3] G. Naulaers,[3] and S. Van Huffel[1,2]

[1]*Department of Electrical Engineering (ESAT), STADIUS Center for Dynamical Systems, Signal Processing and Data Analytics, KU Leuven, Leuven, Belgium*
[2]*imec, Leuven, Belgium*
[3]*Department of Development and Regeneration, Neonatal Intensive Care Unit, UZ Leuven, Leuven, Belgium*
[4]*Department of Development and Regeneration, Child Neurology, UZ Leuven, Leuven, Belgium*

Correspondence should be addressed to M. Lavanga; mlavanga@esat.kuleuven.be

Received 12 May 2017; Revised 28 July 2017; Accepted 6 September 2017; Published 17 October 2017

Academic Editor: Mirjana Popović

Copyright © 2017 M. Lavanga et al. This is an open access article distributed under the Creative Commons Attribution License, which permits unrestricted use, distribution, and reproduction in any medium, provided the original work is properly cited.

In recent years, functional connectivity in the developmental science received increasing attention. Although it has been reported that the anatomical connectivity in the preterm brain develops dramatically during the last months of pregnancy, little is known about how functional and effective connectivity change with maturation. The present study investigated how effective connectivity in premature infants evolves. To assess it, we use EEG measurements and graph-theory methodologies. We recorded data from 25 preterm babies, who underwent long-EEG monitoring at least twice during their stay in the NICU. The recordings took place from 27 weeks *postmenstrual age* (PMA) until 42 weeks PMA. Results showed that the EEG-connectivity, assessed using graph-theory indices, moved from a small-world network to a random one, since the clustering coefficient increases and the path length decreases. This shift can be due to the development of the thalamocortical connections and long-range cortical connections. Based on the network indices, we developed different age-prediction models. The best result showed that it is possible to predict the age of the infant with a *root mean-squared error* ($\sqrt{\text{MSE}}$) equal to 2.11 weeks. These results are similar to the ones reported in the literature for age prediction in preterm babies.

1. Introduction

The brain can be seen as a complex network of interacting regions and hierarchical communications, which are constrained by the anatomy, but not limited to it [1]. The neuronal clusters can actually work together and communicate to perform a joint task beyond their structural locations. The clinical literature [2] distinguishes this type of connectivity from the anatomical one, which is often called structural. The consequence of this functional infrastructure is the generation of complex electrophysiological patterns, which are temporally correlated, by distant cerebral areas [3]. Those spatiotemporal patterns are dynamic; they change according to the individual development trajectory [4]. In particular, the last trimester of gestation is a period of brain development, which includes both anatomical rewiring [5] and electrophysiological modifications [6]. Different authors illustrated that the cortical regions undergo differentiation, folding, and gyrification, while the subcortical areas experience synaptogenesis and myelination as well as neural pruning to establish thalamocortical connections or long distance cortical connections [7, 8]. Based on MRI scans of preterm babies, Dubois et al. [8] showed that the white matter volume and the inner cortical surface increase with gestational age. Furthermore, the same author [8, 9] demonstrated that fractional anisotropy (FA) of the brain fiber bundles increases with postbirth maturation, although the different connection pathways seem to develop in an asynchronous way. According to Batalle et al. [5], FA is a measure of anatomical directivity that describes the connectivity

strength among brain regions together with the density and the percentage of connecting streamlines. Hüppi and Dubois [9] eventually argued that diffusion tensor imaging parameters, such as anisotropy, can be structural markers of network functional organization [5]. A possible implication is that the temporal correlation among brain regions is also expected to change since the functional connectivity is related to the structural topology [1]. However, less is known about functional connectivity and maturation [10]. Therefore, functional connectivity in developmental science received increasing attention in recent years [1]. Moreover, different tools to describe functional connectivity became available in the last two decades. According to Bullmore and Sporns [11], brain networks can be represented as a graph, where the nodes are brain regions and the edges are the connection strengths. The nodes are defined by the neural activity, while the edges define the presence of a coupling between time series and the associated weight represents the coupling degree. Friston [12] recognizes two main types of functional connectivity: the actual functional connectivity, which investigates the temporal correlation among signals, and the effective connectivity, which measures the causality of the coupling. While the former does not imply any directionality, the second one highlights which area or node causes the activity of other ones. Functional connectivity methods generate undirected graphs, while the effective connectivity methods are associated with directed graphs [11]. In different studies of the preterm infant brain [5, 13], the neural activity has been measured using fMRI. Although this neuroimaging technique can investigate the subcortical structures, it is an expensive method and it is not suitable to measure effective connectivity due to fMRI low temporal resolution [14]. In contrast, EEG is a suitable measurement for effective connectivity and has been employed in recent papers to study the brain connectivity maturation [14, 15]. The main drawbacks of those studies are the limited investigated maturation period or the absence of graph-theory metrics to investigate the connectivity changes. Studies about the long term development of effective connectivity based on EEG have not been performed yet. In particular, there is a lack of research that investigates the effective connectivity from birth until full-term age in premature infants. Furthermore, in the literature, there are a few works that study the connectivity maturation in the preterm brain from a graph point of view [5, 13]. The main aim of the present study was a thorough investigation of the effective connectivity evolution during the preterm maturation after birth, exploiting different network metrics (as in [5]). In particular, we measured the effective connectivity by means of transfer entropy [16] and Granger causality [17]. On the obtained directed graph, different graph metrics were computed to track their evolution from 27 to 42 postmenstrual age (PMA) weeks. The network analysis was complemented by a regression study to predict the age of the patient and assess the predictive power of the connectivity analysis (as performed in one of our previous studies [15]). The paper is organized as follows: in Section 2, we introduce the simulated and the real dataset alongside the methods used to estimate effective connectivity. In Section 2, the applied graph-theory metrics are also discussed. Section 3 reports the results, while Section 4 includes our discussion on the reported results.

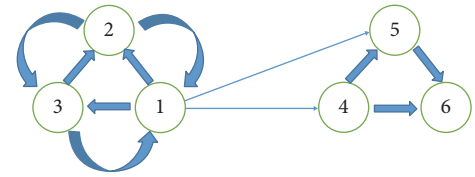

Figure 1: The figure displays the graph associated with model (1).

2. Methods

2.1. Data. Different datasets were used. A simulated dataset was also employed in order to show how connectivity analysis performs in a controlled case. In particular, the main objective of the simulation was to illustrate the meaning of the most common graph indices used in the literature. A dataset comprised of EEG signals was the main part of the maturation study.

2.1.1. Simulated Data. The first experiment of the study consisted of a simulation based on a linear Gaussian regression model (derived from [18]), expressed by the following equations:

$$\begin{aligned}
x_{1,t} &= 0.9x_{1,t-1} + 0.9\beta x_{2,t-1} + 0.7\beta x_{3,t-1} + \xi_{1,t},\\
x_{2,t} &= -0.9\beta x_{1,t-1} + 0.7\beta x_{3,t-1} + \xi_{2,t},\\
x_{3,t} &= 0.8\beta x_{1,t-1} + 0.7\beta x_{2,t-1} + \xi_{3,t},\\
x_{4,t} &= -0.25\beta x_{1,t-1} - 0.6x_{4,t-1} + \xi_{4,t},\\
x_{5,t} &= 0.25\beta x_{1,t-1} + 0.9\beta x_{4,t-1} + \xi_{5,t},\\
x_{6,t} &= 0.9\beta x_{4,t-1} + 0.9x_{5,t-1} - 0.7\beta x_{6,t-1} + \xi_{6,t}.
\end{aligned} \tag{1}$$

The parameter β is a scalar value that varies between 0 and 1 and it influences the strength of the coupling among the $x_{i,t}$ variables. The $\xi_{i,t}$ variables represent white noise with unit variance. The associated graph is reported in Figure 1. In order to give the reader a clear insight of the graph-theory measures, the objective of the simulation was twofold: firstly, we investigated the influence of the strength of the coupling, provided by the parameter β, and show the effect of the weakening of causality among the variables. Secondly, we investigated the influence of the noise using different levels of signal-to-noise ratio (SNR), which were obtained varying the variance of white noise in (1). In the latter objective, time series were simulated using the AR model (1) and the coupling was estimated with the effective connectivity methods discussed in the following paragraphs. We also studied the impact of filtering on the graph based metrics by computing the scores from filtered signals, using a sampling frequency which was set at 200 Hz and a band-pass filter between 1 and 80 Hz was applied on the simulated data. The reason to investigate the impact of filtering is explained in

Section 2.3. The band-pass frequencies were obtained from [19].

2.1.2. EEG Data. The second dataset comprised 25 preterm infants, with gestational age (GA) ≤ 32 weeks, who were recruited for a larger EEG study to assess brain development and automatically detect quiet sleep epochs [20, 21]. Each patient was enrolled with informed parental consent at the Neonatal Intensive Care Unit (NICU) of the University Hospital of Leuven, Belgium. All the included subjects presented good outcome at 2 years. EEG was recorded with 9 electrodes (Fp_1, Fp_2, C_3, C_4, T_3, T_4, O_1, O_2, and reference C_z) according to the 10–20 international system (BRAIN RT, OSG Equipment, Mechelen, Belgium). Throughout connectivity analysis, the channel C_z was disregarded. The measurements were performed twice during their stay in the unit, resulting in 88 recordings ranging from postmenstrual age of 27 weeks to 42 weeks. Mean time of recording EEG was 4 h 55 min. Monopolar signals were recorded at a sampling frequency of 250 Hz. Two independent EEG readers annotated the data for the different sleep stages, namely, quiet sleep (QS) and nonquiet sleep (NQS) epochs. The reason for this binary manual classification is due to the difficulty to discriminate active sleep from the awake state in the very young child.

2.2. Connectivity Analysis. The literature about effective connectivity presents different methods to assess coupling among time series, such as *directed transfer function* (DTF), *partial directed coherence,* or *Granger causality test* (GCT) [22]. With these approaches, the coupling is frequently defined as *G-causality* [23], in the sense that a time series Granger-causes another one when the past values of a time series significantly explain the evolution of the other one. Even though Granger himself pointed out the limited applicability to the bivariate case, the recently published conditional multivariate Granger causality (cMVGC) [24] overcomes the problem. According to [23, 25], these methods are based on the same multivariate or vector autoregressive (VAR) modeling. However, they can show different aspects in the causality analysis. While the DTF estimates the *reachability* from one channel to another (defined also as *G-influentiability* by [23]), both PDC and cMVGC look into the direct active link between two channels, which is defined as *G-connectivity* [23]. Those two methods investigate the same connectivity model in two different domains, which are the frequency (PDC) and time (cMVGC) domain. Since in this paper we are mainly interested in the time-domain coupling, we opted for the cMVGC in its autoregressive (AR) and information dynamics implementations, respectively, described in [18, 24].

2.2.1. Granger Causality. The first method employed to assess the *G-connectivity* among EEG channels was Granger causality (GC) with a VAR modeling framework. In the present study, we followed the formulation by [24]. A pth order multivariate autoregressive model VAR(p) takes the form

$$\mathbf{U}_t = \sum_{k=1}^{p} \mathbf{A}_k \cdot \mathbf{U}_{t-k} + \epsilon(t), \tag{2}$$

where $\mathbf{U}_t$ is a collection of process U_i, while $\mathbf{A}_k$ and $\epsilon(t)$ are, respectively, the regression coefficient matrices and the stochastic process residuals. In the conditional scenario [24], where we want to know the pairwise influence of process $\mathbf{X}_t$ over $\mathbf{Y}_t$ considering the presence of the other U_i variables, $\mathbf{U}_t$ can be rewritten as

$$\mathbf{U}_t = \begin{bmatrix} \mathbf{X}_t \\ \mathbf{Y}_t \\ \mathbf{Z}_t \end{bmatrix}, \tag{3}$$

where $\mathbf{X}_t$ and $\mathbf{Y}_t$ are the two time series of interest, while $\mathbf{Z}_t$ represents the third set of variables involved in the analysis. In our study, $\mathbf{X}_t$ and $\mathbf{Y}_t$ can be two variables $x_{i,t}$ in (1), for example, $x_{4,t}$ and $x_{5,t}$, or two EEG channels, for example, Fp_1 and C_3. Consequently, $\mathbf{Z}_t$ will be a vector time series which contain the remaining $x_{i,t}$ in (1) or the remaining EEG channels. Based on the VAR(p) model (2) and the split defined in (3), we may actually explain the future of $\mathbf{X}_t$ based on the following full and reduced regressions:

$$\begin{aligned} \mathbf{Y}_t &= \sum_{k=1}^{p} \mathbf{A}_{yy} \cdot \mathbf{Y}_{t-k} + \sum_{k=1}^{p} \mathbf{A}_{yx} \cdot \mathbf{X}_{t-k} + \sum_{k=1}^{p} \mathbf{A}_{yz} \cdot \mathbf{Z}_{t-k} \\ &\quad + \epsilon_y(t), \\ \mathbf{Y}_t &= \sum_{k=1}^{p} \widetilde{\mathbf{A}}_{yy} \cdot \mathbf{Y}_{t-k} + \sum_{k=1}^{p} \widetilde{\mathbf{A}}_{yz} \cdot \mathbf{Z}_{t-k} + \widetilde{\epsilon}_y(t). \end{aligned} \tag{4}$$

In both cases we consider the conditioning variable $\mathbf{Z}_t$, although only the first model considers explicitly the influence of $\mathbf{X}_t$. The difference is also highlighted by the two regression coefficient matrices $\mathbf{A}_{yy}$ and $\widetilde{\mathbf{A}}_{yy}$. In order to test whether the coefficient matrices $\mathbf{A}_{yx}$ are significantly different from zero, the Granger causality is defined as the log-likelihood ratio

$$\mathcal{F}_{X \to Y|\mathbf{Z}} = \log \frac{\left|\widetilde{\Sigma}_{yy}\right|}{\left|\Sigma_{yy}\right|}, \tag{5}$$

where Σ_{yy} and $\widetilde{\Sigma}_{yy}$ are the covariance matrices of the residuals $\epsilon_y(t)$ and $\widetilde{\epsilon}_y(t)$. Based on this multivariate framework, the G-causality basically quantifies the reduction of the prediction error if the variable X is added to explanatory variables of Y, one of which is the variable $\mathbf{Z}$ [24]. Unlike the classical Granger causality test limited to the bivariate case, we defined $\mathcal{F}_{X \to Y|\mathbf{Z}}$ *conditional multivariate Granger causality*. A special case of the conditional scenario is the pairwise conditional G-causality, where the pairwise effective couplings among all pair of variables U_i and U_j contained in $\mathbf{U}_t$ are measured. Since we take in account the spurious effect due to the presence of other variables (i.e., the coupling between U_i and U_j conditioned by the presence of the other variables), the pairwise conditional causalities are defined as

$$\mathcal{G}_{ij}(\mathbf{U}) = \mathcal{F}_{U_i \to U_j|\mathbf{U}_{[ij]}} \tag{6}$$

which is an $M \times M$ matrix, where M is the number of processes, and contains all the pairwise coupling estimations.

Those quantities may be considered a weighted directed graph, also known as *G-causal graph,* and the matrix $\mathcal{G}_{ij}$ as the associated adjacency matrix A. The G-causality was computed with the multivariate Granger causality toolbox [24] implemented in MATLAB (Mathworks, Natick, MA, USA).

2.2.2. Transfer Entropy. The second method applied to assess the *G-connectivity* among EEG channels was transfer entropy. According to the information dynamics framework by [16], the expected Kullback-Leibler divergence defines the transfer entropy (TE) from process X to process Y as follows:

$$T_{X\to Y} = \sum p\left(Y_t, \mathbf{X}_t^m, \mathbf{Y}_t^n\right) \log \frac{p\left(Y_t \mid \mathbf{X}_t^m, \mathbf{Y}_t^n\right)}{p\left(Y_t \mid \mathbf{Y}_t^n\right)}, \quad (7)$$

where $p(Y_t \mid \mathbf{X}_t^m, \mathbf{Y}_t^n)$ is the conditional probability that Y at times t is explained by past values of X and Y with respective memory order m and n. $p(Y_t \mid \mathbf{Y}_t^n)$ is the conditional probability that Y at times t is only explained by past values of Y. $p(Y_t, \mathbf{X}_t^m, \mathbf{Y}_t^n)$ is the joint probability distribution among the three variables Y_t, $\mathbf{X}_t^m$, $\mathbf{Y}_t^n$. Transfer entropy inherently implies directionality (i.e., effective connectivity), since it is asymmetric and contains transition probabilities [16, 26]. In order to estimate the information dynamics coupling, Montalto et al. [18] pointed out that TE is equivalent to the difference of two conditional entropies (CE)

$$T_{X\to Y|\mathbf{Z}} = H\left(Y_t \mid \mathbf{Y}_t^n, \mathbf{Z}_t^p\right) - H\left(Y_t \mid \mathbf{Y}_t^n, \mathbf{X}_t^m, \mathbf{Z}_t^p\right). \quad (8)$$

With respect to (7), the variable $\mathbf{Z}_t^p$ is here introduced. In a multivariate analysis, we cannot discriminate the exclusive relationship between two processes [17, 24]. However, it is possible to investigate the contribution of time series X in the evolution of time series Y with respect to all the other agents involved in the analysis. Consequently, we can actually define $\mathbf{Z}_t^p$ as a vector variable that does not contain neither Y nor X as past values and $T_{X\to Y|\mathbf{Z}}$ illustrates the transfer of information from X to Y taking into account other time series involved. If we assume that X, Y, $\mathbf{Z}$ have a joint Gaussian distribution, the two CE in (8) can be expressed as linear regression of past values of the vector variables involved in the multivariate system as follows:

$$\begin{aligned} Y_t &= A^u V^u + \epsilon(t), \\ Y_t &= A^r V^r + \epsilon(t). \end{aligned} \quad (9)$$

The first equation explains Y_t with a regression on the vector $V^u = [V_x, V_y, V_z]$, where V_x, V_y, V_z approximate respectively $\mathbf{X}_t^m$, $\mathbf{Y}_t^n$, $\mathbf{Z}_t^p$ with a vector of size p as follows:

$$\begin{aligned} V_x &= \left[X_{t-1}, X_{t-2}, \ldots, X_{t-p}\right], \\ V_y &= \left[Y_{t-1}, Y_{t-2}, \ldots, Y_{t-p}\right], \\ V_z &= \left[\mathbf{Z}_{t-1}, \mathbf{Z}_{t-2}, \ldots, \mathbf{Z}_{t-p}\right]. \end{aligned} \quad (10)$$

The second equation explains Y_t with a regression on the vector $V^r = [V_y, V_z]$, which only contains V_y, V_z. Equations (9) are usually referred to as full and restricted regressions. The reader can easily recognize the same structure of Granger causality equations (4), which is asymptotically equivalent to transfer entropy [16]. At the light of the previous results, $T_{X\to Y|\mathbf{Z}}$ can be rewritten as

$$T_{X\to Y|\mathbf{Z}} = \frac{1}{2} \log \frac{\sigma^r}{\sigma^u}, \quad (11)$$

where σ^r and σ^u are the variances of the white noise residuals in (9). Except for a scalar factor, (11) is the same expression of (5). It is important to notice that also TE estimates the *G-connectivity* in a conditioned framework. In the present study, the TE entropy has been computed using the MUTE toolbox [18] implemented in MATLAB (Mathworks, Natick, MA, USA).

2.2.3. Graph-Theory Indices. The effective connectivity methods generate an adjacency matrix A that describes a weighted directed graph [24], called *G-causal graph*. Unlike a binary network, those graphs tend to be complete or full without a specific thresholding and the adjacency matrix is asymmetric. Since the maximal number of couplings is $M^2 - M$ (where M is the number of signals), graph-theory measures can be used to summarize the causal connectivity [27]. Although there is no minimal theoretical number of graph nodes, 8 EEG channels can be considered quite limited for a graph analysis. However, there are studies in the neural processing literature where graph theory was applied on a limited number of time series in order to give a concise view of a high-density (or complete) network [27, 28], in particular if the sources-level is concerned. Bullmore and Sporns [11] illustrated a list of measures to describe the graph topology, such as the average characteristic path length, the clustering coefficient, and the diameter. The path length represents the minimum number of edges to reach each other node in the graph starting from one specific node. The average path length is the mean of the nodes' shortest paths and can be considered a measure of network integration capacity [5]. The latter can be also investigated by means of the clustering coefficient. In case of a weighted network, a clustering coefficient is defined as average intensity of all triangles around each node [29]. A common overall measure is the average of nodes clustering coefficients, defined in a similar way to the average path length. The last index to evaluate the integration capacity of the graph is the diameter. Let the node eccentricity be the maximum graph distance from one node to any other node in the network [30]. The diameter is then defined as the maximum eccentricity in the graph. All those indices have been computed thanks to the brain connectivity toolbox [31] implemented in MATLAB (Mathworks, Natick, MA, USA). In addition, we computed also the causal density as the sum of all significant couplings of the adjacency matrix, as defined by [32]. Alongside those network metrics, the spectral indices such as the spectral radius, the spectral gap, and the algebraic connectivity were considered. The spectral radius and the spectral indices were the maximal absolute eigenvalue and the difference between the first and the second absolute eigenvalues of the adjacency matrix, respectively [33, 34]. The

Table 1: An overview of all graph metrics that have been used in the study.

Overview of graph indices	
Path length	Mean of the nodes' shortest paths
Clustering coefficient	Mean of the nodes' triangles intensity around each node
Diameter	Maximum graph eccentricity
Causal density	Sum of all significant couplings in A
Spectral radius	$\lambda_1(A)$: first eigenvalue of adjacency matrix A
Spectral gap	$\lambda_1(A) - \lambda_2(A)$: the difference between the first two eigenvalues of matrix A
Algebraic connectivity	$\lambda_{M-1}(L_{\text{sym}})$: the second smallest eigenvalue of the Laplacian matrix L_{sym}

spectral radius, commonly known as "Page Rank," represents the dominance degree of a node in the network: the higher the value, the higher the centrality of the dominant node in the network. In other words, the dominant node behaves as the center of a hub [33]. Another way to look into the change of dominance is the spectral gap: if the difference between the first and second eigenvalues in the graph matrix decreases, the node with highest eigenvalue (the spectral radius) is less dominant with respect to the other nodes in the network. However, Estrada and Hatano [34] argued that the spectral gap behaves as a measure of clustering in the undirected graph: in case of lower values of spectral gap, the graph can present small clusters in the network. The last spectral measure is the algebraic connectivity, which is the second smallest eigenvalue of the Laplacian matrix L_{sym} and it illustrates how easily a graph can be divided into clusters [30]. In case of a directed graph, the Laplacian matrix can be obtained as follows:

$$\begin{aligned} L_{\text{dir}} &= D - A, \\ L_{\text{sym}} &= \frac{1}{2}\left(L_{\text{dir}} + L_{\text{dir}}^T\right) = D - \frac{A + A^T}{2}, \end{aligned} \tag{12}$$

where A is the adjacency matrix obtained by the effective connectivity tools described above and D is the degree matrix of the associated graph [35]. An overview of all graph indices is reported in Table 1.

2.3. Algorithmic Pipeline and Statistical Analysis. According to different authors [19, 36], filtering could add spurious connectivity in the effective connectivity analysis or make the estimation of the underlying Granger causality VAR model unstable. Although a theoretical invariance of causality estimation has been demonstrated under filtering, the G-causality works in practice if, and only if, the data are stationary. The use of filtering as mean to reach stationarity with filtering has already been investigated by [36]. However, three main reasons can undermine this approach. The first reason is the increase of the estimated VAR model order due to the fitting of *filtered* process of theoretical *infinite* order with a numerical *finite* order. This could lead to a poor, and not robust, parameter estimation or even unstable VAR model, which is the second reason to avoid band-pass filtering. The last reason is the ill-conditioning of the Toeplitz matrix of the autocorrelation sequence $\Gamma_k = \text{cov}(\mathbf{U}_t, \mathbf{U}_{t-k})$, which is necessary for VAR model estimation. All the related theoretical details are explained in [36]. The practical downsides of the band-pass filtering are the dramatic increase of the VAR model order compared to the unprocessed data or the increase of false positive detection of connectivity links with both the GC [36] and the PDC [19]. In particular, the amount of false detection increases with narrowing of the filtering frequency band or the increase of the filter order. In general there is no distinction between FIR and IIR filtering for both the authors. However, in both studies [19, 36], notch filtering and differentiation (or high pass filtering at 1 Hz) were pointed out as methods to keep the VAR model order low and reduce the false detection, even compared to unprocessed data. Those approaches help to achieve stationarity or keep the VAR model order low for nearly nonstationary processes like EEG. In addition, the presence of trends or seasonality can add unit-roots to the time series (poles on the unit circle or outside it in the complex plane), which violates the hypothesis of covariance stationarity. In the presence of unit-roots, the impulse response of the VAR model would be oscillatory or diverge to infinity. Consequently, it is suggested to eliminate trends and seasonality by first-order differentiation or differentiation at various lags (notch filtering). Theoretical and numerical details of the different type of filtering are reported in [24, 36]. Given the stated literature results, on the one hand, we decided to investigate the impact of filtering on the simulated data and, on the other hand, we applied only notch filtering at 50 Hz and 100 Hz and differentiation on the EEG data in order to reduce nonstationarities in the time series. However, the EEG can be affected by muscle artifacts, which can spread out among the different electrodes and bias the connectivity analysis. To mitigate this effect, we applied canonical correlation analysis (CCA) to remove the artifacts caused by the change in the EMG signals [37]. To investigate the effect of the CCA on the analysis, we compared the output of the connectivity analysis in two scenarios: the first one did not consider the usage of CCA; the second one applies CCA and reconstructed the EEG removing the 3 sources with lowest autocorrelation. In the first case, the authors segmented the EEG in 5 s windows and computed the effective coupling with both listed methods. In the second scenario, CCA was applied on 5 s EEG segments. However, before performing any connectivity analysis, we recombined the segments in 30 s intervals in order to increase the rank of the reconstructed EEG matrix. This step was required since both GC and TE request data that do not present collinearity (i.e., the time series matrix cannot be

rank-deficient [24]). The window length was suggested as a further step to keep time series stationarity [24]. For each recording, we computed the adjacency connectivity matrix for EEG segments and we averaged over the QS epochs and NQS epochs. This averaging step did not consider coupling values that were not statistically significant. According to [18, 24], the GC and TE follow an asymptotic F-distribution, like R^2 statistics. Therefore, an F-test was implemented to test the significance of coupling among EEG channels and all the couplings with $p > 0.05$ were set to zero. Consequently, $352 = 88 * 2 * 2$ coupling graphs were obtained, where 88 is the total number of recordings, 2 is the employed causality methods, 2 is the considered number of sleep states. On the average matrices we computed the network indices described above, which results in a tensor $88 \times 7 \times 4$, where 7 is the number of graph features and 4 is the number of combinations considering the number of connectivity methods and sleep states involved (TE in QS, TE in NQS, GC in QS, and GC in NQS). For each feature, we evaluated the maturation trend in three distinctive age groups ($\leq 31, \in (31-37), \geq 37$ PMA weeks) as median (IQR), where IQR is *InterQuartile Range*. Besides, we computed the Pearson correlation coefficient between the variable age and each single feature and its statistical significance were computed. Those results were meant to give a general overview of the feature maturation trend for each connectivity method, for each sleep state, with or without CCA preprocessing. In addition, we computed an ordinary least squares (OLS) regression for each single feature in case of GC during QS and the associated confidence interval at 95%, in order to give a visual representation of any network index prediction power. In particular, we split randomly the single graph index dataset 100 times in 70% training set and 30% testing set and we computed the prediction error on the test set as *root mean-squared error*, $\sqrt{\text{MSE}}$, as shown by [38]. Furthermore, each slice of the tensor (a matrix 88×7) was used to predict the patient's age at the moment of the recording with a multivariate linear regression. Similar to the single feature approach, we randomly split the dataset 100 times, as in [38] and we assessed $\sqrt{\text{MSE}}$ in the test set. At each iteration, R^2 index and the F-test statistics were computed.

3. Results

In the following paragraphs, the results obtained in both the simulated and the real dataset are discussed. In particular, we will show how the network indices behave in both examples, the simulated data and the EEG maturation dataset. The last part summarizes the predictive power of those graph metrics to infer the *postmenstrual age* of the subject.

3.1. Simulation Study. Figures 2(a), 2(b), and 2(c) display the integration graph indices for the AR model defined in (1), whose network is depicted in Figure 1. In the original model ($\beta = 1$), the graph presents two distinct clusters, which are loosely connected by the edges between node 1 and nodes 4 and 5. This two-hubs structure is reflected by Figures 2(a) and 2(b). When the intracluster connectivity is high ($\beta = 1$), the clustering coefficient reaches its highest level, while the path length is at its lowest level. Those results are in line with a rich-club or small-world network [11]. However, when the coefficient β starts decreasing, the clustering coefficient proportionally decreases, while the path length increases. The spectral radius decreases with vanishing values of β, as the clustering coefficient does. Figures 2(d), 2(e), and 2(f) display the ratio between the network indices estimated from the simulated time series via transfer entropy and the original measures (in particular, in (d), $\text{CC}_{\text{TE}}/\text{CC}_{\text{orig}}$, in (e), $\text{length}_{\text{orig}}/\text{length}_{\text{TE}}$, in (f), $\lambda_{\text{TE}}/\lambda_{\text{orig}}$). Different noise levels have been used. The results are quite straightforward for the clustering coefficient and the spectral radius: the higher the signal-to-noise ratio, the higher the values of two indices are and the closer they are to the original values (Figures 2(d) and 2(f)). In the case of the path length, the absolute value is decreasing with higher SNR. However, the estimated value becomes similar to the original one for very low noise variance (Figure 2(e)). Figures 2(d), 2(e), and 2(f) show also the effect on band-pass filtering on the graph indices estimation. The most remarkable results are related to the path length and the clustering coefficient. The estimated clustering coefficient tends to underestimate the original one, while the estimated path length tends to be persistently higher than the original one. On the contrary, the ratio for the spectral radius in case of filtering behaves similar to the one obtained using the raw data.

3.2. EEG Data: Graph Indices. Figure 3 shows graph metrics for the adjacency matrices obtained using the EEG measurements and Granger causality in QS (GC in QS). Figures 3(a), 3(b), 3(c), and 3(d) show the scatter plots with the fitted OLS regression model, while Figures 3(e) and 3(f) display the clustering coefficient and path length dynamics in three distinct age groups. As already mentioned in Section 2.3, Figure 3 gives a visual representation of the trends for the graph features, while Tables 2 and 3 provide a complete overview for all coupling methods and all sleep states. Each single feature has a significant trend with age, although the Pearson correlation coefficient ρ (%) increases when CCA is used as a preprocessing step. Specifically, the trend for the clustering coefficient, the spectral radius, and the spectral gap is negative, while the path length is increasing with age. This result is persistent in each method and each sleep state. The connectivity weakening for GC in QS is also reported in Figure 4, which shows the average connectivity graph for three distinct age groups. The three panels show how the coupling among time series decreases by the reduction in arrows width and the color shift from red to blue. Table 4 reports the results for age prediction with a multivariate linear model, combining all the network features. All the models can predict the age of the infant recording with a $\sqrt{\text{MSE}}$ between 2 and 3 weeks and the CCA models always outperform the model without CCA as a preprocessing step. Furthermore, the explained variance (R^2) is higher with the models that include CCA. It is also interesting to notice that best prediction results are obtained with GC during QS ($\sqrt{\text{MSE}}_{\text{simple}} = 2.52$ PMA weeks, $\sqrt{\text{MSE}}_{\text{CCA}} = 2.10$ PMA weeks). Table 4 does not report the results for one

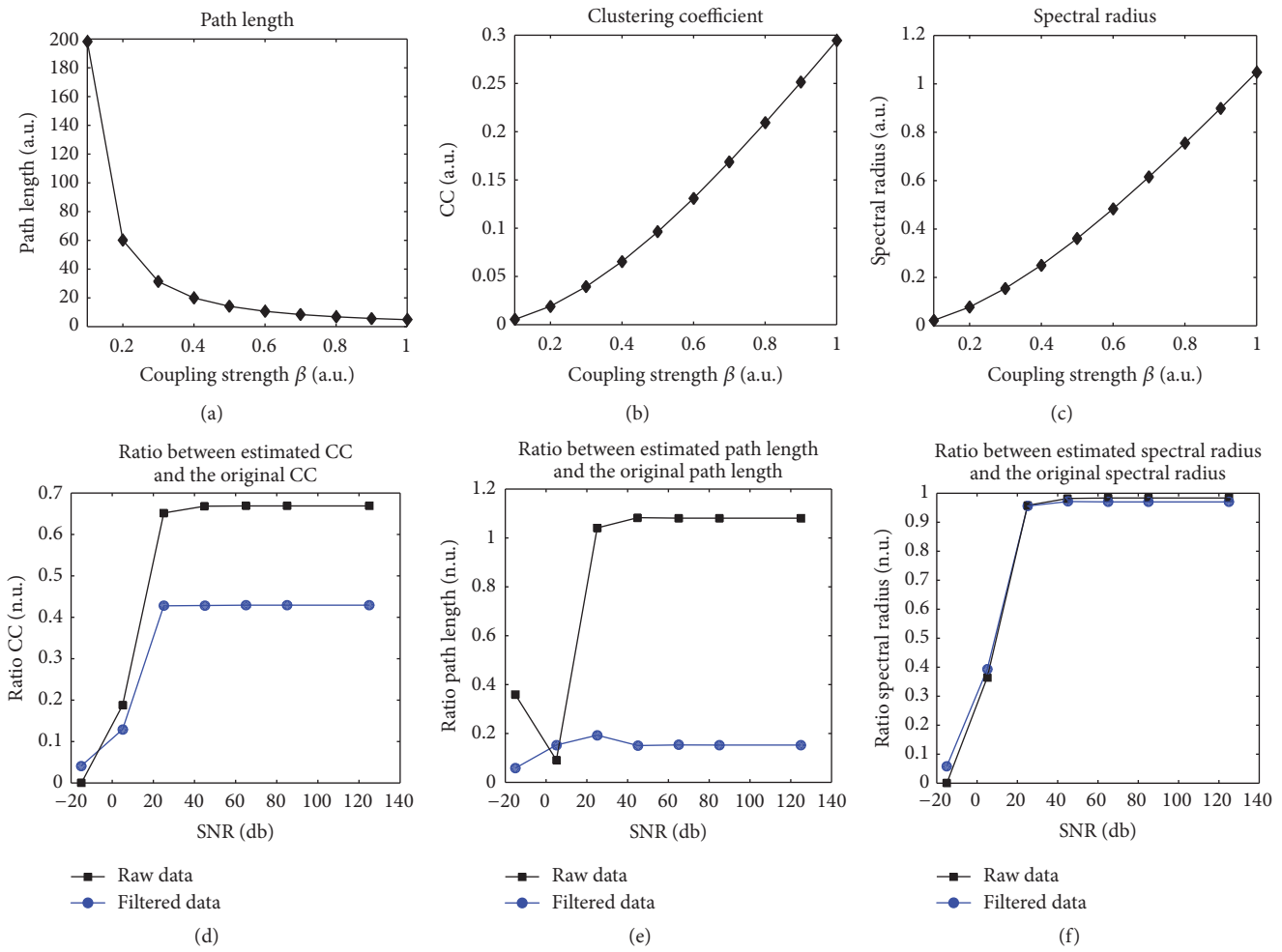

FIGURE 2: The figure shows the results for the simulation dataset. (a, b, c) show how the graph indices behave for different level of coupling in model (1). (d, e, f) investigate how the transfer entropy can estimate the network indices for different level of SNR. In particular, the figure compares the two cases when the data is filtered and when the raw data is used.

single model estimation, but the median and InterQuartile Range (IQR) of the evaluation parameters for 100 bootstrap iterations. In each single iteration, the model proved to be significant as reported by the p value column in Table 4 ($p < 0.01$).

4. Discussion

In the present study, we quantified the effective brain connectivity in preterm infants to track their maturation. Although there are some studies that investigate connectivity in the neonates [4, 5] and its change in the first days of life (short maturation period) [14], this is the first study to track maturity using effective EEG-based connectivity in preterm patients on a wide maturation period, from birth to full-term age. To the best of our knowledge, MRI [8] and fMRI [10] have been the leading method to track maturity. However, fMRI is only suitable for functional connectivity, as discussed above. In this article, we compared two well-known methods to estimate coupling between processes, like GC and TE. Based on the obtained connectivity matrices, we estimated integration and spectral network indices for directed weighted graphs. Those features were used to predict the age of the patient during the recording. The same process was applied on a simulated dataset to investigate how the network measures behaved in a controlled case.

4.1. Simulated Dataset. According to [11], graphs with high clustering coefficient and low path length behave like a rich-club network, while graphs with low clustering coefficient and high path length denote a random network, where the number of edges for each node is normally distributed. Figure 1 portraits two club networks, where the nodes are connected to each other with a short distance. This leads to a high clustering coefficient and low path length when the coupling coefficient is equal to 1. However, when β decreases, the intracluster connectivity weakens and the graph becomes more similar to a random network. This type of graph is characterized by low clustering coefficient and high path length: indeed, the nodes are less connected among each

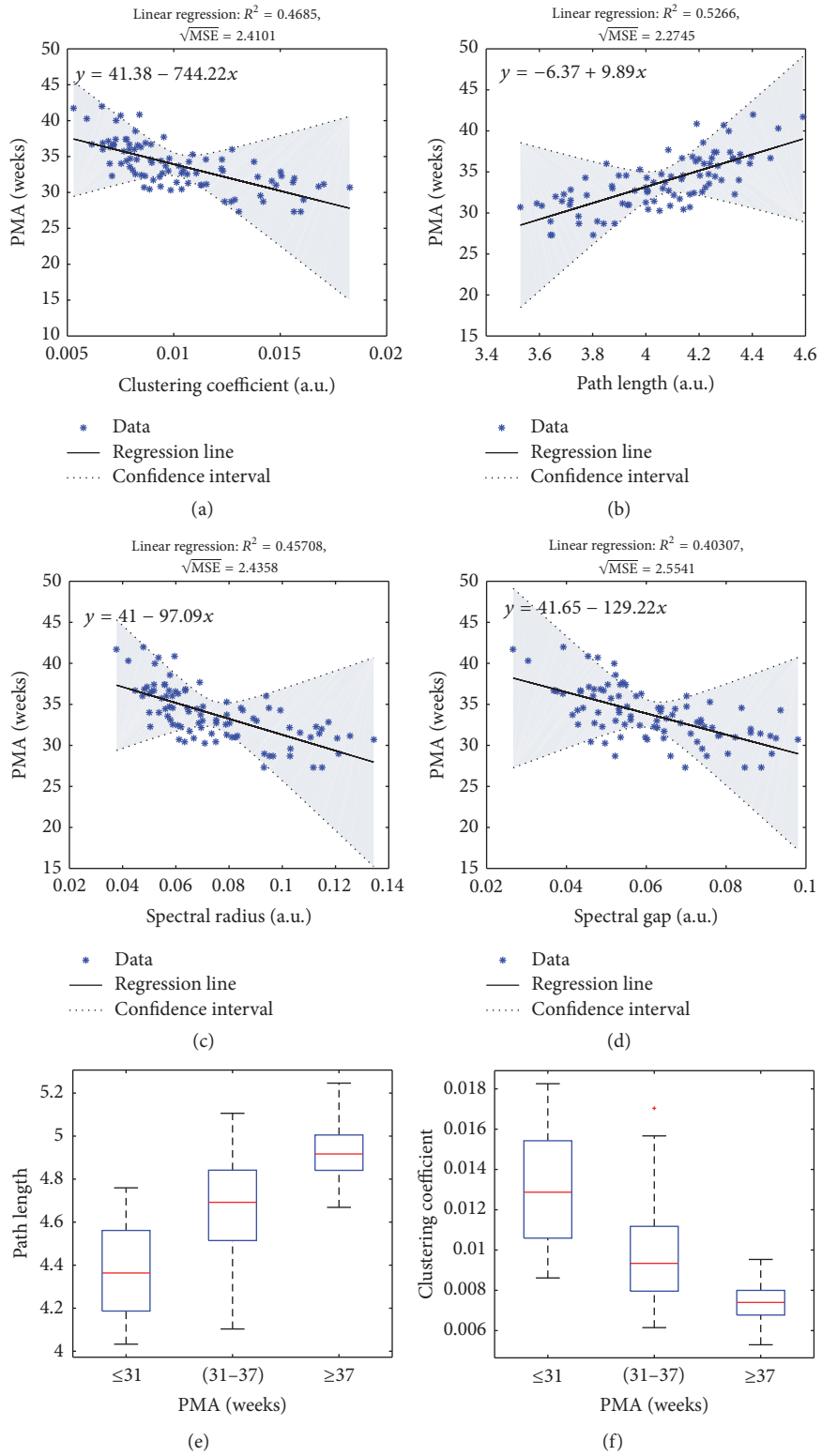

Figure 3: The figure shows the results for EEG data. (a, b, c, d) show OLS regression between 4 main graph indices versus the age (PMA in weeks) for GC in QS. The grey area is the confidence interval at 95%. On the top of the panel, the associated R^2 and $\sqrt{\text{MSE}}$ in PMA weeks on the test set. (e, f) show the trend of the clustering coefficient and the path length in three distinct age groups. The results are reported about GC in QS.

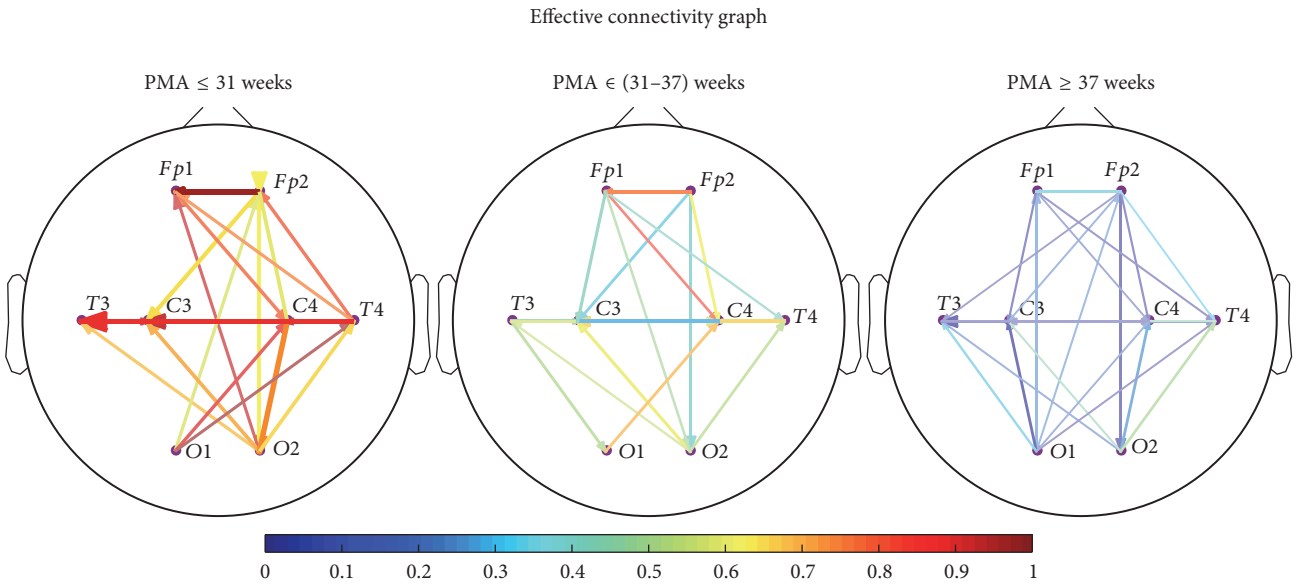

FIGURE 4: The figure shows the average connectivity graph (GC for three different age groups). The strength of the coupling among the electrodes is decoded by the color (the closer to the red color, the higher the coupling) and by the width of the arrow. The connectivity values have been normalized between 0 and 1 for the three groups together. The panels clearly show the weakening of the coupling among EEG channels with maturation. The consequence is the increase of path length and the decrease of the clustering coefficient (Figure 3).

TABLE 2: The main integration and spectral features in three discrete time points. The table shows the indices for both sleep states (QS = quiet sleep, NQS = nonquiet sleep) and they were computed on the transfer entropy connectivity graph. The results are reported as median (IQR), where IQR stands for *InterQuartile Range*. The symbol ρ stands for the Pearson correlation coefficient, while # represents a significant correlation with $p \leq 0.01$. The values 10^{-3} or 10^{-2} mean the reported results are multiplied by a factor 10^{-3} or 10^{-2}.

Network indices: transfer entropy in three age groups				
Median (IQR), PMA weeks	≤31	∈ (31–37)	≥37	ρ (%)
Clustering coefficient				
QS	.025 (.008)	.021 (.005)	.017 (.002)	−53#
NQS	.025 (.006)	.020 (.006)	.018 (.002)	−49#
Path length				
QS	3.73 (.30)	3.89 (.22)	4.07 (.10)	59#
NQS	3.71 (.20)	3.91 (.25)	4.04 (.14)	54#
Spectral radius				
QS	.18 (.07)	.16 (.05)	.12 (.01)	−49#
NQS	.18 (.05)	.15 (.04)	.13 (.02)	−48#
Spectral gap				
QS	.15 (.09)	.12 (.04)	.10 (.02)	−51#
NQS	.15 (.06)	.12 (.04)	.11 (.02)	−48#
Network indices: transfer entropy, CCA				
Median (IQR)	≤31	∈ (31–37)	≥37	ρ (%)
Clustering coefficient				
QS (10^{-3})	9.82 (6.1)	6.21 (3.3)	4.98 (0.9)	−57#
NQS (10^{-3})	9.13 (3.5)	6.29 (2.0)	5.90 (1.0)	−49#
Path length				
QS	4.70 (.57)	5.11 (.47)	5.32 (.18)	64#
NQS	4.73 (.40)	5.09 (.27)	5.16 (.18)	52#
Spectral radius				
QS (10^{-2})	8.20 (4.7)	4.68 (3.1)	3.63 (.6)	−55#
NQS (10^{-2})	6.94 (2.8)	4.74 (1.6)	4.30 (.7)	−48#
Spectral gap				
QS (10^{-2})	5.84 (3.1)	3.93 (2.0)	3.30 (.6)	−52#
NQS (10^{-2})	5.84 (3.1)	3.93 (2.0)	3.30 (.6)	−49#

Table 3: The main integration and spectral features in three discrete time points. The table shows the indices for both sleep states (QS = quiet sleep, NQS = nonquiet sleep) and they were computed on the Granger causality connectivity graph. The results are reported as median (IQR), where IQR stands for *InterQuartile Range*. The symbol ρ stands for the Pearson correlation coefficient, while # represents a significant correlation with $p \leq 0.01$. The values 10^{-3} or 10^{-2} mean the reported results are multiplied by a factor 10^{-3} or 10^{-2}.

Network indices: Granger causality				
Median (IQR), PMA weeks	≤31	∈ (31–37)	≥37	ρ (%)
Clustering coefficient				
QS	.024 (.006)	.019 (.006)	.015 (.002)	$-56^{\#}$
NQS	.024 (.007)	.019 (.005)	.016 (.002)	$-51^{\#}$
Path length				
QS	3.77 (.20)	3.95 (.25)	4.17 (.13)	$61^{\#}$
NQS	3.75 (.33)	3.95 (.27)	4.10 (.14)	$56^{\#}$
Spectral radius				
QS	.18 (.06)	.15 (.04)	.10 (.02)	$-54^{\#}$
NQS	.18 (.05)	.14 (.03)	.10 (.01)	$-51^{\#}$
Spectral gap				
QS	.14 (.06)	.13 (.04)	.09 (.02)	$-58^{\#}$
NQS	.15 (.05)	.11 (.03)	.11 (.01)	$-51^{\#}$
Network indices: Granger causality, CCA				
Median (IQR), PMA weeks	≤31	∈ (31–37)	≥37	ρ (%)
Clustering coefficient				
QS (10^{-3})	12.87 (4.8)	9.34 (3.2)	7.39 (1.2)	$-68^{\#}$
NQS (10^{-3})	12.29 (3.4)	9.08 (2.1)	8.51 (1.2)	$-61^{\#}$
Path length				
QS	4.36 (.37)	4.69 (.33)	4.92 (.16)	$73^{\#}$
NQS	4.41 (.28)	4.71 (.21)	4.77 (.14)	$63^{\#}$
Spectral radius				
QS (10^{-2})	9.52 (3.5)	6.79 (2.6)	5.28 (.8)	$-68^{\#}$
NQS (10^{-2})	8.98 (2.5)	6.50 (1.5)	6.05 (.9)	$-61^{\#}$
Spectral gap				
QS (10^{-2})	7.28 (2.4)	5.87 (2.3)	4.91 (1.1)	$-63^{\#}$
NQS (10^{-2})	6.91 (3.0)	6.07 (1.0)	5.35 (1.4)	$-56^{\#}$

Table 4: Multivariate regression model performances. The table shows the error on the test set (Error), R^2 and the F-statistics ($\mathcal{F}$-stat), and the p value obtained with the different connectivity methods in the different sleep states. The results are reported as median (IQR), where IQR stands for *InterQuartile Range* over the 100 random splits of the dataset. The labels reported are TE = transfer entropy, GC = Granger causality, QS = quiet sleep, and NQS = nonquiet sleep.

Multivariate regression performances				
Median (IQR)	Error (weeks)	R^2	$\mathcal{F}$-stat	p value
Simple filtering				
TE, QS	2.54 (0.41)	0.57 (0.07)	11.64 (3.46)	$p < 0.01 * 100$
TE, NQS	2.88 (0.39)	0.40 (0.07)	6.23 (1.72)	$p < 0.01 * 100$
GC, QS	*2.52 (0.37)*	*0.52 (0.07)*	*10.01 (2.64)*	$p < 0.01 * 100$
GC, NQS	2.79 (0.53)	0.44 (0.07)	7.20 (2.09)	$p < 0.01 * 100$
CCA				
TE, QS	2.23 (0.29)	0.63 (0.06)	12.90 (3.14)	$p < 0.01 * 100$
TE, NQS	2.54 (0.51)	0.57 (0.06)	10.36 (2.66)	$p < 0.01 * 100$
GC, QS	*2.10 (0.38)*	*0.67 (0.05)*	*15.96 (3.64)*	$p < 0.01 * 100$
GC, NQS	2.35 (0.42)	0.63 (0.04)	13.38 (2.61)	$p < 0.01 * 100$

other in a more homogeneous network. This result is also supported by the direct proportionality between spectral radius and coupling coefficient. Another interesting point is related to the filtering. Figure 2 illustrates clearly how the clustering coefficient and the path length estimation can be highly affected by the filtering. Those results are in line with the analysis by [36], which demonstrated that careless filtering can add spurious connectivity in the time courses. In our simulation, the effect of filtering weakens the intracluster connectivity (adding intercluster connectivity). The net effect is a decrease in clustering coefficient and an increase in path length. Therefore, we decided only to apply a notch filter and differentiation as preprocessing steps on the EEG.

4.2. EEG Data. In the literature, a number of studies can be found to have assessed the brain maturation in children and adolescents by graph theory [1, 4, 10] and a few papers focused on preterm brain maturation by network metrics [5, 13]. The first result obtained in our study is the change in effective connectivity with age. Although Schumacher et al. [14] used a different method, they also concluded that there is a change in effective connectivity mainly driven by postnatal maturation. In addition to that, we have been able to demonstrate the existence of a relationship between connectivity and PMA. In this study, we also observed a change in graph parameters that suggest that the EEG-scalp network moved from a rich-club network to a more random network. The integration and spectral indices decreased with age, except for the path length, which reflects a segregation of nodes due to a higher graph distance as well as less intense triangle patterns around the nodes themselves. Hub-networks have high clustering coefficients since they have central club nodes, which are surrounded by triangle patterns. On the contrary, a random network presents nodes, which are connected to any other node in the network with a weak coupling. The net effect is a low clustering coefficient and high path length. This emergence of a normal-distributed network is also confirmed by the decrease of the spectral gap, spectral radius, and the algebraic connectivity. The latter two indices emphasize how easily the graph can be clustered and a negative trend would suggest the absence of modules or groups in the graph. On the contrary, a negative trend of the former index should suggest an increase of modularity, as shown by [34]. However, since the spectral gap is also inversely proportional to the path length, its reduction just shows that the spectral radius is less dominant with respect to the other eigenvalues [33] and it becomes another measure of modularity like the other two spectral indices. The results of the multivariate model further highlight the shift from a rich-club network at younger age to a more random one at full-term age. In particular, the lowest $\sqrt{\text{MSE}}$ on the test set is around 2.11 weeks compared to other studies [15, 39]. Finally, it is important to notice that those negative trends for graph features are consistent for each effective connectivity method and each sleep state. At first sight, the results we obtained seem to be in contradiction with maturation trends that can be found in children or adolescents, where a shift from random to a rich-club network has been discovered. However, it should be taken in account that, on one side, only 9 electrodes on the scalp were used, due to the small size of the preterm brain and, on the other hand, there is a fast development of the brain during this monitoring period with different trajectories for the different cerebral regions [40]. This composite evolution is mainly driven by the different disappearance timing of cortical subplate in the various brain areas [40]. In particular, two main changes took place. The first one is the faster development of the thalamocortical connections compared to the corticocortical ones [5]. The shift from one type of connections to the other happens only at later age [41]; therefore, the maturation process might lead to "separation" of the nodes, as reflected by the results in this study. In simple terms, the EEG-scalp connections became weaker in favour of a connection strengthening between the cortical and subcortical areas. The second important change is the negative correlation between age and short-range corticocortical connections, as shown by [5] via fMRI. In [5], the study results showed that long distance connections develop faster than the short ones. Furthermore, the development is characterized by a strengthening of the former connections and weakening of the short-range couplings [1]. Consequently, the EEG electrodes/nodes (which measure short-range connectivity) tend to separate each other, with an increase of the path length and a reduction of the clustering coefficient. This hypothesis is also supported by the decrease in fronto-frontal and occipito-occipital functional coupling measured by fMRI [5]. This segregation can be emphasized by the fact that there are a few electrodes on infant scalp. However, a study with high-density EEG on preterm infants [13] found an increased modularity on the scalp EEG network and a reduced clustering coefficient in the postcentral network, while the clustering coefficient increases in the precentral network. This result could confirm the segregation or the more local integration of the brain network due to the pruning of short-range connections, as also shown by [42] in the comparison between adults and children. It is important to notice that both models with and without CCA found the same trends, but source filtering increased the prediction power of the model. It is possible that the EMG artifacts disturbed the connectivity analysis and biased the prediction model in the first considered scenario.

5. Conclusions

In the present study, we investigated effective EEG-based brain connectivity in premature infants, whose PMA ranged from 27 to 42 weeks. Results showed that the EEG-graphs changed with age in terms of topology. In particular, the clustering coefficient and the spectral radius decreased with maturation, while the path length increased. This perspective suggests that the EEG graph shifted from a small-world network to a random network. This apparent nodes' segregation can be a consequence of the thalamocortical connections development and the strengthening of the long-range cortical connections. The lowest age-prediction error was 2.11 PMA weeks (obtained with GC in QS), which is in line with literature results. Application of source filtering methods,

like CCA, can improve the performance of the connectivity analysis.

Disclosure

This paper reflects only the authors' views and the Union is not liable for any use that may be made of the contained information.

Conflicts of Interest

The authors declare that there are no conflicts of interest regarding the publication of this paper. The received funding stated in the Acknowledgments does not lead to any conflicts of interest.

Acknowledgments

This research is supported by Bijzonder Onderzoeksfonds KU Leuven (BOF): The Effect of Perinatal Stress on the Later Outcome in Preterm Babies (no. C24/15/036); iMinds Medical Information Technologies (SBO, 2016); Belgian Federal Science Policy Office, IUAP no. P7/19/(DYSCO, "Dynamical Systems, Control and Optimization," 2012–2017); Belgian Foreign Affairs-Development Cooperation (VLIR UOS Programs (2013–2019)); and EU: the research leading to these results has received funding from the European Research Council under the European Union's Seventh Framework Programme (FP7/2007–2013)/ERC Advanced Grant: BIOTENSORS (no. 339804). A. Caicedo is a post doc fellow at Fonds voor Wetenschappelijk Onderzoek-Vlaanderen (FWO), supported by Flemish government. M. Lavanga is a SB Ph.D. fellow at Fonds voor Wetenschappelijk Onderzoek-Vlaanderen (FWO), supported by Flemish government.

References

[1] D. Goldenberg and A. Galván, "The use of functional and effective connectivity techniques to understand the developing brain," *Developmental Cognitive Neuroscience*, vol. 12, article no. 265, pp. 155–164, 2015.

[2] E. W. Lang, A. M. Tomé, I. R. Keck, J. M. Górriz-Sáez, and C. G. Puntonet, "Brain connectivity analysis: A short survey," *Computational Intelligence and Neuroscience*, vol. 2012, Article ID 412512, 21 pages, 2012.

[3] J. L. Vincent, G. H. Patel, M. D. Fox et al., "Intrinsic functional architecture in the anaesthetized monkey brain," *Nature*, vol. 447, no. 7140, pp. 83–86, 2007.

[4] J. D. Power, D. A. Fair, B. L. Schlaggar, and S. E. Petersen, "The development of human functional brain networks," *Neuron*, vol. 67, no. 5, pp. 735–748, 2010.

[5] D. Batalle, E. J. Hughes, H. Zhang et al., "Early development of structural networks and the impact of prematurity on brain connectivity," *NeuroImage*, vol. 149, pp. 379–392, 2017.

[6] M. André, M.-D. Lamblin, A. M. d'Allest et al., "Electroencephalography in premature and full-term infants. Developmental features and glossary," *Neurophysiologie Clinique*, vol. 40, no. 2, pp. 59–124, 2010.

[7] E. Takahashi, R. D. Folkerth, A. M. Galaburda, and P. E. Grant, "Emerging cerebral connectivity in the human fetal Brain: an MR tractography study," *Cerebral Cortex*, vol. 22, no. 2, pp. 455–464, 2012.

[8] J. Dubois, M. Benders, A. Cachia et al., "Mapping the early cortical folding process in the preterm newborn brain," *Cerebral Cortex*, vol. 18, no. 6, pp. 1444–1454, 2008.

[9] P. S. Hüppi and J. Dubois, "Diffusion tensor imaging of brain development," *Seminars in Fetal and Neonatal Medicine*, vol. 11, no. 6, pp. 489–497, 2006.

[10] M. C. Stevens, "The developmental cognitive neuroscience of functional connectivity," *Brain and Cognition*, vol. 70, no. 1, pp. 1–12, 2009.

[11] E. Bullmore and O. Sporns, "Complex brain networks: graph theoretical analysis of structural and functional systems," *Nature Reviews Neuroscience*, vol. 10, no. 3, pp. 186–198, 2009.

[12] K. J. Friston, "Functional and effective connectivity in neuroimaging: a synthesis," *Human Brain Mapping*, vol. 2, no. 1-2, pp. 56–78, 1994.

[13] A. Omidvarnia, P. Fransson, M. Metsaranta, and S. Vanhatalo, "Functional bimodality in the brain networks of preterm and term human newborns," *Cerebral Cortex*, vol. 24, no. 10, pp. 2657–2668, 2014.

[14] E. M. Schumacher, T. A. Stiris, and P. G. Larsson, "Effective connectivity in long-term EEG monitoring in preterm infants," *Clinical Neurophysiology*, vol. 126, no. 12, pp. 2261–2268, 2015.

[15] M. Lavanga, O. De Wel, A. Caicedo Dorado, K. Jansen, A. Dereymaeker, G. Naulaers et al., "Linear and nonlinear functional connectivity methods to predict brain maturation in preterm babies," in *Proceedings of the 8th International Workshop on Biosignal Interpretation*, pp. 37–40, 2016.

[16] T. Schreiber, "Measuring information transfer," *Physical Review Letters*, vol. 85, no. 2, pp. 461–464, 2000.

[17] C. W. J. Granger, "Investigating causal relations by econometric models and cross-spectral methods," *Econometrica*, vol. 37, no. 3, pp. 424-238, 1969.

[18] A. Montalto, L. Faes, and D. Marinazzo, "MuTE: a MATLAB toolbox to compare established and novel estimators of the multivariate transfer entropy," *PLoS ONE*, vol. 9, no. 10, Article ID e109462, 2014.

[19] E. Florin, J. Gross, J. Pfeifer, G. R. Fink, and L. Timmermann, "The effect of filtering on Granger causality based multivariate causality measures," *NeuroImage*, vol. 50, no. 2, pp. 577–588, 2010.

[20] A. Dereymaeker, K. Pillay, J. Vervisch et al., "An automated quiet sleep detection approach in preterm infants as a gateway to assess brain maturation," *International Journal of Neural Systems*, vol. 27, no. 06, p. 1750023, 2017.

[21] N. Koolen, A. Dereymaeker, O. Rasanen et al., "Data-driven metric representing the maturation of preterm EEG," in *Proceedings of the 37th Annual International Conference of the IEEE Engineering in Medicine and Biology Society, EMBC '15*, pp. 1492–1495, IEEE, Milan, Italy, August 2015.

[22] K. J. Blinowska, "Review of the methods of determination of directed connectivity from multichannel data," *Medical Biological Engineering Computing*, vol. 49, no. 5, pp. 521–529, 2011.

[23] L. A. Baccalá and K. Sameshima, "Causality and influentiability: the need for distinct neural connectivity concepts," *Journal of Chemistry*, pp. 424–435, 2014.

[24] L. Barnett and A. K. Seth, "The MVGC multivariate granger causality toolbox: a new approach to granger-causal inference," *Journal of Neuroscience Methods*, vol. 223, pp. 50–68, 2014.

[25] K. Sameshima, D. Y. Takahashi, and L. A. Baccalá, "On the statistical performance of Granger-causal connectivity estimators," *Brain Informatics*, vol. 2, no. 2, pp. 119–133, 2015.

[26] R. Vicente, M. Wibral, M. Lindner, and G. Pipa, "Transfer entropy—a model-free measure of effective connectivity for the neurosciences," *Journal of Computational Neuroscience*, vol. 30, no. 1, pp. 45–67, 2011.

[27] A. K. Seth, "Causal connectivity of evolved neural networks during behavior," *Network: Computation in Neural Systems*, vol. 16, no. 1, pp. 35–54, 2015.

[28] F. D. Fallani and F. Babiloni, "The graph theoretical approach in brain functional networks: theory and applications," *Synthesis Lectures on Biomedical Engineering*, vol. 5, no. 1, pp. 1–92, 2010.

[29] G. Fagiolo, "Clustering in complex directed networks," *Physical Review E—Statistical, Nonlinear, and Soft Matter Physics*, vol. 76, no. 2, part 2, Article ID 026107, 2007.

[30] J. Bondy and U. Murty, *Graph Theory with Applications*, Springer, Berlin, Heidelberg, Germany, 1976.

[31] M. Rubinov and O. Sporns, "Complex network measures of brain connectivity: uses and interpretations," *NeuroImage*, vol. 52, no. 3, pp. 1059–1069, 2010.

[32] A. B. Barrett, L. Barnett, and A. K. Seth, "Multivariate Granger causality and generalized variance," *Physical Review E. Statistical, Nonlinear, and Soft Matter Physics*, vol. 81, no. 4, 041907, 14 pages, 2010.

[33] A. Yu, M. Lu, and F. Tian, "On the spectral radius of graphs," *Linear Algebra and its Applications*, vol. 387, pp. 41–49, 2004.

[34] E. Estrada and N. Hatano, "Communicability angle and the spatial efficiency of networks," *SIAM Review*, vol. 58, no. 4, pp. 692–715, 2016.

[35] F. Chung, "Laplacians and the Cheeger inequality for directed graphs," *Annals of Combinatorics*, vol. 9, no. 1, pp. 1–19, 2005.

[36] L. Barnett and A. K. Seth, "Behaviour of Granger causality under filtering: theoretical invariance and practical application," *Journal of Neuroscience Methods*, vol. 201, no. 2, pp. 404–419, 2011.

[37] W. DeClercq, A. Vergult, B. Vanrumste, W. van Paesschen, and S. van Huffel, "Canonical correlation analysis applied to remove muscle artifacts from the electroencephalogram," *IEEE Transactions on Biomedical Engineering*, vol. 53, no. 12, pp. 2583–2587, 2006.

[38] H. Peng, K. Li, B. Li, H. Ling, W. Xiong, and W. Hu, "Predicting image memorability by multi-view adaptive regression," in *Proceedings of the the 23rd ACM international conference*, pp. 1147–1150, Brisbane, Australia, October 2015.

[39] J. M. O'Toole, G. B. Boylan, S. Vanhatalo, and N. J. Stevenson, "Estimating functional brain maturity in very and extremely preterm neonates using automated analysis of the electroencephalogram," *Clinical Neurophysiology*, vol. 127, no. 8, pp. 2910–2918, 2016.

[40] I. Kostović and M. Judaš, "The development of the subplate and thalamocortical connections in the human foetal brain," *Acta Paediatrica*, vol. 99, no. 8, pp. 1119–1127, 2010.

[41] E. J. Meijer, K. H. M. Hermans, A. Zwanenburg et al., "Functional connectivity in preterm infants derived from EEG coherence analysis," *European Journal of Paediatric Neurology*, vol. 18, no. 6, pp. 780–789, 2014.

[42] D. A. Fair, N. U. Dosenbach, J. A. Church, A. L. Cohen, S. Brahmbhatt, F. M. Miezin et al., "Development of distinct control networks through segregation and integration," *Proceedings of the National Academy of Sciences of the United States of America*, vol. 104, no. 33, pp. 13507–13512, 2007.

Hindawi
Complexity
Volume 2017, Article ID 8953083, 8 pages
https://doi.org/10.1155/2017/8953083

Research Article

Follow-Up and Risk Assessment in Patients with Myocardial Infarction Using Artificial Neural Networks

Tatjana Gligorijević,[1,2] Zoran Ševarac,[3] Branislav Milovanović,[1,2] Vlado Đajić,[4] Marija Zdravković,[1,2] Saša Hinić,[1] Marina Arsić,[1] and Milica Aleksić[1]

[1]*Department of Cardiology, University Hospital Medical Center Bežanijska Kosa, 11080 Belgrade, Serbia*
[2]*Medical Faculty, University of Belgrade, 11000 Belgrade, Serbia*
[3]*Faculty of Organizational Sciences, University of Belgrade, 11000 Belgrade, Serbia*
[4]*Department of Neurology, University Clinical Center of the Republic of Srpska, 78000 Banjaluka, Bosnia and Herzegovina*

Correspondence should be addressed to Zoran Ševarac; sevarac@gmail.com

Received 24 April 2017; Revised 27 July 2017; Accepted 16 August 2017; Published 17 September 2017

Academic Editor: Gaetano Valenza

Copyright © 2017 Tatjana Gligorijević et al. This is an open access article distributed under the Creative Commons Attribution License, which permits unrestricted use, distribution, and reproduction in any medium, provided the original work is properly cited.

Artificial neural networks (ANNs) are machine learning technique, inspired by the principles found in biological neurons. This technique has been used for prediction and classification problems in many areas of medical signal processing. The aim of this paper was to identify individuals with high risk of death after acute myocardial infarction using ANN. A training dataset for ANN was 1705 consecutive patients who underwent 24-hour ECG monitoring, short ECG analysis, noninvasive beat-to-beat heart-rate variability, and baroreflex sensitivity that were followed for 3 years. The proposed neural network classifier showed good performance for survival prediction: 88% accuracy, 81% sensitivity, 93% specificity, 0.85 F-measure, and area under the curve value of 0.77. These findings support the theory that patients with high sympathetic activity (reduced baroreflex sensitivity) have an increased risk of mortality independent of other risk factors and that artificial neural networks can indicate the individuals with a higher risk.

1. Introduction

Many studies have been published on the subject of cardiac risk assessment, with the goal to identify the subgroup of patients who are at high risk of death after myocardial infarction (MI) [1]. The identification of those individuals which are in higher risk of developing the second cardiovascular event is very important so that they can be properly followed and treated. Contemporary cardiac rehabilitation/secondary prevention (CR/SP) programs are designed to reduce cardiovascular risk and event rates, foster healthy behaviors, and promote active lifestyles [2]. The exceedingly difficult challenge for cardiologists is determining which patients are at sufficiently high risk of an arrhythmic death. Therefore it is essential to identify individuals with arrhythmogenic background who will derive benefit from an implantable cardioverter-defibrillators (ICD), in terms of primary prevention of sudden cardiac death (SCD) based on heart-rate variability analysis [3]. In previous studies heart-rate variability parameters are proved to be independent risk predictors of SCD after MI [4]. Despite all this knowledge risk stratification models have limited predictive accuracy. Recently published studies suggest that more than half of all implanted primary prevention devices have not delivered any shocks before battery replacement is required [5]. Precise classification and accurate predictive model can improve clinical pathways of the most vulnerable patients. The predictive power of used statistical models is limited, so the alternative models have arisen, and artificial neural networks (ANNs) become more popular [6].

The ANN presents a machine learning technique that could potentially improve performance of predicting clinical outcomes. Artificial neural networks are excellent solution for classifiers with multiple input parameters and pattern recognition problems [7]. The ANN can predict a specific category of a set of input variables which can be further

used for detailed analysis. The previous studies failed to detect the particular prognostic accuracy in risk assessment after uncomplicated myocardial infarction [8]. To limit the emphasis on incidental associations between input variables, it might be beneficial to guide artificial neural network development by presenting a subset of input variables that are more likely to predict an outcome. This paper deals with the classification and risk assessment of different autonomic nervous system groups based on certain parameters of heart-rate variability using an artificial neural network (ANN). The main motivation in our study for using ANN was their ability to solve the highly nonlinear problems and discover unknown relationships between input parameters. The first aim of the study was to improve the prediction of death using different prediction techniques, like ANN and addition to standard statistical models in early phase after acute myocardial infarction. The second goal was identification of those individuals with higher cardiovascular risk from all-cause mortality. Last but not least, the problem which should be pointed out is the methodology of preparing data, variable selection, determination of cutoff values for suggested variables, and making an accurate model for prediction. The methodology and early results of this study were presented and discussed at The 7th International Symposium on Noninvasive Electrocardiology [9].

Determination of individuals with high cardiovascular risk in the acute phase after myocardial infarction using autonomic nervous system patterns and previously well-established independent risk predictors was improved using ANN [10, 11].

The recognition of variable patterns correlating with an adverse outcome contributed to the understanding of the autonomic background and ability of ANN to "learn" complex relationships between a series of input (predictor) variables and the corresponding output (outcome) variables [12]. Based on relationships identified between input and output variables, trained dataset can be used for pattern recognition or classification tasks in a separate test dataset. Commonly used statistical models use linear combinations of variables and, therefore, are not adept at modeling grossly nonlinear complex interactions as has been demonstrated in complex cardiovascular system [13]. In previously conducted studies some of the advantages of ANN over standard statistical methods have been suggested: neural network models require less formal statistical training to develop, can implicitly detect complex nonlinear relationships between independent and dependent variables, have the ability to detect all possible interactions between predictor variables, and can be developed using multiple different training algorithms [12]. ANN has been successfully applied to a broad range of biomedical problems, and previous studies have demonstrated that various ANN approaches can accurately predict an outcome [14–17].

2. Material and Methods

2.1. Study Population. The patient population used for ANN training consisted of 1705 patients admitted between 2003 and 2013 to Coronary Care Unit of Clinical Hospital Center Bežanijska Kosa, Belgrade, Serbia. The admitted patients were recorded the first day after acute myocardial infarction using the electrocardiogram (ECG) and short-term HRV analysis, while Holter ECG was recorded after two weeks. Date of the first visit was taken as the start date, and survival status was determined by contacting the patient. Survival data were used to assess their hazard ratio and to determine all-cause mortality.

All experimental protocols were approved by the local Scientific Ethical Committee of University Clinical Center "Bežanijska Kosa," license number 1039/3. All the participants were fully informed about the study and gave their written consent in agreement with the Declaration of Helsinki.

Inclusion criteria were man > 40 years old or postmenopausal women, acute ischemic heart disease verified by cardiac biochemical markers, ST-segment depression, or T-wave inversion ≥ 0.1 mV in at least two contiguous leads without the presence of concomitant Q-waves in these leads.

Exclusion criteria were left ventricular hypertrophy, right ventricular hypertrophy, right and left bundle branch block, atrial flutter and fibrillation, anterior and posterior hemiblock, paced rhythm, Wolff-Parkinson-White syndrome, and ventricular tachycardia or incomplete or erroneous data.

2.2. Database. Data were obtained using short ECG analysis (Shiller AT-10), noninvasive beat-to-beat heart-rate variability, and baroreflex sensitivity (Task Force Monitor) and 24-hour ambulatory ECG monitoring with long-term HRV analysis. ECG parameters were obtained from a 12-channel recording over the past 5 minutes using the commercial software (Schiller AT-10, Austria). The Task Force Monitor (CNSystems, Graz, Austria) was used to monitor beat-to-beat heart rate by ECG and beat-to-beat blood pressure by the vascular unloading technique [18], which was corrected automatically to the oscillometric blood pressure measured on the contralateral arm. The Task Force Monitor automatically provides the beat-to-beat spectral analysis of heart rate and systolic and diastolic blood pressure variability, applying an autoregressive methodology. Baroreceptor reflex sensitivity (BRS) was automatically assessed using the sequence technique according to Parati et al. [19]. Intervention marks can be set using the Task Force Monitor; it helps define periods for automated statistical analysis [20]. The mean value and standard deviation (SD) of the measured parameters were computed automatically for defined steady-state period. Twenty-four-hour ambulatory ECG recordings were obtained by a 12-lead electrocardiogram, sampling rate of 1000 Hz per each lead (Cardioscan, DMS, USA), and analyzed by an experienced analyst. The records were screened, corrected, and readied for further analysis. Analysis of the frequency (spectral) domain parameters was performed using Fast Fourier Transformation (FFT) and Hanning window.

2.3. Preprocessing. During the analysis of the gathered data, several problems were identified: extreme values, missing values, and unbalanced data. Extreme values are result of the errors during recording (patient movement, poor connection, etc.) and they were removed manually to be sure

Table 1: Detailed description of input variables used in this study.

Methods	Parameters	Units	Description
ECG parameters	QT interval	ms	Measure of the time between the start of the Q wave and the end of the T wave
	QTc interval	ms	Heart rate corrected QT interval
	PR interval	ms	Measure of time from the beginning of the upslope of the P wave to the beginning of the QRS wave
	QRS complex	ms	Complex of Q wave, R wave, and S wave
	P wave	ms	The P wave is the first positive deflection on the ECG
Time domain analysis	Average HR	bpm	Average heart rate during 24 hours
	SDNN	ms	Standard deviation of NN intervals
	RMSSD	ms	Square root of the mean squared differences of successive NN intervals
	pNN50	%	Proportion of interval differences of successive NN intervals greater than 50 ms
HRV statistics	LFnu-RRI	%	LF power in normalized units
	HFnu-RRI	%	HF power in normalized units
	VLF-RRI	ms^2	Power in very low frequency range
	PSD-RRI	ms^2	Total power
	LF/HF-RRI		Ratio LF [ms^2]/HF [ms^2]
	BRS	ms/mmHg	Change in interbeat interval (IBI) in milliseconds per unit change in BP

that we do not cut off some real data that are not errors. Extreme values were easy to identify since they were usually ten times larger than the expected range. Missing values were replaced with mean value of the corresponding attribute of all instances in the corresponding class. Although this is the simplest technique, it guarantees that it will not disturb dataset statistics. Unbalanced data is the biggest problem for training neural network classifier and classifier performance evaluation. Balanced datasets were created by randomly selecting the same number of patients (200) from both classes of patients (survived and died). These are not the only techniques (and probably not the best) that could be used, but they represent common practice and they gave good results. A detailed description of all fifteen parameters used in this study is provided in Table 1.

Some of these parameters were selected as mortality risk predictors based on the statistical analysis of previously conducted studies [21, 22]. Based on these studies, these parameters have been chosen for ANN training in this study, in order to further investigate their predictive power. Statistical analysis was used to assess the predictive power of the selected parameters.

2.4. Statistical Analysis. Survival curve (Figure 1) was created using the Kaplan-Meier method. The primary endpoint of the study was all-cause mortality. Associations between variables and mortality were assessed using stepwise multivariate Cox regression. The proportional hazard for mortality over time was assessed with Cox regression. The regression model was built by initially including factors with significant ($P < 0.05$) univariate associations. Multivariate Cox regression (SPSS software, version 19; SPSS Inc.) was used to determine a hazard ratio (HR) that was corrected for possible confounding variables. HRs and 95% confidence intervals (CIs) are presented; a P value ≤ 0.05 was considered to be statistically significant. These results show that selected parameters have significant predictive power for predicting all-cause mortality.

2.5. Neural Network Training. To train a neural network classifier, the neural network software Neuroph (http://neuroph.sourceforge.net/) was used (Figure 2). Neuroph is free, open source software and provides a graphical user interface and visual tools (Figure 3), which enable experimentation with different settings for neural network architectures and training.

The multilayer perceptron neural network architecture with back propagation learning algorithm was used to train a neural network. This architecture is well known for its application for classification problems. Randomly selected 70% of the dataset was used to train neural network classifiers, while the rest of it (30%) was used for testing. This kind of dataset split is common practice in neural network training that is used to avoid overfitting the network and achieve good classification performance with data that has not been used for training [23]. The exact split ratio depends mostly on the amount of data, and the optimal ratio can be determined heuristically. The same technique has been used in other related studies [7].

Training and testing procedures were repeated multiple times to determine optimal neural network settings (number of hidden layers and neurons) and learning rule parameters.

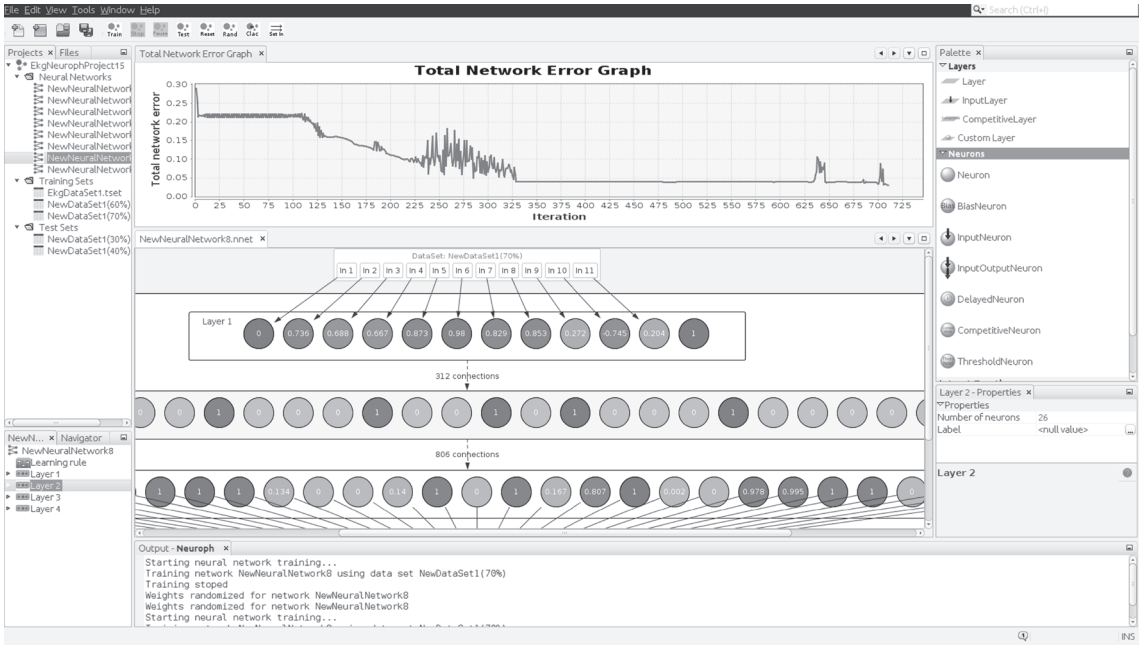

Figure 1: Neuroph software used for neural network training.

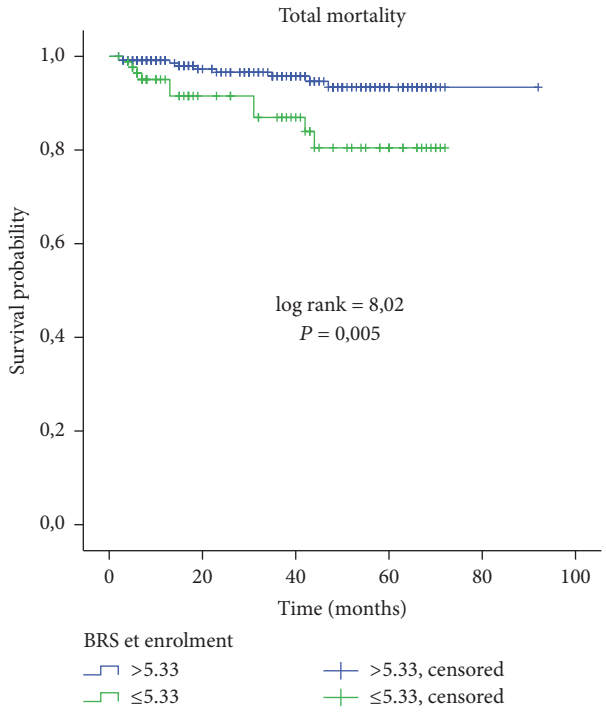

Figure 2: Kaplan-Meier survival curves for cardiac death in patients with reduced BRS at or below 5.33 ms/mmHg in early phase after acute myocardial infarction.

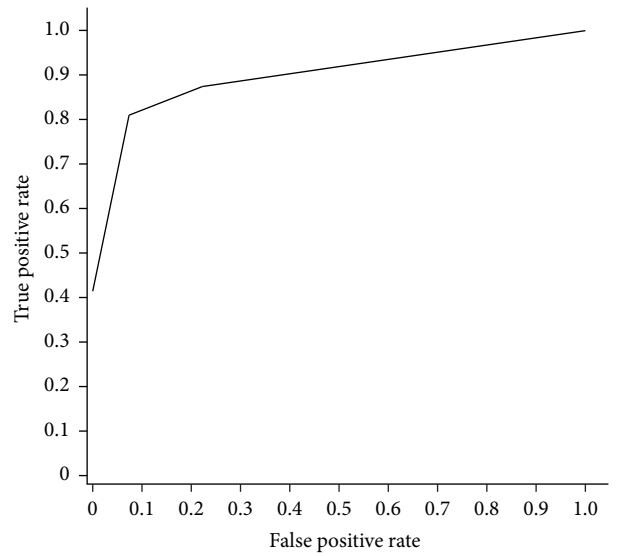

Figure 3: ROC curve for the neural network classifier to predict a survival status.

3. Results

During a median follow-up of 3 years (range, 1.2–4.8 y), 286 (16.77%) of the 1705 patients died from all cardiac causes. Unadjusted Kaplan-Meier survival showed worse survival for reduced BRS under 5,33 ms/mmHg (P = 0,005) (Figure 2). Univariable Cox proportional-hazards model showed statistically significant hazard ratio for the following covariates presented in Table 2, with suggested cutoff values and intervals which were used for further classification and prediction. Multivariable regression revealed significant associations of reduced BRS under 5,33 ms/mmHg (HR: 5.58, 95% CI: 1.25–24.95, P = 0.047) with survival. There were no statistically significant differences between the hazard ratios of either all-cause or cardiovascular mortality for LFnu-RRI, HFnu-RRI, and LF/HF-RRI.

Table 2: Association of risk variables with cardiac mortality in univariable analysis.

Method	Variable (values)	Hazard ratio, 95% CI (univariable)	P
ECG parameters	QT interval (≤378)	1.38 (1.08–1.76)	0.009
	QTc interval (>434)	1.28 (1.00–1.67)	0.050
	PR interval (151–184)	0.69 (0.52–0.91)	0.008
	QRS complex (≤87)	0.56 (0.42–0.75)	0.001
	P wave (64.19–72.36)	2.14 (1.06–4.34)	0.034
Time domain analysis	Average HR (>84.7)	1.73 (1.05–2.86)	0.032
	SDNN (≤120.0)	9.33 (1.31–66.7)	0.026
	RMSSD (>53.7)	1.58 (1.04–2.40)	0.030
	pNN50 (≤2.7)	8.84 (1.14–68.56)	0.037
HRV statistics	VLF-RRI (351.4–406.2)	3.68 (1.06–12.84)	0.041
	PSD-RRI (≤276.5)	2.55 (1.02–6.35)	0.044

SDNN: standard deviation of all the RR intervals; RMSSD: square root of the mean of squared differences of two consecutive RR intervals; pNN50: percent of beats with consecutive RR interval difference of more than 50 milliseconds; VLF: very low frequency component of HRV; PSD: total power of HRV; HRV: heart rate variability; ECG: electrocardiogram.

Table 3: Classifier performance for different neural network architectures.

Number	Neural network architecture	Learning Rate	Accuracy	Sensitivity	Specificity	F-measure
(1)	11-13-1	0.2	0.73	0.6	0.8	0.6
(2)	11-15-1	0.2	0.8	0.6	0.9	0.6
(3)	11-30-1	0.3	0.8	0.6	0.9	0.6
(4)	11-15-7-1	0.1	0.73	0.6	0.8	0.6
(5)	11-25-30-1	0.2	0.88	0.81	0.93	0.85
(6)	11-25-40-1	0.25	0.73	0.8	0.7	0.6

During the neural network training, a number of different settings for neural network architecture were tested. For each trained model a set of standard classification performance measures were calculated using a test set. The most critical parameters for successful training and classifier performance turned out to be a number of hidden layers, a number of hidden neurons, and error threshold. The results are shown in Table 3.

All architectures had 11 input neurons which correspond to 11 input parameters and one output neuron which corresponds to a single binary output. The neural network architecture with 25 neurons in the first hidden layer and 30 neurons in the second hidden layer (number (5)) showed the best classification performance: 88% accuracy, 81% sensitivity, 93% specificity, and 0.85 F-measure. The Receiver Operating Characteristics (ROC) curve for the best neural network classifier (architecture number (5)) is shown in Figure 3. The area under the curve value is as follows: AUC = 0.77.

Another critical parameter for getting good generalization ability of the network and testing results was the error threshold. The value of 0.03 for error threshold showed the best results.

4. Discussion

The electrocardiogram and blood pressure monitoring can be used in evaluation of patients in early phase after myocardial infarction. Over the last several years, computer-based learning models significantly improved the ability to predict adverse cardiac events [24]. The current understanding of the clinically relevant predictors in patients after AMI is reviewed in this article. Impaired baroreflex sensitivity following MI has been extensively documented in previous studies [25, 26]. In humans, depressed BRS after myocardial infarction is a clinical predictor of increased mortality [27–29]. In our study, multivariate analysis showed that reduced value of baroreflex sensitivity below 5.33 ms/mmHg in the observed group of patients is the only independent risk predictor of all investigated parameters.

The prediction model was built on initially included factors which were statistically significant in univariate analysis. The main disadvantage of univariate analysis is that it describes the survival with respect to the factor under investigation but necessarily ignores the impact of any others [30]. Nevertheless, it is likely that the assumptions required by the Cox model may not be satisfied because the model assumes that the underlying hazard rate is a function of independent variables, instead of the survival time [31]. Survival analysis using the Cox regression model generally shows the results based on the whole population, but it is insufficient to predict on individual level. In predictions of survival for individual patients, neural networks constitute good alternatives for classical statistical methods [32].

Although some previous studies have shown the association between prolonged QTc interval and cardiovascular mortality or all-cause mortality in the general population, other studies suggest that the relationship is not consistent

and the risk is likely to be small [33, 34]. In our study, univariate Cox regression analysis of individual risk predictors using ECG parameters, short-term heart-rate variability parameters, and 24-hour Holter monitoring parameters did not show statistical significance for survival in patients after myocardial infarction using fundamental analysis. Making the autonomic nervous system patterns for each parameter and its analysis for the particular value interval gave statistical significance which pointed to the advantage of using this method in statistics. One study had performed serial ECG follow-up after AMI and showed that QTc interval > 440 ms at hospital discharge had independent value for predicting major cardiac events [35]; another group suggested that QTc interval > 445 ms independently predicts all-cause death and heart failure in patients with STEMI [36]. Our study showed statistical significance for all-cause cardiac mortality in a group with QTc interval > 434 ms. The ATRAMI study showed that low values of either heart-rate variability (SDNN < 70 ms) or BRS (<3.0 ms/mm Hg) are a significant multivariate risk of cardiac mortality [37] compared to our study where reduced SDNN < 120 ms suggested higher risk. The predictive value of a variety of parameters has been assessed using ANN. Adding the artificial neural networks in data analysis in patients with acute myocardial infarction, the survival methodology was significantly improved, confirming that this model is fully applied and accurate in risk stratification and follow-up. Using standard statistical models we have concluded that the group with higher cardiovascular risk has sympathetic hyperactivity. In accordance with the results, therapy which includes adrenergic blockade should be proposed (beta blockers, ACE inhibitors, etc.). Similar results have been published in other studies [38, 39]. The ANN showed significantly better results in predicting survival of patients than the other models commonly used in different studies [40–42].

The proposed neural network classifier showed good performance for survival prediction, although the sample size was insufficient to ensure the statistical satisfaction. Part of the problem in preparing the data is incomplete and erroneous data, which were manually resolved by calculating corresponding values or removing samples.

The neural network training required a lot of experimenting to figure out the best architecture (number of hidden layers and neurons) and achieve the optimal classification performance. The good results were already obtained with one hidden layer with 15 hidden neurons; however increasing that number to 30 hidden neurons did not give any improvement in classification performance. So the conclusion was that using a single hidden layer with more than 15 neurons increases computational requirements, without increasing classifier performance, and probably leads to overfitting the model.

Adding another hidden layer and using the architecture with 11-15-7-1 neurons in layers, respectively, also did not give any improvements. So the conclusion was that adding one more layer on top of the first hidden layer also does not lead to classifier performance improvement.

Using architecture number 5, with 11-25-30-1 neurons in layers, gave the best classification performance. It is also interesting to note that adding more hidden neurons to second hidden layer (architecture (6)) gave worse results than architecture (5) (almost as architecture (1)). These results show that using more hidden neurons and layers does not bring improvement in classifier performance and that it is one of the critical parameters that needs to be further investigated for this type of applications. The optimal architecture and classification performance largely depends on which input parameters are used. The results showed that the statistical analysis can indicate a reliable choice of input parameters.

5. Limitations

The present study has some limitations. One of the limitations in this study considers the signal required for heart-rate variability analysis. In order to obtain clear signal, the samples with any noise or arrhythmias were eliminated, which reduced a group of patients with higher cardiovascular risk after myocardial infarction. To overcome the limitations, it is necessary to conduct research on a larger group of patients. ECG parameters like QTc intervals at discharge and after discharge are not measured or analyzed, and it is unknown whether they will have better predictive value. During post-MI period, assessment of cardiovascular risk parameters should be repeated multiple times. Another limitation is related to black-box nature of algorithm. At this point, it is hard to explain and debug results, as well as to understand possible different results. Making bigger dataset with more input variables during longer time of follow-up would provide more precise conclusion especially about very complex mechanisms involved in pathogenesis of cardiovascular diseases. The selection of risk factors which will be used as inputs for the neural network should be derived through a feature selection procedure on the training set, within the ANN cross-validation procedure. Further investigation needs to be established, but a good survival predictor must be able to deal with these obstacles.

6. Conclusion

This study proposed a survival status predictor based on ANN classifier trained with data obtained from HRV analysis. The trained ANNs achieved satisfying contribution in the prediction of outcome in patients with higher risk after MI. The study outlined the procedure for building neural network based clinical decision-making algorithm, including data preprocessing, attribute selection, neural network tuning, and performance evaluation. Classification based on the autonomic nervous system patterns can reliably indicate the individuals with a higher risk. This knowledge is crucial for making decisions about further observation and treatment.

Classifier performance largely depends on the input parameters which are used for training the ANN and number of hidden layers and neurons. Good candidates for input parameters for ANN training can be determined using statistical analyses and Kaplan-Meier survival curves for cardiac death. The optimal neural network architecture (number of hidden layers and neurons) can be determined experimentally by systematically adding hidden neurons and layers

and observing the classifier performance for each setting. The performance of the proposed method should be further investigated using databases from other sources.

Conflicts of Interest

The authors declare that there are no conflicts of interest regarding the publication of this article.

Acknowledgments

This work is supported by the Ministry of Education, Science and Technological Development of Serbia under Grants TP-32040 and III 45003.

References

[1] J. Lette, B. W. Colletti, M. Cerino et al., "Artificial intelligence versus logistic regression statistical modelling to predict cardiac complications after noncardiac surgery," *Clinical Cardiology*, vol. 17, no. 11, pp. 609–614, 1994.

[2] S. C. Smith Jr., J. Allen, S. N. Blair et al., "AHA/ACC guidelines for secondary prevention for patients with coronary and other atherosclerotic vascular disease: 2006 update—endorsed by the national heart, lung, and blood institute," *Circulation*, vol. 113, no. 19, pp. 2363–2372, 2006.

[3] M. O. Sweeney, M. S. Wathen, K. Volosin et al., "Appropriate and inappropriate ventricular therapies, quality of life, and mortality among primary and secondary prevention implantable cardioverter defibrillator patients: results from the pacing fast VT REduces shock ThErapies (PainFREE Rx II) trial," *Circulation*, vol. 111, no. 22, pp. 2898–2905, 2005.

[4] M. T. La Rovere, G. D. Pinna, S. H. Hohnloser et al., "Baroreflex sensitivity and heart rate variability in the identification of patients at risk for life-threatening arrhythmias," *Circulation*, vol. 103, no. 16, pp. 2072–2077, 2001.

[5] F. M. Merchant, T. Quest, A. R. Leon, and M. F. El-Chami, "Implantable cardioverter-defibrillators at end of battery life: opportunities for risk (Re)-stratification in ICD recipients," *Journal of the American College of Cardiology*, vol. 67, no. 4, pp. 435–444, 2016.

[6] P. E. Puddu and A. Menotti, "Artificial neural network versus multiple logistic function to predict 25-year coronary heart disease mortality in the Seven Countries Study," *European Journal of Cardiovascular Prevention and Rehabilitation*, vol. 16, no. 5, pp. 583–591, 2009.

[7] S. Joo, K.-J. Choi, and S.-J. Huh, "Prediction of spontaneous ventricular tachyarrhythmia by an artificial neural network using parameters gleaned from short-term heart rate variability," *Expert Systems with Applications*, vol. 39, no. 3, pp. 3862–3866, 2012.

[8] R. Bigi, D. Gregori, L. Cortigiani, A. Desideri, F. A. Chiarotto, and G. M. Toffolo, "Artificial neural networks and robust Bayesian classifiers for risk stratification following uncomplicated myocardial infarction," *International Journal of Cardiology*, vol. 101, no. 3, pp. 481–487, 2005.

[9] Z. Sevarac, B. Milovanovic, and T. Gligorijevic, "Follow up and risk assessment using artificial neural networks in patients with myocardial infarction," in *Proceedings of the 7th International Symposium on Noninvasive Electrocardiology (NEUROCARD '16)*, Belgrade, Serbia, October 2016.

[10] D. V. Exner, "Noninvasive risk stratification after myocardial infarction: rationale, current evidence and the need for definitive trials," *Canadian Journal of Cardiology*, vol. 25, supplement A, pp. 21A–27A, 2009.

[11] T. Huebner, M. Goernig, M. Schuepbach et al., "Electrocardiologic and related methods of non-invasive detection and risk stratification in myocardial ischemia: state of the art and perspectives," *German Medical Science*, vol. 8, article Doc27, 2010.

[12] J. V. Tu, "Advantages and disadvantages of using artificial neural networks versus logistic regression for predicting medical outcomes," *Journal of Clinical Epidemiology*, vol. 49, no. 11, pp. 1225–1231, 1996.

[13] B. Eftekhar, K. Mohammad, H. E. Ardebili, M. Ghodsi, and E. Ketabchi, "Comparison of artificial neural network and logistic regression models for prediction of mortality in head trauma based on initial clinical data," *BMC Medical Informatics and Decision Making*, vol. 5, no. 1, article 3, 2005.

[14] L. Bottaci, P. J. Drew, J. E. Hartley et al., "Artificial neural networks applied to outcome prediction for colorectal cancer patients in separate institutions," *The Lancet*, vol. 350, no. 9076, pp. 469–472, 1997.

[15] P. E. Puddu and A. Menotti, "Artificial neural networks versus proportional hazards Cox models to predict 45-year all-cause mortality in the Italian Rural Areas of the Seven Countries Study," *BMC Medical Research Methodology*, vol. 12, article 100, 2012.

[16] M. Kusy, B. Obrzut, and J. Kluska, "Application of gene expression programming and neural networks to predict adverse events of radical hysterectomy in cervical cancer patients," *Medical and Biological Engineering and Computing*, vol. 51, no. 12, pp. 1357–1365, 2013.

[17] F. E. Ahmed, "Artificial neural networks for diagnosis and survival prediction in colon cancer," *Molecular Cancer*, vol. 4, article 29, 2005.

[18] G. Parati, G. Ongaro, G. Bilo et al., "Non-invasive beat-to-beat blood pressure monitoring: new developments," *Blood Pressure Monitoring*, vol. 8, no. 1, pp. 31–36, 2003.

[19] G. Parati, M. DiRienzo, and G. Mancia, "How to measure baroreflex sensitivity: from the cardiovascular laboratory to daily life," *Journal of Hypertension*, vol. 18, no. 1, pp. 7–19, 2000.

[20] G. Gratze, R. Rudnicki, W. Urban, H. Mayer, A. Schlögl, and F. Skrabal, "Hemodynamic and autonomic changes induced by Ironman: prediction of competition time by blood pressure variability," *Journal of Applied Physiology*, vol. 99, no. 5, pp. 1728–1735, 2005.

[21] W. S. Choi, Y. Cho, N. Y. Kim et al., "Prognostic value of standard electrocardiographic parameters for predicting major adverse cardiac events after acute myocardial infarction," *Circulation*, vol. 122, supplement 21, pp. A9026–A9026, 2010.

[22] E. S. Williams, K. L. Thomas, S. Broderick et al., "Race and gender variation in the QT interval and its association with mortality in patients with coronary artery disease: results from the Duke Databank for Cardiovascular Disease (DDCD)," *American Heart Journal*, vol. 164, no. 3, pp. 434–441, 2012.

[23] M. C. Bishop, *Neural Networks for Pattern Recognition*, Clarendon Press, Oxford, UK, 1995.

[24] C. Castaneda, K. Nalley, C. Mannion et al., "Clinical decision support systems for improving diagnostic accuracy and achieving precision medicine," *Journal of Clinical Bioinformatics*, vol. 5, no. 1, p. 4, 2015.

[25] O. Kjellgren and J. A. Gomes, "Heart rate variability and baroreflex sensitivity in myocardial infarction," *American Heart Journal*, vol. 125, no. 1, pp. 204–215, 1993.

[26] A. J. Minisi, T. B. Nashed, and M. S. Quinn, "Regional left ventricular deafferentation increases baroreflex sensitivity following myocardial infarction," *Cardiovascular Research*, vol. 58, no. 1, pp. 136–141, 2003.

[27] A. D. Michaels and N. Goldschlager, "Risk stratification after acute myocardial infarction in the reperfusion era," *Progress in Cardiovascular Diseases*, vol. 42, no. 4, pp. 273–309, 2000.

[28] G. M. De Ferrari, A. Sanzo, A. Bertoletti, G. Specchia, E. Vanoli, and P. J. Schwartz, "Baroreflex sensitivity predicts long-term cardiovascular mortality after myocardial infarction even in patients with preserved left ventricular function," *Journal of the American College of Cardiology*, vol. 50, no. 24, pp. 2285–2290, 2007.

[29] C. M. Jones, M. S. Quinn, and A. J. Minisi, "Reflex control of sympathetic outflow and depressed baroreflex sensitivity following myocardial infarction," *Autonomic Neuroscience: Basic and Clinical*, vol. 141, no. 1-2, pp. 46–53, 2008.

[30] M. Babińska, J. Chudek, E. Chełmecka, M. Janik, K. Klimek, and A. Owczarek, "Limitations of Cox proportional hazards analysis in mortality prediction of patients with acute coronary syndrome," *Studies in Logic, Grammar and Rhetoric*, vol. 43, no. 56, pp. 33–48, 2015.

[31] M. J. Bradburn, T. G. Clark, S. B. Love, and D. G. Altman, "Survival analysis part II: multivariate data analysis—an introduction to concepts and methods," *British Journal of Cancer*, vol. 89, no. 3, pp. 431–436, 2003.

[32] L. Ohno-Machado, "A comparison of Cox proportional hazards and artificial neural network models for medical prognosis," *Computers in Biology and Medicine*, vol. 27, no. 1, pp. 55–65, 1997.

[33] S. M. Straus, J. A. Kors, M. L. de Bruin et al., "Prolonged QTc interval and risk of sudden cardiac death in a population of older adults," *Journal of the American College of Cardiology*, vol. 47, no. 2, pp. 362–367, 2006.

[34] A. Montanez, J. N. Ruskin, P. R. Hebert, G. A. Lamas, and C. H. Hennekens, "Prolonged QTc interval and risks of total and cardiovascular mortality and sudden death in the general population: a review and qualitative overview of the prospective cohort studies," *Archives of Internal Medicine*, vol. 164, no. 9, pp. 943–948, 2004.

[35] S. Ahnve, "QT interval prolongation in acute myocardial infarction," *European Heart Journal*, vol. 6, supplement D, pp. 85–95, 1985.

[36] J. F. Lin, S. Y. Hsu, S. Wu et al., "QT interval independently predicts mortality and heart failure in patients with ST-elevation myocardial infarction," *International Journal of Medical Sciences*, vol. 12, no. 12, article 968, 2015.

[37] M. T. La Rovere, J. T. Bigger Jr., F. I. Marcus, A. Mortara, and P. J. Schwartz, "Baroreflex sensitivity and heart-rate variability in prediction of total cardiac mortality after myocardial infarction," *The Lancet*, vol. 351, no. 9101, pp. 478–484, 1998.

[38] L. N. Graham, P. A. Smith, J. B. Stoker, A. F. Mackintosh, and D. A. S. G. Mary, "Time course of sympathetic neural hyperactivity after uncomplicated acute myocardial infarction," *Circulation*, vol. 106, no. 7, pp. 793–797, 2002.

[39] B. S. Huang and F. H. H. Leenen, "The brain renin-angiotensin-aldosterone system: a major mechanism for sympathetic hyperactivity and left ventricular remodeling and dysfunction after myocardial infarction," *Current Heart Failure Reports*, vol. 6, no. 2, pp. 81–88, 2009.

[40] G. Qiao, J. Li, A. Huang, Z. Yan, W.-Y. Lau, and F. Shen, "An artificial neural networking model for the prediction of post-hepatectomy survival of patients with early hepatocellular carcinoma," *Journal of Gastroenterology and Hepatology*, vol. 29, no. 12, pp. 2014–2020, 2014.

[41] C. G. Raji and S. S. Vinod Chandra, "Graft survival prediction in liver transplantation using artificial neural network models," *Journal of Computational Science*, vol. 16, pp. 72–78, 2016.

[42] J. H. Peng, Y. J. Fang, C. X. Li et al., "A scoring system based on artificial neural network for predicting 10-year survival in stage II A colon cancer patients after radical surgery," *Oncotarget*, vol. 7, no. 16, Article ID 22939, 2016.

Hindawi
Complexity
Volume 2017, Article ID 8365685, 15 pages
https://doi.org/10.1155/2017/8365685

Research Article

On Consistency of Cross-Approximate Entropy in Cardiovascular and Artificial Environments

Tamara Skoric,[1] Olivera Sarenac,[2] Branislav Milovanovic,[3] Nina Japundzic-Zigon,[2] and Dragana Bajic[1]

[1]*Faculty of Technical Sciences-DEET, Center of Excellence CEVAS, University of Novi Sad, Trg Dositeja Obradovica 6, 21000 Novi Sad, Serbia*
[2]*School of Medicine, Institute of Pharmacology, Clinical Pharmacology and Toxicology, University of Belgrade, Dr. Subotica 1, 11129 Belgrade, Serbia*
[3]*Department of Cardiology, Neurocardiology Laboratory, University Hospital Medical Center "Bezanijska Kosa", Bezanijska Kosa bb, 11080 Belgrade, Serbia*

Correspondence should be addressed to Dragana Bajic; dragana.bajic@gmail.com

Received 26 February 2017; Revised 8 June 2017; Accepted 7 August 2017; Published 17 September 2017

Academic Editor: Zoran Obradović

Copyright © 2017 Tamara Skoric et al. This is an open access article distributed under the Creative Commons Attribution License, which permits unrestricted use, distribution, and reproduction in any medium, provided the original work is properly cited.

Cross-approximate entropy *(XApEn)* quantifies the mutual orderliness of simultaneously recorded time series. Despite being derived from the firmly established solitary entropies, it has never reached their reputation and deployment. The aim of this study is to identify the problems that preclude wider *XApEn* implementation and to develop a set of solutions. Exact expressions for *XApEn* and its constitutive parts are derived and compared to values estimated from artificial data. This comparison revealed vast regions within the parameter space that do not guarantee reliable probability estimation, making *XApEn* estimates inconsistent. A simple correction to one of the *XApEn* procedural steps is proposed. Three sets of formulae for joint parameter selection are derived. The first one is intended to maximize threshold profile. The remaining ones minimize *XApEn* instability according to the strong and weak criteria. The derived expressions are verified using cardiovascular signals recorded from rats (long signals) and healthy volunteers (short clinical signals), proposing a change of traditional parameter guidelines.

1. Introduction

Approximate entropy *(ApEn)* is among the most exploited nonlinear techniques to quantify the complexity and unpredictability of time series [1–3], with a citation rate highlighted in [4]. *ApEn* is approved as a supporting tool in preclinical and clinical studies, with the most prominent applications in cardiovascular studies.

In spite of the vast and firmly established implementation, the activities on *ApEn* improvement have never ceased. Research efforts are oriented towards modifications, including sample entropy *(SampEn)* [5], corrected conditional entropy *(CApEn)* [6], K-nearest neighborhood entropy *(KNNCE)* [7], fuzzy entropy *(FuzzyEn)* [8], multiscale entropy *(MultiScaleEn)* [9], distance entropy *(DistEn)* [10], binarized entropy *(BinEn)* [11], *ApEn* based on wave mode [12], and speeding-up algorithms [13, 14], and towards the consistency studies, including threshold selection [15–20], time lag [21], and consistency in general [4].

One of the very first *ApEn* modifications is *Cross-ApEn (XApEn)* [22] that estimates mutual predictability of two simultaneously recorded time series. In view of *ApEn* as a complexity measure of solitary signal, *XApEn* should have become an equivalent tool for paired physiological processes. However, the reputation and deployment of its predecessor have never been reached. Except for a recent improvement [23], *XApEn* applications follow classical *ApEn* guidelines, although (a) the parameters should be adjusted even for *ApEn* (e.g., [4, 15–20]) and (b) properties of *XApEn* are different and straightforward *ApEn* guidelines might not be proper.

The aim of this paper is to identify the problems that preclude wider *XApEn* implementation and to propose methods for their adjustment. It is proved that the fundamental source of *XApEn* inconsistency is unreliable estimation of

conditional probabilities that are its constitutive elements. It is shown that the parameters required for *XApEn* are mutually dependent, so the traditional guidelines for their choice need an update. In order to locate the unstable parameter regions, the *XApEn* values estimated from the artificially simulated data are compared to the true *XApEn* values calculated by a formula. Following these observations, we derived equations that jointly select stable parameters for reliable *XApEn* estimation in real signals, for which exact mathematical descriptions are unavailable. The derived equations are tested using a wide variety of cardiovascular signals: using typical short records of ambulatory patients and using long signals recorded from small laboratory animals.

2. Materials and Methods

2.1. Experimental Data. The study used three types of data: artificial, animal, and human. The purpose of artificial data was to test the stability of estimated values, comparing them to the exact values calculated by the derived formulae, and also to develop a new set of threshold equations. The data recorded from animals were also used for method development and for its repeated testing, enabled by the record length. The data recorded from human volunteers were used to validate the derived methods in typical real applications where the records are short.

The animal data include systolic blood pressure (SBP) signals and pulse interval (PI) signals recorded from two groups of rats: the first group comprised outbred male Wistar normotensive rats, while the second group comprised outbred male borderline hypertensive rats. Ten days before the recordings, radiotelemetric probes (TA11PA-C40, DSI, Transoma Medical) were implanted in the abdominal aorta. Blood pressure (BP) waveforms were digitally recorded and transmitted using Dataquest A.R.T. 4.0 equipment (DSI, St. Paul, MN, USA) with sampling frequency $fs = 1000$ Hz. The systolic blood pressure (SBP) was determined at the receiver as waveform local maxima. The pulse interval was determined as an interval between the successive moments of maximal gradients $(\Delta(\mathrm{BP})/\Delta T)_{\max}$, that is, the local maximal change (Δ) of blood pressure (BP) waveform per sampling interval ΔT. Pulse interval is an acceptable alternative to R-R interval of an electrocardiogram. During the experiments, the animals were exposed to two types of stress: shaker stress, with rats positioned on a platform shaking at 200 cycles/min, and restraint stress, with rats placed in a Plexiglas restrainer tube (ID 5.5 cm with pores) in the supine position, with a detailed description given in [24]. These data were already used for other research purposes [20, 24, 25]. The duration of records in baseline, restraint stress, and shaker stress was 20 minutes, 60 minutes, and 20 minutes, respectively. Such a wide variety of data (different types of rats and different stressing surroundings) ensured the correct validation of the derived methods. Very slow signal component (trend), an outcome of free rat movements, was eliminated using a high-pass filter designed specifically for biomedical signals [26]. The cut-off frequency f_H is tuned to the mean pulse interval of a subject: f_H [Hz] = 0.011/(mean(PI) [s]). Its value ranges from 0.055 Hz to 0.085 Hz in this experiment. The time series passed the stationarity, so the remaining signals were taken from 12 Wistar normotensive rats (total of 24 signals: 12 baseline, 6 restraint, and 6 shaker) and from 13 borderline hypertensive rats (total of 26 signals: 13 baseline, 7 restraint, and 6 shaker signal sets). All experimental procedures in this study conformed to the European Communities Council Directive of 24 November 1986 (86/609/ECC) and the Guidelines on Animal Experimentation of the School of Medicine, University of Belgrade.

Short data series (number of samples $N \leq 750$) were recorded from 41 medically examined male healthy volunteers positioned in a hospital bed, using Task Force® Monitor with sampling frequency equal to 1000 Hz (CNSystems Medizintechnik AG, Graz, http://www.cnsystems.com/products/task-force-monitor). Systolic blood pressure was obtained as local maxima of blood pressure waveforms, while R peaks were found as local maxima of electrocardiogram waveforms. The intervals between the successive R peaks form the R-R interval time series. Sensors were attached by medical professionals and patients were motionless, ensuring the reduced number of artifacts and stationarity of the signals. Short data lengths are typical for ambulatory monitoring, up to 10 minutes, and also ensure tranquility of the patient and stationarity of the recorded data. The experiment followed the ethical standards stated by the School of Medicine, University of Belgrade, and a signed permission was collected from each volunteer.

Artificial data included samples with uniform distributions, generated using a reliable proprietary machine independent random number generator, and the samples with normal distribution generated using the polar method. For each one of the parameter sets, a hundred of the artificial data series were generated, each one comprising up to $N = 5000$ data samples. Program code was written in Matlab 2014b.

An illustration of the time series referenced within this study is shown in Figure 1.

2.2. XApEn in Brief. The procedure for *XApEn* estimation [22] implies $x_i \in \mathbf{X}$, $i = 1, \ldots, N$, as a "*master*" time series and $y_j \in \mathbf{Y}$, $j = 1, \ldots, N$, as its "*follower*," where N is the number of signal samples. In biomedical data, SBP is considered as a master signal $\mathbf{X}$, and PI is considered as its follower $\mathbf{Y}$. The series are divided into the vectors of length m:

$$\begin{aligned} \mathbf{X}_m^{(i)} &= \left[x_i, x_{i+\tau}, \ldots, x_{i+(m-1)\cdot\tau}\right], \\ &\qquad i = 1, \ldots, N-(m-1)\cdot\tau \\ \mathbf{Y}_m^{(j)} &= \left[y_j, y_{j+\tau}, \ldots, y_{j+(m-1)\cdot\tau}\right], \\ &\qquad j = 1, \ldots, N-(m-1)\cdot\tau. \end{aligned} \tag{1}$$

Parameter τ can be introduced for vector decorrelation [21] but in most studies it is set to 1 [beat]. A vector from the master series is usually regarded as a "*template*."

Distance between two vectors is defined as a maximal absolute sample difference:

$$d\left(\mathbf{X}_m^{(i)}, \mathbf{Y}_m^{(j)}\right) = \max_{k=0,\ldots,m-1} \left|x_{i+k\cdot\tau} - y_{j+k\cdot\tau}\right|, \quad i, j = 1, \ldots, N-(m-1)\cdot\tau. \tag{2}$$

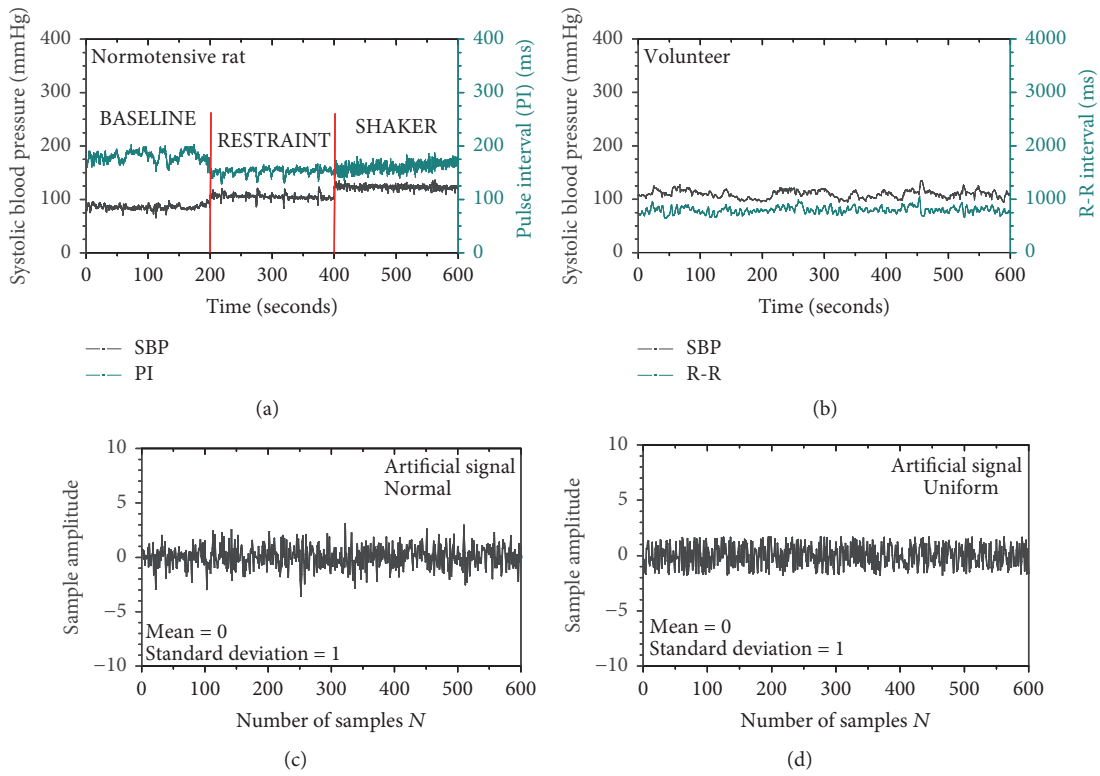

FIGURE 1: Examples of real cardiovascular signals and of artificially generated signals. (a) SBP signal (gray) and PI signal (green) recorded from a rat at baseline condition, exposed to restraint stress and exposed to shaker stress. (b) SBP (gray) and R-R (green) signals recorded from a healthy volunteer. (c, d) Artificially generated signals with zero mean and standard deviation equal to 1; normal distribution (c) and uniform distribution (d).

The vectors are considered as "*similar*" if their distance is less than or equal to the predefined threshold (tolerance) r. The procedure of finding the similarities is called "*template matching*." Standard scoring of time series must be performed; otherwise, vectors from different sources would be incomparable [22]. Standard scoring implies centralization and normalization of series x, $(x - \mu)/\sigma$, where μ denotes mean and σ denotes standard deviation. For a correct estimation of μ and σ, the observed time series must be stationary at least in a wide sense.

A conditional probability that a vector $\mathbf{Y}$ is within the distance r from a particular template $\mathbf{X}_m^{(i)}$, $i = 1, \ldots, N-(m-1)\cdot\tau$, is estimated as follows:

$$\begin{aligned}\widehat{p}_i^m(r) &= \Pr\left\{d\left(\mathbf{X}_m, \mathbf{Y}_m\right) \le r \mid \mathbf{X}_m = \mathbf{X}_m^{(i)},\ \mathbf{Y}_m \in \mathbf{Y},\ r > 0\right\} \\ &= \frac{1}{N-(m-1)\cdot\tau} \sum_{j=0}^{N-(m-1)\cdot\tau} I\left\{d\left(\mathbf{X}_m^{(i)}, \mathbf{Y}_m^{(j)}\right) \le r\right\},\end{aligned} \tag{3}$$

where "^" denotes an estimate and $I\{\cdot\}$ denotes an indicator function that is equal to 1 if the condition it indicates is fulfilled (distance less than or equal to r). Denoting the number of "ones" with $N_1(i)$, the conditional probability (3) can be also expressed as

$$\begin{aligned}\widehat{p}_i^m(r) &= \frac{N_1(i)}{N-(m-1)\cdot\tau}, \\ N_1(i) &= \sum_{j=0}^{N-(m-1)\cdot\tau} I\left\{d\left(\mathbf{X}_m^{(i)}, \mathbf{Y}_m^{(j)}\right) \le r\right\},\ i = 1, \ldots, N-(m-1)\cdot\tau.\end{aligned} \tag{4}$$

Probabilities (3) and (4) describe a binary event, as the vector $\mathbf{Y}_m^{(j)}$ can either match or mismatch its template $\mathbf{X}_m^{(i)}$. A precise mathematical derivation of the number of binary events necessary for reliable probability estimation is given in [27]. The derivation in [27] is based assuming a normal approximation of binomial distribution, in our case observing the number of matches found during $N - m + 1$ template matching trials. The resulting tables and graphs point out the probability that the estimated value $\widehat{p}_i^m(r)$, for a given number of matching trials, lies within specific boundaries known as "confidence interval." From the graphically presented results in [27], it can be seen that a 95% confidence interval of about $(0.55 \cdot p_i^m(r), 1.8 \cdot p_i^m(r))$, which is generally considered to be a reasonable uncertainty, is assessed if the number of trials is $10/p_i^m(r)$. So, if the number of tests exceeds $10/p_i^m(r)$, it is considered as a "weak criterion" that yields satisfactory good estimates of binary probabilities [27].

The number of matches that is equal to $100/p_i^m(r)$ is considered as a "strong criterion" for which the boundaries are tighter, with probability estimation less uncertain, but usually it is more difficult to be achieved as it requires long time series. The corresponding confidence intervals, both for weak and for strong criteria, are derived in [27] as follows:

$$\begin{aligned} &\Pr\left\{0.55 \cdot p_i^m(r) \le \widehat{p}_i^m(r) \le 1.8 \cdot p_i^m(r)\right\} = 0.95 \\ &\qquad\qquad\qquad\qquad\qquad\qquad \text{weak criterion;} \\ &\Pr\left\{0.8 \cdot p_i^m(r) \le \widehat{p}_i^m(r) \le 1.25 \cdot p_i^m(r)\right\} = 0.95 \\ &\qquad\qquad\qquad\qquad\qquad\qquad \text{strong criterion.} \end{aligned} \tag{5}$$

The next step in *XApEn* estimation is to average logarithms of the probability estimates (4) over all template values and to form a summand $\widehat{\Phi}^{(m)}$:

$$\widehat{\Phi}^{(m)}(r, N, \tau) = \frac{1}{N - (m-1)\cdot\tau} \sum_{i=0}^{N-(m-1)\cdot\tau} \ln\left(\widehat{p}_i^m(r)\right). \tag{6}$$

The procedure is repeated for the vectors of length $m + 1$, yielding the estimate:

$$\begin{aligned} \widehat{X}ApEn(m, r, N, \tau) &= \widehat{\Phi}^{(m)}(r, N, \tau) \\ &\quad - \widehat{\Phi}^{(m+1)}(r, N, \tau). \end{aligned} \tag{7}$$

Due to the fact that in *XApEn* two different time series are compared, a self-match (matching a template to itself), alleged source of bias in *ApEn*, cannot occur. Unfortunately, comparison of vectors from different series also means that there is no guarantee that a template of length m in the master time series has at least one match in the follower time series; hence, a lack of matches ($\widehat{p}_i^m(r) = 0$) can occur. The consequence is a logarithm of zero in (6) that makes *XApEn* estimate impossible, pointed out in [5] as well. A usual correction ignores and skips $\widehat{p}_i^m(r) = 0$ cases. Such a correction decreases the numerator in (6) with respect to its denominator and considerably underestimates the summand $\widehat{\Phi}$. We propose two summand $\widehat{\Phi}^{(m)}$ corrections, both different from the corrections in [5]. The first one is analogous to *ApEn* and implements artificial self-matches $\widehat{p}_i^m(r) = 1/(N - (m-1)\cdot\tau)$ (see (8)). The second correction excludes $\widehat{p}_i^m(r) = 0$ cases from the numerator of (6) (see (9)). If $N_0 = \sum_{i=0}^{N-(m-1)\cdot\tau} I\{\widehat{p}_i^m(r) = 0\}$ denotes a total number of zero matches, then

$$\begin{aligned} &\widehat{\Phi}_{\mathrm{COR1}}^{(m)}(r, N, \tau) \\ &= \frac{\left(\left(\sum_{i=0,\, \widehat{p}_i^m(r)\neq 0}^{N-(m-1)\cdot\tau} \ln\left(\widehat{p}_i^m(r)\right)\right) - N_0 \cdot \ln\left(N - (m-1)\cdot\tau\right)\right)}{\left(N - (m-1)\cdot\tau\right)} \end{aligned} \tag{8}$$

$$\widehat{\Phi}_{\mathrm{COR2}}^{(m)}(r, N, \tau) = \frac{\sum_{i=0,\, \widehat{p}_i^m(r)\neq 0}^{N-(m-1)\cdot\tau} \ln\left(\widehat{p}_i^m(r)\right)}{\left(N - (m-1)\cdot\tau - N_0\right)}. \tag{9}$$

A simple abstract experiment analyzes the proposed corrections. Suppose that all nonzero probabilities are equal to an arbitrary constant, $\widehat{p}_i^m(r) = e^{-k}$, $k > 0$. Then, summands $\widehat{\Phi}$ given by (6) with $\widehat{p}_i^m(r) = 0$ skipped and given by (8) and by (9) are equal to

$$\widehat{\Phi}^{(m)}(r, N, \tau) = \begin{cases} -k \cdot \left(1 - \dfrac{N_0}{(N - (m-1)\cdot\tau)}\right) & (6) \text{ with } \widehat{p}_i^m(r) = 0 \text{ skipped;} \\ -k \cdot \left(1 - \dfrac{N_0}{(N - (m-1)\cdot\tau)}\right) - N_0 \cdot \dfrac{\ln\left(N - (m-1)\cdot\tau\right)}{(N - (m-1)\cdot\tau)}, & \text{correction } (8); \\ -k & \text{correction } (9). \end{cases} \tag{10}$$

If N tends to infinity, N_0 converges to zero and all $\widehat{\Phi}$ estimates converge to the same true value, that is, to $-k$. But if N is limited, the underestimation of $\widehat{\Phi}$ in (6) (with $\widehat{p}_i^m(r) = 0$ skipped) and (8) is proportional to N_0. Equation (8) additionally suffers from a nonlinear bias due to the false self-matching, thus repeating the problem of genuine self-matching in *ApEn*. The preferred correction is given by (9) and it was used in further evaluation. However, as it would be clarified later on, if the *XApEn* parameters are properly chosen, the need for this adjustment is reduced.

2.3. Parameter-Induced XApEn Inconsistency. The parameters necessary for *XApEn* estimation—time series length N, threshold level r, vector size m, and time lag τ—create a huge working space, but with unstable regions. Recent *ApEn* contributions have reviewed this problem [4, 19], earlier also noticed in [6, 8, 15–18, 20]. But parameter study for *XApEn* does not exist, except for a brief comment in [5] (to the best of the authors' knowledge). A few contributions that implement *XApEn* follow the standard guidelines from the original *ApEn*/*XApEn* papers [1–3, 22]: parameters $m = 1$ and $r = 0.2$ are implemented in [27]; parameters $m = 2$ or 3, $r = 0.15$, and $N = 1000$ are implemented in [28, 29], while parameters $m = 1$ and $r = 0.35$ are used in [30]. It should be noted that the threshold value r in *ApEn* studies is calculated with respect to the standard deviation σ, for example, $r = 0.2 \cdot \sigma$. In *XApEn* studies, standard deviation is by definition set to $\sigma = 1$, due to the obligatory standard scoring [22].

An illustrative example of contradictory results induced by different working points is presented in Figure 2. The contradictory results are noticed in borderline hypertensive rats exposed to shaker stress. Embedded plots show a "*XApEn threshold profile*" [17]: *XApEn* values estimated for a range of threshold r values, keeping all the other parameters fixed.

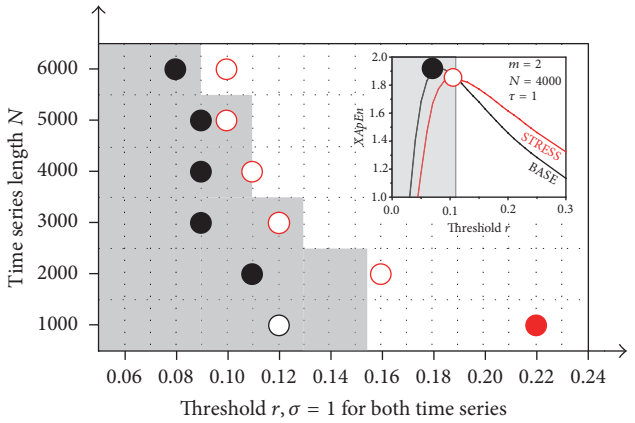

FIGURE 2: Illustrative example of inconsistent results: a threshold-length (r-N) plane for *XApEn* estimated from SBP and PI signals of rats at baseline (black lines and circles) and stress (red lines and circles). Gray regions: estimated *XApEn* is higher at baseline than at stress. White regions: *XApEn* is higher at stress than at baseline. Circles: threshold $r_{\max}$ for which *XApEn* reaches its maximal value; for a particular N, the empty circle denotes the lower of two maximal *XApEn* values. Embedded plot shows a complete threshold profile for $N = 4000$. Results are obtained from borderline hypertensive rats exposed to shaker stress.

To obtain a profile, threshold level was gradually increased with increments equal to 0.01 for $r < 0.2$ and equal to 0.05 for $r \geq 0.2$. The black line corresponds to *XApEn* estimated from SBP and PI signals of rats in baseline conditions, while the red line corresponds to the threshold profile estimated from rats at stress. An intersection of these two lines divides the plot area into two regions: in the "gray" region, *XApEn* values are higher in baseline conditions than in stress, while in the "white" region *XApEn* contradictorily becomes lower at baseline than at stress. The maximal value of *XApEn* (the maximum of the threshold profile line) is denoted by a circle. An "empty" circle denotes the lower one of these two maximums. A complete threshold-length (r-N) plane is shown in the remaining part of Figure 2. A threshold profile is estimated for each particular time series length N. The thresholds positions $r_{\max}$ for which *XApEn* profile reaches its maximum [17] are shown by circles. We have assumed a time lag $\tau = 1$.

The symbolic presentation in Figure 2 distinguishes three different sources of contradictory results (flip-flop effect):

(A) For a fixed length N, the *XApEn* "flips" from being lower during stress for lower threshold r to being higher during stress for higher threshold r; for example, for $N = 1000$, this change occurs for $r \approx 0.15$.

(B) For a fixed threshold r, an undesirable change of *XApEn* from being lower at stress to being higher at stress occurs at particular time series lengths; for example, if $r = 0.12$, this change occurs between $N = 3000$ and $N = 4000$.

(C) For $r_{\max}$ chosen for a threshold ($r_{\max}$ is a threshold for which *XApEn* reaches its maximal value, [15–17]), *XApEn* changes from being higher at stress, if $N = 1000$, shown by a full red circle, to being lower at stress for $N > 2000$, shown by empty red circles.

2.4. Explicit Formulae for Error Estimation. The constitutive *XApEn* elements are conditional probabilities $\widehat{p}_i^m(r)$ ((3) and (4)), which are subject to an estimation error $\varepsilon_i^m(r)$ each:

$$\varepsilon_i^m(r) = p_i^m(r) - \widehat{p}_i^m(r) \Longrightarrow$$
$$\widehat{p}_i^m(r) = p_i^m(r) \cdot \left(1 - \frac{\varepsilon_i^m(r)}{p_i^m(r)}\right), \quad i = 1, \ldots, N - (m-1)\cdot\tau. \tag{11}$$

These errors are logarithmically accumulating to form a summand $\widehat{\Phi}^{(m)}(r, N, \tau)$ estimation error $\varepsilon_\Phi^m(r, N, \tau)$,

$$\widehat{\Phi}^{(m)}(r, N, \tau) = \frac{1}{N - (m-1)\cdot\tau} \cdot \sum_{i=0}^{N-(m-1)\cdot\tau} \left(\ln\left(p_i^m(r)\right) + \ln\left(1 - \frac{\varepsilon_i^m(r)}{p_i^m(r)}\right)\right) \Longrightarrow$$
$$\varepsilon_\Phi^m(r, N, \tau) = \frac{-1}{N - (m-1)\cdot\tau} \cdot \sum_{i=0}^{N-(m-1)\cdot\tau} \ln\left(1 - \frac{\varepsilon_i^m(r)}{p_i^m(r)}\right), \tag{12}$$

and *XApEn* error $\varepsilon_X^m(r, N, \tau)$,

$$\varepsilon_X^m(r, N, \tau) = \frac{1}{N - m\cdot\tau} \sum_{i=0}^{N-m\cdot\tau} \ln\left(1 - \frac{\varepsilon_i^{m+1}(r)}{p_i^{m+1}(r)}\right) - \frac{1}{N - (m-1)\cdot\tau} \sum_{i=0}^{N-(m-1)\cdot\tau} \ln\left(1 - \frac{\varepsilon_i^m(r)}{p_i^m(r)}\right). \tag{13}$$

To find a stable parameter region where estimation errors would be minimized, the true conditional probabilities $p_i^m(r)$ must be evaluated for each template $\mathbf{X}_m^{(i)}$:

$$p_i^m(r) = \prod_{k=0}^{m-1} \int_{x_{i+k\cdot\tau}-r}^{x_{i+k\cdot\tau}+r} f_y(y) \cdot dy, \quad i = 1, \ldots, N - (m-1)\cdot\tau, \tag{14}$$

where $f_y(y)$ denotes the probability density function (p.d.f.) of the signal $\mathbf{Y}$ (follower). A probability $\int_{x_{i+k\cdot\tau}-r}^{x_{i+k\cdot\tau}+r} f_y(y) \cdot dy$ corresponds to an event where a sample $y_{j+k\cdot\tau}$ is within the distance $\pm r$ from a template sample $x_{i+k\cdot\tau}$.

Unfortunately, biomedical signals are an outcome of numerous complex physiological inputs and feedback, so exact formulae for their p.d.f. have not been determined yet. Instead, we used artificially generated data with normal and uniform distribution:

$$f_y^{(U)}(y) = \begin{cases} \dfrac{1}{2\cdot\sqrt{3}}, & -\sqrt{3} \le y \le \sqrt{3} \\ 0, & \text{elsewhere,} \end{cases} \quad \text{uniform p.d.f.}$$

$$f_y^{(N)}(y) = \left\{ \frac{1}{\sqrt{2\cdot\pi}} \cdot e^{-y^2/2}, \quad \text{normal p.d.f.} \right. \tag{15}$$

The artificial data were used both for the master and for the follower series, generating four experimental data sets: a master and its follower both normal, both uniform, normal master with uniform follower, and uniform master with normal follower.

The corresponding true values of conditional probabilities, assuming $\tau = 1$, are

$$p_i^m(r) = \begin{cases} \dfrac{\prod_{k=0}^{m-1}\left(\min\left(\sqrt{3}, x_{i+k}+r\right) - \max\left(-\sqrt{3}, x_{i+k}-r\right)\right)}{\left(2\cdot\sqrt{3}\right)^m}, & \left|x_{i+k}\right| - r < \sqrt{3}, \text{ uniform p.d.f.} \\ 0, & \left|x_{i+k}\right| - r \ge \sqrt{3} \text{ uniform p.d.f.} \\ \prod_{k=0}^{m-1} \dfrac{1}{\sqrt{2\cdot\pi}} \int_{x_{i+k}-r}^{x_{i+k}+r} e^{-y^2/2}\cdot dy = \prod_{k=0}^{m-1}\left(\varphi\left(x_{i+k}+r\right) - \varphi\left(x_{i+k}-r\right)\right) & \text{normal p.d.f.} \end{cases} \tag{16}$$

Normal cumulative distribution function $(1/\sqrt{2\cdot\pi})\int_{-\infty}^{z} e^{-y^2/2}\cdot dy$ in the lower part of (16) is denoted by $\varphi(z)$ instead of $\Phi(z)$, to avoid confusion with the summand Φ. With (16) known, all the relevant estimation errors (11)–(13) can be found.

2.5. Reference Thresholds for Cardiovascular Signals. The error analysis in artificial data has a privilege to evaluate a reference point (true value) using an exact formula. The problem with natural signals is that their data samples are statistically dependent. Besides, the signal nature is not completely revealed and there are no mathematical expressions to describe it. So, there exists no calculated reference value to which the estimated results could be compared. The first auxiliary point of reference considering *ApEn* was empirically obtained in [17], where the authors pointed out the existence of *ApEn* maximum and the corresponding threshold $r_{\max}$ for which this maximum is reached. $r_{\max}$ is found by performing a tedious task of estimating *ApEn* for each threshold value separately, thus obtaining a threshold profile. In [15], tedious estimation is substituted by a set of expressions that automatically evaluate a theoretical threshold $r_{\text{TH-A}}$ that is (almost) equal to $r_{\max}$. In [16], the same authors proposed an alternative set of formulae for $r_{\text{TH-A}}$. It was shown [15, 16] that the empirical threshold level $r_{\max}$ for which maximal value of *ApEn* is obtained when plotting the threshold profile depends on the time series length N, on standard deviations σ of time series $x(i)$, and on standard deviations σ_D of lagged differential signal $(x(i) - x(i-\tau))$, where τ is a time lag (delay) between the samples, $\tau = 1$. The observed dependency was shown to be linear with respect to the square root of σ_D and σ ratio, so the authors performed a computer search for the coefficients that yield the best fit in the least-squares sense to obtain (18). We have adopted the same method to find the $m = 1$ case of a theoretical threshold $r_{\text{TH-A}}$ in (18), necessary for our evaluations, but not covered in [15, 16].

A method for automatic evaluation of auxiliary reference point does not exist for *XApEn*. We observed [25] that the threshold $r_{\text{TH-A}}$ of master time series influences the threshold $r_{\max}$ of *XApEn* and that their difference is linearly related to the square root of $\sigma_{DX} + \sigma_{DY}$, where σ_{DX} and σ_{DY} are standard deviations of the lagged differential series $(x(i) - x(i-\tau))$ and $(y(i) - y(i-\tau))$ [25]. Then, for each artificially created master **X**-follower **Y** combination (normal-normal, normal-uniform, uniform-normal, and uniform-uniform), we generated 100 normalized signal pairs, in total 400 signal pairs per parameter set. For each signal pair, we found the maximum of the threshold profile and the corresponding $r_{\max}$, and we also estimated σ_{DX} and σ_{DY}. Then, the least-squares fitting is performed with respect to $r_{\max}$, thus obtaining particular coefficients $a(m)$, $b(m)$, and $c(m)$. The procedure is repeated for different N values, from 300 to 5000 with an increment equal to 100. The results were averaged for each particular $m \in \{1, 2, 3, 4\}$ giving the coefficient sets $a(m)$, $b(m)$, and $c(m)$. Since several sets had almost the same averaged least-squares error, ten out of 25 baseline signals from rats were randomly selected for justification, and the coefficient set with minimal absolute error (averaged over all values of N and m) was selected for a threshold $r_{\text{TH-X}}$, for which *XApEn* approaches its maximal value:

$$r_{\text{TH-X}}(m) = r_{\text{TH-A}}(m) + \left| a(m) + \frac{b(m) + c(m)\cdot\sqrt{\left(\sigma_{DX}+\sigma_{DY}\right)/2}}{\sqrt[4]{N/1000}} \right|,$$
$$(a, b, c) = \begin{cases} (0, -0.015, 0.03), & m = 1 \\ (-0.02, 0, 0.023), & m = 2 \\ (0, -0.006, 0.043), & m = 3 \\ (0, -0.11, 0.13), & m = 4, \end{cases} \tag{17}$$

where $r_{\text{TH-A}}$ is evaluated from the master time series according to

$$r_{\text{TH-A}}(m) = \frac{e(m) + f(m) \cdot \sqrt{\sigma_{DX}/\sigma_X}}{\sqrt[4]{N/1000}},$$
$$(e, f) = \begin{cases} (-0.01, 0.05), & m = 1 \\ (-0.02, 0.23), & m = 2 \\ (-0.06, 0.43), & m = 3 \\ (-0.11, 0.65), & m = 4. \end{cases} \quad (18)$$

Here, σ_X is standard deviation of a time series $\mathbf{X}$ (in *XApEn* it is always equal to one) while σ_{DX} and σ_{DY} are standard deviations of the lagged differential series $(x(i) - x(i-\tau))$ and $(y(i) - y(i-\tau))$. The expression for $m = 1$ in (18) is presented for the first time in this study, while the expressions for $m = 2, 3, 4$ are taken from [15]. As it is shown in Table 3, the expressions from [15] yield a lower amount of relative error for cardiovascular data used in this study, so they are more appropriate than the similar expressions derived in [16]. The subset of thresholds (17) for $m = 2$ and $m = 3$ was presented in [25].

The threshold $r_{\text{TH-X}}$ is only halfway towards the reliable working point. As it would be shown, if threshold $r_{\text{TH-A}}$ is applied, the reliability criteria stated by $N > 10/p_i^m(r)$ (or $100/p_i^m(r)$) are not satisfied. A different interpretation of these criteria states that at least 10 (or 100) events should be found, in order to have the estimated event probability fitted within the confidence bounds (5) with the certainty of 95%.

Obviously, increased m reduces the matching probability of the template and its follower, and thus a threshold increase had to be proportional to it. The coefficients in (19) and (20) are obtained using the same data sets as for (17). In this case, the conditional probabilities were estimated, and the fitting was performed among the coefficients that yield less than 5% of unreliable probabilities, over all values of m and over all data lengths:

$$\begin{aligned} r_{\text{XW}}(m) &= 0.2 \cdot (m+1) + r_{\text{TH-X}}(m), && m \le 4,\ N \le 500, \\ r_{\text{XW}}(m) &= 0.17 \cdot (m+1) + r_{\text{TH-X}}(m), && m \le 4,\ 500 < N \le 2000, \\ r_{\text{XW}}(m) &= 0.15 \cdot (m+1) + r_{\text{TH-X}}(m), && m \le 4,\ N > 2000. \end{aligned} \quad (19)$$

In the case of strong reliability criteria, a relationship of threshold (20) with respect to vector length m is nonlinear:

$$r_{\text{XS}}(m) = \left(m + 1 + \frac{10^5}{N^2}\right) \cdot \left(r_{\text{TH-X}}(m) + \frac{(5-m)}{10}\right), \quad m \le 4. \quad (20)$$

For the sake of clarity, the different threshold values are summarized in Table 1.

Table 1: Threshold abbreviations and definitions.

Abbreviation	Definition
$r \cdot \sigma$	*ApEn* threshold, expressed in units of time series
r	*XApEn* threshold, dimensionless
$r_{\max}$	Threshold obtained from threshold profile, for which $(X)ApEn$ reaches its maximal value [17]
$r_{\text{TH-A}}$	Automatically calculated *ApEn* threshold using (18)
$r_{\text{TH-X}}$	Automatically calculated *XApEn* threshold using (17)
r_{XW}	Automatically calculated *XApEn* threshold for which at least 95% of the estimated probabilities satisfy weak criterion.
r_{XS}	Automatically calculated *XApEn* threshold for which at least 95% of the estimated probabilities satisfy strong criterion.

2.6. Reliability Criteria in Statistically Dependent Data. The confidence bounds (5) hold for statistically independent binary events [27]. Template matching in artificial data satisfies this constraint: observing an $m = 1$ template $[x_k]$, its successive matching tests $|x_k - y_i| \le r$ and $|x_k - y_{i+1}| \le r$ at the respective positions i and $i + 1$ are independent, as an absolute difference of a constant x_k and independent samples y_i and y_{i+1} does not destroy independency. A similar line of reasoning holds if $m > 1$. It follows that the estimated probabilities $\widehat{p}_i^m(r)$ have a scaled binomial distribution [27], so the reliability criteria and confidence intervals (5) can be applied. If the data were statistically dependent, the only change is an increase of confidence bounds, without affecting the estimated values or the reliability criteria [27]. However, true confidence bounds in real biomedical data cannot be defined as true $p_i^m(r)$ is unknown, so statistical dependency is of no importance for real data. The reliability still can be tested in a form of $N - m + 1 > (10 \text{ or } 100)/\widehat{p}_i^m(r)$, showing whether the obtained value $\widehat{p}_i^m(r)$ is estimated from a sufficient amount of data.

3. Results and Discussion

3.1. Estimation Errors in Artificial Data. For *XApEn* error estimation, master series $\mathbf{X}$ and a hundred of its followers $\mathbf{Y}$ were artificially generated for a range of $(r, N, m, (\tau = 1))$ parameters, and the same values exactly were calculated using the derived formulae. The results for all four data sets, due to the size, are presented within the Supplementary Material (available online at https://doi.org/10.1155/2017/8365685).

Relative conditional probability errors $|\varepsilon_i^m(r)|/p_i^m(r)$ [%] are plotted in Figure 3, for series $\mathbf{X}$ and $\mathbf{Y}$ both normally distributed and for $\tau = 1$. Satisfactory results are obtained for an extremely atypical threshold level $r = 1.50$. For a typical threshold $r = 0.15$, error is below 10% only for large N and $m = 1$. The results are in accordance with reliability criteria $N - m + 1 > (10 \text{ or } 100)/p_i^m(r)$ stating that N or $p_i^m(r)$ should be large. Indeed, $p_i^m(r)$ is defined as a product of m probabilities (14), so it is at its largest if $m = 1$, while increased threshold r augments the number of template matches $N_1(i)$ (4), again enlarging $p_i^m(r)$.

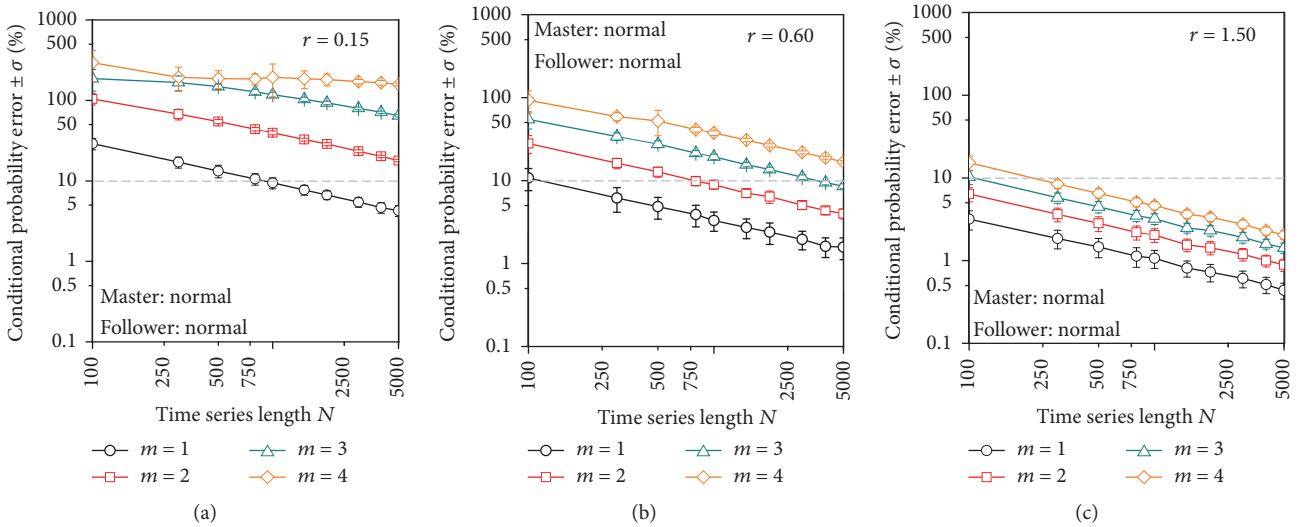

FIGURE 3: The relative conditional probability error [%] in artificial data for a typical threshold value $r = 0.15$ (a), for a higher threshold $r = 0.60$ (b), and for an unusually high threshold $r = 1.50$ (c); the gray dashed horizontal line marks 10% error; results are presented in a log-log plane as mean ± σ (standard deviation). Artificial master and follower series are both normally distributed.

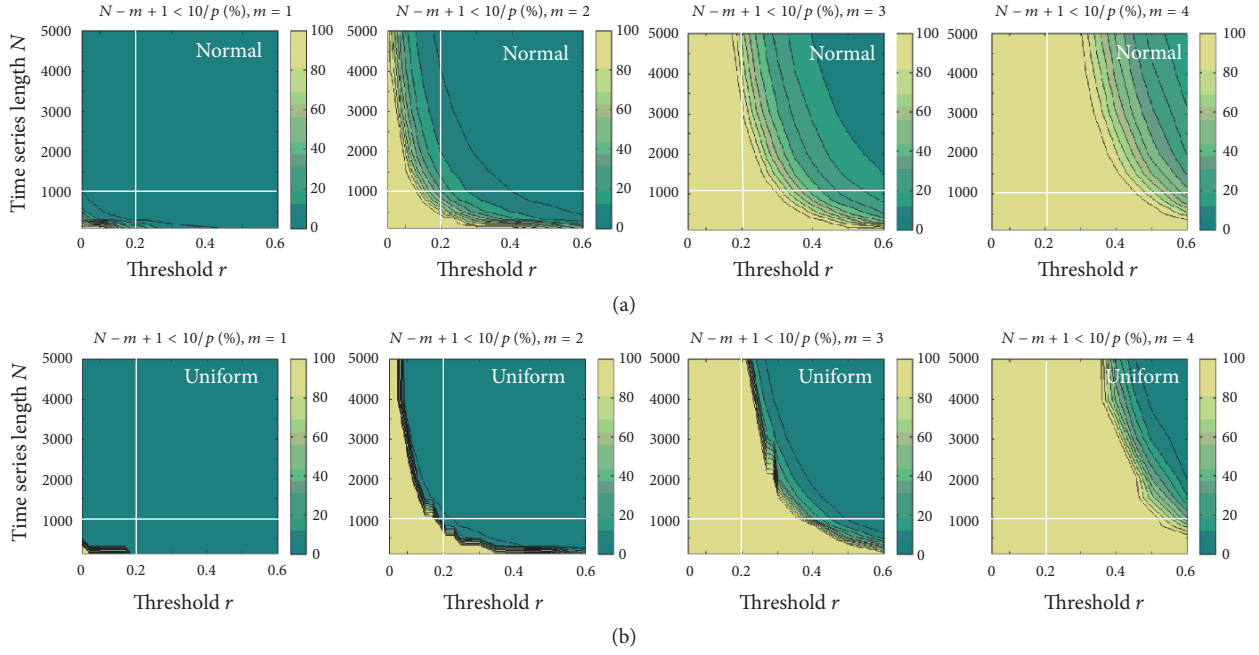

FIGURE 4: Percentage of estimates $\widehat{p}_i^m(r)$ in artificial data that fail to satisfy the criterion $N - m + 1 \geq 10/\widehat{p}_i^m(r)$ [%], presented in threshold-length (r-N) plane, for $m = 1, 2, 3, 4$; failures are presented by color changes from green (0% failures) to yellow (100% failures); (a) **X** and **Y** normally distributed; (b) **X** and **Y** uniformly distributed; white horizontal and vertical lines cut each plane at typical parameter values $r = 0.2$ and $N = 1000$.

The reliability of $\widehat{p}_i^m(r)$ estimate is checked comparing the data length $N - m + 1$ with the required minimum $10/p_i^m(r)$. The percentage of test failures is presented in Figure 4, in an r-N plane, where 0% failures are presented by green color that gradually changes to yellow (100% failures). The white line marks classical r and N values, revealing that, for $m = 3$ and 4, the estimates that implement classical parameters are unreliable. Nonlinear interrelation of r, N, and m in Figure 4 also points out that the choice of parameters that would yield a stable working point is not a straightforward task.

The estimation error of summand $\widehat{\Phi}$ (12) exposes two problems. The first one is a lack of matches ($\widehat{p}_i^m(r) = 0$) that induce logarithms of zero in (6) which is, as shown in Figure 5, a subset of all unreliable probabilities from Figure 4. The second problem is an error accumulation (12).

Figure 6 shows a line graph of summand Φ and its changes with respect to series length N if it is evaluated by a formula (exact values), if it is estimated in a traditional way, and if a correction (9) is applied. This correction does attenuate estimation errors, even for high m values, but it

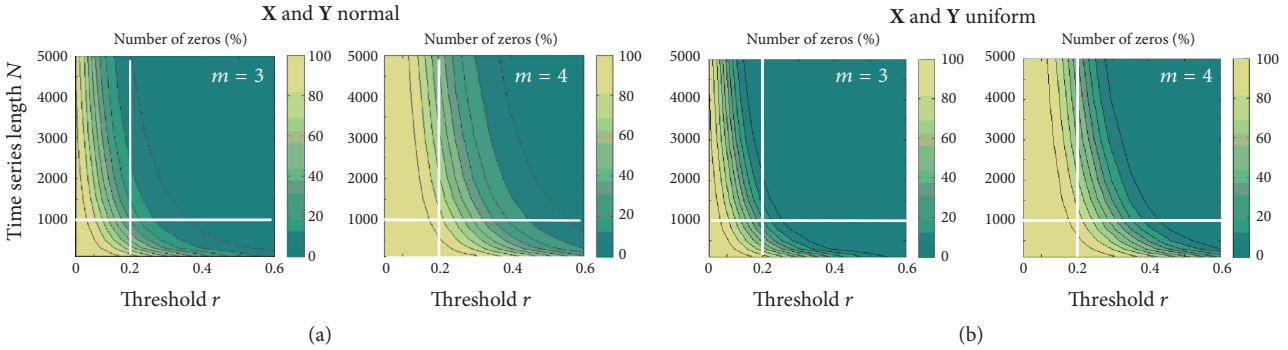

FIGURE 5: Number of $\widehat{p}_i^m(r) = 0$ estimates [%] in artificial data presented in threshold-length (r-N) plane for $m = 3$ and 4; color changes from green (0% zero matches) to yellow (100% zero matches); (a) **X** and **Y** normally distributed; (b) **X** and **Y** uniformly distributed.

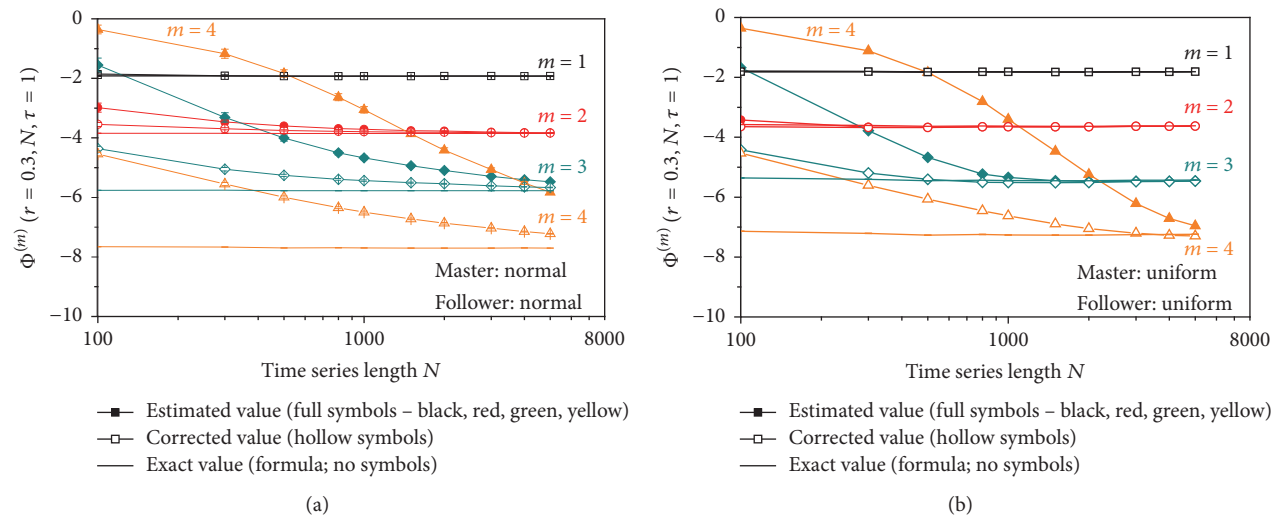

FIGURE 6: Summand Φ for $r = 0.3$: estimated omitting the zero probability, estimated and corrected, and calculated exactly using a formula; (a) **X** and **Y** normally distributed; (b) **X** and **Y** uniformly distributed.

cannot be used alone, as it removes a subset of the problem only. The convergence of summand $\widehat{\Phi}$ towards its true value depends on data type: uniform data achieve the correct limit for shorter lengths N. The convergence is also m-dependent, requiring different data lengths to achieve the same limit. Since $\widehat{X}ApEn$ is defined as a difference of $\widehat{\Phi}$ values (7), the fact that each summand $\widehat{\Phi}$ adds its own and independent estimation error is a further source of $\widehat{X}ApEn$ instability.

Figure 7 shows two-dimensional $XApEn$ profiles. Values calculated using the derived formulae ((a) and gray lines in (b) and (c)) verify the known fact that $XApEn$ linearly decreases with the logarithm of threshold value [5]. The major conclusion is that the true $XApEn$ values are influenced neither by time series length N nor by template length m. Frequent notions that $XApEn$ monotonously increases with N until a plateau is reached or that its value decreases with m are a consequence of probability underestimation that decreases with series length and eventually disappears. The panels in the second row of (a) show corrected $\widehat{X}ApEn$ estimates that are in good accordance with true values for $m = 1$, but showing increased discrepancies for $m = 2$ and 3. If no correction is applied (the third row of (a)), $\widehat{X}ApEn$ substantially diverges from the correct values. (b) and (c) show $\widehat{X}ApEn$ as a line graph. The discrepancy between the true and estimated values points out that generally accepted guidelines for parameter choice do not offer a safe $\widehat{X}ApEn$ estimation.

3.2. Stable Working Point in Cardiovascular Environment. To verify the accuracy of the derived equation (17), we followed the recommendations from [15, 16], where their equations are validated with respect to $ApEn$ relative error. For each one of SBP-PI (or R-R) and PI (or R-R)-SBP signal pairs, of animals (or volunteers), a threshold $r_{\text{TH-X}}$ was evaluated according to (17) and used as a parameter for $XApEn(r_{\text{TH-X}})$ estimation. The true maximal $XApEn(r_{\max})$ value is provided by a time-consuming procedure of finding a threshold profile. The corresponding relative error $\varepsilon_{\text{XA_max}}$ is presented in Table 2. The results estimated from signals recorded in human volunteers are presented in the italic part of Table 2. The relative error is below 2%, except for very short data lengths ($N = 300$) and $m = 1$ when it reaches 6%; unfortunately,

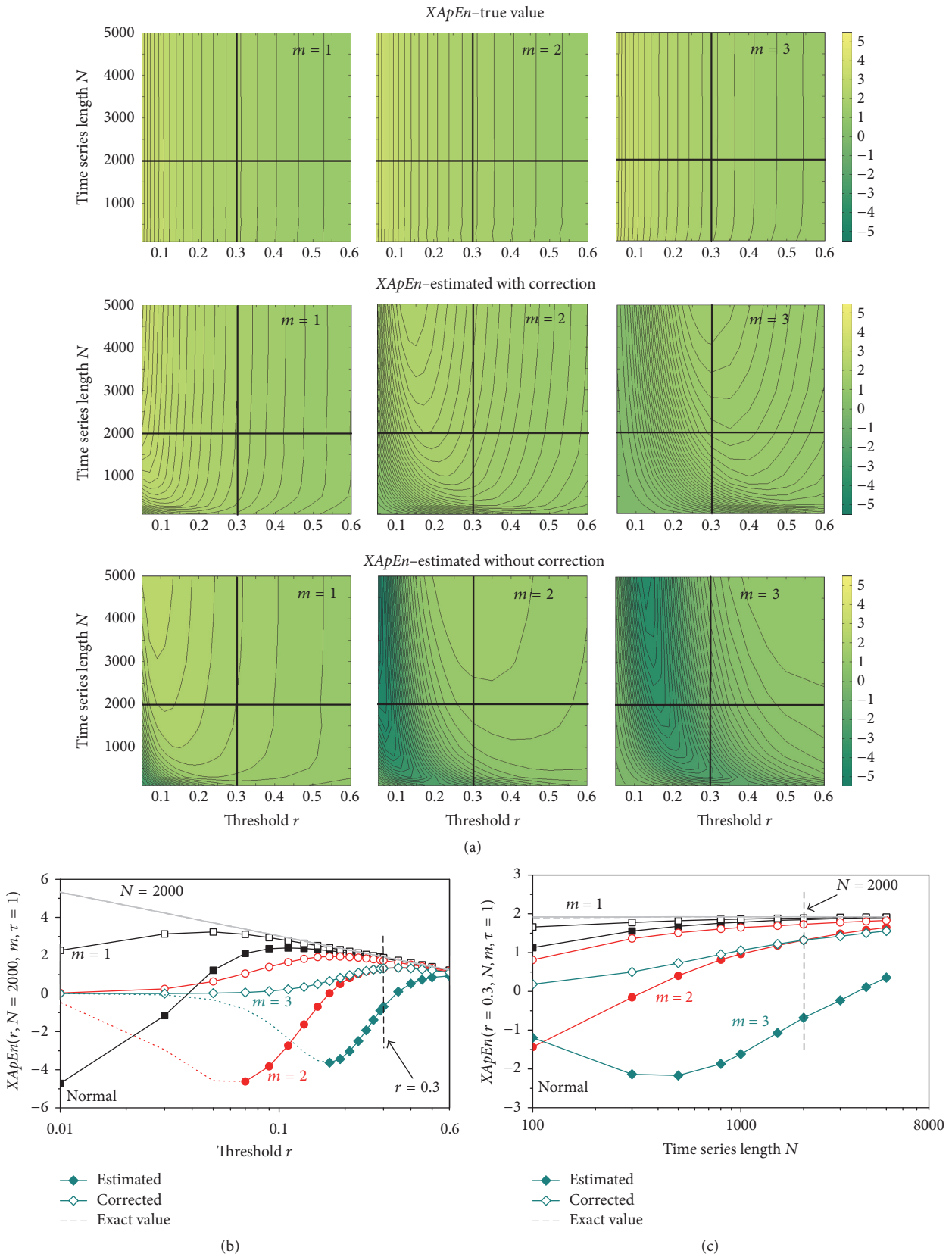

FIGURE 7: *XApEn* of artificial data with normal distribution in threshold-length (r-N) plane, for $m = 1, 2$, and 3. The three rows of (a) show, respectively, calculated (true) *XApEn*, *XApEn* estimated with correction, and *XApEn* estimated omitting log(0). Dark green color corresponds to *XApEn* estimated within the unstable N-r-m parameter region. Light green indicates low *XApEn*, while yellow color indicates high *XApEn*. Horizontal cuts at $N = 2000$ are presented as line graph in (b); vertical cuts at $r = 0.3$ are presented as line graph in (c).

Table 2: Relative error of $XApEn(r_{\text{TH-X}})$ with respect to $XApEn(r_{\max})$ in real signals [%].

N	$\varepsilon_{\text{XA_max}} = (\lvert XApEn(r_{\text{TH-X}}) - XApEn(r_{\max})\rvert / XApEn(r_{\max})) \cdot 100$							
	X = PI, Y = SBP				**X = SBP, Y = PI**			
	$m = 1$	$m = 2$	$m = 3$	$m = 4$	$m = 1$	$m = 2$	$m = 3$	$m = 4$
300	*5.16 ± 0.40*	*1.25 ± 0.28*	*1.61 ± 0.21*	*5.51 ± 0.75*	*6.40 ± 0.61*	*2.42 ± 0.49*	*2.85 ± 0.65*	*5.60 ± 0.88*
500	*2.57 ± 0.25*	*1.13 ± 0.21*	*2.61 ± 0.51*	*2.91 ± 0.57*	*3.61 ± 0.39*	*1.74 ± 0.29*	*1.68 ± 0.34*	*2.83 ± 0.60*
750	*1.57 ± 0.18*	*0.90 ± 0.21*	*1.93 ± 0.49*	*2.06 ± 0.44*	*2.09 ± 0.26*	*1.09 ± 0.25*	*1.56 ± 0.28*	*1.62 ± 0.43*
2000	0.64 ± 0.17	1.07 ± 0.26	1.50 ± 0.45	1.83 ± 0.54	0.49 ± 0.16	1.43 ± 0.29	1.96 ± 1.40	2.62 ± 0.47
2500	0.46 ± 0.07	0.88 ± 0.14	1.29 ± 0.29	1.61 ± 0.42	0.32 ± 0.05	1.01 ± 0.22	1.45 ± 0.29	2.99 ± 0.47
3000	0.80 ± 0.16	0.91 ± 0.18	0.99 ± 0.25	1.22 ± 0.26	0.33 ± 0.08	0.99 ± 0.18	0.94 ± 0.16	2.03 ± 0.38
3500	0.67 ± 0.12	1.04 ± 0.19	1.89 ± 0.67	2.68 ± 1.28	0.52 ± 0.14	1.41 ± 0.33	1.58 ± 0.47	2.64 ± 0.58
4000	1.03 ± 0.20	1.65 ± 0.28	1.58 ± 0.26	1.15 ± 0.23	1.08 ± 0.25	1.22 ± 0.23	1.09 ± 0.24	1.79 ± 0.45
4500	0.68 ± 0.18	1.41 ± 0.39	1.72 ± 0.59	2.80 ± 0.73	0.94 ± 0.18	1.20 ± 0.30	1.90 ± 0.92	2.28 ± 1.33
5000	1.59 ± 0.36	1.57 ± 0.44	1.73 ± 0.61	2.26 ± 0.75	0.42 ± 0.08	2.20 ± 0.39	1.74 ± 0.56	1.64 ± 0.40

Results are presented as mean ± SEM. Results of 41 human volunteers are shown in the first three italic rows. Results of 25 rats in different conditions (total of 50 signals) are presented in roman rows.

Table 3: Relative error of $ApEn(r_{\text{TH-A}})$ with respect to $ApEn(r_{\max})$ [%] in real signals.

N	$\varepsilon_{\text{A_max}} = (\lvert ApEn(r_{\text{TH-A}}) - ApEn(r_{\max})\rvert / ApEn(r_{\max})) \cdot 100$			
	X = PI		**X = SBP**	
	$r_{\text{TH-A}}$ [15]	$r_{\text{TH-A}}$ [16]	$r_{\text{TH-A}}$ [15]	$r_{\text{TH-A}}$ [16]
2000	3.46 ± 0.53	4.07 ± 0.54	1.95 ± 0.33	2.33 ± 0.35
3000	3.23 ± 0.54	3.82 ± 0.56	2.30 ± 0.35	2.91 ± 0.48
4000	3.72 ± 0.65	4.40 ± 0.67	2.86 ± 0.48	3.33 ± 0.51
5000	3.75 ± 0.67	6.45 ± 1.26	2.68 ± 0.43	5.63 ± 1.29

Error is evaluated according to the guidelines from [15] and from [16]. Results are presented as mean ± SEM, averaged over 100 time series: 50 data series of Wistar and borderline hypertensive rats in baseline and in stress, repeated for $m = 2$ and for $m = 3$.

this corresponds to the ambulatory records that cannot be too long.

For the sake of comparison, we estimated *ApEn* error from our data as well. We applied $r_{\text{TH-A}}$ calculated according to [15] (see (18)) and according to [16]. The $r_{\text{TH-A}}$ relative error is shown in Table 3, providing the following conclusions: (1) error level is lower if the equations from [15] are used and (2) comparison of results in Tables 2 and 3 verifies that our expressions (17) are equal in performance to expressions (18) derived by Lu et al. in [15, 16].

The value $r_{\text{TH-X}}$ cannot be applied, since the percentage of the probabilities that fail the weak and strong criteria is almost 100% (Figure 8). But this threshold reflects the nature of data and it can be used as a reference for thresholds r_{XW} and r_{XS}. Their implementation reduces the failures, as shown in Figure 8.

The actual threshold values calculated from real signals are shown in Table 4. For the sake of comparison, threshold values for normally distributed artificial data are also plotted (Figure 9). These thresholds show that the traditional guidelines (0.15, 0.2, and 0.35) considerably underestimate the actual requirements for the reliable *XApEn* estimation. Even if $m = 1$, the threshold required for strong reliability may exceed $r = 3$. Although it was speculated [1] that detailed system information would be lost if r values were larger than $0.1 \cdot \sigma$ or $0.2 \cdot \sigma$ (for *ApEn*), meaning that if the threshold exceeds these values a template would always match its follower, in investigated cardiovascular signals, this assumption does not hold as the evaluated high threshold levels are considerably below the amplitude range of the observed data.

The developed sets of threshold expressions are primarily intended for cardiovascular signal analysis. The artificial signals used as well are uniform on segment (with bounded amplitudes) and Gaussian (with increased incidence of small amplitudes, but unbounded). Both artificial distributions are symmetric. The amplitudes of real signals (PI, SBP, and R-R) are bounded by physiological constraints. Signal asymmetry is expressed by skewness factor, shown in Table 5. Cardiovascular data can be skewed to the left and to the right, so Table 5 presents the average of absolute skewness values. SBP and PI signals exhibit a level of asymmetry comparable to Rayleigh distribution (skewness ≈ 0.631), but below the skewness of exponential distribution (skewness ≈ 2). Threshold evaluation in signals with highly skewed distribution would be a subject for follow-up studies. In particular, it would be precious to explore an important class of interspike interval time series, with distributions that are close to exponential. A memoryless property of exponential distribution might affect the values of differential time series standard deviation σ_D, necessary for (17) and (18).

Table 4: Threshold values obtained from real signals.

(a) Threshold $r_{\text{TH-X}}$ for which *XApEn* reaches its maximal value (17)

N	**X = PI, Y = SBP**				**X = SBP, Y = PI**			
	$m = 1$	$m = 2$	$m = 3$	$m = 4$	$m = 1$	$m = 2$	$m = 3$	$m = 4$
300	*0.05 ± 0.01*	*0.24 ± 0.01*	*0.44 ± 0.01*	*0.62 ± 0.01*	*0.05 ± 0.00*	*0.22 ± 0.01*	*0.40 ± 0.01*	*0.55 ± 0.02*
500	*0.05 ± 0.01*	*0.21 ± 0.00*	*0.39 ± 0.01*	*0.53 ± 0.00*	*0.04 ± 0.00*	*0.19 ± 0.00*	*0.35 ± 0.01*	*0.47 ± 0.01*
750	*0.04 ± 0.01*	*0.18 ± 0.04*	*0.35 ± 0.01*	*0.47 ± 0.01*	*0.04 ± 0.01*	*0.16 ± 0.00*	*0.31 ± 0.01*	*0.41 ± 0.01*
2000	0.05 ± 0.01	0.19 ± 0.00	0.37 ± 0.01	0.51 ± 0.01	0.04 ± 0.00	0.14 ± 0.00	0.27 ± 0.00	0.60 ± 0.01
2500	0.05 ± 0.01	0.18 ± 0.00	0.35 ± 0.01	0.48 ± 0.01	0.04 ± 0.00	0.13 ± 0.00	0.25 ± 0.01	0.34 ± 0.01
3000	0.04 ± 0.01	0.18 ± 0.00	0.33 ± 0.01	0.46 ± 0.01	0.03 ± 0.00	0.13 ± 0.00	0.24 ± 0.00	0.33 ± 0.05
3500	0.04 ± 0.01	0.17 ± 0.00	0.32 ± 0.01	0.45 ± 0.01	0.03 ± 0.00	0.12 ± 0.00	0.23 ± 0.00	0.31 ± 0.05
4000	0.04 ± 0.01	0.17 ± 0.00	0.31 ± 0.01	0.44 ± 0.01	0.03 ± 0.00	0.17 ± 0.00	0.22 ± 0.00	0.30 ± 0.05
4500	0.04 ± 0.01	0.11 ± 0.00	0.30 ± 0.01	0.43 ± 0.01	0.03 ± 0.00	0.11 ± 0.00	0.21 ± 0.00	0.29 ± 0.01
5000	0.04 ± 0.01	0.16 ± 0.00	0.29 ± 0.01	0.42 ± 0.01	0.03 ± 0.00	0.11 ± 0.00	0.20 ± 0.00	0.29 ± 0.01

(b) Threshold r_{XW} for which at least 95% of the probabilities satisfy $N - m + 1 > 10/\widehat{p}_i^m(r_{\text{XW}})$ (19)

N	**X = PI, Y = SBP**				**X = SBP, Y = PI**			
	$m = 1$	$m = 2$	$m = 3$	$m = 4$	$m = 1$	$m = 2$	$m = 3$	$m = 4$
300	*0.46 ± 0.00*	*0.84 ± 0.01*	*1.24 ± 0.01*	*1.62 ± 0.01*	*0.45 ± 0.00*	*0.82 ± 0.01*	*1.20 ± 0.01*	*1.55 ± 0.02*
500	*0.45 ± 0.00*	*0.81 ± 0.00*	*1.19 ± 0.01*	*1.53 ± 0.01*	*0.44 ± 0.00*	*0.78 ± 0.00*	*1.15 ± 0.01*	*1.47 ± 0.01*
750	*0.38 ± 0.00*	*0.69 ± 0.00*	*1.03 ± 0.01*	*1.32 ± 0.01*	*0.38 ± 0.00*	*0.67 ± 0.00*	*0.99 ± 0.01*	*1.26 ± 0.01*
2000	0.39 ± 0.00	0.70 ± 0.00	1.05 ± 0.01	1.36 ± 0.01	0.37 ± 0.00	0.65 ± 0.00	0.95 ± 0.01	1.21 ± 0.01
2500	0.35 ± 0.00	0.63 ± 0.00	0.95 ± 0.01	1.23 ± 0.01	0.34 ± 0.00	0.58 ± 0.00	0.85 ± 0.01	1.09 ± 0.01
3000	0.34 ± 0.00	0.63 ± 0.00	0.93 ± 0.01	1.22 ± 0.01	0.33 ± 0.00	0.59 ± 0.00	0.84 ± 0.00	1.08 ± 0.01
3500	0.34 ± 0.00	0.62 ± 0.00	0.92 ± 0.01	1.20 ± 0.01	0.33 ± 0.00	0.57 ± 0.00	0.83 ± 0.00	1.06 ± 0.01
4000	0.34 ± 0.00	0.62 ± 0.00	0.91 ± 0.01	1.19 ± 0.01	0.33 ± 0.00	0.57 ± 0.00	0.82 ± 0.00	1.05 ± 0.01
4500	0.34 ± 0.00	0.61 ± 0.00	0.90 ± 0.01	1.18 ± 0.01	0.33 ± 0.00	0.56 ± 0.00	0.81 ± 0.00	1.04 ± 0.01
5000	0.34 ± 0.00	0.61 ± 0.00	0.89 ± 0.01	1.17 ± 0.01	0.33 ± 0.00	0.56 ± 0.00	0.80 ± 0.00	1.04 ± 0.01

(c) Threshold r_{XS} for which at least 95% of the probabilities satisfy $N - m + 1 > 100/\widehat{p}_i^m(r_{\text{XS}})$ (20)

N	**X = PI, Y = SBP**				**X = SBP, Y = PI**			
	$m = 1$	$m = 2$	$m = 3$	$m = 4$	$m = 1$	$m = 2$	$m = 3$	$m = 4$
300	*1.42 ± 0.00*	*2.21 ± 0.02*	*3.28 ± 0.04*	*4.37 ± 0.09*	*1.40 ± 0.01*	*2.12 ± 0.02*	*3.07 ± 0.05*	*3.99 ± 0.10*
500	*1.08 ± 0.00*	*1.73 ± 0.14*	*2.60 ± 0.04*	*3.41 ± 0.01*	*1.06 ± 0.00*	*1.65 ± 0.01*	*2.41 ± 0.00*	*3.06 ± 0.07*
750	*0.96 ± 0.00*	*1.54 ± 0.01*	*2.28 ± 0.03*	*2.93 ± 0.05*	*0.96 ± 0.00*	*1.47 ± 0.01*	*2.13 ± 0.03*	*2.64 ± 0.04*
2000	0.91 ± 0.00	1.50 ± 0.01	2.29 ± 0.03	3.06 ± 0.05	0.88 ± 0.00	1.33 ± 0.01	1.89 ± 0.02	2.29 ± 0.00
2500	0.90 ± 0.00	1.46 ± 0.01	2.21 ± 0.03	2.93 ± 0.05	0.88 ± 0.00	1.31 ± 0.01	1.82 ± 0.02	2.20 ± 0.03
3000	0.89 ± 0.00	1.44 ± 0.00	2.14 ± 0.03	2.83 ± 0.04	0.87 ± 0.00	1.29 ± 0.01	1.77 ± 0.02	2.14 ± 0.03
3500	0.89 ± 0.00	1.41 ± 0.01	2.08 ± 0.03	2.76 ± 0.04	0.87 ± 0.00	1.27 ± 0.01	1.72 ± 0.02	2.07 ± 0.02
4000	0.88 ± 0.00	1.40 ± 0.01	2.05 ± 0.02	2.72 ± 0.04	0.86 ± 0.00	1.25 ± 0.01	1.67 ± 0.02	2.00 ± 0.03
4500	0.88 ± 0.00	1.39 ± 0.01	2.00 ± 0.02	2.66 ± 0.04	0.86 ± 0.00	1.24 ± 0.01	1.63 ± 0.02	1.95 ± 0.02
5000	0.88 ± 0.00	1.37 ± 0.01	1.97 ± 0.02	2.62 ± 0.04	0.86 ± 0.00	1.23 ± 0.01	1.60 ± 0.00	1.93 ± 0.02

Results are presented as mean ± SEM, averaged over 50 time series of both Wistar and borderline hypertensive rats, both in baseline and in stress, and averaged over 41 time series of volunteers; results from human volunteers are in italics.

Table 5: Level of asymmetry of real signals (skewness).

	Rats		Volunteers	
	SBP	PI	SBP	R-R
Absolute skewness	0.64 ± 0.86	0.48 ± 1.02	0.42 ± 0.54	0.35 ± 0.33
Portion of signals with negative skewness [%]	36%	24%	46%	60%

Absolute skewness is expressed as mean ± σ; each signal set comprises a couple of highly skewed signals that influence the standard deviation.

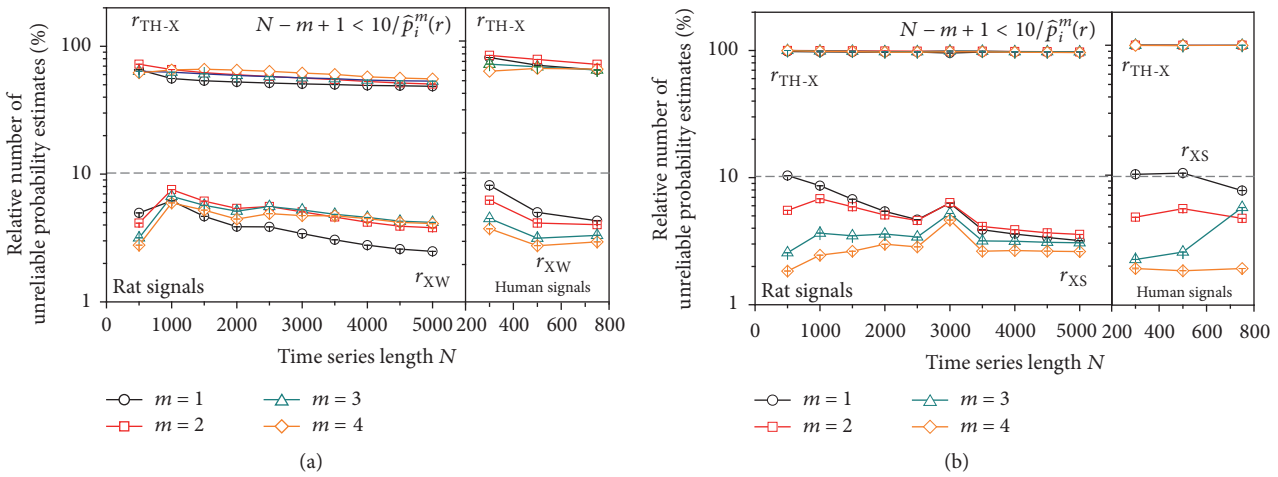

FIGURE 8: Unreliable estimated probabilities $\hat{p}_i^m(r)$ [%] in real signals; (a) $r \in \{r_{XW}, r_{TH-X}\}$ and weak criterion is applied; (b) $r \in \{r_{XS}, r_{TH-X}\}$ and strong criterion is applied. The gray dashed horizontal line marks 10% of the unreliable probability estimates. The left part of each panel shows the results of Wistar and borderline hypertensive rats at baseline and stress; the right part of each panel shows the results of volunteers.

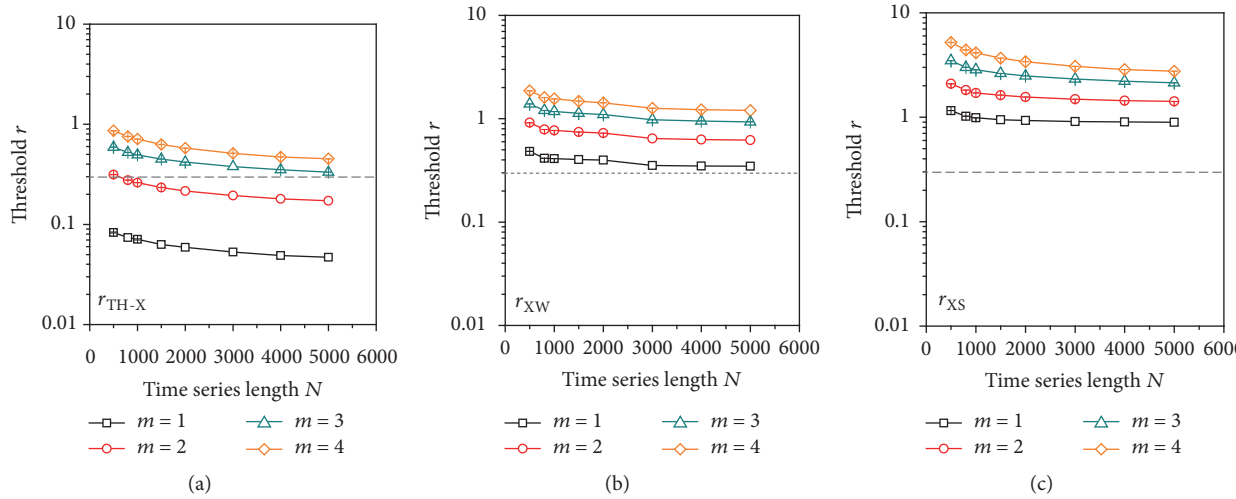

FIGURE 9: Calculated threshold values for artificial data, with signals **X** and **Y** both normally distributed. (a) Threshold for which *XApEn* gets maximal value (see (17)). (b) Threshold for which at least 95% of the probabilities satisfy weak criterion (see (19)). (c) Threshold for which at least 95% of the probabilities satisfy strong criterion (see (20)). The gray horizontal dashed line corresponds to $r = 0.3$.

Finally, Table 6 presents a brief recap of the steps necessary for reliable *XApEn* estimation.

4. Conclusion

This paper performed an analysis of *XApEn* parameter space and proposed methods for adjusting both the procedure and its parameter choice. Artificial environment with known data distribution allowed exact mathematical evaluation of reference *XApEn* values and their comparison to the estimated ones. The comparison indicated vast regions in *XApEn* parameter space (threshold r, data length N, and template length m) with unstable estimation of both *XApEn* and its constitutive components. It is also shown that parameter interrelationship is nonlinear and depends on data type. An established relationship between the theory of binary probability estimation [27] and template matching procedure proved that the source of instability is unreliable probability estimation, which is a consequence of working within the unstable region. Stable *XApEn* estimates should remain constant for increased data lengths and the frequently observed monotonous increase with N is just another form of instability. It is also shown that the traditional guidelines work within the regions of instability. The proposed correction attenuated but did not eliminate the problem.

The solution is to target the parameters within the stable region of the parameter space and to perform the parameter choice jointly, due to the nonlinear properties of their relationship. Real environment does not offer an advantage of exact mathematical error analysis, so a set of parameters for stable and reliable estimation is ensured deriving a novel set of threshold r expressions. The expressions take into

Table 6: Steps for reliable *XApEn* estimation.

Step	Explanation
(1)	Choose two time series and specify which one would be master series; define N and m (preferably $m = 2$); perform standard scoring of both series.
(2)	Find the differential time series both for master and for follower time series, and calculate their respective standard deviations σ_{DX} and σ_{DY}.
(3)	Calculate $r_{\text{TH-A}}$ (see (18)).
(4)	Calculate $r_{\text{TH-X}}$ (see (17)).
(5)	Select reliability criterion; a strong criterion requires long data sets, so a weak criterion is suggested.
(6)	Calculate r_{XW} (see (19)), weak criterion (preferably); or calculate r_{XS} (see (20)), strong criterion.
(7)	Estimate $XApEn(N, m, r_{\text{XW}})$.

account length N, template m, statistical data properties, and reliability criterion (weak or strong, [27]). The consistency of estimates is validated for typical cases of short records (ambulatory patients) and long records (small laboratory animals). It is shown that classical guidelines underestimate the threshold levels and data lengths required for consistent results.

This analysis can be employed for all the entropy measures that rely on probability estimation. The proposed *XApEn* improvements may contribute to its wider implementation in the domain of related physiological processes such as baroreflex studies. In order to facilitate and promote the wider *XApEn* deployment, we have included the detailed instructions within the Supplementary Material.

Although the method is validated in cardiovascular data, it can be equivalently applied for finding correct parameters for *XApEn* analysis of processes that are not necessarily biomedical, provided that their distribution is not too skewed. Further investigation would consider the signals with highly asymmetric distribution, for example, interspike interval time series, but also the signals with mismatched distribution where zero probability is not an error, but inherent signal property.

Conflicts of Interest

The authors declare that there are no conflicts of interest regarding the publication of this paper.

Acknowledgments

This work was supported by the Serbian Ministry of Education, Science and Technology Development, under Grants TR32040 and III41013. The authors acknowledge the support from the EU COST-Action CA15104-Body Communications Group. The authors are also grateful to Professor Dr. Harald Straus, University of Iowa, and to Professor Dr. Suave Lobodzinski, UCLA, for the inspiring discussions in October 2016.

References

[1] S. M. Pincus, "Approximate entropy as a measure of system complexity," *Proceedings of the National Academy of Sciences of the United States of America*, vol. 88, no. 6, pp. 2297–2301, 1991.

[2] S. Pincus, "Approximate entropy (ApEn) as a complexity measure," *Chaos*, vol. 5, no. 1, pp. 110–117, 1995.

[3] S. Pincus and B. H. Singer, "Randomness and degrees of irregularity," *Proceedings of the National Academy of Sciences of the United States of America*, vol. 93, no. 5, pp. 2083–2088, 1996.

[4] J. M. Yentes, N. Hunt, K. K. Schmid, J. P. Kaipust, D. McGrath, and N. Stergiou, "The appropriate use of approximate entropy and sample entropy with short data sets," *Annals of Biomedical Engineering*, vol. 41, no. 2, pp. 349–365, 2013.

[5] J. S. Richman and J. R. Moorman, "Physiological time-series analysis using approximate entropy and sample entropy," *American Journal of Physiology—Heart and Circulatory Physiology*, vol. 278, no. 6, pp. H2039–H2049, 2000.

[6] A. Porta, G. Baselli, D. Liberati et al., "Measuring regularity by means of a corrected conditional entropy in sympathetic outflow," *Biological Cybernetics*, vol. 78, no. 1, pp. 71–78, 1998.

[7] A. Porta, P. Castiglioni, V. Bari et al., "K-nearest-neighbor conditional entropy approach for the assessment of the short-term complexity of cardiovascular control," *Physiological Measurement*, vol. 34, no. 1, article no. 17, pp. 17–33, 2013.

[8] W. T. Chen, Z. Z. Wang, H. B. Xie, and W. Yu, "Characterization of surface EMG signal based on fuzzy entropy," *IEEE Transactions on Neural Systems and Rehabilitation Engineering*, vol. 15, no. 2, pp. 266–272, 2007.

[9] M. Costa, A. L. Goldberger, and C. Peng, "Multiscale entropy analysis of biological signals," *Physical Review E*, vol. 71, no. 2, Article ID 021906, 2005.

[10] P. Li, C. Liu, K. Li, D. Zheng, C. Liu, and Y. Hou, "Assessing the complexity of short-term heartbeat interval series by distribution entropy," *Medical and Biological Engineering and Computing*, vol. 53, no. 1, pp. 77–87, 2015.

[11] T. Skoric, O. Mohamoud, B. Milovanovic, N. Japundzic-Zigon, and D. Bajic, "Binarized cross-approximate entropy in crowdsensing environment," *Computers in Biology and Medicine*, vol. 80, pp. 137–147, 2017.

[12] X. Ning, Y. Xu, J. Wang, and X. Ma, "Approximate entropy analysis of short-term HFECG based on wave mode," *Physica A: Statistical Mechanics and its Applications*, vol. 346, no. 3-4, pp. 475–483, 2005.

[13] Y.-H. Pan, Y.-H. Wang, S.-F. Liang, and K.-T. Lee, "Fast computation of sample entropy and approximate entropy in biomedicine," *Computer Methods and Programs in Biomedicine*, vol. 104, no. 3, pp. 382–396, 2011.

[14] S. Zurek, P. Guzik, S. Pawlak, M. Kosmider, and J. Piskorski, "On the relation between correlation dimension, approximate entropy and sample entropy parameters, and a fast algorithm for their calculation," *Physica A: Statistical Mechanics and its Applications*, vol. 391, no. 24, pp. 6601–6610, 2012.

[15] S. Lu, X. Chen, J. K. Kanters, I. C. Solomon, and K. H. Chon, "Automatic selection of the threshold value r for approximate entropy," *IEEE Transactions on Biomedical Engineering*, vol. 55, no. 8, article no. 8, pp. 1966–1972, 2008.

[16] K. Chon, C. Scully, and S. Lu, "Approximate entropy for all signals," *IEEE Engineering in Medicine and Biology Magazine*, vol. 28, no. 6, pp. 18–23, 2009.

[17] P. Castiglioni and M. Di Rienzo, "How the threshold "r" influences approximate entropy analysis of heart-rate variability," in

Proceedings of the Computers in Cardiology 2008, CAR, pp. 561–564, Bologna, Italy, September 2008.

[18] C. Liu, C. Liu, P. Shao et al., "Comparison of different threshold values r for approximate entropy: Application to investigate the heart rate variability between heart failure and healthy control groups," *Physiological Measurement*, vol. 32, no. 2, pp. 167–180, 2011.

[19] J. F. Restrepo, G. Schlotthauer, and M. E. Torres, "Maximum approximate entropy and r threshold: A new approach for regularity changes detection," *Physica A: Statistical Mechanics and its Applications*, vol. 409, pp. 97–109, 2014.

[20] A. Boskovic, T. Loncar-Turukalo, O. Sarenac, N. Japundzic-Zigon, and D. Bajic, "Unbiased entropy estimates in stress: A parameter study," *Computers in Biology and Medicine*, vol. 42, no. 6, pp. 667–679, 2012.

[21] F. Kaffashi, R. Foglyano, C. G. Wilson, and K. A. Loparo, "The effect of time delay on approximate & sample entropy calculations," *Physica D. Nonlinear Phenomena*, vol. 237, no. 23, pp. 3069–3074, 2008.

[22] S. M. Pincus, T. Mulligan, A. Iranmanesh, S. Gheorghiu, M. Godschalk, and J. D. Veldhuis, "Older males secrete luteinizing hormone and testosterone more irregularly, and jointly more asynchronously, than younger males," *Proceedings of the National Academy of Sciences of the United States of America*, vol. 93, no. 24, pp. 14100–14105, 1996.

[23] P. Li, K. Li, C. Liu, D. Zheng, Z.-M. Li, and C. Liu, "Detection of coupling in short physiological series by a Joint Distribution Entropy Method," *IEEE Transactions on Biomedical Engineering*, vol. 63, no. 11, pp. 2231–2242, 2016.

[24] O. Šarenac, M. Lozić, S. Drakulić et al., "Autonomic mechanisms underpinning the stress response in borderline hypertensive rats," *Experimental Physiology*, vol. 96, no. 6, pp. 574–589, 2011.

[25] T. Ceranic, T. Loncar-Turukalo, B. Milovanovic, N. Japundzic-Zigon, and D. Bajic, "Cross-entropy of systolic blood pressure - Pulse interval: Automatic threshold and its reliability," in *Proceedings of the 2013 40th Computing in Cardiology Conference, CinC 2013*, pp. 1219–1222, Zaragoza, Spain, September 2013.

[26] M. P. Tarvainen, P. O. Ranta-aho, and P. A. Karjalainen, "An advanced detrending method with application to HRV analysis," *IEEE Transactions on Biomedical Engineering*, vol. 49, no. 2, pp. 172–175, 2002.

[27] M. C. Jeruchim, "Techniques for Estimating the Bit Error Rate in the Simulation of Digital Communication Systems," *IEEE Journal on Selected Areas in Communications*, vol. 2, no. 1, pp. 153–170, 1984.

[28] H.-T. Wu, C.-Y. Lee, C.-C. Liu, and A.-B. Liu, "Multiscale cross-approximate entropy analysis as a measurement of complexity between ECG R-R interval and PPG pulse amplitude series among the normal and diabetic subjects," *Computational and Mathematical Methods in Medicine*, vol. 2013, Article ID 231762, 2013.

[29] S. Alesci, P. E. Martinez, S. Kelkar et al., "Major depression is associated with significant diurnal elevations in plasma interleukin-6 levels, a shift of its circadian rhythm, and loss of physiological complexity in its secretion: Clinical implications," *Journal of Clinical Endocrinology and Metabolism*, vol. 90, no. 5, pp. 2522–2530, 2005.

[30] H.-T. Wu, C.-C. Liu, M.-T. Lo et al., "Multiscale cross-approximate entropy analysis as a measure of complexity among the aged and diabetic," *Computational and Mathematical Methods in Medicine*, vol. 2013, Article ID 324325, 7 pages, 2013.